Studies of Stellar Clusters

# Steps towards Asteroseismology

and

# A Search for Giant Planets

Ph. D. Dissertation

Hans Bruntt

Department of Physics and Astronomy
University of Aarhus
Denmark
DK-8000 Aarhus C

30 November 2002

Printed in Denmark by the “repro-center” at the
Department of Physics and Astronomy, University of Aarhus.

Cover design by Bo Jørgensen (*cf.* page 86).

ISBN 87–87548–03–8

Studies of Stellar Clusters

# Steps towards Asteroseismology

and

# A Search for Giant Planets

Ph. D. Dissertation

Hans Bruntt

# Preface

*At the end of days, at the end of time*
*When the Sun burns out will any of this matter?*
*Who will be there to remember who we were?*
*Who will be there to know that any of this had meaning for us?*
– Further (VNV Nation, © Mindbase 2000)

In the spring of 1996 I went to La Silla to observe with the Danish 1.54 m telescope for the first time. At that time I was an inexperienced but hopeful astronomy student. I was observing with the Ph. D. student Michael Viskum to complete a 24 night run on the $\delta$ Scuti star FG Virginis with two telescopes simultaneously (spectroscopy and photometry). A few nights we also observed two open clusters in order to perform Strömgren photometry which was the data for my master's thesis.

I learned to love the process of data reduction. At the risk of sounding like a border-line maniac scientist, but with the intent to express my profound interest I state that "juggling" with multi-dimensional data structures within the IDL language is to me like solving jig-saw puzzles. Also, the process of observing the same stellar clusters night after night to look for minute changes in the flux is a fascinating albeit exhausting experience. Furthermore my interest in astronomy and the pursuit of unravelling new wonders has kept me going until now.

That is why I went on from my master's thesis to take on another three years as a Ph. D. student. The title of my project in my application was "The Search for Giant Planets in the Globular Cluster 47 Tuc". In this application I had made a three-year schedule of what I would do. Basically, I stated that "we" would detect the transits of a few planets in 47 Tuc, observe these with spectroscopy with the `UVES/VLT` spectrograph, and constrain their masses and radii to within a few percent. Unfortunately, the title of the present dissertation is not "The Giant Planets in 47 Tuc". Despite 8.3 days of observations with the *Hubble Space Telescope*, no planets were detected in 47 Tuc.

The title became "Studies of Stellar Clusters..." which is an attempt to condense everything I have worked with in astronomy for the last three years. As the reader will soon realize, it is a trade-off between being concise and accurate at the same time. The title emphasizes that most of my work is based on photometric time-series of open clusters (NGC 6134 and NGC 6791) and globular clusters (Messier 4 and 47 Tucanae). The important point is that by observing clusters one has a sample of stars with the same approximate age and chemical composition. From theoretical calculations one can constrain the mass, temperature, and luminosity quite well for any object in the cluster (provided it really is a member).

Knowledge of the fundamental atmospheric parameters of a star is very important. This is essential if one seeks to (a) extract information from observed oscillation frequencies of a variable star (the M 4 project, *cf.* Chapter 3) or (b) understand the properties of a giant planet eclipsing the parent star (search for planets in NGC 6791, *cf.* Chapter 4).

Several space missions will be launched in the future to study the oscillations of nearby stars to probe the physical conditions in their interior (*e.g.* MOST, COROT, RØMER/MONS, EDDINGTON). This is analogous to the detailed studies of the "stellar quakes" on our Sun through *helioseismology*. Again, knowing the fundamental parameters of the stars is important. In most cases (EDDINGTON is the exception) these missons will study field stars. To know the properties of these stars we must rely on photometric colours and detailed spectroscopic studies. I have developed an automated software package (VWA) to carry out the otherwise time-consuming analysis of spectra of the main target stars of the COROT and RØMER/MONS missions (Chapter 5).

During the past years I have received great support from my supervisor Søren Frandsen. I especially thank Frank Grundahl who has taught me a lot about "old-school" photometry, while Brandon Tingley has always managed to make me smile even in my darkest hour ("Hans ... you are *plotting* your own downfall"). I also thank Hans Kjeldsen, Bjarne Thomsen, and Poul-Erik Nissen for always being willing to listen. I am grateful to Michael Viskum and especially Torben Arentoft for convincing me that astrophysics is the right path. Also thanks to Dennis Stello for reading the first draft of this dissertation.

I thank my external supervisor Werner W. Weiss from Vienna and the people I met during the eight months I lived there for, and who taught me the fine art of spectroscopy: Tanya Ryabchikova, Christian "James" Stütz, Paul "Mannhart" Knoglinger, Peter Mittermayer, Fritz Kupka, Ulrike Heiter, Theresa Lüftinger, and Konstanze Zwintz. Also thanks to Michael Maitzen and Ernst Paunzen for our collaboration on NGC 6134.

Special thanks to Peter B. Stetson with whom I survived a 10-night run at the CFHT telescope in Hawaii at an altitude of 4 200 meters. Thanks to Ron Gilliland at STScI for our fruitful collaboration on the 47 Tuc project. Also thanks to Claude Catala, Ilfan Bikmaev, and Conny Aerts: I hope we will be able to continue our collaboration.

Outside the yellow brick walls of the University of Aarhus I would not have survived long without the support of Søren "Tjum" Dideriksen, Lars B. "comatose delusion" Pedersen, Ole "xV" Munk, and Thomas "1999" Wernberg. A special thanks to Lars A. for technical advice and to Bo Jørgensen for designing the cover (showing NGC 6791 and M 4) of this dissertation ("18 pt Courier will *not* work, Hans..."). Mad props go out to Lasse/Cold187um. I also express my love for the expanding Bruntt family.

Above all – my warmest love goes to Malene Vestergård.

Hans Bruntt
Aarhus, November 28th, 2002

This is the second edition of the dissertation in which several typing errors have been corrected. I stress that only a few sentences have been changed or added, while the results and conclusions have not been changed. I am very grateful to T. Arentoft and D. Stello for their help with improving this final version.

Hans Bruntt
Aarhus, January 12th, 2003

# Contents

# Chapter I

# Introduction

## 1.1 Probing the Interior of the Stars

The work in this thesis presents the results of the projects I have worked on in the three years I have been a Ph. D. student with the asteroseismology group at the Department of Physics and Astronomy at the University of Aarhus in Denmark from September 1999 to November 2002. I have been working with Søren Frandsen as my supervisor for six years: first as a master's student and afterwards as a Ph. D. student. These have been some exciting years with my involvement in several projects. To be very concise, I can say that my work has been focused on variable stars with the aim of applying asteroseismology to probe the interior of stars.

Below I will give a brief introduction to fields I have studied. The subjects are asteroseismology of stars in clusters (chapters 2 and 3), the search for transits caused by giant planets (chapter 4), and the spectroscopic analysis of target stars for asteroseismology space missions (chapter 5).

## 1.2 The Birth of Asteroseismology

The discovery of the oscillations of the Sun has given astronomers a unique tool for probing the interior of our nearest star. This field of research is called helioseismology: the study of global oscillation modes which penetrate the gas sphere and which can be seen on the surface of the Sun. The oscillations are stochastically excited by the convective layers which constitute the outer $\sim 30\%$ of the Sun. For example the `MDI` instrument on the `SOHO` satellite measures the motion of thousands of grid points on the Solar surface (*e.g.* Vorontsov (2002)). When this data is processed through Fourier techniques from "changes with time" to the "frequency amplitude" domain, the Solar oscillations are seen as thousands of peaks in a distinct broad comb-like pattern at frequencies corresponding to periods of roughly five minutes.

Apart from the measurement of the neutrino flux coming from the fusion processes in the core, helioseismology is the only tool available for probing the physical conditions inside the Sun. The frequencies correspond to global eigenmodes that penetrate to different depths and hence the various modes of oscillation are affected by the physical nature in different layers of the gas. With inversion techniques a direct comparison with theoretical models can be made. Thus, one can measure how well the theoretical models describe the Sun and in turn find out if the physical assumptions (equation of state, opacity, nuclear generation rates, *etc.*) used as input to the model are correct or if there is evidence of processes (*e.g.* diffusion of chemical elements and the description of convection) that need a better description.

In the past two decades astronomers have attempted to measure the oscillations of stars other than the Sun, with the ultimate goal of studying these stars through *asteroseismology* in a way analogous to the highly successful use of helioseismology of the Sun.

Variable stars are found all over the Hertzsprung-Russell (luminosity *vs.* temperature) diagram. Several classes of variables are found in the "classical" instability strip – a region in the HR diagram where oscillations are driven through the so-called $\kappa$-mechanism (in these stars the energy of an oscillation perturbation can be stored where the opacity of the gas changes, *i.e.* at the location of different ionization states of H, He, or Fe). Variable stars in the Cepheid instability strip range from the A–F-type stars, *i.e.* the $\delta$ Scuti stars and $\gamma$ Doradus stars on the hydrogen main sequence, to more evolved stars in the helium-burning state, *i.e.* the RR Lyrae stars.

The problem is that in order to use the oscillation frequencies to compare with theoretical models, one must know which oscillation *modes* have been observed. An example of the successful application of asteroseismology is for the double mode oscillators of the RR Lyrae and SX Phœnicis type. In these cases one can often deduce that the modes that have been observed are radial (*i.e.* spherically symmetric): for RR Lyrae and SX Phe stars astronomers have constrained the mass of the stars to within 10% (*e.g.* Bono et al. (1996)). I have carried out a study of the SX Phe stars in 47 Tucanae in order to constrain the masses of these stars based on accurate period ratio estimates of double mode pulsators (Bruntt et al. 2001). These results will be discussed in chapter 2. Another particularly successful example of the application of asteroseismology concerns the constraints that can be placed on nuclear generation rates from the seismology of white dwarfs (see *e.g.* Metcalfe et al. (2001)).

I will now turn to the discussion of main sequence stars where oscillations are found in a wide range of stars, among them are $\beta$ Cephei-type, SPB, roAp, $\delta$ Scuti, $\gamma$ Dor, and solar-like stars. Below I will briefly discuss the problems and results related to $\delta$ Scuti stars and solar-like stars which I have studied.

Much research has been done in the field of $\delta$ Scuti stars of which more than 300 are known (Rodríguez et al. 2000). The goal of the Delta Scuti Network (Zima 1997) is to carry out multi-site multi-colour photometric surveys of a carefully selected sample of $\delta$ Scuti stars. The DSN recognize that in order to do detailed asteroseismic studies one needs not only to detect several modes but also to be able to identify as many modes as possible: this can be done through the phase differences seen in different colour bands (Garrido et al. 2002; Breger et al. 2002). So far, mode identification has been successful in a few cases for the field $\delta$ Scuti stars, *e.g.* FG Virginis (Breger et al. 1999), XX Pyx (Handler et al. 2000), and a few others (see Breger et al. (2002)). Today the problem of mode identification and the understanding of the physics that determines which modes are excited – or alternatively, which modes are damped – in $\delta$ Scuti stars is far from well-understood (Garrido et al. 2002; Balona & Evers 1999).

Astronomers have recognized the potential of applying asteroseismology to stars similar to the Sun. The most dominant global modes in the Sun have typical photometric amplitudes of $\delta L/L \simeq 4{\cdot}10^{-6}$. When measured though spectroscopy this corresponds to velocities of 25 cm s$^{-1}$. Hence, to be able to measure such small perturbations one needs very accurate photometry and spectroscopy. The measurement of solar-like oscillations in flux are seriously hampered by the scintillation noise due to the turbulent atmosphere of the Earth (see *e.g.*, Gilliland et al. (1993)). Therefore several space missions are now being planned to carry out asteroseismic studies of stars, *e.g.* `MOST` (Matthews et al. 2000), `COROT` (Baglin et al. 2001), `RØMER/MONS` (Christensen-Dalsgaard 2002), `EDDINGTON` (Roxburgh 2002), and `KEPLER` (Borucki et al. 1997). The only option for detecting solar-like oscillations from ground is through spectroscopy which requires extremely stable instruments[1]. Two different spectroscopic methods have been used to measure solar-like oscillations in nearby field stars: (a) either through direct observations of the Doppler shift of spectral lines (*e.g.* Brown & Gilliland (1990); Brown et al. (1991)) due to the motion of the surface of the star or (b) the monitoring of changes in the equivalent width of spectral lines (*e.g.* Kjeldsen et al. (1995), Kjeldsen et al. (2002)) because of changes in the temperature of the photosphere due to the oscillations.

In the last few years astronomers working in the field of solar-like oscillations have been quite successful[2]. After several tentative results during the past decade (Kjeldsen et al. 1995; Brown et al. 1991) oscillations have finally been unambiguously detected in the "solar twin" star $\alpha$ Centauris A (Bouchy & Carrier 2001) and $\beta$ Hyi (Bedding et al. 2001; Carrier et al. 2001). A particularly interesting case is the detection of oscillations in the G7-III giant star $\xi$ Hya (Frandsen et al. 2002). This star has a mass of around $3M_{\odot}$ (Frandsen et al. 2002; Stello 2002) and is in a much later evolutionary state than the Sun. This star is on the Hayashi track since core hydrogen burning has ceased, the outer layers of the star have expanded, and the outer convection zone has penetrated deep into the star.

The comb-like pattern which characterizes the solar-like oscillations is observed in $\eta$ Boo, $\alpha$ Cen, $\beta$ Hyi, and $\xi$ Hya. Tentative mode identification has been attempted and the theoretical modelling of the stars is ongoing. Already now much has been learned, but more detailed studies are required (*e.g.* long time series) to be able to use the observed frequencies to derive detailed information about the interior of these stars.

At this time the strategy of the future observational work must be considered. On one hand it is possible to organize relatively short campaigns dedicated to searches for oscillations in more stars, *e.g.* a sample of stars in different evolutionary stages. The strategy which I would recommend, would be to arrange multi-site

[1]The velocity amplitude of a few tens of cm s$^{-1}$ must be compared to the speed of light, *e.g.* at 5000 Å the shifts in wavelength will be of the order $10^{-6}$ Å.

[2]I have used the title of an article by Gough (2001) – "The Birth of Asteroseismology" – for this section.

spectroscopic campaigns and focus on just a small number of stars which would be studied in great detail. The preliminary results of $\alpha$ Cen, $\beta$ Hyi, and $\xi$ Hya suggest that we need much longer time-series from multiple sites in order to be able to detect additional low-amplitude modes and to get better frequency resolution to avoid problems with aliasing and thus be able resolve closely spaced modes.

## 1.3 Steps towards Asteroseismology

When attempting to use the tools of asteroseismology it is important to know the fundamental parameters ($T_{\rm eff}$, $\log g$, metallicity) of the stars with the highest possible accuracy (Brown et al. 1994; Pijpers 2003). One possibility is to study variable stars in stellar clusters. The advantage is that the stars which are members of a cluster have similar age and composition, and from the position in the colour-magnitude diagram one can put relatively tight constraints on the mass, radius, and evolutionary state – information which is not always available for field stars. An example of the study of $\delta$ Scuti stars in a cluster is the STEPHI campaign on Praesepe by Michel et al. (1999) and Hernandez et al. (1998), who found that high rotation rates are a limiting factor for the seismological interpretation (briefly mentioned in section 5.1).

The title of this dissertation – *"Studies of Stellar Clusters: Steps towards Asteroseismology [...]"* – emphasizes that I have specifically searched for oscillations among stars belonging to a cluster for the reasons mentioned above.

I have worked on several projects aimed at providing results to be able to use asteroseismic tools on stars. I have studied several classes of variable stars in the open clusters NGC 6134 ($\delta$ Scuti stars), NGC 6791 (detached eclipsing binary stars), and in the globular clusters 47 Tuc (SX Phe stars) and M 4 (giant stars). My work on NGC 6134 was published in the papers by Bruntt et al. (1999) and Rasmussen et al. (2002). The results from extensive campaigns on NGC 6791, 47 Tuc, and M 4 will be presented in chapters 2, 3, and 4.

Another part of my work has been dedicated to detailed spectroscopic analysis to determine the fundamental parameters of *field stars* which are the targets of future asteroseismology space missions. I have developed an automatic software package (VWA) to do this which is described in chapter 5. Furthermore, I have included three papers at the end of this dissertation in which the software package has been used (page 133ff).

## 1.4 The Hunt for Extra-solar Planets

One of the most interesting astronomical discoveries during the past decade has been the giant planets around other stars. The two first suspected (Earth-sized) planets to be found outside our solar system were detected in the changes in timing of a milli-second pulsar (Wolszczan 1994). Soon after the discovery of this rather exotic system the first giant exo-planet around a dwarf star was detected. Mayor & Queloz (1995) reported periodic radial velocity changes of the star 51 Pegasi which were interpreted as being due to the motion of the star caused by an orbiting giant gas planet in a close-in orbit. Since then *more than 100 planets* have been found by measuring radial velocities. The information that can be extracted from the spectroscopic velocity curves is orbital period, eccentricity, and a lower limit on the mass, *i.e.* $M \sin i$.

Several groups are hunting for planets. The most "productive" groups so far – in terms of the number of discovered planets – have concentrated on monitoring velocity changes in nearby F and G dwarfs with the use of ultra-stable spectrographs on moderate or large telescopes (Marcy & Butler 1998). After several years and many months of telescope observing time the impressive result is a data base of the orbital parameters of these (sometimes multiple) planet-star systems, ranging from the mass of Saturn up to 17 times the mass of Jupiter (Butler et al. 2002).

About 15% of the discovered giant planets are found within 0.1 A.U. of their parent star, hence they are often called hot Jupiters. The periods of these close-in giant planets are of the order of a few days. In the cases where the inclination of the orbital plane is close to the line of sight, transit-depths of a few percent are expected. This makes it feasible to search for transits through CCD photometry of dense fields of stars. According to Butler et al. (2002) around $P_{\rm GF} = 0.7\%$ of G and F–type stars in the solar neighbourhood have a giant planet within 0.1 A.U. and for around $P_{\rm geom} = 10\%$ of these the orbit of the planet will cause a transit. Assuming that binary stars will not harbour close-in planets and with an approximate binary fraction of $P_{\rm bin} = 50\%$, one would expect to find a planetary transit for every $1/[P_{\rm GF} * P_{\rm geom} * (1 - P_{\rm bin})] = 1/[0.007 * 0.10 * 0.5] \simeq 3\,000$ stars monitored. Additional factors must be taken into account and will be discussed in chapter 4: (1) The metallicity of the targets stars is important as demonstrated by Laughlin (2000) (see below). (2) In crowded fields an unresolved star may cause the detection of a "false" transit (see section 4.2). (3) The duration and duty-cycle of the observational campaign is important (see section 4.3.2 and Mallén-Ornelas et al. (2002)).

Only one of the giant planets found by the radial velocity searches has been confirmed by a transit in the measured flux light curve, *i.e.* the G0-type sub-dwarf star HD 209458. This was first reported by Henry et al. (1999) who observed part of the transit from the ground, and subsequently by Charbonneau et al. (2000) who used the `STIS` spectrograph on `HST` to obtain an ultra-high signal-to-noise light curve of four transits. With the combination of the orbital parameters from spectroscopy and the transit depth and duration from `HST`, Charbonneau et al. (2000) could constrain the radius of the planet to $1.27 \pm 0.02\ R_{\rm Jup}$ and its mass to $\simeq 0.63 M_{\rm Jup}$. The resulting density of the planet is $\rho \simeq 0.38$ g/cm$^3$: the low density is explained by the very hot atmosphere of the planet. More recently, Charbonneau et al. (2002) have used the `STIS` spectrograph on `HST` to find evidence for sodium in the atmosphere of the planet.

In order to understand under what conditions planets form, Laughlin (2000) and Gonzalez et al. (2001) have analysed spectra of some of the stars which have planets to look for systematic effects. Both studies agree that stars hosting planets have a significantly higher metallicity than the average of F and G stars in the solar neighbourhood. Laughlin (2000) finds the intriguing evidence that the more massive stars tend to have the highest metallicity which can be understood from the following scenario: when the cores of giant planets form, a fraction of the protoplanetary disc will fall into the star, thus causing a higher metallicity. Since hot stars have shallow convection zones, the in-fall of planetesimals will be distributed through a small fraction of the outer layers of the star compared to cooler stars which have deeper convection zones. Another possibility is that giant planets are more easily formed in a metal-rich environment.

I have been involved in two projects with the aim of detecting hot Jupiters in stellar clusters. The first one was the HST observations of the globular cluster 47 Tucanae in which no planets were found (Gilliland et al. 2000). Inspired by the results of Laughlin (2000) we made a search for planets in the metal-rich open cluster NGC 6791. The results of this will be given in chapter 4.

## 1.5 A Brief Summary of my Efforts

To conclude this introduction I will give a brief summary of the work I have done in the field of asteroseismology, the search for giant planets in stellar clusters, and the automated analysis of stellar spectra.

- *SX Phœnicis Stars in 47 Tucanae:* I have analysed a truly unique data set from the HST: a continuous light curve of 8.3 days in the $V$ and $I$ filters of the globular cluster 47 Tuc. The main goal was to search for exo-planet transits, but I used the data set to put firm constraints on the period ratio of the double-mode SX Phœnicis stars in the cluster. This proved to be a difficult task, since the brightest SX Phe stars were saturated in all images, and special care had to be taken when extracting the PSF magnitudes. By comparing the observed and theoretical pulsation period ratios, I was able to constrain the masses of the SX Phe stars to within 0.10–0.15 $M_\odot$ (Bruntt et al. 2001). The results will be presented in chapter 2.

- *Search for Oscillations in the Giant Stars in M 4:* This project is based on 39 nights of observations obtained over a period of 2.5 months of the globular cluster M 4 by using mainly the Danish 1.54m telescope, at La Silla, Chile. I have used the image subtraction software ISIS (Alard & Lupton 1998) which is probably the best option when trying to obtain milli-magnitude precision photometry of variable stars in crowded regions. The aim of the project is to detect the oscillations of the giant stars in the cluster and measure the large separation in the amplitude spectrum, which is predicted from theory. This will eventually lead to unique knowledge about the late evolution of stars. My preliminary results will be presented in chapter 3.

- *$\delta$ Scuti Stars in NGC 6134:* For my master's thesis I wrote a paper on Strömgren photometry of stars in the open clusters NGC 6134 and NGC 3680. The former cluster contains six known $\delta$ Scuti stars, some of which are multimode pulsators. In order to be able to compare the observed frequencies with the calculated ones, the fundamental parameters of the stars must be constrained. Unfortunately, we do not know which of the several possible excited modes have been observed. In the master's thesis of Rasmussen (2001) the rotational velocities of the $\delta$ Scuti stars were determined from low-resolution spectra. I used these spectra to do an abundance analysis to confirm the high metallicity of the cluster found by Bruntt et al. (1999). The rotational velocities and abundance analysis was published by Rasmussen et al. (2002) and in the IAU 210 proceedings (Bruntt & Frandsen (2003); reproduced on page 147).

- *Search for Transits of Giant Planets:* I have been involved in two projects to photometrically detect the transit of giant planets when they pass in front of their parent star. The first project was a search for planets with the Hubble Space Telescope. The globular cluster 47 Tuc was followed continuously for 8.3 days but unfortunately, no transits were detected. I have been part of a project with the aim of detecting planetary transits in the open cluster NGC 6791. I have observed this cluster for seven nights with the Nordic Optical Telescope in July 2001 and again from the Canada-France-Hawaiian Telescope in July 2002 as part of a multi-site campaign over 10 nights. The results of the first campaign will be presented in chapter 4.

- *Spectroscopy of Targets for Space Missions:* In November 2000 I left the University of Aarhus to work with the spectroscopy and asteroseismology group at the university of Vienna, led by Werner W. Weiss. Here I developed a software package (VWA) that can do abundance analysis of stellar spectra semi-automatically. This tool has been used to characterize the targets for the upcoming asteroseismology mission COROT (French) and will also be used on the targets for the RØMER/MONS (Danish) mission. It is important to know the fundamental parameters of the target stars for two reasons: (1) To be able to reject "complicated" stars (*i.e.* fast rotators, stars with anomalous abundances, *etc.*). (2) When the frequencies of the stars have been extracted, one needs accurate parameters of the stars to be able to make theoretical models of the stars which are as close as possible to the real star. These models will then be used as starting points when extracting the information from the observed frequency spectrum. I have attached three papers on spectroscopy at the end of this dissertation (page 133ff) which all make use of the software package VWA, which is described in detail in chapter 5.

# Chapter II

# SX Phœnicis Stars in 47 Tuc

> "I am optimistic that we can keep ourselves usefully occupied with $\delta$ Scuti stars until (and probably long after) the detection problems with Sun-like stars have been solved." – Brown (1998)

## 2.1 A Search for Planets in the Globular Cluster 47 Tucanae

In the spring of 1999 Ronald Gilliland (Space Telescope Science Institute, USA) proposed to use the Hubble Space Telescope to search for planets in the globular cluster 47 Tucanae. The idea was to search for the transits caused by giant planets when occulting the stellar surface. With the WFPC/II camera on HST around 40 000 stars at the turn-off and fainter were monitored over a period of 8.3 days. From the observed number of giant planets in close orbits around their parent star and the fact that geometrically 10% of such stars would cause a transit, it was expected that 5-10 transits would be observed. Despite the magnificent data set no planets were detected (Gilliland et al. 2000). There are at least two explanations for this which were already mentioned in the proposal for the observing time: (1) The metallicity of 47 Tuc is lower than the stars in which planets have been found (Laughlin 2000), yet 47 Tuc has [Fe/H] $= -0.7$ dex which makes it one of the most metal rich globular clusters. (2) The extreme environment of a globular cluster may perturb the creation of proto-planetary discs, thus preventing the formation of giant planets.

## 2.2 SX Phœnicis Stars in 47 Tuc

I have been working on the same data set, but I was not directly involved in the search for planets. Instead I did photometry of the saturated SX Phe stars (population II variable blue stragglers) known to populate the cluster. In Sections 2.3-2.10 I have reproduced the original paper (Bruntt et al. 2001) which presents the results for the SX Phe stars. A few very minor errors have been corrected and two references have been updated. The references for the paper are found in Section 2.11.

Since this publication an interesting theoretical paper on SX Phe stars has appeared. Templeton et al. (2002) have investigated the effects of changes in pulsation models due to the expected changes in global chemical composition when blue stragglers form. From their model calculations Templeton et al. (2002) conclude that it will be difficult to determine the amount of mixing when SX Phe form from the period ratios of double-mode SX Phe stars, and thus to determine if they are formed as a result of head-on collisions, coalescence of binary stars, or both. This is only briefly discussed in Section 2.8.2, so the reader may like to consult Templeton et al. (2002).

**SX Phœnicis Stars in the Core of 47 Tucanae**[1], 2001, A&A, 371, 614–625

Bruntt, H., Frandsen, S., Gilliland, R. L., Christensen-Dalsgaard, J., Petersen, J. O., Guhathakurta, P., Edmonds, P. D., Bono, G.

## 2.3 Abstract

We present new results on five of six known SX Phœnicis stars in the core of the globular cluster 47 Tucanae. We give interpretations of the light curves in the $V$ and $I$ bands from 8.3 days of observations with the Hubble Space Telescope near the core of 47 Tuc. The most evolved SX Phe star in the cluster is a double-mode pulsator (V2) and we determine its mass to be $(1.54 \pm 0.05)\ M_\odot$ from its position in the Hertzsprung-Russell diagram and by comparing observed periods with current theoretical pulsation models. For V14 we do not detect any pulsation signal. For the double-mode pulsators V3, V15, and V16 we cannot give a safe identification of the modes. We also describe the photometric techniques we have used to extract the light curves of stars in the crowded core. Some of the SX Phœnicis are saturated and we demonstrate that even for stars that show signs of a bleeding signal we can obtain a point-to-point accuracy of 1-3%.

## 2.4 Introduction

Blue straggler stars (BSS) are found in all globular clusters where thorough searches for them have been made (Bailyn 1995). BSS are thought to be the results of direct collisions between stars or perhaps the gradual coalescence of binary stars (Guhathakurta et al. 1998, Bailyn 1995). The BSS are hotter and brighter than the turn-off stars in a globular cluster and some BSS will cross the classical instability strip for $\delta$ Scuti stars. The variable globular cluster BSS are called SX Phœnicis (SX Phe) stars, using the name for the prototype population II field star.

[1]Based on observations made with the NASA/ESA Hubble Space Telescope, obtained at the Space Telescope Science Institute, which is operated by the Association of Universities for Research in Astronomy Inc., under NASA contract NAS5-26555.

**Table 2.1** Fundamental parameters for 47 Tucanae. Values are taken from VandenBerg (2000).

| [Fe/H] | $E(B-V)$ | Age [Gyr] | $V_{TO}$ | $(m-M)_V$ |
|---|---|---|---|---|
| $-0.83$ | 0.032 | 11.5 | 17.65 | 13.37 |
| $\pm0.10$ | $\pm0.005$ | $\pm0.8$ | $\pm0.10$ | $\pm0.05$ |

When discussing globular clusters it is important to realize that they are not just a large group of individual independent stars. BSS are but one piece of evidence for non-standard stellar evolution due to dynamical processes (Camilo et al. 2000, Bailyn 1995). For the past five years a number of globular cluster cores have been probed to look more closely at the populations of stars that are direct evidence that the dynamics of stars have influence on the evolution of globular clusters as a whole. This is possible with the Hubble Space Telescope (HST) and has indeed yielded some interesting surprises: 1) BSS are found in all globular clusters (Bailyn 1995). 2) The horizontal-branch morphology possibly depends on the dynamical evolution of the cluster, although the metallicity is the most important parameter (Fusi Pecci et al. 1996). 3) The discovery of cataclysmic variables in NGC 6397 (Cool et al. 1998).

BSS and in turn SX Phe stars are found primarily near the cluster core as a result of mass segregation (see *e.g.* Edmonds et al. 1996). With the exceptional resolving power of HST it is possible to probe the cores of globular clusters, examples of such research are 47 Tuc (Gilliland et al. 1998) and M 5 (Drissen & Shara 1998) — but see also Piotto et al. (1999).

### 2.4.1 Variable Stars in 47 Tuc

The globular cluster 47 Tucanae is one of several clusters which have been searched for binaries and variable stars with the HST (the parameters of 47 Tuc are given in Table 2.1). Early results showed that 47 Tuc contained a significant number of BSS (Guhathakurta et al. 1992). With observations carried out with the uncorrected optics of HST (September 1993) a study of variable stars in 47 Tuc was made by Edmonds et al. (1996). In this search a few SX Phe and several eclipsing binaries were found (Edmonds et al. 1996) as well as variable K giant stars (Edmonds & Gilliland 1996).

In particular the BSS in 47 Tuc were analyzed by Gilliland et al. (1998) who found six SX Phe stars. From the location of the double-mode variables in the *Petersen diagram* (Petersen & Christensen-Dalsgaard 1996) Gilliland et al. (1998) were able to estimate the *pulsation masses* for the four double-mode SX Phe stars. Indeed, they showed that the pulsation masses and the *evolutionary masses*, which were estimated from the positions in the HR diagram, agreed quite well. Combining these two methods of *weighing* stars, they found masses from $(1.35 \pm 0.1)$ to $(1.6 \pm 0.2)\,M_\odot$, well above the turn-off mass at $\approx 0.85\,M_\odot$ in agreement with the generally accepted merging or colliding star scenario for BSS (Bailyn 1995).

### 2.4.2 Asteroseismology of SX Phe Stars

Among the SX Phe stars the double-mode pulsators are particularly interesting. In some cases it is possible to identify the pulsation modes. This class of star is comparable to the classical double-mode Cepheids (Petersen & Christensen-Dalsgaard 1996). The SX Phe stars are often pulsating in the fundamental mode and the first overtone or perhaps in two modes of higher overtones (second and third, third and fourth, *etc.*). Detections of double-mode SX Phe oscillation have been made in 47 Tuc (Gilliland et al. 1995, 1998), $\omega$ Cen (Freyhammer et al. 1998), and in a few field variables including SX Phe itself (*e.g.* Garrido & Rodriguez 1996).

The observed period ratio and the period of the main mode depend quite sensitively on the mass, metallicity, and evolutionary stage of the star (*i.e.* the age for a given mass). The ratio of the periods of the double-mode pulsators are well determined from theoretical models: as discussed in Section 2.8.4 below, the intrinsic precision of the theoretical period ratio is better than 0.01 percent (see also Petersen & Christensen-Dalsgaard 1996). Hence it is certainly possible to infer physical properties of the double-mode SX Phe stars.

There is evidence that some observed SX Phe stars oscillate in non-radial modes and it may become possible to extract information about the properties of the cores of these stars. Examples of observed SX Phe stars that show evidence of non-radial modes are SX Phe itself (Garrido & Rodriguez 1996) and V3 in 47 Tuc (Gilliland et al. 1998). Progress in the understanding of SX Phe stars can also be made if one can detect low-amplitude modes, which may provide more detailed information about the internal structure of these stars.

Section 2.5 contains a description of the data set. In Section 2.6 we discuss the reduction of the data including the task of dealing with saturated bleeding pixels on the CCD. Section 2.7 contains the details of the time-series analysis while in Section 2.8 we present the results with emphasis on the double-mode SX Phe stars. Finally, Section 2.9 summarizes our conclusions.

## 2.5 Observations

In the present work we have analyzed an 8.3 day time series of the stars in the central part of 47 Tuc. The data were obtained with `WFPC/II` on the `HST` in July 1999. The main goal of the project was to search for giant planets around the main-sequence stars of the cluster (Gilliland et al. 2000). The primary exposure times were 160 s in F555W and F814W filters ($V$ and $I$[2]) and optimized for stars at and below the turn-off. Consequently, the luminous BSS stars are all saturated in $V$ and some are also saturated in $I$.

The PC1 CCD of `WFPC/II` was placed near the center of 47 Tuc. This is where the density of stars is highest and most of the BSS stars are found. Five of the six known SX Phe stars in the core of 47 Tuc (Gilliland et al. 1998) are within the field of view (V1 fell outside).

The present study is an improvement compared to the results by Gilliland et al. (1998). They used `HST` photometry (with the aberrated `WF/PC`) in the $U$ band with

[2] $I$ magnitudes refer to the Cousins filter

a total coverage of 39 hours. Although ideal for the detection of stellar oscillations the exposure time was 1000 s compared to 160 s for the present data set. The new time series are more than five times longer with a total of 1289 data points compared to the 99 points in the old data set. Although the amplitudes are about a factor of two smaller (using $V$ and $I$ instead of $U$) for the present data set and some of the stars are saturated, we expect to be able to derive more accurate periods for the SX Phe stars.

## 2.6 Data Reduction

We have used the DAOPHOT/ALLSTAR (D-A) software which is designed for doing photometry in crowded fields (Stetson 1987). For this study we have only reduced the PC1 frames as the BSS stars are found near the core of 47 Tuc. We use D-A to construct an empirical PSF model from about 60 stars. Because of the extreme crowding near the core of 47 Tuc this is a difficult task. The PSF model is iteratively improved by cleaning the neighbouring stars around the stars used for creating the PSF model.

It is well known that the PSF changes with time due to the *breathing* of HST (Suchkov & Casertano 1997). We also need a good description of the PSF wings as this has serious impact on the accuracy of the photometry of the saturated SX Phe stars: for these stars the light in the core is not used in the D-A analysis, and we have to look for oscillations in the wings of the PSF profile. Thus we constructed empirical PSF models for all frames.

To improve the photometry we have stacked all the frames in each filter to create a *super frame*. This technique is described in Gilliland et al. (1999). In this way we are able to combine the information from all frames to obtain accurate positions of the stars in each individual frame. This is done by calculating the offset position from the stars in the super frame to each individual frame from the position of several hundred reasonably isolated and bright stars. In order to be able to account for geometric distortion, we find the six coefficients $(a_1 - a_6)$ in the transformation

$$X_i = a_1 + a_2\,x_i + a_3\,y_i + a_4\,x_i^2 + a_5\,y_i^2 + a_6\,x_i\,y_i$$

for each frame; here $(x, y)$ is the position in the super frame for star $i$, and $X$ is the horizontal position on a given frame. The same is done for the $Y$ coordinate.

We then redo the D-A photometry with the improved positions of the stars being *fixed*; thus the magnitudes are the only parameters which are fitted by D-A. This step greatly improves the photometric accuracy.

### 2.6.1 Bleeding Pixels

We find that the photometry of the brightest saturated stars is quite poor. By inspecting contour levels around stars with different degrees of saturation it is obvious that the signal from the saturated core starts to *bleed* along the read-out direction. Thus the stellar profile is slightly elongated, *i.e.* the nice symmetry of

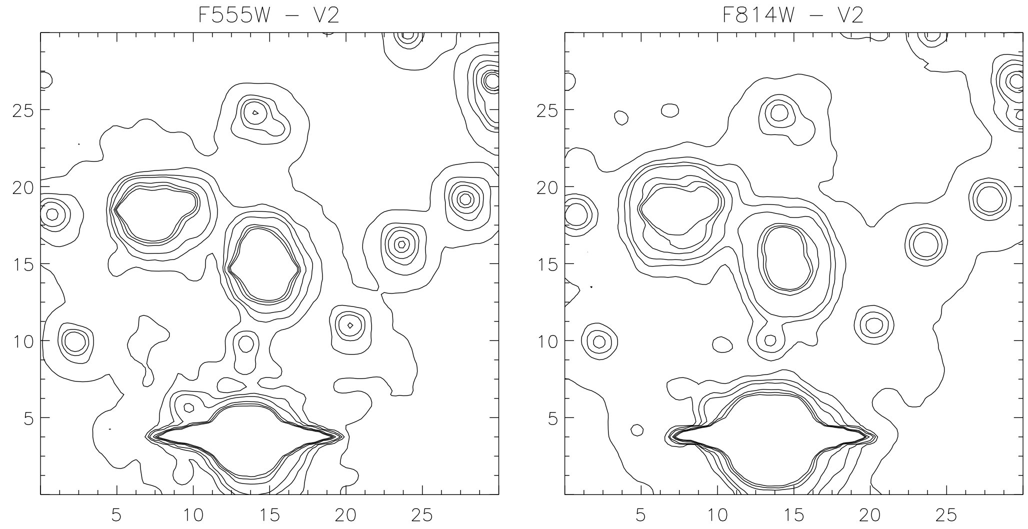


**Figure 2.1** Contour plots around the SX Phe star V2 in the super frame with the F555W and F814W filter. V2 is at position (15,15) and is clearly contaminated by another bright star above it (15,16). In F555W it can be seen that both stars are *bleeding* in the horizontal (CCD read-out) direction.

the PSF is broken due to the contamination from the bleeding pixels. A specific example of bleeding stars is shown in Figure 2.1. Note that the data analyzed here have been rotated by 90 degrees from normal `WFPC/II` conventions, hence bleeding along $x$. We assume that the signal in pixels that are neighbours to saturated cores may not be reliable. To correct for this we used different methods to find the pixels that were affected. It turned out that a simple correction gave good results: we have found that the contamination due to bleeding pixels seems to set in at a certain degree of saturation, *i.e.* stars for which only the central one or two pixels are saturated *do not* suffer from contamination. The best result was obtained by *flagging* pixels which are neighbours to three or more pixels (in the read-out direction) that are above the saturation limit. Flagging simply means that the pixel value is set to a value above the saturation limit, and is hence treated as such by D-A, *i.e.* it is not used for the PSF fitting and hence the determination of the magnitude.

The improvement for the saturated stars is significant. In Figure 2.2 we show the difference in internal standard deviation (ISD) for the light curves of all stars on PC1 before (N) and after flagging (F) the contaminated pixels. The final ISD for all stars is shown in Figure 2.3 in which the five SX Phe stars have been emphasized. We define

$$\sigma_{\mathrm{ISD}}^2 = \sum_{i=1}^{N-1} (m_i - m_{i+1})^2 / [2(N-1)] \tag{2.1}$$

where $N$ is the number of observations.

A specific example of the importance of flagging the contaminated pixels is shown in Figure 2.4. This shows the light curve in both F555W ($\circ$) and F814W

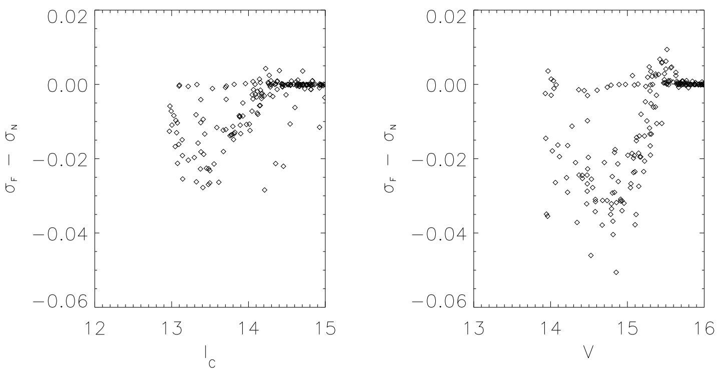


**Figure 2.2** Difference in internal standard deviation of light curves for two different reduction techniques for the $I$ (*left*) and $V$ (*right*) filters. A significant improvement is obtained for the brightest stars.

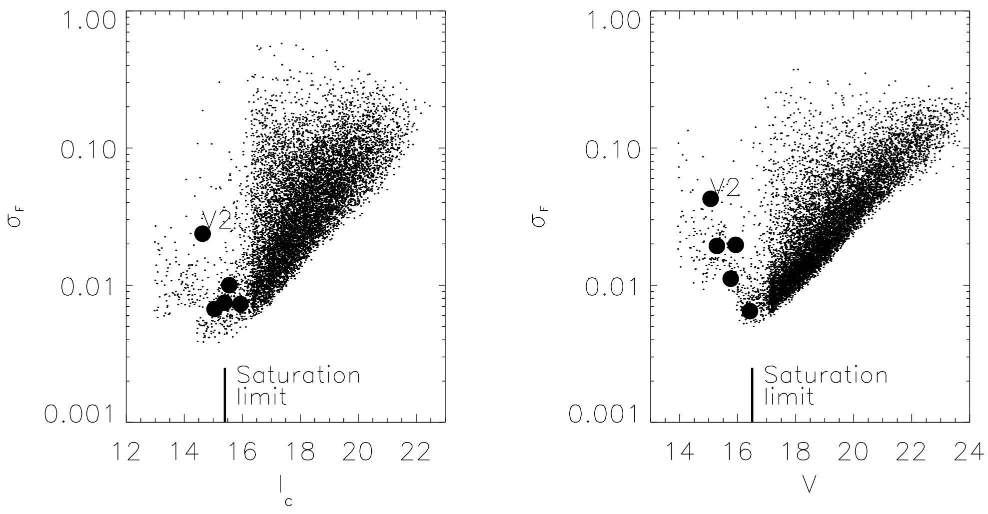


**Figure 2.3** The final internal standard deviation of light curves for the $I$ (*left*) and $V$ (*right*) filters. The SX Phe stars have been clearly marked.

($\times$) before and after the flagging. Due to the amplitude dependence on wavelength the F555W light curve has been scaled by an empirical factor of $A_{814}/A_{555} = 0.639$ (this scaling is also made before the time-series analysis in Section 2.7).

### 2.6.2 Further Analysis

Two other time-series analyses should be mentioned here. Gilliland et al. (2000) describe use of difference image analyses for obtaining optimal results for the unsaturated stars comprising the primary data use. The difference image analysis provided time-series precisions averaging a factor of two better than those presented here for unsaturated stars, but cannot be applied at all to the saturated stars. A second approach to saturated-star extractions has been developed by one of us (RLG, Gilliland 1994) making use of aperture photometry including the sa-

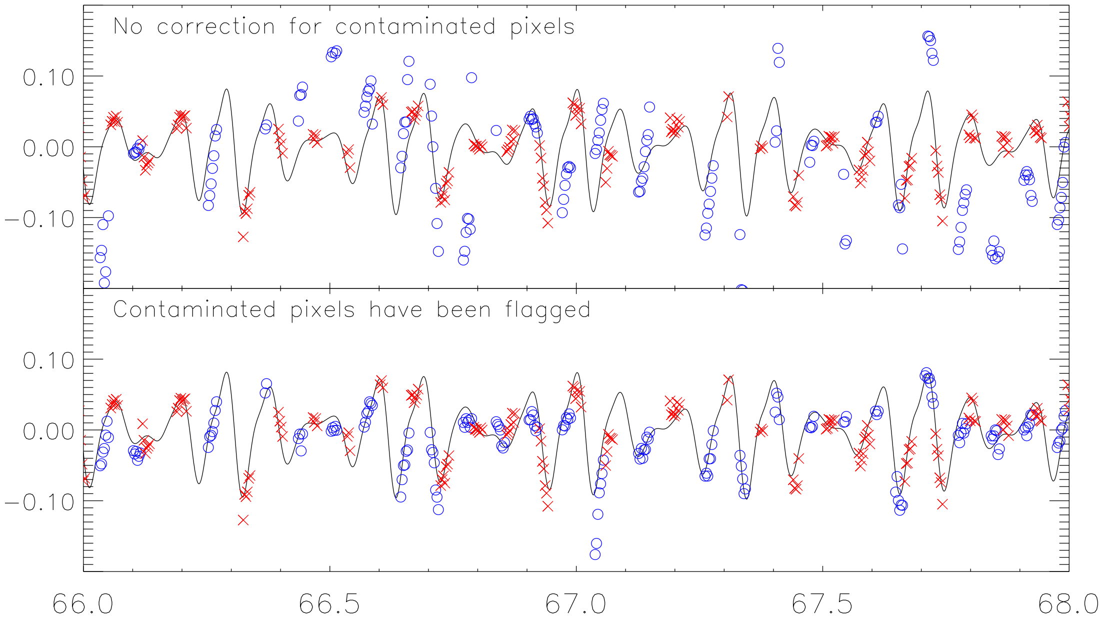


**Figure 2.4** Light curve for SX Phe star V2 in F555W (○) and F814W (×) when using two different reduction techniques (see text for details). The abscissa is the heliocentric Julian date minus 2 451 300.

turated pixels. The latter approach provides generally comparable results to those described here for the PC1 extractions.

## 2.7 Time-series Analysis

To perform the frequency analysis of the light curves we used the software package PERIOD98 developed by Sperl (1998). Figure 2.5 shows the amplitude spectrum for the SX Phe star V2 (top left plot) and also the resulting amplitude spectra when the variation corresponding to the most significant peaks has been subtracted. The arrows show the frequencies in cycles per day (c/d) — one barely significant peak at 14.88 c/d is labelled "HST", and may be due to the 96.4 minutes orbital period of the observatory. The dotted line is the empirically determined $4\sigma$ detection limit; peaks below this are not considered to be significant. All mode frequencies, amplitudes, phases, and errors are quoted in Table 2.2. We note that the light curves have been analyzed independently by three of the authors using different software — and our results agree.

The primary modes of V2 have sufficient amplitude to provide unambiguous detections from both the 1993 (Gilliland et al. 1998) and 1999 time series. We now consider the other four SX Phe stars for which some of the modes claimed previously were near the detection limit provided by the 1993 data. Figure 2.6 shows the amplitude spectra for V3, V14, V15, and V16 with the original $U$-band (1993) and $I$-band (1999) amplitudes transformed to a common $V$ estimate by scaling by central wavelength ratios. Time series for V3 and V15 are based upon combined $V$ and $I$ (as for V2) data making use of techniques previously described for analyz-

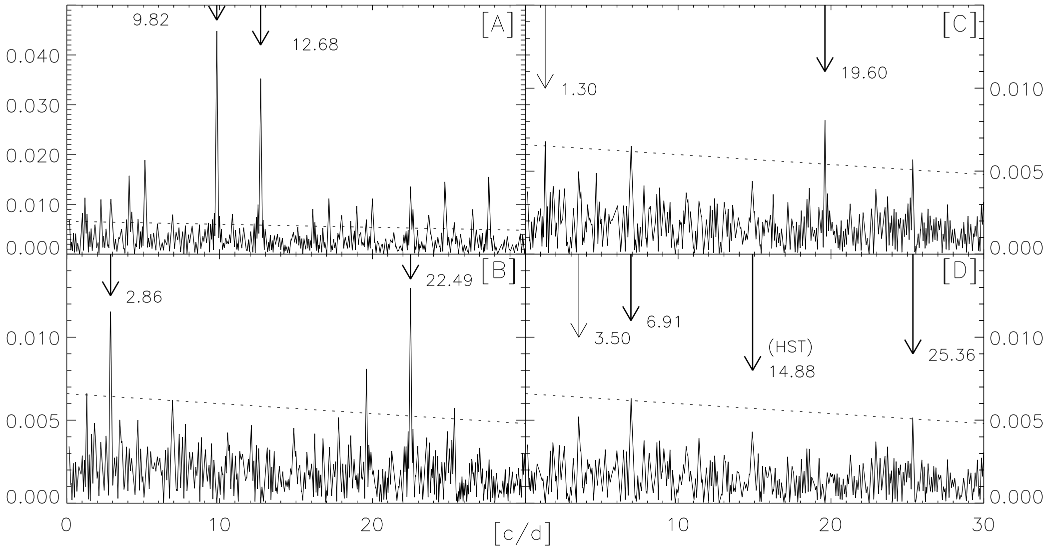


**Figure 2.5** Amplitude spectra for the SX Phe star V2 computed when using the combined F555W and F814W light curve (top left plot and labelled A). The other three plots (labelled B,C, and D) show the resulting amplitude spectra when the modes marked by arrows have been subtracted. Note that the scales on the ordinate differ. The dotted line is the $4\sigma$ detection limit.

ing saturated stars. For V14 and V16 the stars never saturate in *I* exposures; for these we use only the 653 unsaturated images and the more precise photometry provided by difference image analyses. Results for V3, V15, and V16 show that all primary modes claimed from the 1993 data are present, and these will be further discussed in Section 2.8.5. V14 was the least significant detection from the 1993 data, and was only selected (Gilliland et al. 1998) as a likely variable by searching for repeated low amplitude peaks with spacing characteristic of successive radial modes. The 1999 data for V14 clearly show that not even a slight hint of the claimed modes exists; the most likely interpretation is that V14 is not a variable and we will not further consider V14 as an SX Phe star. The V14 amplitude spectrum for 1999 nicely illustrates a characteristic of the extensive HST observations – a very clean spectrum that in fact stays flat from below 1 cycle/day out to the Nyquist frequency of 180 cycles/day. V16 was also only found as a variable from the 1993 data based on a search for successive radial overtone peaks; in this case the 1999 data clearly confirm oscillations are again present.

In Figures 2.7 and 2.8 we show the phase diagrams for the three largest amplitude double-mode stars in our sample. In each diagram all known modes have been subtracted except for one mode, the frequency of which is shown in the top left corner. Note the different scale on the ordinates.

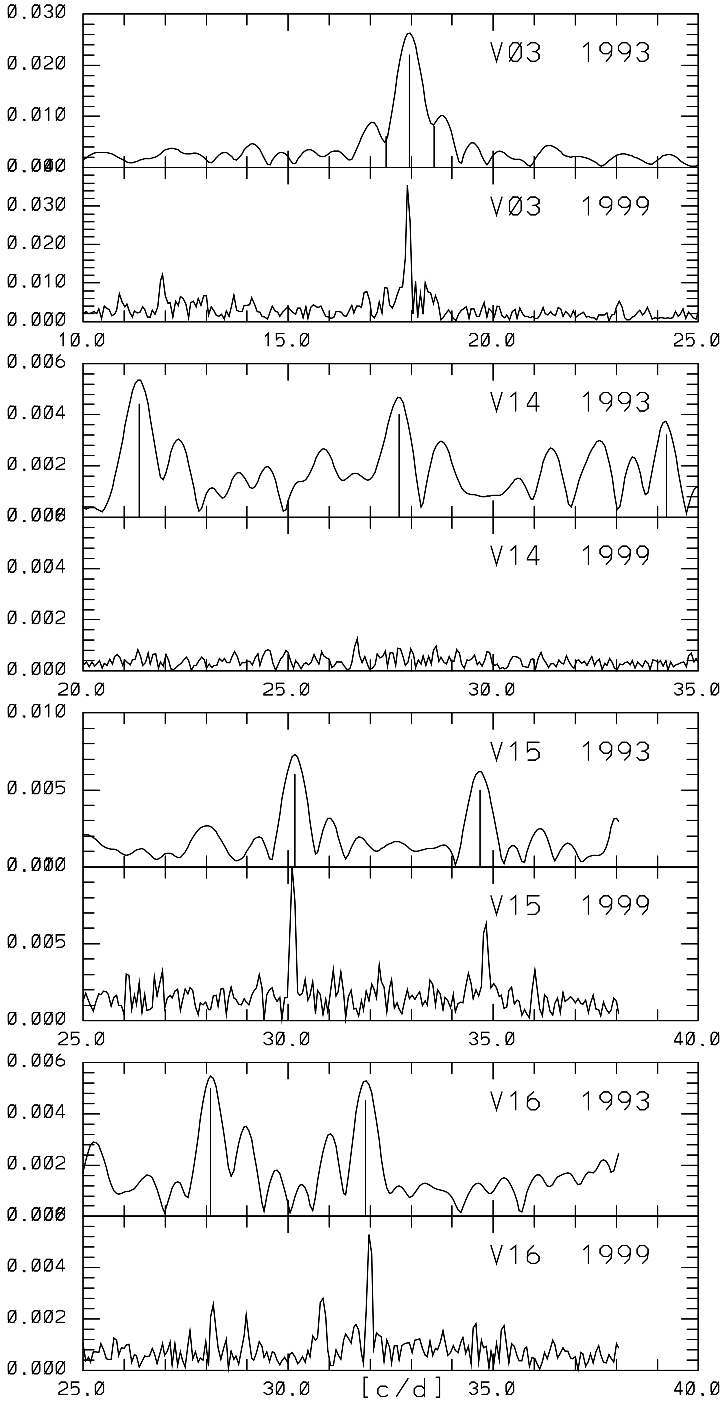


**Figure 2.6** Amplitude spectra for V3, V14, V15, and V16 are shown comparing the 1993 (Gilliland et al. 1998) results with the new 1999 data. All amplitudes have been scaled as needed by wavelength to provide $V$ band equivalent magnitudes. Frequency units are cycles per day. All modes claimed from the 1993 data are marked with vertical bars under the corresponding peaks.

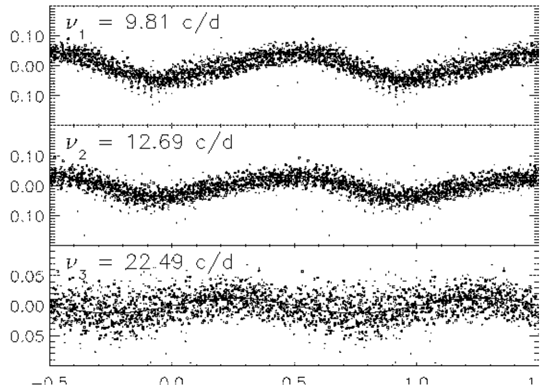


**Figure 2.7** Phase diagrams for V2 for the three main modes.

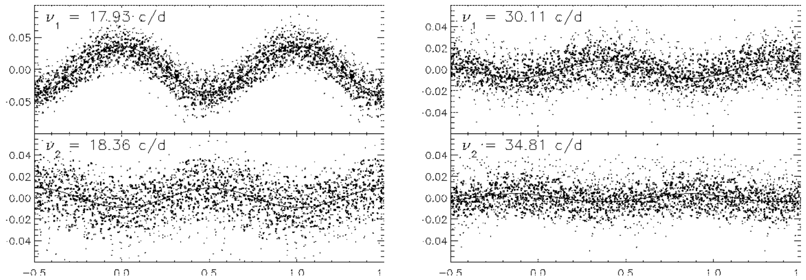


**Figure 2.8** Phase diagram for V3 and V15 for two modes.

**Table 2.2** Frequencies, amplitudes, and phases for modes for the observed SX Phe stars. Modes above the $4\sigma$ level are marked with $*$ while less significant modes are marked with ?. Numbers in parenthesis are the statistical errors. The frequencies found by Gilliland et al. (1998) are given in the rightmost column. Note that the formal errors on the frequencies of the new results are lower by almost an order of magnitude compared to Gilliland et al. (1998). In column 5 $\nu_1$ and $\nu_2$ are the frequencies of the primary and the secondary mode.

| Star | Frequency [c/d] | $V$ Amplitude [mag] | Phase [c] | Mode combination | Gilliland et al. |
|---|---|---|---|---|---|
| V2 | **9.816**(0.002) | **0.044**(0.001) | **0.662**(0.004) | * $\nu_1$ | **9.807**(0.013) |
| | **12.684**(0.002) | **0.034**(0.001) | **0.488**(0.005) | * $\nu_2$ | **12.700**(0.016) |
| | **22.490**(0.005) | **0.012**(0.001) | **0.187**(0.014) | * $\nu_1 + \nu_2$ | **22.494**(0.057) |
| | **2.866**(0.007) | **0.011**(0.001) | **0.620**(0.014) | * $\nu_2 - \nu_1$ | |
| | **19.604**(0.020) | **0.008**(0.001) | **0.564**(0.076) | * $2\nu_1$ | |
| | **25.354**(0.013) | **0.005**(0.001) | **0.351**(0.035) | ? $2\nu_2$ | |
| | **6.914**(0.013) | **0.005**(0.001) | **0.179**(0.025) | ? $2\nu_1 - \nu_2$ | |
| V3 | **17.929**(0.001) | **0.036**(0.005) | **0.624**(0.007) | * $\nu_1$ | **17.948**(0.022) |
| | **18.359**(0.004) | **0.009**(0.005) | **0.925**(0.017) | ? $\nu_2$ | **18.585**(0.064) |
| V15 | **30.110**(0.004) | **0.0084**(0.0004) | **0.727**(0.007) | * $\nu_1$ | **30.157**(0.053) |
| | **34.807**(0.010) | **0.0038**(0.0004) | **0.493**(0.016) | * $\nu_2$ | **34.671**(0.070) |
| V16 | **31.988**(0.005) | **0.0039**(0.0005) | **0.055**(0.016) | * $\nu_1$ | **31.894**(0.064) |
| | **28.165**(0.008) | **0.0016**(0.0005) | **0.256**(0.016) | ? $\nu_2$ | **28.116**(0.071) |

### 2.7.1 Search for New SX Phe Stars

The original HST data (WF/PC; Gilliland et al. 1998) used to find SX Phe variables in 47 Tuc covered an area of $66 \times 66$ arcsec$^2$, with the cluster centre about 10 arcsec from the field of view centre. The new search domain with WFPC/II observing in 1999 is such that the PC1 field of view is almost entirely contained within the original search area, while the much larger field of view of the WF CCDs is (at the 90% level) outside the original search space. We have extracted time series for 2968 saturated stars on the 4 WFPC/II CCDs using the technique of Gilliland (1994). Near the domain in the CMD where the previous SX Phe stars were found the root-mean-square variations in the resulting time series are $\sim 1 - 2\%$ (albeit with non-Gaussian characteristics). We note that the previously detected SX Phe variables V2, V3, V15, and V16 are easily observed in these new time series. Although the new survey field of view is much larger than that previously surveyed, it is also on average farther from the cluster center. In the domain $15.0 < V < 17.0$, $0.2 < V - I < 0.45$ the original search contained about 25 stars of which 6 are SX Phe variables. The number of new stars surveyed within this box in the CMD is only 7 consistent with the known, strong central concentration of BSS. The time series for all of the newly surveyed BSS were analyzed by taking power spectra and searching for significant peaks; no convincing evidence of variables was found. Amplitudes of 0.01 magnitudes would in general be easily seen unless the period is similar to the 96.4 minute HST orbital period or its harmonics.

## 2.8 Results

### 2.8.1 The Colour-magnitude Diagram

The conversion from the instrumental to standard $V, I$ (Johnson-Cousins) magnitudes was done following the "photometric cookbook" of Holtzman et al. (1995). We correct for geometric distortion and the "34th row effect" (Anderson & King 1999). We have corrected for the charge-transfer efficiency (CTE) problem by following the formulation of Stetson (1998) and we include his new photometric zero-points.

Systematic differences between long and short exposures obtained with the HST have been reported in the literature (see *e.g.* Kelson et al. 1998). There is a tendency that measurements of stellar brightness from frames with long exposure times yield brighter magnitudes than short-time exposures. To be able to correct for the "long-short anomaly" we reduced some additional short exposures obtained for our field: Four 1.6 s exposures in F555W and F814W (the same field as the 160 s exposures).

We then determined the offsets in $V$ and $I$ from frames with different exposure times. The offsets are: $\Delta V$(160-1.6s)$= -0.104 \pm 0.004$ (1042 stars), and $\Delta I$(160-1.6s)$= -0.0554 \pm 0.0035$ (1034 stars). We stress that this is after correcting for the CTE effect, *i.e.* the long-short anomaly is "real" and not only a part of the CTE problem. A possible explanation for the offsets is the difficulty of determining the 0.5 arcsec aperture correction due to crowding. This correction is needed when following the calibration "cookbook" of Holtzman et al. (1995).

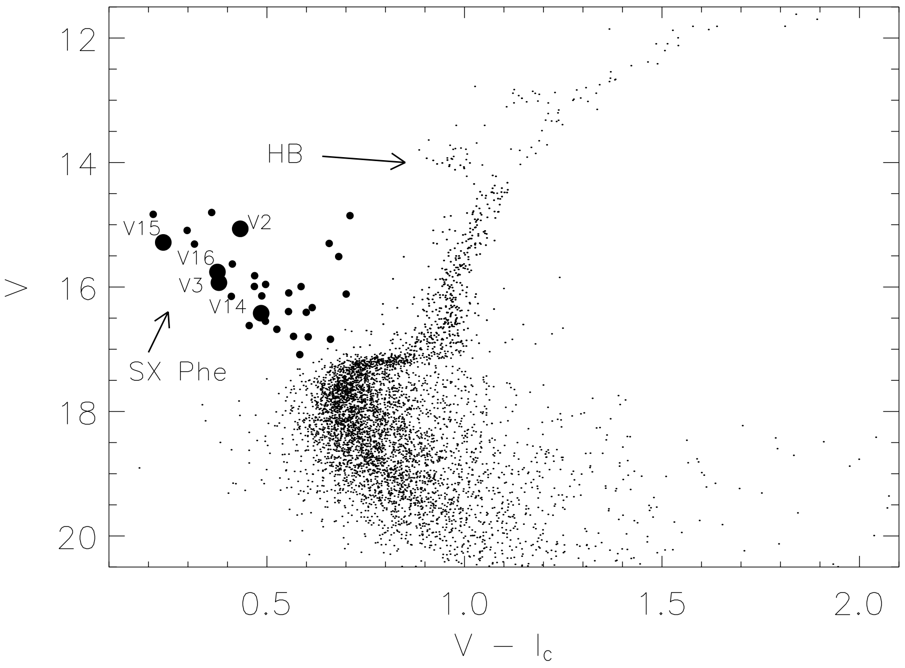


**Figure 2.9** Combined CMD for 47 Tuc. Filled dots mark the BSS stars, and the SX Phe stars have been labelled.

After the removal of the offsets we compare our CMD with several results from the literature. We have found the average $V$ of the stars in the transition between the turn-off and the red giant branch: $V_{\rm TO/RGB} = 17.31$ near $V - I = 0.80$. The mean of Hesser et al. (1987), Kaluzny et al. (1998), and Alcaino & Liller (1987) is $V_{\rm TO/RGB} = 17.18 \pm 0.04$. We thus apply an offset of $\Delta V = 17.18 - 17.31 = -0.13$. The offset in $I$ is found from the colour of the turn-off. The mean colour from Kaluzny et al. (1998) and Alcaino & Liller (1987) is $(V - I)_{\rm TO} = 0.695 \pm 0.02$. We find $\Delta I = -0.096$.

The final colour-magnitude diagram (CMD) is shown in Figure 2.9 where the BSS stars have been marked. The parameters of the SX Phe stars are given in Table 2.3.

Two groups in our team have performed the standard photometry in order to detect systematic differences. The first group reduced each short exposure image individually while the second group worked on combined images. The photometry of the SX Phe stars and the CMD presented here are the results of the first group — here we mention the main differences. After correcting for the offsets mentioned above (TO/RGB transition level and colour of the turn-off) the results from both groups based on the short exposures generally agree: We note that for the CMD presented here, the brightest part ($V < 14.5$) of the giant branch is more red ($\Delta(V - I) = 0.10$) than the ground-based study by Da Costa & Armandroff (1990). Our second group finds $\Delta(V - I) = -0.05$ for these stars. In the interesting case of the SX Phe star V2 both groups agree that $V = 15.07 \pm 0.02$ while we find discrepant results for the red filter: $I = 14.63 \pm 0.03$ and $I = 14.80 \pm 0.03$. The most immediate explanations for this are the crowding around V2 (*cf.* Figure 2.1) and that the images are under-sampled. We note that systematic errors of the order 0.03 magnitudes may still be present (see *e.g.* Stetson 1998) for all stars.

To transform the empirical data into the theoretical plane we adopted the bolometric corrections (BCs) and the colour-temperature relations provided by Bessell, Castelli, & Plez (1998)[3]. By means of a linear interpolation of the tables for [Fe/H] $= -0.5$ and $-1.0$ we estimated a new list of BCs for [Fe/H] $= -0.83$. For MS stars we use $\log g = 4.5$, while for BSS we use $\log g = 4.0$. As a special case we assumed $\log g = 3.7$ for V2, since this SX Phe has already evolved off the MS. Note that such a value is somewhat lower than the value obtained on the basis of an evolutionary track with $M/M_{\odot} = 1.5$ (VandenBerg, *private communication*). On the basis of these assumptions and of the observed colour (two independent determinations) we find that the effective temperature for V2 ranges from $T_{\rm eff} = 7100$ K ($(V-I)_0 = 0.39$) to $T_{\rm eff} = 7700$ K ($(V-I)_0 = 0.23$). We have used $T_{\rm eff} = 7100$ K for V2 and find BC $= -0.02$ mag. The BCs for all stars were estimated by adopting a similar procedure. The BC for the SX Phe stars are listed in Table 2.3.

The distance modulus of 47 Tuc has been determined several times in the literature. VandenBerg (2000) found $(m-M)_V = 13.37 \pm 0.05$ (using new isochrones and $B, V$ photometry by Hesser et al. 1987). Grundahl et al. (2002) made Strömgren photometry on 47 Tuc and 14 field sub dwarfs. By fitting the lower main sequence of 47 Tuc to the field stars they find a distance modulus $(m-M)_V = 13.32 \pm 0.04$. The quoted errors ignore systematic errors, *e.g.* the zero point of the metallicity scale and the error on the interstellar reddening. The systematic error is of the order 0.10 magnitudes. These three independent studies all seem to deviate significantly from Carretta et al. (2000) and Salaris & Weiss (1998) who find $(m-M)_V = 13.55 \pm 0.09$ and $13.50 \pm 0.05$, respectively. We finally draw attention to the study of the white dwarf cooling sequence by Zoccali et al. (1999). They find a distance modulus of $(m-M)_V = 13.15 \pm 0.12$ (assuming again $E(B-V) = 0.032$). In the following, we adopt the value obtained by VandenBerg (2000), *i.e.* $(m-M)_V = 13.37 \pm 0.05$.

### 2.8.2 The Hertzsprung-Russell Diagram

Figure 2.10 is the Hertzsprung-Russell (HR) diagram for 47 Tuc in which all BSS stars and main-sequence stars with the best photometry are shown. The five known SX Phe stars have been labelled. Also seen in the plot are evolutionary tracks for models computed with the evolution code by Christensen-Dalsgaard (Petersen & Christensen-Dalsgaard 1996, 1999). The abundances of hydrogen, helium, and heavy elements are $(X, Y, Z) = (0.754, 0.241, 0.005)$ which is appropriate for 47 Tuc according to VandenBerg (2000).

We note that Salaris & Weiss (1998) discuss the evidence for a somewhat higher value of $Y = 0.273$ for 47 Tuc. For example they use the $R$-method (Buzzoni et al. 1983) with $R = 1.75 \pm 0.21$ and $1.86 \pm 0.36$ based on Buzzoni et al. (1983) and

[3] http://kurucz.harvard.edu/grids.html, no overshooting models

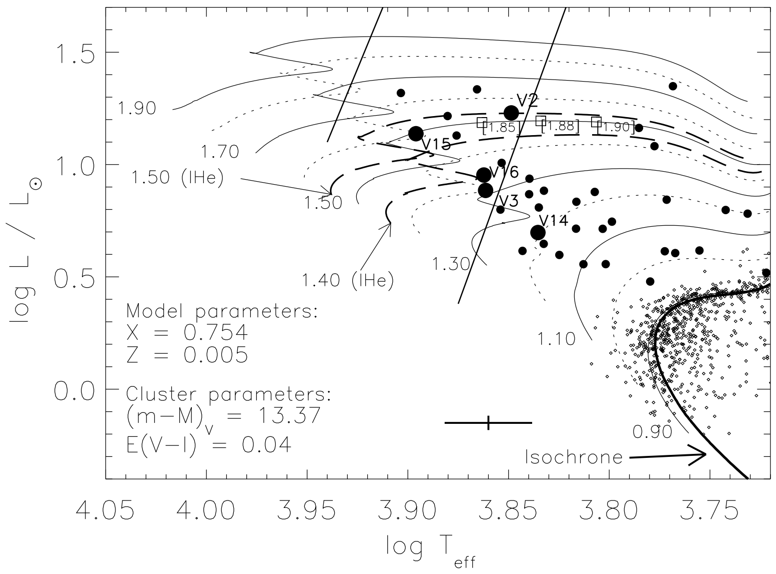


**Figure 2.10** HR diagram of 47 Tuc. Several theoretical evolutionary tracks are shown. For models in the mass interval $M/M_\odot = 0.9$ to 1.9 and standard chemical composition tracks are plotted with either solid or dotted lines. Two tracks with increased helium content are also shown with dashed lines. For the $1.5 M_\odot$ model the age in Gyr is indicated at three points. The filled circles mark the BSS stars and the SX Phe stars have been labelled. The turn-off region can be seen in the lower right corner. The age of the isochrone is 12.5 Gyr (computed by VandenBerg, *private communication*).

Hesser et al. (1987), respectively. This corresponds to a mean $Y = 0.28 \pm 0.04$ which is roughly consistent with the value we have adopted (using the calibration by Buzzoni et al. 1983). We note that a more recent determination of the $R$ parameter was done by Zoccali et al. (2000) based on observations with HST. They find $R = 1.52 \pm 0.13$ corresponding to $Y = 0.246 \pm 0.012$ (again using Buzzoni et al. 1983). Based on this short discussion we have adopted the same helium content as VandenBerg (2000), *i.e.* $Y = 0.241$.

The age of the cluster was determined to be 11.5 Gyr by VandenBerg (2000) from the $B, V$ photometry by Hesser et al. (1987). The new combined $V, I$ photometry from HST indicates that this age estimate may be a bit too young. In Figure 2.10 we have also shown an isochrone of age 12.5 Gyr computed by VandenBerg (*private communication*). For comparison the $0.9\,M_\odot$ evolutionary model in Figure 2.10 reaches the turn-off at $\log T_{\rm eff} = 3.78$ after $\approx$ 10 Gyr and starts climbing the Hayashi-track around $\approx$ 13 Gyr: This evolutionary model is indeed comparable with stars near the observed turn-off. Thus our models are in qualitative agreement with VandenBerg. We note that Salaris & Weiss (1998) find an age of $(9.2 \pm 1.0)$ Gyr for 47 Tuc.

The BSS population is clearly seen in the HR diagram in Figure 2.10. The "life span" for models with the metallicity of 47 Tuc and masses $1.4\,M_\odot$ and $1.6\,M_\odot$ (typical for BSS stars) is only about 1.8 Gyr and 1.3 Gyr, respectively (the time to reach the hook). Thus it is evident that these stars have formed late in the evolution of the cluster, probably by a merger or collision between two stars of mass below the turn-off mass.

The observed instability strip for *population I* $\delta$ Scuti stars is also shown in Figure 2.10 (Breger 1990). Four of five SX Phe stars are located inside the instability region. Even when taking into account the uncertainty of the temperature V14 is not inside the instability region — possibly explaining the lack of variation for this BSS (*cf.* the amplitude diagram in Figure 2.6).

Detailed modelling of the BSS stars is hampered by the uncertainties relating to their formation (*e.g.* Benz & Hills 1987, 1992; Bailyn & Pinsonneault 1995). This is likely to lead to changes in composition due to mixing; in the extreme case where stars at the turn-off are completely mixed, the resulting homogeneous helium content would be $Y \approx 0.34$. Furthermore, it is plausible that, for example, the orbital angular momentum in a merging binary star would lead to a very rapidly rotating BSS. A detailed investigation of such effects is beyond the scope of the present paper. However, we have explored the effects of a change in the composition: In addition to the models with the standard helium abundance (*SHe*, $Y = 0.241$), we have considered models with increased helium content (*IHe*, $Y = 0.261$) and masses $1.40\,M_\odot$ and $1.50\,M_\odot$; these are also shown in Figure 2.10 (dashed lines).

From the evolutionary tracks it is possible to estimate the masses of the SX Phe stars. A unique case is V2 for which an unambiguous estimate can be given: The evolutionary tracks are almost horizontal around V2, hence the uncertainty in $T_{\rm eff}$ is not so important for the mass estimation from the position in the HR diagram. For V2 we find $M_{\rm HR}/M_\odot \simeq 1.54 \pm 0.05$ for the standard helium abundance; using instead the models with increased helium abundance (*IHe*) we obtain $M_{\rm HR}/M_\odot = 1.50 \pm 0.05$. The other SX Phe stars all lie around the hooks of the evolutionary tracks and the mass estimate is more uncertain for these stars ($\pm 0.10\,M_\odot$). In Table 2.3 we have given mass estimates and various parameters of the SX Phe stars.

In Figure 2.10 the model ages in Gyr are given at three points along the $1.5\,M_\odot$ track which is below V2 (in square brackets). Consequently the age of V2 must be somewhat lower than the $\approx 1.9$ Gyr found from this track. If we assume that V2 is following the evolutionary track of a standard model (ignoring formation history, *e.g.* mixing of the merging stars) and that the position in the HR diagram is correct we can conclude (from an evolutionary track of mass $1.54 M_\odot$): The age of V2 is around $(1.7 \pm 0.2)$ Gyr, $L/L_\odot = 17.0 \pm 0.5$, core burning of hydrogen has ceased ($X_{\rm core} = 0$), and the star has only a few hundred million years left before it will start climbing the Hayashi track and eventually go into the helium-burning phase.

### 2.8.3 Double-mode SX Phe Stars

For some double-mode SX Phe stars a safe mode identification is possible. Most double-mode pulsators oscillate in radial modes ($l = 0$) of low radial order ($n = 1 - 6$). One can put constraints on the astrophysical properties (mass, helium content) of these stars by comparing observed and theoretical data in a period-ratio versus

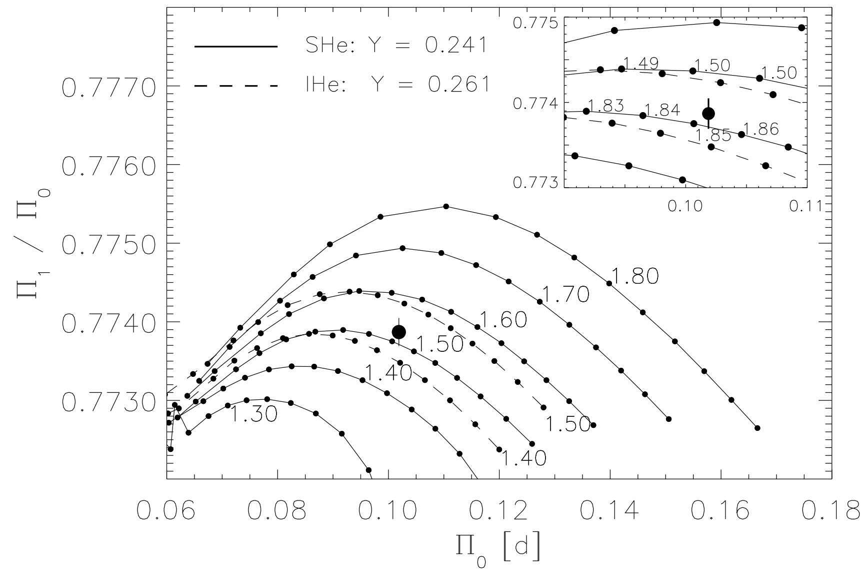


**Figure 2.11** The Petersen diagram for several stellar model series. The helium content of the different model series is explained in the top left corner; as indicated, the *SHe* models cover the mass range $M/M_\odot = 1.3 - 1.8$, while *IHe* models are shown for $M/M_\odot = 1.4$ and 1.5. In the inserted plot the ages of models with $Y = 0.241$ and mass $M/M_\odot = 1.5$ and 1.6 are given in Gyr.

period diagram, the so-called *Petersen diagram*. In the following we look more closely at the double-mode SX Phe star V2, and then discuss the more difficult stars V3, V15, and V16.

### 2.8.4 The Double-mode SX Phe Star V2

We interpret the dominant observed modes as the the fundamental mode and the first overtone and obtain a period ratio of $\Pi_1/\Pi_0 = 0.7739 \pm 0.0002$. Gilliland et al. (1998) found $\Pi_1/\Pi_0 = 0.7722 \pm 0.0014$, *i.e.* the results are essentially consistent. With the more accurate period ratio obtained from the new longer time series we can constrain the mass of V2 to within a formal error of $0.03\,M_\odot$ at a given composition from the position in the Petersen diagram. The error in the mass estimate

**Table 2.3** Fundamental parameters for the observed SX Phe stars. Typical errors are $(0.03, 0.04, 0.14, 0.02, 200\text{ K})$ for $(V, V-I, M_{\rm bol}, {\rm BC}_V, T_{\rm eff})$. For the mass in column 7 the error estimate is $\pm 0.05\,M_\odot$ for V2 and $\pm 0.10\,M_\odot$ for the other variables.

| Star | $V$ | $V-I$ | $M_{\rm bol}$ | ${\rm BC}_V$ | $T_{\rm eff}$ | $M/M_\odot$ |
|---|---|---|---|---|---|---|
| V2 | 15.07 | 0.43 | 1.68 | -0.02 | 7100 | 1.54 |
| V3 | 15.93 | 0.38 | 2.54 | -0.02 | 7300 | 1.35 |
| V15 | 15.28 | 0.24 | 1.91 | -0.01 | 7900 | 1.65 |
| V16 | 15.76 | 0.38 | 2.37 | -0.02 | 7300 | 1.35 |

will be discussed further below.

We have used a series of pulsation models which are extracted from the grid of evolutionary tracks in Figure 2.10. From the HR diagram we make a rough estimate of the range of stellar masses that are relevant ($1.8 > M/M_\odot > 1.3$). As before, in addition to the standard models we have also calculated pulsation models with higher helium content.

Figure 2.11 compares the observed period ratio of V2 with data for several stellar oscillation models. Solid lines are computed from models with standard helium abundance (*SHe*, $Y = 0.241$), dashed lines have increased helium content (*IHe*, $Y = 0.261$). A decrease in effective temperature causes an increase in the pulsation period and as a consequence a stellar model moves from left to right in Figure 2.11 during its post-main-sequence evolution.

The double-mode SX Phe star V2 is shown in the plot. We estimate the mass of V2 to be $(1.53 \pm 0.03)\,M_\odot$ for *SHe*. From the models with *IHe* we infer the mass to be $(1.45 \pm 0.03)\,M_\odot$.

The good accuracy of the observed period ratio for V2 — the error bars can be seen in the inserted plot — is due to the long time series with good sampling. In comparison the result by Gilliland et al. (1998) is $\left(1.4^{+0.25}_{-0.15}\right) M_\odot$ (*cf.* their Figure 22).

The mass determination is obviously also sensitive to errors in the stellar modelling used in computing periods and period ratios. We have estimated the intrinsic errors arising from numerical effects in the computation of the evolutionary models and their oscillation frequencies; the effect on the computed period ratio $\Pi_1/\Pi_0$ is minute, less than $10^{-4}$. On the other hand, major contributions to the uncertainty in the mass determination arise from uncertainties in the composition parameters and possible effects from rotation of V2. The possible effects on the helium abundance of mixing associated with the formation of BSS have already been mentioned. To this must be added the uncertainties in the determination of the overall composition of the cluster. Also, it is well known that rotation affects the evolution of stellar models and the derived oscillation frequencies (*e.g.* Pamyatnykh 2000, Goupil et al. 2000). Fast rotation modifies the evolutionary tracks in the HR and Petersen diagrams , particularly in the post-main-sequence stages where V2 is located. Although the frequency corrections are expected to be relatively small for radial modes, they may be significant. For the high-amplitude $\delta$ Scuti stars (with amplitude $A_V > 0.3$ mag) rotation is usually slow. However, V2 has relatively low amplitude ($A_V = 0.15$) and its rotational velocity ($v \sin i$) is not known. Finally, we recall from Section 2.8.1 that basic parameters of the star, *i.e.* the effective temperature and the distance modulus, are subject to substantial uncertainty.

Given these uncertainties, to what extent can we trust our mass determinations? A very significant aspect in the interpretation is the *consistency* between different determinations. As an example, consider the effects of the helium abundance, exemplified by the *SHe* and *IHe* model series. From the analysis of the HR diagram (Figure 2.10) V2 has *evolutionary mass* $M_{\rm HR} \simeq (1.54 \pm 0.05)\,M_\odot$ with *SHe*, for which the period-ratio mass is $(1.53 \pm 0.03) M_\odot$; for *IHe* the corresponding values are $M_{\rm HR} \simeq (1.50 \pm 0.05)\,M_\odot$ and $(1.45 \pm 0.03) M_\odot$ from the period ratio. Thus for both compositions the two mass determinations agree within the formal error bars,

**Table 2.4** Mass determination of the SX Phe star V2 from its position in the HR diagram and from comparison of observed modes with pulsation models. The results when using different chemical compositions are given (see text for details).

| Composition | *SHe* | *IHe* | *S-W* |
|---|---|---|---|
| $Y$ | 0.241 | 0.261 | 0.273 |
| $Z$ | 0.005 | 0.005 | 0.008 |
| Method | Mass estimates $(M/M_\odot)$ | | |
| HR-diagram | 1.54 | 1.50 | 1.56 |
| Pulsation modes | 1.53 | 1.45 | 1.67 |

although the match is somewhat better for *SHe*. We also note that the mass estimates allow a better constraint on the change in the helium abundance resulting from complete mixing. Assuming that the progenitor stars had masses of around $0.75 M_\odot$ and had evolved for 10 Gyr before the merger, the average helium abundance would be increased by around 0.04 relative to the original value, *i.e.* twice the difference between *SHe* and *IHe*. Since complete mixing is thought to be unlikely during BSS formation, the *SHe* abundance solution is favoured ($Y = 0.241$).

We have adopted a metal content $Z = 0.005$ for the models. However, the value of $[\mathrm{Fe/H}] = -0.83$ from Table 2.1 with the original definition $[\mathrm{Fe/H}] = \log(Z/Z_\odot)$ and $Z_\odot = 0.019$ gives $Z = 0.0028$, and Salaris & Weiss (1998) use $Z = 0.008$, since they account for $\alpha$-element enhancement. In addition to the analysis based on standard stellar model series with $Z = 0.005$, we have also performed mass estimations using the composition used by Salaris & Weiss (1998), *i.e.* $Y = 0.273, Z = 0.008$. We find that for this composition we cannot obtain consistent modelling satisfying the observational constraints: V2 fits an evolutionary track in the HR diagram of mass $1.56\,M_\odot$ and the period ratio yields the mass $1.67\,M_\odot$.

From the period and period ratio we may also infer the age and effective temperature of V2. For the *SHe* models of mass 1.6 and $1.5\,M_\odot$ we have indicated the age of the models in Gyr in the inserted plot in Figure 2.11; this can be compared with the ages in the HR diagram in Figure 2.10 for the $1.5 M_\odot$ model. The analysis indicates that $T_{\mathrm{eff}}$ may be somewhat higher than inferred from our adopted $V - I$ photometry: From the Petersen diagram we infer that $T_{\mathrm{eff}} = (7400 \pm 150)$ K. The ages roughly agree with Figure 2.10 when taking the error on $T_{\mathrm{eff}}$ into account, leading to an age of $(1.7 \pm 0.1)$ Gyr.

The determination of $M_{\mathrm{HR}}$ is sensitive to errors in the distance modulus. An independent estimate of this may be obtained from the period-luminosity-colour-metallicity (PLCZ) relation for SX Phe stars, derived by Petersen & Christensen-Dalsgaard (1999) from theoretical stellar models. This relation is sensitive to the adopted values of $Z$ and in particular of $T_{\mathrm{eff}}$. In the above analysis of V2 we have considered the $T_{\mathrm{eff}}$-interval 7100 to 7700 K. For the preferred $Z = 0.005$ the PLCZ relation gives the corresponding interval in $M_{\mathrm{bol}}$ of 1.98 to 1.56 mag. We note that this is in rough agreement with the value given in Table 2.3 for V2 ($M_{\mathrm{bol}}$ = 1.68) and hence justifies our use of the VandenBerg (2000) distance modulus. Although this is somewhat speculative, a higher temperature for V2, as inferred from the period, seems to be necessary to explain the distance modulus inferred from the main period. We recall from Section 2.8.1 that independent estimates of $V-I$ gave discrepant results for V2.

We thus have two clues that indicate the $T_{\rm eff}$ of V2 may be higher than what we find from the colour (*i.e.* $V-I = 0.43$ or $T_{\rm eff} = 7100$ K): 1) A comparison of the theoretical model ages that best fit the position in the Petersen diagram and the HR diagram do not agree. 2) The PLCZ calibration from Petersen & Christensen-Dalsgaard (1999) gives a small distance modulus ($(m-M)_V = 13.1 \pm 0.1$) for $Z = 0.005$ and $T_{\rm eff} = 7100$ K. Both these observations indicate a higher value of $T_{\rm eff}$. If for V2 we assume $T_{\rm eff} = (7500 \pm 200)$ K appropriate to the independent $V-I = 0.27$ determination we find that the PLCZ relation gives a distance modulus of $(m-M)_V = 13.4 \pm 0.1$ in agreement with VandenBerg (2000) and Grundahl et al. (2002) — and with this temperature the new position of V2 in the HR diagram agrees with the position in the Petersen diagram within error-bars.

It is evident that there are a number of uncertainties concerning the parameters and modelling of V2. Also, we have not been able to take into account the possible effects of rotation on the inferences. However, the fact that we obtain a consistent description of V2 using standard modelling without rotation — which is the simplest possibility — gives us some confidence in this modelling. Since V2 is a relatively evolved and hence old BSS at $\sim$1.7 Gyr it could by now have lost significant angular momentum even if it was formed initially as a rapid rotator. Thus, from this discussion we maintain that a reasonable estimate for the mass of V2 is $M/M_\odot = 1.54 \pm 0.05$; we stress, however, that this assumes V2 to have the same chemical composition as an average star in the cluster.

In Table 2.4 we present the results of the mass estimation of V2 for the three different chemical compositions discussed above.

We finally note that we have also found new low-amplitude modes for V2 (see Table 2.2), but their frequencies are simply linear combinations of the frequencies of the two main modes. This indicates that the modes are interacting non-linearly as was also noted by Gilliland et al. (1998), and the pattern given in Table 2.2 is in perfect agreement with predictions from Garrido and Rodriguez (1996).

### 2.8.5 V3, V15, and V16

The interpretation of the modes of V3 is difficult since the period ratio is close to unity. Gilliland et al. (1998) propose that it is a rotationally split non-radial mode ($l = 1$). If this is true the rotational period of V3 (based on the splitting in Table 2.2) is $P_{\rm rot} = (2.33 \pm 0.03)$ days. Gilliland et al. (1998) found a significantly faster rotation period $P_{\rm rot} = (1.65 \pm 0.2)$ days.

The interpretation of the double-mode SX Phe star V15 is also difficult. If this star is assumed to be a "classical" double-mode pulsator oscillating in radial modes, it must be oscillating in high overtones. The observed period ratio is $\Pi_N/\Pi_n = 0.8651 \pm 0.0003$ which is below the ratio calculated from theoretical models with radial orders 5 and 6 — but above the calculated ratio for radial orders 4 and 5. Figure 2.12 shows several series of models oscillating in these high overtones. The $10\,\sigma$ error bars are shown.

The result for V15 by Gilliland et al. (1998) was $\Pi_N/\Pi_n = 0.8698 \pm 0.0023$.

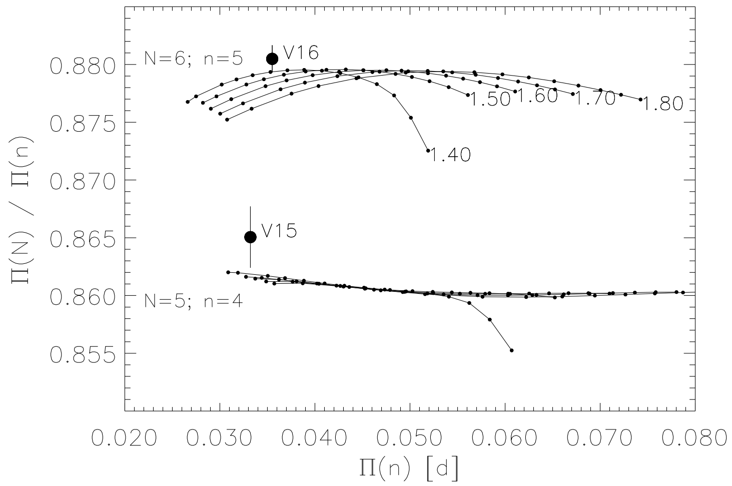


**Figure 2.12** Petersen diagram showing radial overtones of orders four to six for several stellar model series. The • symbols mark the SX Phe stars V15 and V16. The vertical bars are the $10\,\sigma$ error on the period ratio.

This result was consistent with V15 oscillating in two high overtones with their analysis, *i.e.* orders 4 and 5. With the new results none of the calculated models fits the observed properties of V15. This is also the case when using the composition from Salaris & Weiss (1998), *i.e.* models with higher helium and heavy element content.

Possible explanations for the apparent discrepancy are *e.g.* (i) that at least one of the observed modes is a non-radial mode, or (ii) that the frequencies are modified by rotation of the star. A clear interpretation of the modes in V15 cannot yet be made.

We note that for the two modes in V15 the periods determined from the 1993 and 1999 observations agree to $0.8\,\sigma$ and $2.0\,\sigma$ for the large- and small-amplitude peaks, respectively. Either spurious agreement with radial overtone period ratios was allowed by the larger errors in the results of Gilliland et al. (1998), or the lower-amplitude peak represents different modes having been excited 6 years apart.

Interpretation of the double-mode star V16 is also problematic here. The mode near 32 cycles/day from 1993 is clearly present in the 1999 observations with the new frequency $1.2\,\sigma$ from the original value. The mode near 28 cycles/day is at a lower amplitude in 1999 and at marginal $\sim 3\,\sigma$ significance in each epoch separately. Taking the agreement (to $0.8\,\sigma$ from the 1999 period) as confirmation of this mode and evaluating the period ratio yields $\Pi_N/\Pi_n = 0.8805 \pm 0.0002$ (compared to 1993 data result of $0.8816 \pm 0.0028$) which falls just above the period ratios for orders 5 and 6 in Figure 2.12. However, there are evidently other modes present to equal or higher significance – these cannot all be radial modes. The significance of amplitudes quoted in Table 2.2 represent very conservative values based upon establishing a *local* mean in the amplitude spectra and considering the ratio of the mode amplitude to this. Since our power spectra for non-variable stars remain flat consistent with white noise, it may well be appropriate to base the errors on means over the full available frequency range. As an example, for V16 adopting a global normalization for the amplitude spectrum noise would increase the significance of the three modes near 28, 29, and 31 cycles/day to over 8 $\sigma$ each with the possibility that yet weaker modes are also present.

### 2.8.6 Future Work

How can the analysis of the SX Phe variables in 47 Tuc be improved in the future? From the discussion above it is evident that accurate determinations of effective temperatures will give stronger constraints on the modelling. Secure determinations of the chemical composition and studies of rotation will also be important.

A more ambitious project is simultaneous modelling of several SX Phe variables in 47 Tuc following the philosophy of the programme for asteroseismology in open clusters (*e.g.* Frandsen et al. 1996). The new results for V15 and V16 are consistent with the presence of some non-radial modes, perhaps with high overtone radial modes present as well. Another challenging case is V1, which Gilliland et al. (1998) found to be a triple-mode variable with period ratios that cannot be explained by radial oscillations of standard evolutionary models with the accepted composition of 47 Tuc. Either this star, with an amplitude of about 0.15 mag, has a low $Z \approx 0.001$, its modes are non-radial, or perhaps a large effect from rotation needs to be considered. It seems clear that more detailed studies of the SX Phe stars in 47 Tuc will provide valuable asteroseismological information.

## 2.9 Conclusions

The unique time series of 8.3 days from HST of 47 Tuc analyzed here was optimized to look for planets around stars fainter than the turn-off. We have shown that it is possible to obtain good photometry for the saturated stars by identifying and flagging (*i.e.* not using) pixels that are contaminated by neighbouring pixels due to *bleeding* signal. We have thus extracted good (1-3% noise) light curves for the saturated stars. No new variable BSS stars were found in the sample but have analyzed five of the six known SX Phe stars in the core of 47 Tuc (V1 was not in the field of view). For V14 we do not detect the oscillation signal that has been claimed previously. For three of the double-mode stars (V2, V15, and V16) we have used theoretical stellar models to attempt to determine their masses: both through the position in the HR diagram (using the observed magnitudes) and in the Petersen diagram (using the observed periods).

The most striking result from this study is the determination of the mass of the SX Phe star V2. From the HR diagram (not depending on the uncertainty of $T_{\rm eff}$) and the Petersen diagram we infer a mass of $M_{\rm V2} = (1.54 \pm 0.05)\, M_{\odot}$. Important sources of error in this mass estimate of V2 are the chemical composition and effects of rotation; even so, we believe that we have obtained the so far most precise determination of the mass of a BSS (see Shara et al. 1997). Further progress requires a spectroscopic study to constrain $T_{\rm eff}$, rotational velocity, and chemical composition for V2; this would be difficult from the ground due to crowding, but it is feasible with HST. Our results indicate that, with such additional data, we would be able to obtain strong constraints on the processes that lead to the formation of BSS.

## 2.10 Acknowledgements

We wish to express our gratitude to Don VandenBerg for providing us with a set of independently calculated evolutionary models and an isochrone for 47 Tucanae. This research was supported by the Danish Natural Science Research Council through its Centre for Ground-based Observational Astronomy and by the Danish National Research Foundation through its establishment of the Theoretical Astrophysics Center. U.S. investigators were supported in part by STScI Grant GO-8267.01-97A to the Space Telescope Science Institute and several STScI grants from the same proposal to co-I institutions.

## 2.11 References

Alcaino G., Liller W., 1987, ApJ, 319, 304

Anderson J., King I.R., 1999, PASP, 111, 1095

Bailyn C.D., 1995, ARA&A 33, 133

Bailyn C.D., Pinsonneault M.H., 1995, ApJ, 439, 705

Benz W., Hills J.G., 1987, ApJ, 323, 614

Benz W., Hills J.G., 1992, ApJ, 389, 546

Bessell M.S., Castelli F., Plez B., 1998, A&A, 333, 231

Breger M., 1990, ASP Conf. Ser., 11, 211, Cacciari C., Clementini G. (eds.)

Buzzoni A., Fusi Pecci F., Buonanno R., Corsi C., 1983, A&A, 128, 94

Camilo F., Lorimer D.R., Freire P., Lyne A.G., Manchester R.N., 2000, ApJ, 535, 975

Carretta E., Gratton R.G., 1997, A&AS, 121, 95 Carretta E., Gratton R.G., Clementini G., Fusi Pecci F., 2000, ApJ, 533, 215

Cool A.M., Grindlay J.E., Cohn H.N., Lugger P.M. Bailyn C.D., 1998, ApJ, 508, L75

Da Costa G.S., Armandroff, T.E., 1990, AJ, 100, 162

Drissen L., Shara M.M., 1998, AJ, 115, 725

Edmonds P.D., Gilliland, R.L., 1996, ApJ, 464, L157

Edmonds P.D., Gilliland R.L., Guhathakurta P., Petro L.D, Saha A., Shara M.M., 1996, ApJ, 46, 241

Frandsen S., Balona L., Viskum M., Koen C., Kjeldsen H., 1996, A&A, 308, 132

Freyhammer L.M., Andersen M.I., Petersen J.O., 1998, ASP Conf. Ser., 135, 458

Fusi Pecci F., Bellazzini M., Ferraro F.R., Buonanno R., Corsi C.E., 1996, ASP Conf. Ser., 92, 221, Morrison H., Sarajedini A. (eds.)

Garrido R., Rodriguez E., 1996, MNRAS, 281, 696

Gilliland R.L., 1994, ApJ, 435, L63

Gilliland R.L., Edmonds P.D., Petro L., Saha A., Shara M.M., 1995, ApJ, 447, 191

Gilliland R.L., Bono G., Edmonds P.D., Caputo F., Cassisi S., Petro L.D., Saha A., Shara M.M., 1998, ApJ 507, 818

Gilliland R.L, Nugent P.E., Phillips M.M, 1999, ApJ, 521, 30

Gilliland R.L, et al., 2000, ApJ, 545, L47

Goupil M.-J., Dziembowski W.A., Pamyatnykh A.A., Talon S., 2000, ASP Conf. Ser., 210, 267, Breger M., Montgomery M.H. (eds.)

Grundahl F., Stetson P.B., Andersen M.I., 2002, A&A, 395, 481

Guhathakurta P., Yanny B., Schneider D.P., Bahcall J.N., 1992, AJ, 104, 1790

Guhathakurta P., Webster Z.D., Schneider D.P., Yanny B., Bahcall J.N., 1998, AJ 116, 1757

Hesser J.E., Harris W.E., VandenBerg D.A., Allwright J.W.B., Shott P., Stetson, P.B, 1987, PASP, 99, 739

Holtzman J.A., Burrows C.J., Casertano S., Hester J.J., Trauger J.T., Watson A.M., Worthey G., 1995, PASP, 107, 1065

Kaluzny, J., Kubiak, M., Szymanski, M., et al. 1998, A&AS, 128, 19

Kelson D.D., Illingworth G.D., Freedman W.D., et al., 1996, ApJ 463, 26

Pamyatnykh A.A., 2000, ASP Conf. Ser., 210, 215, Breger M., Montgomery M.H. (eds.)

Petersen J.O., Christensen-Dalsgaard J., 1996, A&A, 312, 463

Petersen J.O., Christensen-Dalsgaard J., 1999, A&A, 352, 547

Piotto G., Zoccali M., King I.R., Djorgovski S.G., Sosin C., Dorman B., Rich R.M., Meylan G., 1999, AJ, 117, 264

Rodriguez E., López-González M.J., 2000, A&A, 359, 597

Salaris M., Weiss A., 1998, A&A, 335, 943

Shara M.M., Saffer R.A., Livio M., 1997, ApJ, 489, L59

Sperl M., 1998, Comm. in Asteroseismology, 111, 1

Stetson P.B., 1987, PASP, 99, 191

Stetson P.B., 1998, PASP, 110, 1448

Suchkov A., Casertano S., 1997, STScI Instrument Science Report WFPC/II 97-01, http://www.stsci.edu/instruments/wfpc2/Wfpc2_isr/wfpc2_isr9701.html

Taylor B.J., 1986, ApJS, 60, 577

VandenBerg D.A., 2000, ApJS, 129, 315

Weiss A., Salaris M., 1999, A&A 346, 897

Zoccali M. et al., 1999, ASP Conf. Ser., 167, 336, Egret D., Heck A. (eds.)

Zoccali M., Cassisi S., Bono G., Piotto G., Rich R.M., Djorgovski S.G., 2000, ApJ, 538, 289

# Chapter III

# The Search for Oscillations of Giant Stars in M 4

> "It is important to remember that we are very close to producing noise levels equal to the solar oscillation signal, and that some stars are expected to oscillate with higher amplitudes than our own Sun."
> – Bedding & Kjeldsen (1998)

### Overview

The content of the following chapter concerns the search for oscillations in the giant stars in the globular cluster Messier 4 (M 4 = NGC 6121). Many aspects of this project are described and hence the "casual reader" (if such exist) may be overwhelmed by the amount of information given here.

The chapter has three main parts, namely a description of the background and prospects of the project on M 4, the details of the data reduction, and a presentation of the preliminary results for giant stars and other potentially interesting stars in the cluster. The title of each section is followed by a symbol which tells the reader which of the three parts it belongs to: background = $\circ$, data reduction = $*$, or results = $\bullet$.

The *number* of symbols indicates the "importance" I have assigned to each section. Thus a reader only concerned with the results of the search for oscillations of giant stars should go directly to the sections with a single $\bullet$ symbol.

A brief description of the contents of this chapter is given below.

### ○ Background: Asteroseismology and Variability of Giant Stars

- In section 3.1° I discuss the potential use of asteroseismology to probe the interior of stars and give a review of previous studies of the variability of giant stars.

- In section 3.2° I give a description of the background and prospects of the project to detect oscillations of the giant stars in the globular cluster M 4.

### ∗ Data Reduction: Photometry and Weighting of Data Points

- In section 3.3* the photometric reduction is described. I have used difference imaging software, but encountered several problems which are discussed.
- In section 3.4* the decorrelation of the light curves to remove any *extrinsic* dependencies of the measured light curves on *e.g.* airmass, sky background *etc.* is described.
- In section 3.5* the weighting of data points is discussed. This is crucial since the data quality varies from night to night. Furthermore, the detection of outlier data points is treated.
- In section 3.6*** the influence of crowding on the photometry is discussed.
- In section 3.7*** I compare the quality of the data from two different telescopes: the 1.5 m CTIO, Cerro Telolo and the Danish 1.54 m Telescope, La Silla.

### ● Results: The Variable Stars in M 4

- In section 3.8• I present the search for oscillations among the bump stars.
- In section 3.9•• I give results for the search for oscillations among the potential sdB-type variables.
- In section 3.10•• I present a few examples of light curves for known variable stars in M 4.

Finally, I will give my conclusion of the work presented here in section 3.11.

## 3.1 The Detection of Solar-like Oscillations°

The characteristic comb-like pattern seen in the amplitude spectrum of the Sun with peaks corresponding to periods around five minutes are due to pressure driven oscillations ($p$ modes) which are stochastically exited by convection in the outer envelope of the Sun. Theoretical model calculations predict that stars similar to the Sun will also show a more or less similar comb-like envelope. In the past decade astronomers have attempted to detect oscillations in stars similar to the Sun (a review was given by Brown (1998)). The prospects of being able to use the tools of helioseismology on other stars – the field of asteroseismology – are tremendous and much effort has been invested to pursue this.

The first detection of solar-like oscillations in stars similar to the Sun can be debated[1] but perhaps the first successful detection was in the sub-giant star $\eta$ Boo by Kjeldsen et al. (1995). During the past few years, oscillations have finally been unambiguously detected in a small number of solar-like stars, *i.e.* Procyon (Martić

[1] One could mention a long list of "near detections", *e.g.* the work of Brown et al. (1991) based on Doppler velocity measurements of Procyon – but few of these earlier results are truly convincing.

et al. 1999), $\beta$ Hyi (Bedding et al. 2001; Carrier et al. 2001), and the "solar twin" $\alpha$ Cen (Bouchy & Carrier 2001). Recently, oscillations have been detected in three stars in a much later stage of evolution, namely the giant stars $\xi$ Hya (Frandsen et al. 2002), $\delta$ Eri (Carrier et al. 2003), and $\nu$ Ind (T. Bedding, *private communication*).

These detections all rely on time series of the Doppler velocity shift caused by the slight movements of the surface of the stars. To be able to do this requires very accurate measurements and has become possible with the development of ultra-stable spectrographs capable of observing with an accuracy of 3 m s$^{-1}$ or better over periods of several days. One of the secrets of achieving precise velocity measurements is the use of an iodine cell or a thorium comparison spectrum which will define a very stable wavelength reference. These spectrographs have been developed primarily for the search for extra-solar planets through the monitoring of the movement of stars caused by orbiting giant planets (Marcy & Butler 1998). It is fortunate that astronomers concerned with asteroseismology can use the "few m s$^{-1}$" spectrographs[2].

I have worked on a project with the aim of detecting solar-like oscillations in giant stars in the globular cluster M 4 through *photometric* monitoring. In this chapter I will first give an overview of previous research on variable giant stars before giving a detailed account of the data reduction of the data for the M 4 project, and then give the preliminary results for this ongoing project.

### 3.1.1 Variability among Giant Stars°

The most easily observed variable stars in the sky belong to the Mira class (M-III type stars) and have been known for at least four hundred years (Petit 1987). Their amplitudes are typically a few magnitudes while periods range from days to years (Bedding & Zijlstra 1998). They belong to the brightest red giant branch stars of which most are variable and they are believed to be "simple pulsators", *i.e.* they pulsate in purely radial modes.

In the past decade observations of variability has been reported among giant stars of earlier spectral classes at much lower amplitude (mmag) and with shorter periods (days). Among the explanations for the observed variations are rotational modulation of star spots, planetary companions or non-radial pulsation (Hatzes & Cochran 1993). Some K-III-type giants are variable at unexpectedly (if seen as a continuation of the Mira instability) long periods – from a fraction of a day to a few days. This would indicate that the modes are not radial modes but rather $g$-mode or mixed $p/g$-mode oscillations (Edmonds & Gilliland 1996; Henry et al. 2000). If the comb-like pattern of frequencies expected from theoretical calculations are measured, one could potentially gain knowledge about the interior of the giant stars (see Frandsen et al. (2002)). If the oscillations are $p$-modes the mean density of the star can be determined by measuring the large separation (see *e.g.* Toutain & Froehlich (1992)). It would be extremely valuable to be able to compare theoretical

[2]Examples are CAT at Lick, ELODIE at observatoire d'Haute Provence, CORALIE at La Silla, HIRES/KECK on Hawaii, UVES at Paranal, and soon HARPS, La Silla.

models of giant stars with the observed stars in order to better understand stars in their late state of evolution, *i.e.* to be able to use the tools of asteroseismology on the giant stars to obtain detailed information about their interior. It would be very interesting to compare this with the knowledge that can be learned from photometric indices and spectroscopic studies that to date are the only option. For an excellent review on the spectroscopic and photometric tools used to constrain models of giant stars see Salaris et al. (2002).

Obviously, the recent definitive detection of oscillations in the giants $\xi$ Hya (Frandsen et al. 2002) and $\nu$ Ind (T. Bedding, *private communication*) based on Doppler measurements is the first step into a new era in the understanding of the physics of stars that have departed from the hydrogen burning main sequence.

### 3.1.2 Observations of Variability among Giant Stars°°

The observed variability of the K1 giant $\alpha$ Boo (Arcturus) has puzzled astronomers for about 15 years. Ten individual modes have been observed through spectroscopic measurements, but the modes are not stable with time (Merline 1999). Furthermore, theoretical modelling of $\alpha$ Boo (Hatzes & Cochran 1994) fails to describe the observed oscillations.

Conclusive detection of variability among K-type Giants was reported in the study by Edmonds & Gilliland (1996). They detected definite photometric variability among the 15 brightest red giants in the metal rich globular cluster 47 Tuc. They used 38.5 hours of observations with the Hubble Space Telescope in the $U$ band (F336W). They compared the *combined* power spectrum of the giant stars with other stars with similar luminosity in the cluster. From this comparison it was evident that the giant stars showed significant excess power around 2-4 days. Unfortunately, the time-span of the data set was too short to be able to extract periods of individual stars.

Several spectroscopic studies have been conducted to detect the variations on K giants (see Hatzes & Cochran (1998)), but no clear evidence of solar-like oscillations has been seen so far. In most cases where a giant star has been observed more than once the same exact periods are not seen again. The exception is perhaps $\alpha$ UMa (a K0–III type star) for which both spectroscopic and photometric campaigns seem to agree on some of the detected frequencies. Buzasi et al. (2000) used 4 million data points from the 52 mm aperture star camera on board the `WIRE` satellite to make the "detection of multi-modal oscillations on $\alpha$ Ursae Majoris". They identified 10 frequencies in the range 1.82–43.53 $\mu$Hz and interpreted them as being stellar oscillations[3]. Dziembowski et al. (2001) have calculated pulsation models of $\alpha$ UMa but they find very poor agreement with the observed frequencies and their relative amplitudes. One might speculate that the variation of $\alpha$ UMa is not due to $p$-mode oscillations.

Jorissen et al. (1997) presented their results from 10 years of observations with the 50 cm SAT photo-electric telescope, La Silla, in a publication entitled "the onset of photometric variability in red giants". They measured the photometric stability

[3] Buzasi et al. (2000) claimed that Hatzes et al. confirmed this variability in the same range from spectroscopy but these results have not been published.

of a sample of about 50 red giants and concluded that giant stars with spectral classes G to early K were "stable" at $\sigma_y < 6$ mmag, which was significantly above the photometric precision at 2–3 mmag. On the other hand, Jorissen et al. (1997) found that the measured noise level increased dramatically when going to spectral classes later than K3-III, hence the title "the onset of variability [...]." They defined the "minimum variability boundary" which refers to the noise *vs.* colour diagram ($\sigma_y$ *vs.* Strömgren $b - y$). In this diagram no giant with low noise, *i.e.* as expected from the photon-noise statistics, was found for spectral class later than K3-III. For three of the giant stars Jorissen et al. (1997) were able to determine approximate periods (from 37–117 days) and amplitudes (0.15–0.3 mag in $y$). From this small sample they concluded that periods and amplitudes increase – as expected – when going to later spectral types (*i.e.* higher luminosities) and – very interestingly – that the periodicity is more stable for the later spectral types. For two of the giants they compared the observed noise in the measured spectroscopic radial velocities ($\sigma(v_{\rm rad-vel}) \simeq 1.5$ km s$^{-1}$) with the photometric noise and found good agreement with the predicted ratio from Kjeldsen & Bedding (1995).

Henry et al. (2000) have presented the results of a large campaign on 187 G and K-type giants from three photo-electric telescopes that lasted five years (1993–98) in which most targets were observed 1–3 seasons, each of which consisted of one or more observing runs with a typical duration of one month. The noise level of the observations made with the smallest telescope (0.4 m) was $\simeq$4 mmag, while the two larger telescopes – which carried out the majority of the campaign – produced light curves at $\simeq$1.1 mmag internal precision. Hence, the noise limit was a factor of two lower than the study by Jorissen et al. (1997) and it would be possible to detect any low amplitude variability among the giants earlier than type K2-III if the "minimum variability boundary" found by Jorissen et al. (1997) extended to earlier types. Indeed Henry et al. (2000) found evidence for variability among giants down to the limit of the sample, *i.e.* as early as G0 at a level of 3–5 mmag. Their results agree with Jorissen et al. (1997) who found that stars earlier than K3 were "stable" below 6 mmag – and that for giant stars later than K3 the noise level grows considerably. Henry et al. (2000) confirmed the result from the HIPPARCOS satellite (Eyer et al. 1994) that stars of type G8-III are among the most stable stars to be observed, *i.e.* no variability is found around G8 while a significant fraction of stars of both later and earlier type are variable[4].

Interestingly, Henry et al. (2000) have also obtained spectroscopic observations of some of their giant targets in order to make a spectral classification of the giants, determine $v \sin i$, and measure the surface activity level from the Ca II H and K lines.

Henry et al. (2000) discern between giants cooler and hotter than the "coronal dividing line" (CDL, Haisch (1999)) which is roughly the boundary between chromospherically active hot stars and cold non-active stars with massive winds. They find strong evidence that different mechanisms determine the variability on either

[4]In this context I mention the case of the G7 giant $\xi$ Hya in which oscillations have been observed by Frandsen et al. (2002). In this case the observed amplitude in Doppler velocity is only one third of what is predicted by the $L/M$ scaling relation of Kjeldsen & Bedding (1995). These results might indicate that some damping mechanism is active for stars of spectral types around G8.

side of the CDL: from the measured $v \sin i$, estimated stellar radius, and measured periodicity of 29 stars they were able to determine what the inclination angle, $i$, would be if the variability of the giants was due to star spots. For stars on the cool side of CDL the predicted angles lie at very low values for all stars ($i < 2°$). For the 11 giants on the hot side of CDL the scatter in $i$ is larger but all stars have $i < 60$. If the angles were randomly distributed half of these 11 stars should be above 60°. From the Ca activity index Henry et al. (2000) find very low activity for the stars on the cool side of CDL while weak activity is measured for some of the stars on the hot side of CDL.

To summarize, the $v \sin i$ distribution seems to exclude star surface spots as the source of variability for both the cool and hot giant stars observed by Henry et al. (2000), while the measured Ca-indices seem to support star spots as the explanation for some (about half) of the cool stars.

The periods estimated by Henry et al. (2000) for the giants agree with theoretical predictions for low-order radial $p$-modes for the cool giants while the predicted periods are significantly longer than has been observed for the hot giants. This is in agreement with Edmonds & Gilliland (1996) who suggested that non-radial $p/g$-modes are the explanation for the observed short-period variations they found evidence for in the giant stars in 47 Tuc.

### 3.1.3 Evolution of K Giants: The Origin of the Bump Region°°°

Since the topic of this chapter is giant stars it is sensible to describe in some detail the evolution of a star from the main sequence when the hydrogen fuel has been exhausted in the core and through the giant phase.

To illustrate this evolution I present the observed colour-magnitude diagram (CMD) of M 4 as seen from La Silla in Figure 3.1. I have used about 70 images in each of the $B$ and $V$ filters which were reduced with ALLFRAME (Stetson 1994). Below the turn-off only the least crowded stars are plotted (around 6 000 stars in total). M 4 suffers from differential reddening (Alcaino et al. 1997) and hence the main sequence appears as quite broad (as opposed to CMD of the open cluster NGC 6791 in Figure 4.2).

The *turn-off* is at $V = 17, B - V = 0.9$ where stars have begun to leave the main sequence since the hydrogen fuel is depleted in the core. The outer parts of the stars will then expand while hydrogen is still being processed in a shell source around the helium core. During the evolution towards the *Hayashi-track* the outer convection envelope becomes exceedingly deep before reaching its maximum depth (in terms of mass) around the base of the red giant branch (RGB). As the stars ascend the RGB their outer envelope expands to several solar radii and the luminosity grows significantly while the stars become only somewhat cooler ($L \propto R^2 {T_{\text{eff}}}^4$).

In the CMD in Figure 3.1 it can be noticed that a significant amount of giant stars occupy the region around $V = 13.5$ and $B - V = 1.3$: this is the so-called *bump region*. As the giant stars evolve up the giant branch the hydrogen-burning shell moves outward to larger radii and at one point it will reach the *chemical abundance discontinuity* that occurs where the outer convection zone reached its max-

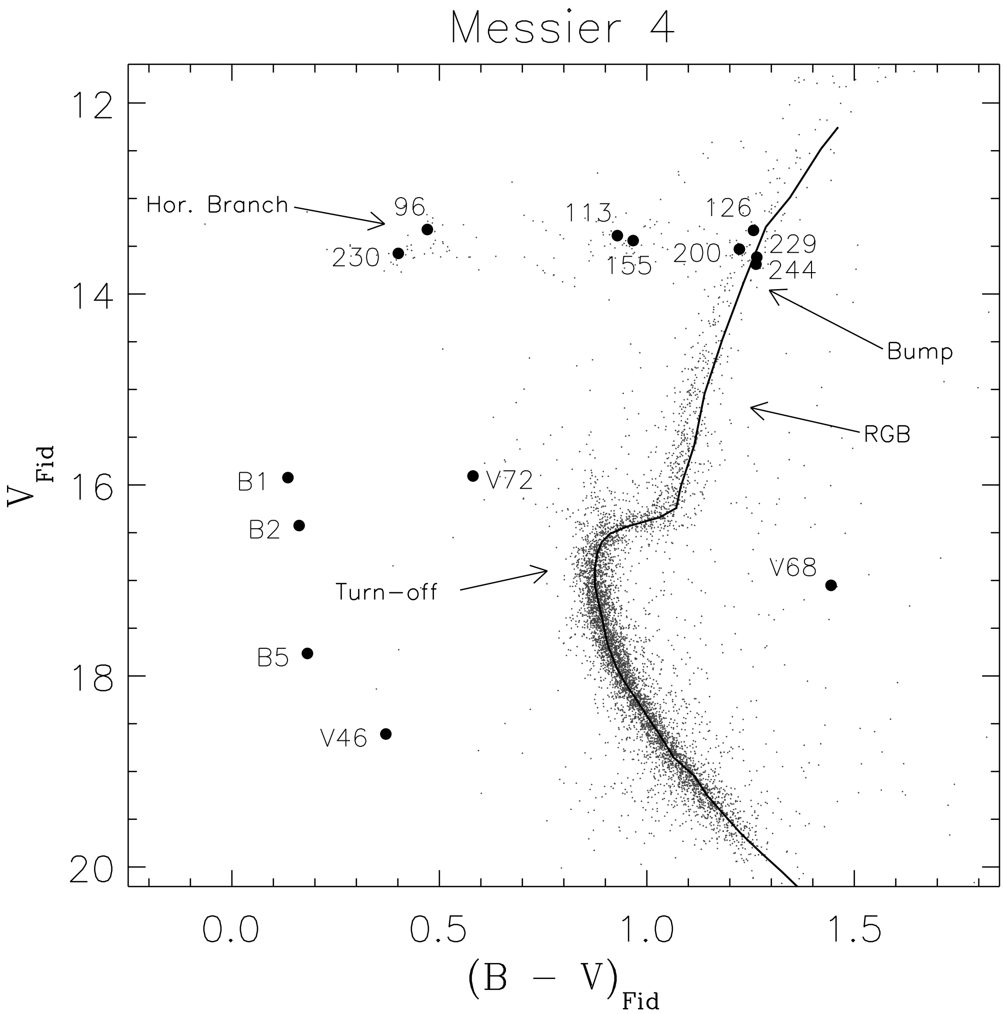


**Figure 3.1** Colour–magnitude diagram of M4. The magnitudes are instrumental, but have been shifted to fit the fiducial sequence from Mochejska et al. (2002a) (black solid line). Note that for stars fainter than $V = 16.5$ only the least crowded stars are plotted (above line $B$ in Figure 3.10). The horizontal branch, turn-off, red giant branch (RGB), and the bump region are marked. Several individual stars which are discussed in the text have been identified.

imum depth. The extra supply of hydrogen at this point will cause the hydrogen-burning shell to expand and the stars will temporarily halt their ascend of the giant branch for a significant time compared to the evolution time scale of the giant stars (Salaris et al. 2002) which is the reason for the observed "bump".

Eventually the stars will evolve to the tip of the giant branch while losing perhaps as much as 20% of their mass (Salaris et al. 2002). The helium core will be degenerate for the relatively low-mass stars in M 4, but the hydrogen-burning shell will eventually heat up the core and thus lift the degeneracy which causes a thermal run-away – the so-called *helium flash*. This starts the triple–$\alpha$ fusion process and the stars will settle on the horizontal branch. The amount of mass loss during the ascend of the upper giant branch largely determines the location of the star on the horizontal branch.

For further information on stellar evolution of giant stars consult Salaris et al. (2002) and Kippenhahn & Weigert (1994).

## 3.2 The M 4 Campaign: a Search for Oscillations in Giant Stars°

Inspired by the K Giant oscillations observed by Edmonds & Gilliland (1996), S. Frandsen and F. Grundahl from the University of Aarhus orgainzed an ambitious campaign to detect oscillations of giant stars in the globular cluster M 4. Since the periods of the oscillations are relatively long (several hours) for such evolved stars, the time baseline must be several weeks in order to resolve the modes. Hence, observations from the ground with medium-sized telescopes was the only realistic option.

Our proposals for observing time were very successful and we were given $\sim 65$ telescope nights (51 clear) at the Danish 1.54 m telescope, the 1.5 m CTIO (both in Chile) and the wide field imager on the 1 m telescope at Siding Springs Observatory (SSO) in Austrialia.

The ultimate goal of the M 4 campaign is to measure the oscillations of stars on the upper part of the red giant branch and determine the large separation expected from theory for $p$-mode oscillations (see *e.g.* Toutain & Froehlich (1992)). If successful, we could in principle measure the change in density (the large separation is proportional to the square root of the density, *cf.* Eq. 3.5) of the giant stars at different evolutionary stages across the *bump region* on the red giant branch (*cf.* section 3.1.3). From the detailed comparison of observed frequencies and theoretical models, much progress is to be expected in the understanding of stars at this late stage of evolution.

A significant advantage in the modelling of the giant stars in M 4 will be that the bump stars have approximately the same mass and temperature in addition to similar metallicities[5] and age. From the fitting of isochrones to M 4 we will obtain a relatively accurate measure of mass of the stars in the bump region. The model parameters could be improved significantly by other means which will be the subject of future studies of the present data set: specifically, we will make a

[5]However, significant star-to-star differences in the surface abundance of light elements among giant stars have been reported (see section 7 of Salaris et al. (2002)).

thorough search for detached eclipsing binaries in M 4. The mass of binary stars can be determined to within a percent as was done by Kaluzny et al. (2002) for binary stars in $\omega$ Cen. If one of the binary components is located after the turn-off, the age of the cluster can be constrained from theoretical isochrones (from turn-off mass *vs.* age relations). We could then constrain the distance to the cluster, and in turn give very accurate determinations of the mass of the bump stars.

Furthermore, if we can measure the large separation of several giant stars and hence their density, we can deduce their relative radii to excellent accuracy (since the mass is virtually the same). This would lead to estimates of how fundamental parameters like $\log g$ and $T_{\rm eff}$ change during their evolution across the bump region.

If some of these goals can be achieved from the present data set we can put strict constraints on the theoretical models of red giant stars. Depending on the output we may be able to shed new light onto the inadequacies of the physics going into the models.

For a recent review of the theoretical modelling of red giant stars see Salaris et al. (2002).

### 3.2.1 The M 67 Campaign°

In this context one should mention the M67 campaign described by Gilliland et al. (1993). They carried out an ambitious multi-site campaign with 4 m class telescopes on 12 target stars in the open cluster M 67 with the aim of detecting solar-like oscillations in main sequence G-type stars. Using deliberately defocused images from 22 telescope nights spread over one week, they reached a noise level in the amplitude spectrum of 6 ppm in the best cases. This must be compared with the amplitude of the modes seen on the Sun, *i.e.* $A \simeq 5$ ppm. For this project the atmospheric scintillation noise set the limit. The results of this project emphasizes the need to go to space to be able to do asteroseismology of solar-like stars.

However, the amplitudes of the brightest giant stars in M 4 will be much larger than in the Sun while the period will also be much longer. For comparison the giants are expected[6] to have amplitudes of about 500 ppm and periods of $P \simeq 600$ minutes.

The M 67 and M 4 campaigns are also very different in other aspects which I will briefly mention. The field of M 67 was uncrowded and defocusing was possible, thus maximizing the collection of photons. For the crowded M 4 field good seeing and focusing were important, and consequently the duty cyle became low (*e.g.* a CCD read-out time of 50 s and integration times of 30 s in $V$). Secondly, most of the M 4 observations were made from a single site and thus problems with 1/day aliases will be present.

[6]Based on the scaling relation of Kjeldsen & Bedding (1995). Although this relation is found from main-sequence stars the relation seems to hold for more evolved stars to within a factor of two. The reader may consult the theoretical work by Houdek et al. (1999) and the observational results for the giant stars $\alpha$ UMa (Buzasi et al. 2000) and $\xi$ Hya (Frandsen et al. 2002).

**Table 3.1** Log of observations of Messier 4 from La Silla, CTIO, and SSO in the year 2001. The total number of nights is excluding the data from SSO which has not yet been reduced.

| Telescope | Dates UT | Number of Nights | Observer | Seeing | Number of images $N_B$ | $N_V$ | $N_R$ |
|---|---|---|---|---|---|---|---|
| Danish 1.54 m | 12/4–17/4 | 5 | Bruntt | $1''.1$–$1''.3$ | 149 | 239 | 372 |
| Danish 1.54 m | 26/4–30/4 | 5 | Bruntt | $1''.1$–$1''.6$ | 157 | 200 | 339 |
| Danish 1.54 m | 1/5–12/5 | 10 | Frandsen | $1''.2$–$1''.7$ | 184 | 270 | 453 |
| Danish 1.54 m | 24/5–29/5 | 6 | Matthiesen | $1''.1$–$1''.3$ | 105 | 175 | 311 |
| CTIO 1.5 m | 2/6– 7/6 | 6 | Michel | $1''.1$–$1''.7$ | 143 | 274 | 446 |
| Danish 1.54 m | 23/6–31/6 | 7 | Kjeldsen | $1''.0$–$1''.4$ | 252 | 474 | 334 |
| SSO 40 inch | 1/5–13/5 | (8) | Grundahl/Jacob | $\sim 2''.5$ | - | - | - |
| SSO 40 inch | 4/6–11/6 | (4) | Jacob | $\sim 2''.5$ | - | - | - |
| Total | 12/4 - 31/6 | 39 (+12) | - | $1''.0$–$1''.5$ | 990 | 1632 | 2255 |

### 3.2.2 Summary of Observations of M 4°°

A group of astronomers from Aarhus: F. Grundahl, S. Frandsen, J. Matthiesen, H. Kjeldsen, the author of this thesis, Eric Michel from France, and A. Jacob from Australia observed M 4 with the Danish 1.54 m at La Silla, CTIO 1.5 m at Cerro Telolo in Chile for a total of 39 clear nights, and 12 nights with the wide field imager at Siding Springs Observatory (SSO), Australia.

A log of the observations is given in Table 3.1. Each row contains the name of the telescope used, the period of observation, the number of nights, the name of the observer, the average seeing of the best 30 images and the median seeing in the $V$ filter, and the last three columns give the number of images obtained in each of the filters $B$, $V$, and $R$. In addition to this a few images were taken in the Strömgren $ubvy - \beta$ filters. We also observed several standard fields for calibration purposes.

The target of our search for oscillations in the K giants will be concentrated on the stars in the bump region which contains the highest number of giants per luminosity bin. To optimize the observations we adjusted the exposure times during the night so the giant stars $\simeq 0.5$ mag brighter than the horizontal branch would not saturate.

For the observations with the Danish 1.54 m the median exposure times were 180, 30, and 15 seconds in $B$, $V$, and $R$. The Danish 1.54 m and the CTIO 1.5 m telescopes are expected to be comparable in terms of data quality. Both cameras have 2k by 2k CCDs and the pixel scale is $0''.395$/pixel and $0''.44$/pixel. In section 3.7 I compare the data quality from the two telescopes. The SSO 40 inch telescope has a mosaic camera with eight 2k by 4k CCDs and the pixel scale is $0''.375$/pixel.

The fundamental parameters of M 4 are given in Table 3.2.

**Table 3.2** Fundamental properties of Messier 4. Right ascension, declination, metallicity, and interstellar reddening are taken from Dixon & Longmore (1993). The age and distance modulus are from Richer et al. (2002). Additional systematic errors must be added to the formal $1\sigma$ errors noted in parenthesis (as given the authors).

| $\alpha_{2000.0}$ | $\delta_{2000.0}$ | Age [Gyr] | $(m-M)_V$ | [Fe/H] | $E(B-V)$ |
|---|---|---|---|---|---|
| $16^{h}23^{m}35^{s}$ | -26° 31′ 32″ | $\sim$12.7(4) | 12.5(1) | $-1.1(2)$ | 0.37(1) |

## 3.3 Photometric Reduction of the Data from the M 4 Campaign*

The basic reduction consisted of generating and subtracting a master bias frame from each night. The flat fields were made from dome flats taken before dusk and sometimes at dawn. Most observers at Chile took several dome flats with different rotations of the camera in order to average out large-scale scattered light effects. We also took several sky flats but decided not to use them. The "philosophy" concerning whether one should use sky flats or dome-flats will not be discussed here (see Andersen et al. (1995)). Finally, we also made a linearity calibration of the CCD camera on the Danish 1.54 m.

In order to compare the performance of different photometry techniques we have worked with two different software packages to reduce the large M 4 data set: Frank Grundahl (University of Aarhus) has used the DAOPHOT/ALLFRAME packages (Stetson 1987, 1994) which rely on a combination of aperture and PSF photometry. I have used the difference imaging software ISIS (Alard & Lupton 1998) which should be better for crowded regions near the core of M 4. I will briefly describe the two techniques we have used and emphasize the problems we have encountered.

Note that we have not yet begun the reduction of the data from Siding Springs Observatory (SSO). The seeing conditions were quite bad on most nights, *i.e.* around $2''\!.5$ – but down to $1''\!.5$ on the best night. Still, the *window function*[7] will be improved when including this data.

### 3.3.1 DAOPHOT Reductions of M 4***

At the time of this writing, the ALLFRAME reduction of the entire M 4 data set has not been completed. Hence, the results presented in this chapter are based on results only from the ISIS reductions, which will be described in the next section. Since some of the results obtained with ISIS also rely on ALLFRAME due to fundamental problems encountered with ISIS (also described below) I will give a short description of how the ALLFRAME reductions are carried out.

With DAOPHOT the approximate positions of all stars in each image are determined and a PSF model is generated from the brightest and least blended stars. By fitting the PSF model with ALLSTAR more accurate positions and magnitudes are determined. The routines MATCH and MASTER determine the transformation of coordinates from a reference image to each individual image.

With ALLFRAME the *reference position* of each star is determined from all observed frames. The position of a star in a given image is then described by a linear transformation with three coefficients in $x$ and $y$. Thus, when fitting the PSF model to determine the magnitudes of the stars in the frame, the positions are found from the transformation coefficients and the position in the reference list. This technique greatly reduces errors introduced by erroneous centering of the PSF model (this is the main difference between ALLSTAR and ALLFRAME). This is especially the case for images where the sampling is comparable to the seeing.

[7] If one only has data from a single site, side-lobes will appear in the amplitude spectrum corresponding to a splitting of 1/24 h = 11.606 c/day (siderial time).

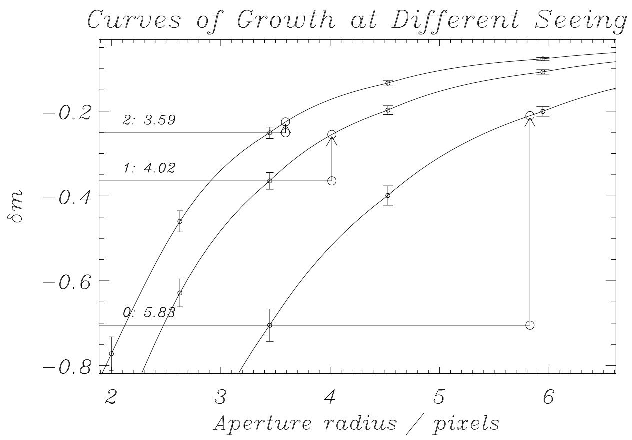


**Figure 3.2** The growth curves found with DAOGROW for three images at different seeing, *i.e.* FWHM of 3.59, 4.02 and 5.83 pixels. The points with error bars are placed at the aperture radii for the three images. The circles mark the points on the growth curves with radii equal to the seeing = FWHM, and the plot illustrates that when using apertures with this radius the aperture correction is the same within the error bars, *i.e.* $0.23 \pm 0.02$ mag.

Furthermore, we used a recent modification of the photometry routine (called "neda"). The idea is to subtract all neighbour stars from the frame except star $i$. The flux in this star is then measured in a range of apertures increasing in size as recommended by Stetson (1990). For each frame the growth curve is determined with DAOGROW and the aperture size with the lowest photometric noise is selected for each star. This will depend on magnitude, filter, seeing, degree of crowding, *etc.* The growth curve gives the aperture correction that must be applied to extend the aperture to infinity.

In Figure 3.2 I show examples of the growth curves for three images with different seeing. The ordinate gives the correction to obtain the flux when extending the aperture to infinity. The circles mark the aperture size corresponding to the FWHM of the PSF of each image. It can be seen that when using an aperture with a radius equal to the FWHM the correction is about the same, *i.e.* $\sim 0.23 \pm 0.02$ mag.

### 3.3.2 Image Subtraction with ISIS*

I have used the ISIS (Alard & Lupton 1998) package which is one of several available photometric packages which applies difference imaging. In difference imaging one constructs a reference image of high quality in terms of good seeing and high signal–to–noise. For each science frame a spatially variant kernel is determined which translates the reference image to the science frame. After convolution of the reference image by the kernel this image is subtracted from the science frame. What will remain in the *subtracted* image will be anything that has changed intrinsically from the reference image to each individual image, while the *overall* change in flux level due to different transparency (or exposure time) and the *distribution* of flux due to changes in seeing have been taken into account by the kernel. This is the fundamental difference from PSF profile photometry, and in principle the extraction of information (*i.e.* variability) in crowded regions should be more accurate (used successfully by the OGLE experiment, *e.g.* Udalski et al. (2002a)). Residuals in the subtracted images will result from bad columns, saturated stars, and of course variable stars.

### A *Tour de Force*: Problems with ISIS**

Unforturnately, I have had many problems with the ISIS software, which I will shortly describe here. Specific examples of how this affects the search for oscillations in the giant stars will be discussed in section 3.8. Also, in section 3.7 I compare the ISIS reduction of data from two different telescopes.

The M 4 images from La Silla have several bad columns. We used two amplifiers to read out the CCD and two bad columns appear in the middle of the CCD as result of this. Before processing the images I replaced the values on the bad columns by interpolation of the values on either side perpendicular to the bad columns. This was done in order to minimize any effect the bad data might have on the determination of the kernel by ISIS (see below).

To construct the reference image in ISIS one should choose several images with the best seeing and the best signal-to-noise ratio in each filter (Alard & Lupton 1998). I have done this for every "observing period" of the campaign. I found that if I used the same reference image to subtract images taken more than one or two weeks later the residuals were systematically larger.

ISIS consists of several routines which can be run independently. To make the reference image ISIS does the following: (1) interpolation of images to the same position as a selected image with good seeing, and subsequently (2) addition of the interpolated images to make the reference image. Despite having tweaked every parameter in the ISIS configuration files I have not been able to make a clean reference image. Large asymmetric residuals are seen for the brightest stars. To make the reference image I simply added the interpolated images made in step (1) by calculating the median of each pixel to remove cosmic ray events.

For the subtraction ISIS (1) interpolates the images to the same position as the reference image, (2) determines the kernel to convert the reference image to the same seeing as the science frame, and finally (3) subtracts the convolved reference image. ISIS then (4) detects significant residuals from variable objects, and (5) determines a PSF model and computes fluxes in the subtracted image relative to the reference image.

The subtraction routine seems to work quite well (points 1–3 above). When comparing the subtracted images from CTIO and DFOSC there appears to be larger systematic residuals in the latter. I will discuss this in great detail in section 3.7. I have not been able to make the photometry package in ISIS work (*cf.* section 4.4.2). Instead I have used DAOPHOT to extract the residual flux in the subtracted images using aperture photometry. I then use growth curves measured for each image (*cf.* section 3.3.1) to extend the aperture to infinity. To determine which aperture to use for a given star I calculate the average noise level for stars with similar magnitudes and consequently select the aperture with the lowest noise level. The flux measured in the extracted image is then added to the flux in the reference image. Finally, the offsets between the different reference images are subtracted from the light curves.

This way of extracting the photometry from ISIS is certainly not optimal. Still, I have reached a noise level only 20-30% above the photon noise limit. I note that I have tried to contact the author of the ISIS software but I have not received any response. Ultimately, we must develop our own image-subtraction software or try to probe the ISIS code itself.

The problems described here were also encountered during the ISIS reductions of NGC 6791, which are described in section 4.4.2.

#### A Short Note on Computing Times for the Data Reduction**

On a Pentium 2 GHz machine each image of 2k by 2k pixels can be processed in roughly 25 minutes including all DAOPHOT reduction steps described above. To process the $\sim$4 500 images from DFOSC and CTIO will take about 10 weeks on a single machine. The numbers are the same for the ISIS reductions. We have used a local cluster with eight 2 Ghz processors to reduce the data.

#### Scaling of the Light Curves**

The amplitude measured for a variable star will be different when measured in different colour-bands. As demonstrated by Kjeldsen & Bedding (1995) the amplitude scales with the inverse of the central wavelength. I have thus scaled the relative light curves from ISIS and normalized them to the central wavelength of the $V$ filter.

## 3.4 Decorrelation of Light Curves*

The light curves extracted with both ISIS and ALLFRAME contain systematic errors. For example, changes in airmass, seeing, rotator angle of the camera, sky level *etc.* will to some extent influence the measured flux. In the *top* and *middle* plots of Figure 3.3 I have plotted the relative $V$ magnitudes measured by ISIS over five nights for a single star *vs.* the mentioned parameters.

I have written the software package DECOR which detects statistically significant correlations with any extrinsic parameter associated with the frames, but which should be independent of the intrinsic change in flux of the star itself.

In the *top* and *middle* plots of Figure 3.3 there is a clear dependence of the measured magnitudes on seeing and a weaker dependence on the sky level. If the DECOR program detects any significant slope ($> 3\sigma$) for any of the linear fits, it will subtract the most significant slope first. The resulting data are then examined again for any remaining correlation which is also subtracted, and this is repeated until there is no correlation with any of the extrinsic parameters.

The *bottom* plots in Figure 3.3 show the correlation before and after decorrelation. On each plot the noise level is given ($\sigma_{\rm ISD}$, Eq. 2.1). Although the improvement in noise level is only 14% another important effect has been taken out: on

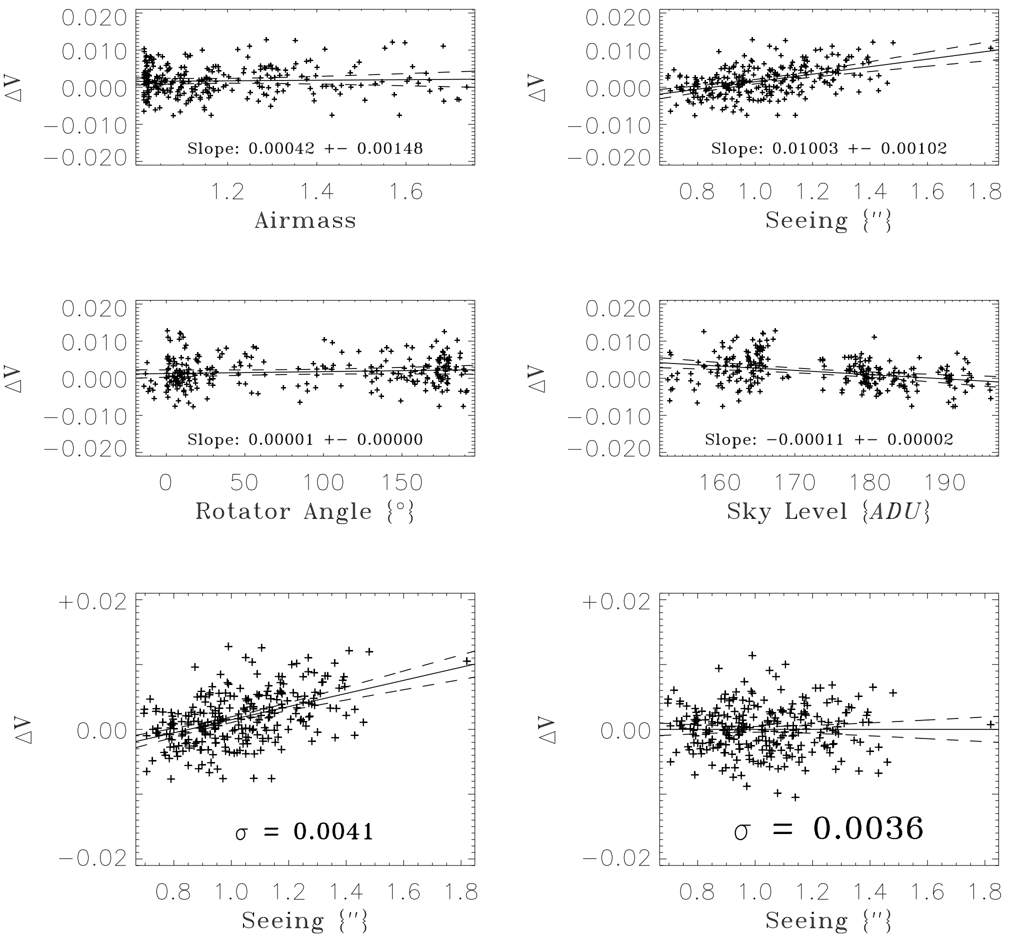


**Figure 3.3** The *top* and *middle* plots show the relative magnitude of a single star *vs.* airmass, seeing, rotator angle of the CCD camera, and the measured sky level. The solid line is a linear fit to the data points. In the two *bottom* plots the correlation with seeing is shown before and after decorrelation, *i.e.* subtraction of the linear fit.

photometric nights seeing correlates with time. For the M 4 observations the airmass (which correlates with the seeing) is high at the beginning and end of each night while the cluster was right above La Silla around midnight, *i.e.* airmass = 1.0. Hence, there will be a systematic error entering the light curves with a period of about $(8/24) = 1/3$ days since the duration of the night is about 8 hours. This periodic signal will show up in the amplitude spectrum with several harmonics at frequencies of $n$ c/day, where $n$ is an integer. We have made simulations of this and find that such correlation with airmass will result in broad peaks at 1, 2, 3, and 4 c/day. Unfortunately, the frequencies we are trying to find in the giant stars also lie around 2–4 c/day (20–45 $\mu$Hz). Hence, it is important to remove the extrinsic variation due to airmass, seeing *etc.*

Another source of systematic error is differential extinction (*i.e.* colour-extinction). With ISIS the overall frame–to–frame offset is determined from the stars

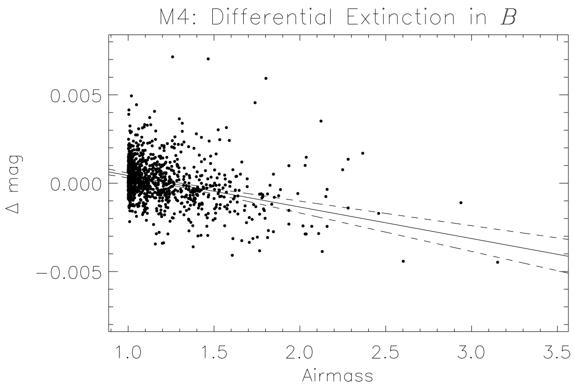


**Figure 3.4** The relative ISIS $B$ magnitudes from five nights of data plotted *vs.* airmass for a blue horizontal branch star in M 4. Colour-extinction at a level of a few mmag is seen. The solid line is a robust linear fit to the data.

providing most of the light. In the case of the M 4 data this will be the red stars on the giant branch and possibly the brightest stars near the turn-off. Since blue stars suffer more from atmospheric extinction than red stars the blue stars will leave negative residuals in a subtracted frame taken at relatively high airmass. This effect is observed for the blue horizontal branch stars. An example is given in Figure 3.4.

## 3.5 Weighting Data Points*

The quality of the data obtained for M 4 on 39 nights over a period of 2.5 months not only varies from night to night (*e.g.* depending on the atmospheric conditions) but in principle from frame to frame. The expected periodic signal from the bump stars will have an amplitude of around 0.5 mmag and periods of about 10 hours. On the other hand the typical point-to-point scatter is 2–3 mmag. Hence, it is very important to remove genuine outliers and give low weight to data of low quality when calculating the amplitude spectra (*cf.* section 3.8.1).

In the following subsections I will describe the technical details of how I have computed the point weights. The contents are briefly summarized here:

- In section 3.5.1 I give an example of a very simple weighting scheme which is *not optimal*, but which will serve as an illustrative example.
- In section 3.5.2 I describe how I have assigned more realistic weights to each data point by using carefully selected comparison stars.
- In section 3.5.3 I outline how genuine outliers (bad data points) are detected in the light curves by comparing the light curve of each star with several comparison stars.

For the "casual reader" I refer to Figure 3.9 which serves to explain the difference between data points that are genuine outliers and data points of low quality (*i.e.* high intrinsic noise level).

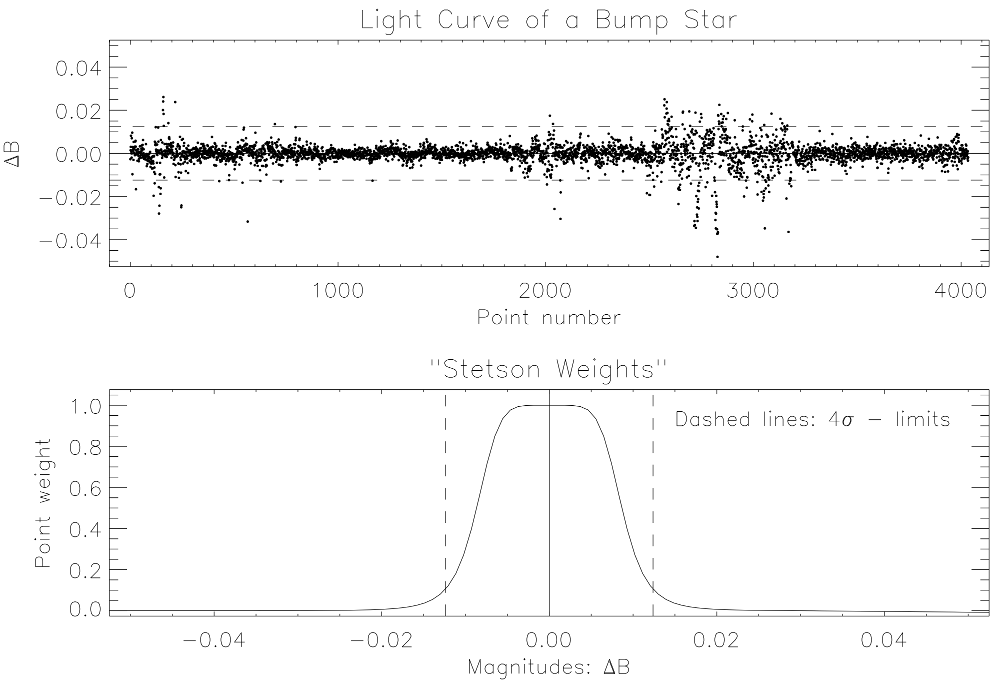


**Figure 3.5** The simple weighting scheme discussed in section 3.5.1 is illustrated here. The *top* plot is the light curve in the $B$ filter of a bump star *vs.* the data point number. The dashed lines correspond to $\pm 4\,\sigma$, where $\sigma$ is the internal standard deviation (ISD, *cf.* Eq. 2.1). In the *bottom* plot the weights from Eq. 3.1 are shown *vs.* relative magnitude. The dashed lines mark the $4\,\sigma$ limits also shown in the *top* plot. Note that data points within $\pm 2\sigma$ get virtually the same *high weight* while data points deviating $3\,\sigma$ or more are given lower weight depending on their deviation.

### 3.5.1 A Simple Weighing Scheme**

For illustrative purposes I will start with a simple example of assigning weights.

In the top plot in Figure 3.5 I have plotted the light curve of a bump star in M 4, *i.e.* I plot the relative magnitude *vs.* the data point number. The dashed lines correspond to four times the noise level, *i.e.* $\pm 4\,\sigma$. While the noise level seems to be constant most of the time, certain intervals have very high noise, *e.g.* around data points 200, 2 000, and 3 000. Even during time intervals of low noise there are evident outliers.

The formula for calculating the weights is inspired by the "fudge factor" in Stetson (1990)[8]:

$$F_k = [\,1 + (\frac{|\Delta m_k|}{a * \sigma})^b\,]^{-1}, \tag{3.1}$$

where $\Delta m_k$ is the relative magnitude for the $k$th data point and $\sigma$ is the noise level measured for the complete light curve[9]. I have used coefficients $a = 6$ and $b = 3$ which results in the solid curve in the *bottom* plot in Figure 3.5. Note that data points within $2\,\sigma$ all have equally high weights which is reasonable since 95.5% of

[8]Following the discussion in point 5 in section 4 of Stetson (1990).

[9]Actually it is a "robust" estimate where $3\,\sigma$ outliers are removed.

all points should be within this limit if the noise were purely Gaussian white noise. Also, 99.7% of the points should be within 3 $\sigma$ and here the assigned weight is about 40% relative to the data points within 2 $\sigma$. Thus, the weighting described here will completely suppress the data in the "outer wings" of the *assumed* Gaussian distribution that describes the white-noise. The width of the "plateau" is determined by the mean noise in the data and the selected $a$ and $b$ coefficients.

This simple way of assigning weights will give low weights to seriously deviating points. Many data points around 3 000 in Figure 3.5 fall outside the 2 $\sigma$ limit and will be given lower weight, but the points inside this limit will also be of *low quality*. The data points that "happen" to fall within the 2 $\sigma$ limit still have *intrinsically* high noise level unlike, *e.g.* the data points around number 1 000–1 500. Hence, the weighting of data points described in this section has not been used.

Ultimately, one must know the quality of each data point. Fortunately, there are many stars in each science frame from which the quality can be estimated. I will discuss this in the next section.

### 3.5.2 Assigning Weights for each Data Point: $W_{\mathrm{ptp}}$**

I have selected about 250 comparison stars among the brightest and least crowded stars (see *cf.* section 3.6). For each light curve I calculate the internal standard deviation ($\sigma_{\mathrm{ISD}}$, Eq. 2.1) in each of the three filters $B$, $V$, and $R$. From this I measure the average ISD for stars in a given magnitude bin with a width of 1 mag, *i.e.* $\sigma_{f;\mathrm{bin}}$, where $f$ is the filter.

For each comparison star $l$ and for each data-point $k$ I measure how much the data point itself and the two neighbouring data points ($k-1$ and $k+1$) deviate from zero in units of $\sigma_{f;\mathrm{bin}}$[10]:

$$\delta_{k,l} = (1/3) * [\,|\Delta m_{k+1}| + |\Delta m_k| + |\Delta m_{k-1}|\,]/\sigma_{f;\mathrm{bin}}. \tag{3.2}$$

I then compute the average deviation of the $N$ comparison stars for each point in time $k$ as $\Delta_k = <\delta_k> = \sum_{l=1}^{N} \delta_{k,l}/N$. The point-to-point weight for the $k$th data point will be the inverse of the average deviation squared, *i.e.* $W_{k;\mathrm{ptp}} = 1/\Delta_k^2$. Thus, the point-to-point weights depend on the actual noise level relative to the expected noise-level for the star, measured as an average of the neighbouring data points.

An example of the calculated point-to-point weights is given in Figure 3.16. Here I have plotted $W_{\mathrm{ptp}}$ *vs.* the relative magnitude in the $V$ filter of a bright star. The two plots correspond to `DFOSC` images with good (*top*) and bad seeing (*bottom*). The pyramid-like shape of the distribution of points seems to be intuitively correct in the sense that a low scatter implies high weights. Figure 3.16 will be further discussed in section 3.7.

[10] The neighbouring data points must be within a certain time limit set arbitrarily to ten times the median time step beween frames (for a given filter). If there is only one neighbouring data point I use only this to compute the deviation $\delta_{k,l}$. If there are no neighbouring data points within the time limit (rarely the case) I assign a weight which is the mean of the weight of data points just before and after this data point.

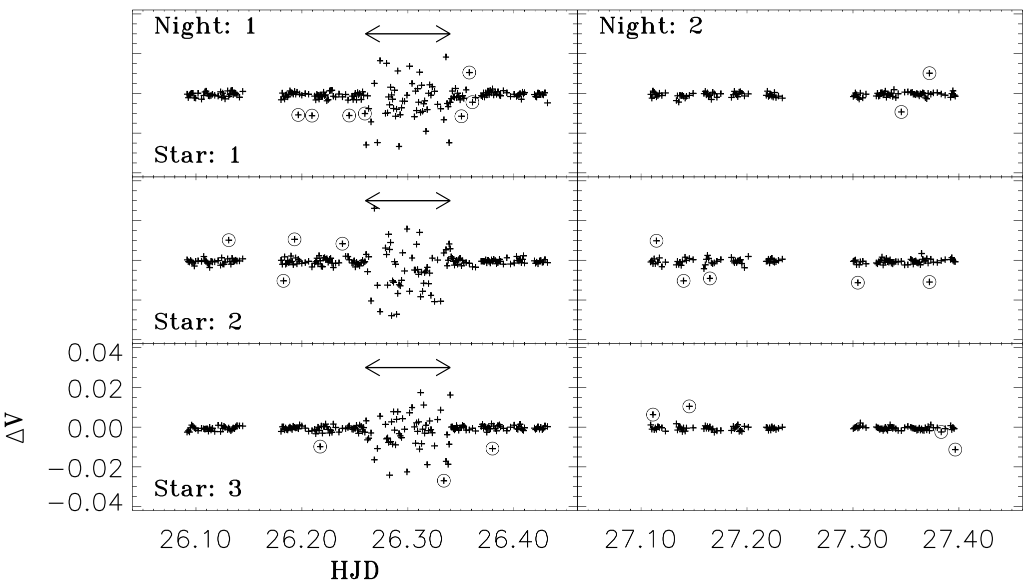


**Figure 3.6** Detecting "true" outliers in the artificial light curves of three stars on two nights. I have inserted a random number of outliers: each point in the light curve has been given a 3.0% chance of being an outlier – in which case the point is offset by ±0.01 mag. The points marked with circles are the detected outliers.

### 3.5.3 Detecting Outlier Data Points in Light Curves**

To illustate the problem of detecting genuine outlier points I show the *artificial* light curves of three stars on two different nights in Figure 3.6. I have inserted a random number of outliers: each point in the light curve has been given a 3.0% chance of being an outlier – in which case the point is offset by ±0.01 mag.

Notice the increase in noise level for all three stars on night 1 around the time 26.3 (the noise is eight times higher than the rest of that night). The points in this interval are not *outliers*, but indeed the data are of *lower quality*. This is taken into account by assigning weights to each data point based on the estimated noise level in each frame from a large group of comparison stars as described in section 3.5.2.

#### The Use of Comparison Stars to Detect Genuine Outliers

To detect outliers I compare the light curves of each individual star (from this point called the "target" star) and 250 comparison stars selected as in section 3.5.2. In Figure 3.7 I plot the light curve of a comparison star *vs.* the target star: the *left* plot is for $B$ measurements and the *right* plot is for $R$ measurements. I have computed the ISD for each star, *i.e.* $\sigma_{\rm targ}$ and $\sigma_{\rm comp}$ (*cf.* Eq. 2.1). The ellipses have major and semi-major axes corresponding to $n\,\sigma_{\rm targ}$ and $n\,\sigma_{\rm comp}$ where $n = 2$ for the dashed ellipse and $n = 3$ for the ellipse drawn with a solid line. The ellipses are shown to aid the eye, *e.g.* the $B$ measurements for the comparison star are more precise than for the target star. Intuitively, there are too many points outside the $3\,\sigma$ ellipse for both plots in Figure 3.7. If the noise were Gaussian white noise the fraction of

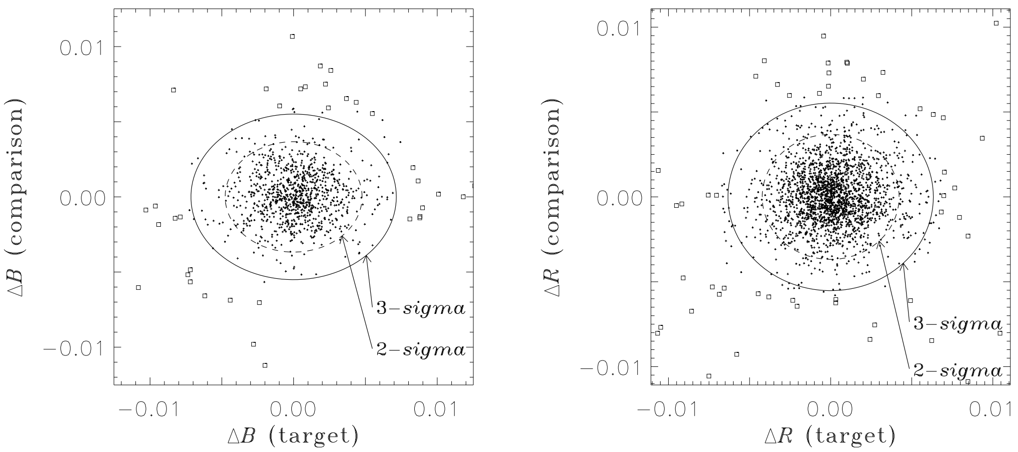


**Figure 3.7** The two plots show the light curve of a comparison star plotted *vs.* the light curve of the target star in the $B$ and $R$ filter. The standard deviation $\sigma$ for each light curve corresponds to two and three times the major and semi-major axis in the ellipses, *i.e.* the dashed ellipse corresponds to $2\,\sigma$ while to solid line corresponds to $3\,\sigma$. Note that the noise level is higher for the target star in the $B$ filter, hence the "flatness" of the ellipse in the *left* plot. The points that fall outside the $3\,\sigma$ limit are assigned lower weight by using Eq. 3.3. The points are marked by a box symbol if the weight, $W_{\rm out} < 0.3$.

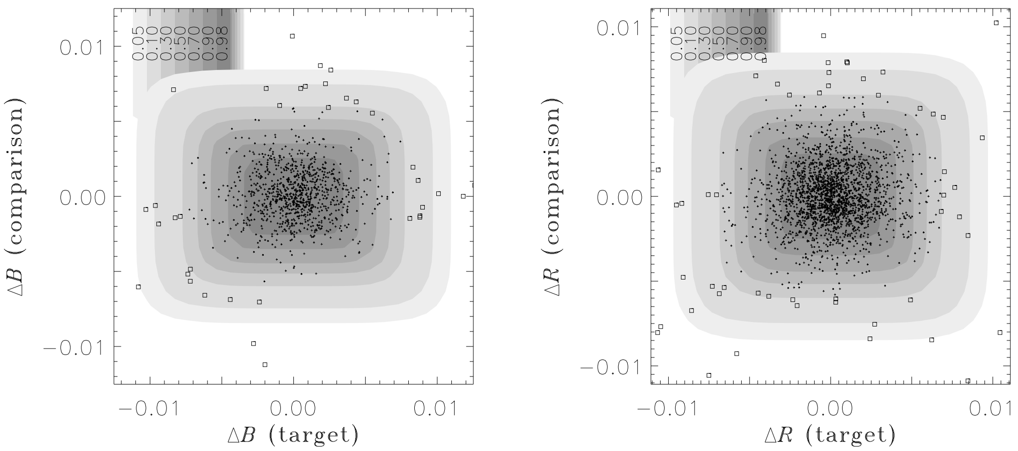


**Figure 3.8** The same plots as in Figure 3.7 but now the outlier weights ($W_{\rm out}$) are indiated by colour contours. The scale is given in the top left corner. Notice that the weights shown here assume that all data points have the same noise level (see text for details).

points that would fall outside the $3\,\sigma$ limit would be merely $P_{>3\sigma}(2\mathrm{D}) = 7 \cdot 10^{-6}$. The points marked by box symbols in Figure 3.7 are the outliers I have found by the method described in the following.

### Determination of the Outlier Weights: $W_{\mathrm{out}}$

The weight factor expressed in Eq. 3.1 give high and equal weight to points within $2\,\sigma$ and lower weights to deviating points. I extend this equation to two dimensions now giving low weight to points which have a large deviation in *either* the target star or the comparison star – measured relative to the *expected* standard deviation for a given data point: $\sigma_k$. This is expressed in the equation for the weight of the $k$th data point for the $l$th comparison star for a given target star in a given filter:

$$W_{k,l} = (\,1. + [\,|\Delta m_k(\mathrm{targ})|/(a * \sigma_k(\mathrm{targ}))\,]^b + [\,|\Delta m_{k,l}(\mathrm{comp})|/(a * \sigma_{k,l}(\mathrm{comp}))\,]^b\,)^{-1}, \tag{3.3}$$

where $\Delta m_k(\mathrm{targ})$ is the relative magnitude for the target star and $\sigma_k(\mathrm{targ})$ is the *estimated* noise level – both values are for the $k$th data point. Likewise $\Delta m_{k,l}(\mathrm{comp})$ and $\sigma_{k,l}(\mathrm{comp})$ are the corresponding values for the $l$th comparison star. I do not have a direct estimate of the noise level of each measurement of each star. To estimate the expected noise level of the $k$th data point for star $l$, I use the weights $W_{k;\mathrm{ptp}}$ calculated in section 3.5.2 which is a measure of the expected noise level in science frame $k$. I then approximate $\sigma_k = \sigma * \eta_k$, where $\sigma$ is the ISD (Eq. 2.1) of the complete light curve (for a given star and filter) and $\eta_k^2 =< W_{\mathrm{ptp}} > / W_{k;\mathrm{ptp}}$. Thus, $\eta$ measures the *relative* change in noise level from frame to frame. The final "outlier" weights $W_{\mathrm{out}}$ for the target star at each data point is the median value of $W_{k,l}$ at each data point $k$ when using all $l$ comparison stars.

### The Final Point Weight: Illustrative Examples

In Figure 3.8 I plot the same points as in Figure 3.7 but I have over-plotted the contours which give the weights corresponding to Eq. 3.3. For illustrative purposes I have used a fixed value of $\sigma_k =< \sigma_k >$, *i.e.* the ISD for the complete light curve of the target and comparison star ($\eta = 1$). Some of the data points that appear to be outliers are probably not. For example, a data point corresponding to a frame with much shorter exposure time will have a higher noise level due to the fewer photons, but relative to photon noise the point will not be an outlier.

Returning to Figure 3.7 the points with assigned weights $W_{k,l} < 0.3$ are marked with box symbols, *i.e.* these points all fall outside the $3\,\sigma$ ellipse (solid line). For the artificial light curves in Figure 3.6 the outlier points are marked by circles, *i.e.* if the weight $W_{\mathrm{out}}$ is lower than 0.3.

In Figure 3.9 I have plotted the light curves of three *observed* bump stars in M 4 on three nights. The size of the symbols is linearly scaled with $1/W_{\mathrm{out}}$ and outliers are marked by circles. In the *bottom* plot the symbols are scaled with the point-to-point weights $1/W_{\mathrm{ptp}}$ which emphasize the data quality. For example the "noisy" data in the beginning of night 2 get the lowest weight.

Note that the *final weight* attributed to each point is the product $W_{\mathrm{out}} * W_{\mathrm{ptp}}$. Thus genuine outliers are suppressed and low quality data are given lower weight.

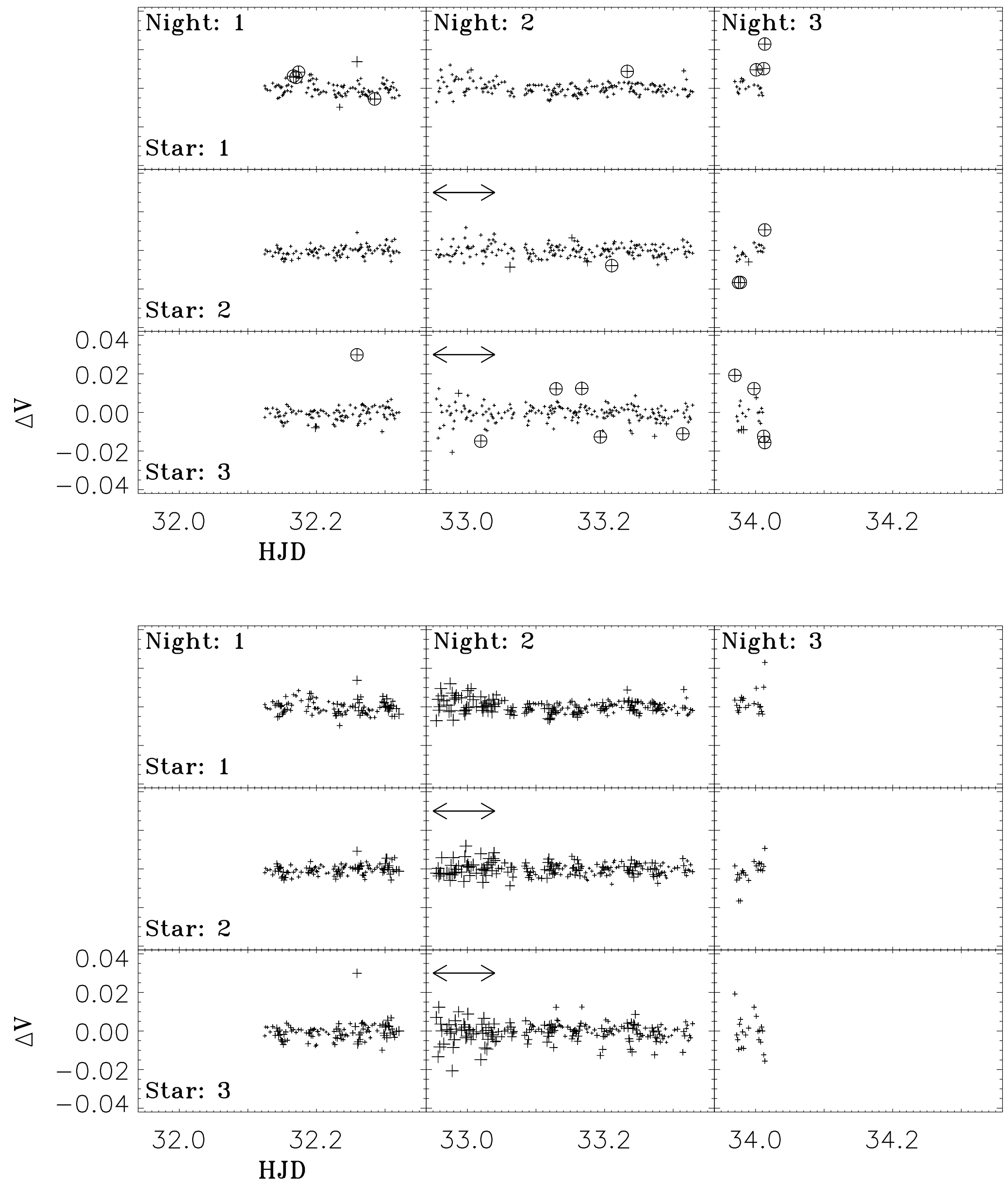


**Figure 3.9** The *observed* light curves for three bump stars in M 4 on three nights. In the *top* panel the symbol size is scaled with the outlier weights as $1/W_{\rm out}$ and points with $W_{\rm out} < 0.3$ are marked with circles. In the *bottom* panel the symbol size is scaled by the point-to-point weights as $1/W_{\rm ptp}$. Note the higher noise level in the beginning of night 2 (marked by the horizontal arrows) where the data points have been given lower weight. The two panels emphasize the difference between data points that are outliers (*top*) and data points of low quality (*bottom*).

## 3.6 Crowding and its Influence on the Photometry***

The term "crowding" is a *qualitative* measure often used by astronomers to describe how much the photometry of a given star is influenced by nearby stars. Clearly the core of a globular cluster has *worse* crowding than the outer parts of the cluster. But how much will it really affect the photometry? To explore quantitatively to what extent a given star is affected by neighbouring stars I have measured the ratio of the "total intensity of star $i$" to the intensity from the neighbouring stars within an aperture of some relevant radius (*e.g.* a few times the FWHM of the stellar profile).

To do this I generated an artificial image around star $i$ in which I placed the neighbouring stars using a Gaussian profile. The positions and magnitudes of the stars were taken from a master list resulting from an ALLFRAME run on 70 $V$ images with good seeing. The width of the Gaussian profiles is related to the seeing in the $V$ filter (FWHM $= 2.35 \cdot \sigma_{\mathrm{Gauss}}$). I then measured the amount of light within an aperture with a radius of four times the FWHM. I then divided the "neigbouring flux" into the total flux from star $i$ to obtain the contamination parameter $R_i = F_i/F_{<4*\mathrm{FWHM}}$.

I have plotted $R$ *vs.* $V$ magnitude in Figure 3.10. As expected it can be seen that the fainter stars generally suffer from a larger contamination of light from neighbouring stars. The box symbols mark the mean $< R_i >$ at different magnitude bins computed in intervals of $\pm 1$ mag. This "average contamination" is marked by the line labelled "C". The lines "A", "B", "D", and "E" correspond to lines at $< R_i > + n\sigma(< R_i >)$, where $n = 6, 3, -3$, and $-6$ and $\sigma(< R_i >)$ is the standard deviation of $R_i$ in each magnitude interval. Thus, stars above the line "A" are the least crowded stars in the images of M 4 while stars below "E" are the most crowded stars.

To illustrate the meaning of the $R$ parameter I have plotted finding charts for four non-crowded stars (*top*) and four crowded stars (*bottom*) in Figure 3.11. The non-crowded stars are found between lines "A" and "B" with $V$ magnitudes around $17 \pm 0.1$ and are marked in Figure 3.10. Similarly, the four crowded stars shown in the *bottom* plots of Figure 3.11 are found between lines "D" and "E" and with $V$ magnitudes around $17 \pm 0.1$ and they are also marked in Figure 3.10.

The measured noise level (ISD) for crowded and non-crowded stars is plotted *vs.* $V$ magnitude in Figure 3.12. The solid grey symbols ($\bullet$) are the crowded stars which lie significantly above the non-crowded stars ($\circ$ symbols). The images were reduced with ISIS but still the photometry of the most crowded stars is clearly affected by the contamination of neighbours.

This may partly be explained by the fact that I have not used the photometric package of ISIS, but instead conventional aperture photometry on the subtracted images (*cf.* section 3.3.2).

## 3.7 Comparison of Data from DFOSC and CTIO***

In Figure 3.13 I show images from a non-crowded region in M 4 as seen with DFOSC and CTIO and in Figure 3.14 I show a crowded region near the core of M 4 where

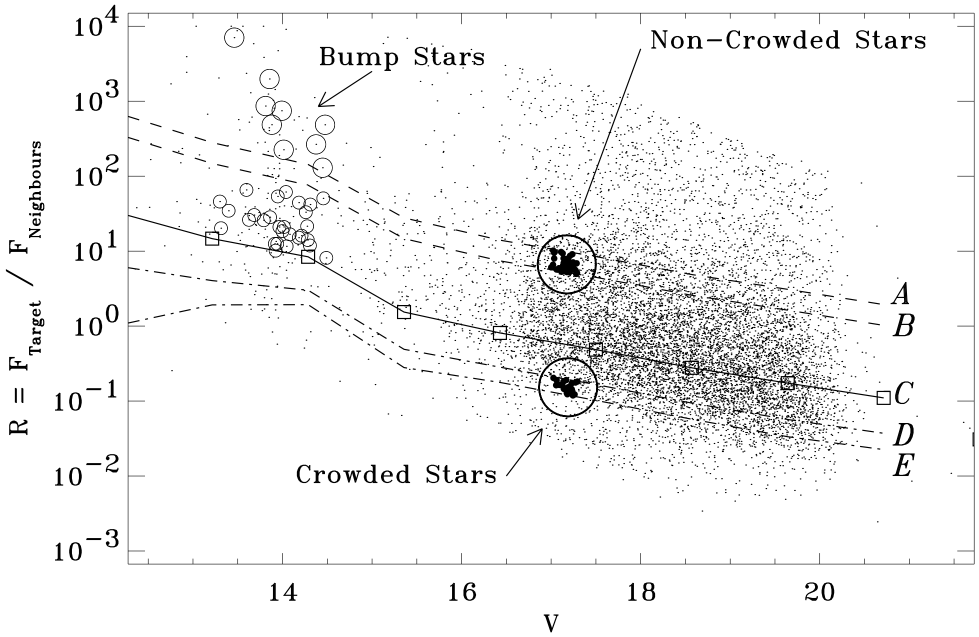


**Figure 3.10** The “contamination” index $R$ *vs.* $V$ magnitude. $R$ measures the intensity of each star relative to the intensity of neigbouring stars within an aperture with a radius of $r = 4 *$ FWHM. Thus stars above the line $A$ are the least crowded stars in the M 4 images. Some of the stars are identified as “crowded stars” and “non-crowded stars” and are plotted in Figure 3.11. The circles around $V = 14$ mark the bump stars in M 4. The large circles are used for the least crowded bump stars.

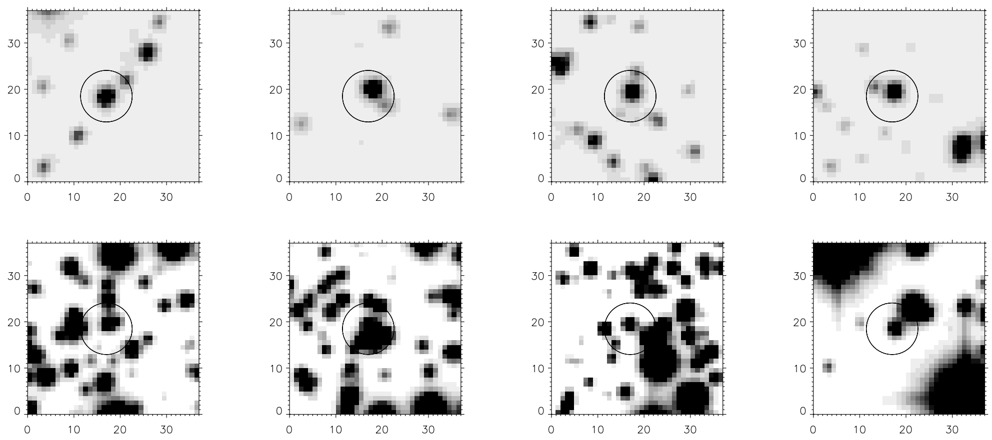

**Figure 3.11** The *top* plots show four non-crowded stars. They were selected from Figure 3.10 where they lie between lines $A$ and $B$ and have magnitudes $|V - 17| < 0.1$. The *bottom* plots are four crowded stars in the same magnitude range but found between lines $D$ and $E$ in Figure 3.10.

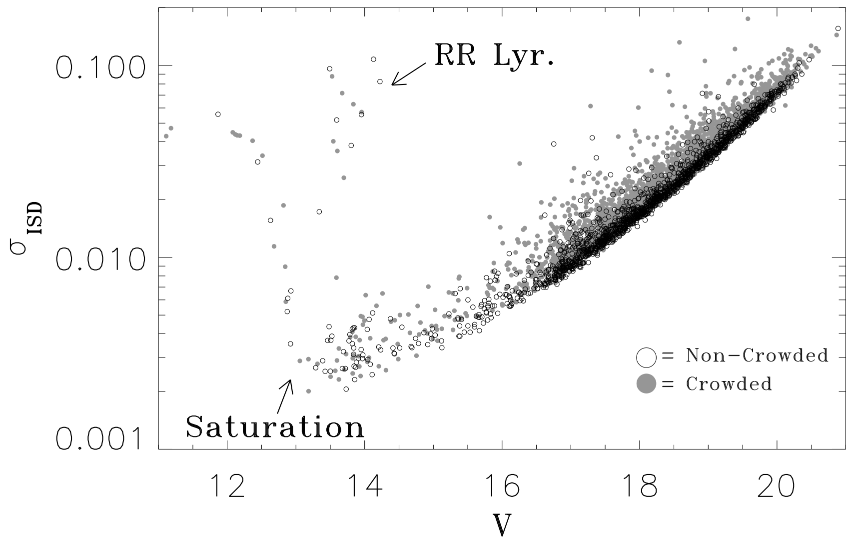


**Figure 3.12** The internal noise level for the ISIS light curves *vs.* $V$ magnitude. Both the crowded (grey • symbols) and non-crowded (∘ symbols) stars are plotted, *i.e.* stars between the $D$ and $E$ lines and $A$ and $B$ lines in Figure 3.10. The location of the RR Lyrae stars and the magnitude at which saturation sets in has been marked.

two RR Lyrae stars leave large residuals. The two regions in Figures 3.13 and 3.14 are shown for for both good (*left*) and bad seeing (*right*). Note that the "pixel scale" to "seeing" ratio is the same for the DFOSC and CTIO images. I have also shown the difference images made with the ISIS software.

It seems that in some cases the subtraction is more "clean" for the CTIO data. This is especially the case near the core of M 4 where the crowding is severe. It is likely that these differences may be due to the large PSF variation across the field in the DFOSC data due to more more complex optics of the focal reducer instrument.

I have made a direct comparison of the noise level obtained with the DFOSC and CTIO. To do this I selected a number of images from each telescope in which the relative sampling was the same for the two instruments, *i.e.* the "pixel scale" to "seeing" ratio was the same within 10%. The image scales are $0''.39$/pix and $0''.44$/pix for DFOSC and CTIO, thus I selected 50 and 47 images with a seeing of $1''.1 \pm 0.1$ and $1''.2 \pm 0.1$ for the two telescopes, respectively. I then measured the noise level in the light curves of several non-crowded stars for both data sets, *i.e.* the stars lie above the "B" line for stars $V < 16$ and above the $A$ line for $V > 16$ in Figure 3.10.

In Figure 3.15 I plot the measured noise level for DFOSC (open circles) and CTIO data (solid grey circles) for the $V$ filter. It is evident that for the bright stars CTIO is superior to DFOSC by almost a factor of two.

To further explore the problems with the subtracted ISIS images for the DFOSC data, I have used the point-to-point weights ($W_{\rm ptp}$, *cf.* section 3.5.2) for the DFOSC data from five nights. In Figure 3.16 I have plotted $W_{\rm ptp}$ for a non-crowded single bright star *vs.* the relative magnitude in the $V$ filter. The *top* and *bottom* panels

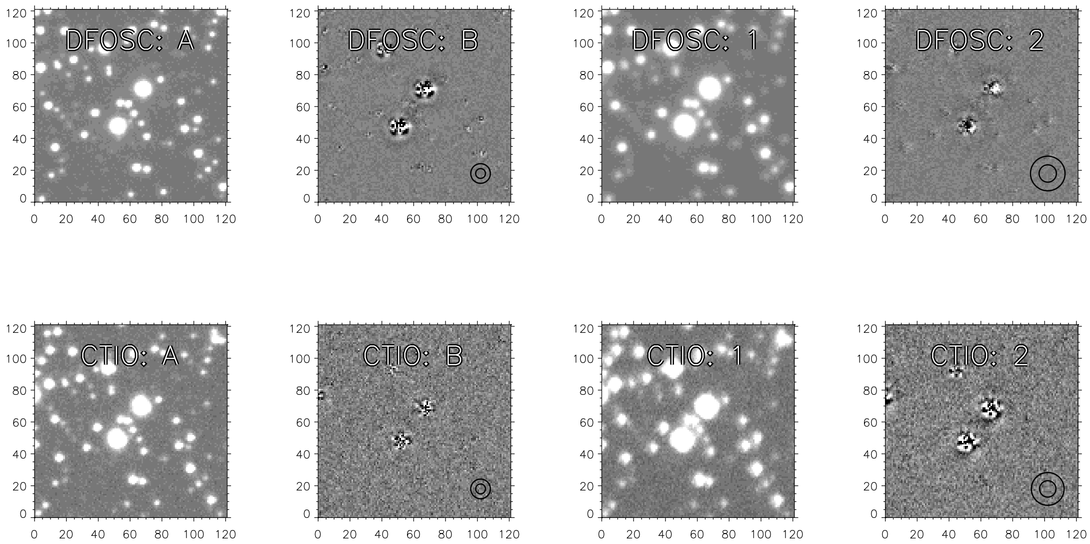


**Figure 3.13** The eight plots show a small region around two RR Lyrae stars in M 4. Both the direct images from DFOSC (*top*) and CTIO (*bottom*) and the subtracted images made with ISIS during different seeing conditions are shown. The images labelled with letters (*left*) are taken during good seeing and the images marked with numbers are taken during bad seeing (*right*). To be able to make a comparison of the quality of the subtracted images from DFOSC and CTIO the images were required to have the same ratio: "CCD pixel scale" / "seeing". Thus, the seeing was $1''.10$ and $1''.53$ for the DFOSC images and $\sim 10\%$ larger for the CTIO images (the ratio of the pixel scales is $\sim 1.1$). The two circles in the lower right corners have radii of one and two times the FWHM of the stellar profiles.

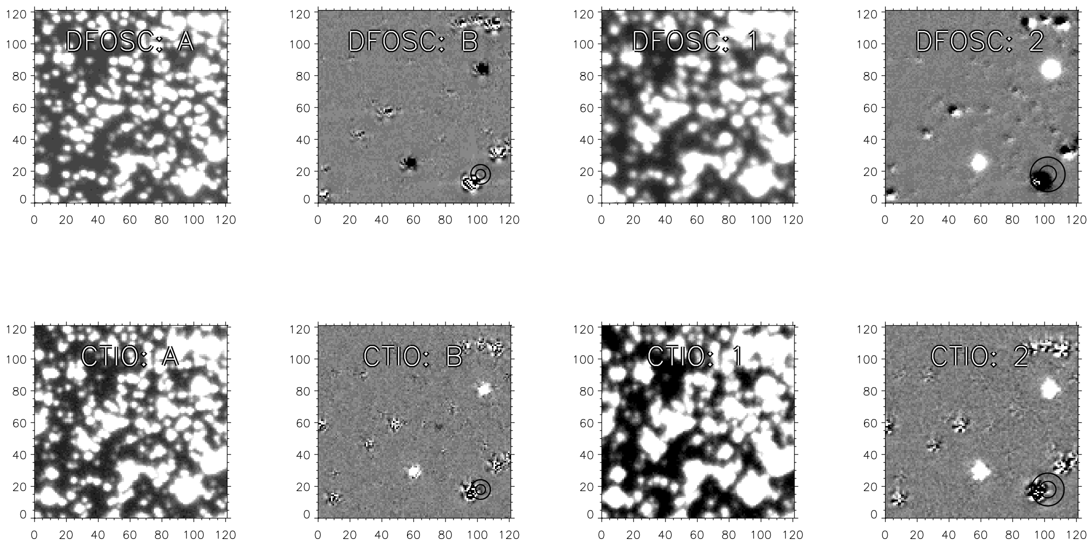


**Figure 3.14** A crowded region in M 4 as seen with the DFOSC (*top*) and CTIO (*bottom*) during good (*left*) and bad seeing (*right*). Both the direct and subtracted images are shown. The CCD science frames are the same as in Figure 3.13 – see the caption of that Figure for details.

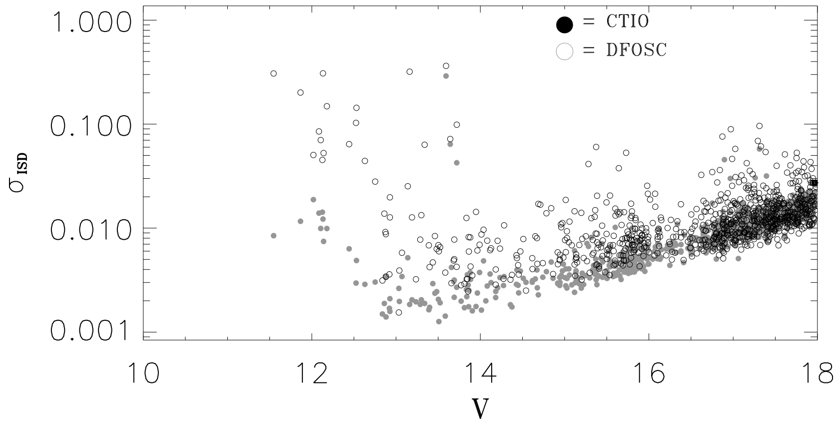


**Figure 3.15** Noise level measured for `DFOSC` (open circles) and `CTIO` data (solid grey circles) for the $V$ filter. The noise level is computed from the ISIS light curves extracted from 50 and 47 images from each telescope. Each set of images was obtained on the same night. The `DFOSC` and `CTIO` frames have been chosen to have similar relative sampling (the image scales are 0″.39/pix and 0″.44/pix), *i.e.* the seeing is about $1''.1 \pm 0.1$ and $1''.2 \pm 0.1$ in the two data sets, respectively. Only non-crowded stars are plotted, *i.e.* above the "B" line for stars $V < 16$ and above the $A$ line for $V > 16$ in Figure 3.10.

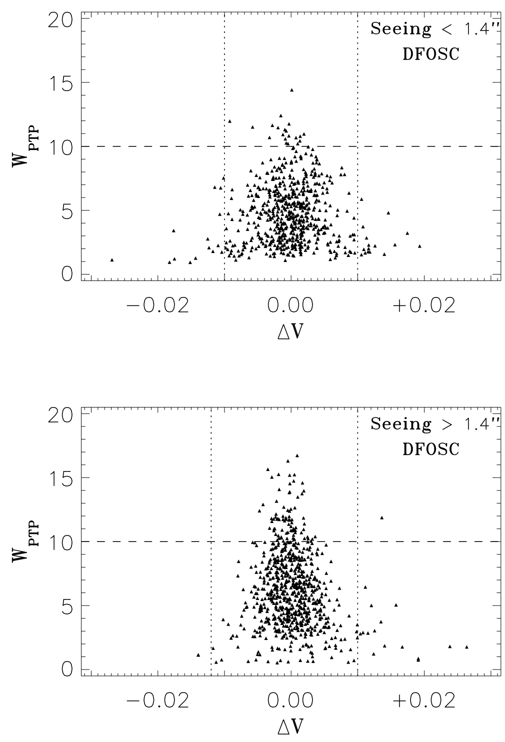


**Figure 3.16** The point-to-point weight is shown *vs.* the relative $V$ magnitude for a bright star observed with the `DFOSC`. The *top* plot are data points obtained during good seeing and the *bottom* plot are data points from frames with bad seeing. Note that good seeing does not imply high weight.

contain data obtained during good seeing and bad seeing, respectively. Notice how the shape of the distribution is intuitively correct: many of the points which are assigned low weight deviate more. But it seems that the images with the best seeing does not imply that the data quality is better. The distribution of points in the *top* plot of Figure 3.16 (good seeing) is broader than the *bottom* plot (bad seeing). This is an indication that the ISIS software fails for images with bad sampling, *i.e.* when the ratio "PSF-width / pixel-size" becomes low.

To examine whether the problems could be due to under-sampling I made a "digital defocusing" of the images. I selected the 80 best $V$ images obtained with the DFOSC and concolved them by a Gaussian function[11] so the resulting images all would have a seeing of about $1''.2$. Surprisingly, the noise level in the light curves extracted from the defocused frames was unchanged for stars in a given magnitude bin. Thus I believe that the reason for the unexpectedly high noise level in the images with good seeing is due to under-sampling of the PSF.

I note that for the reductions of the NGC 6791 data from NOT (*cf.* chapter 4) the subtraction seems less problematic despite the ALFOSC camera also being a focal reducer. The reason is probably that the pixel size is only $0''.188$ for ALFOSC, *i.e.* almost a factor of two better than than DFOSC. To make this comparison it should be noted that the best seeing was $0''.6$ for the NOT data of NGC 6791 and $0''.8$ for the La Silla data of M 4.

## 3.8 Search for Oscillations among Giant Stars in M 4•

In the following I will present the preliminary results from the search for oscillations among the giant stars in M 4. This section contains the following:

- In section 3.8.1 I will present the amplitude spectra of several stars to point out a serious problem with "$1/f$"-noise.
- In section 3.8.2 I discuss the large separation which is a characteristic of solar-like oscillations.
- In section 3.8.3 I discuss the auto-correlation method to search for structure in amplitude spectra.
- In section 3.8.4 I will demonstate how the large separation can be extracted from the amplitude spectrum when using auto-correlation.
- In section 3.8.5 I present the preliminary results of the search for the large separtion in the amplitude spectra of stars on the giant branch in M 4.

[11] I assume the stellar PSF is a Gaussian function. Hence the width of the Gaussian I used for the convolution is $\sigma_{\rm conv} = (\sigma^2_{\rm new} - \sigma^2_{\rm PSF})^{1/2}$, where $\sigma_{\rm new}$ corresponds to the new "digital" seeing of $1''.2$ and $\sigma_{\rm PSF}$ corresponds to the measured seeing in a given frame. Note that $\sigma \simeq$ FWHM/2.35.

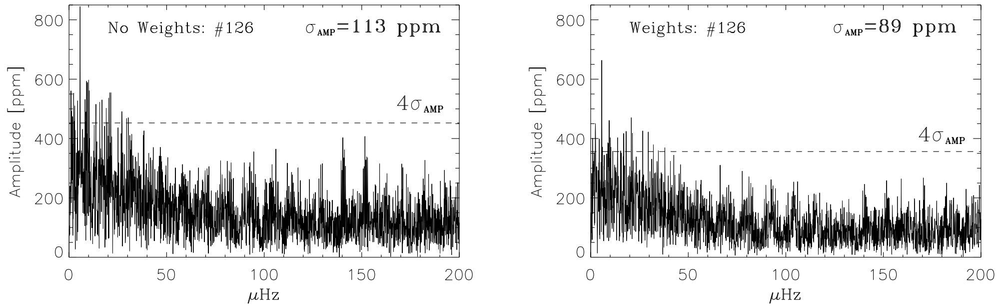


**Figure 3.17** Amplitude spectra of bump star # 126 in M 4. In the *left* plot the data have been decorrelated but the data points have equal weights. In the *right* plot the data points are weighted (*cf.* section 3.5). The noise level is given in the top right corner and the dashed line marks the $4\,\sigma$ level.

### 3.8.1 Amplitude Spectra of Selected Stars•

The amplitude spectra of seven bright stars in M 4 will be presented in the following. They are found in very different positions in the CMD which is shown in Figure 3.1 on page 39: three stars in the bump region (# 126 / # 229 / # 244), two stars on the red part of the horizontal branch (HB; # 113 / # 155), and two on the blue part of the HB (# 96 and # 230).

In Figure 3.17 I show two amplitude spectra of bump star # 126 in M 4. The amplitude spectra are computed without (*left*) and with (*right*) individual point weights. The effect of assigning weights is to lower the noise level by $\sim$20%. A crude estimate gives that this would have required $(1.20^2 - 1) * 100 = 44\%$ more data points or roughly 17 nights of observation. The noise level for the weighted amplitude spectrum is 89 ppm when calculated at frequencies in the range 150–200 $\mu$Hz. The noise level of the light curve of bump star # 126 is $\sigma_{\rm ISD} = 0.0030$. Thus, the theoretical noise in the amplitude spectrum is $\sigma_{\rm amp} = (\pi/N)^{1/2} * \sigma_{\rm ISD} = 84$ ppm for $N \simeq 4\,000$ data points and the measured noise is just 6% above the theoretical limit at high frequencies.

As can be seen in Figure 3.17 there is a significant rise in the noise level when going to low frequencies. This is the "$1/f$–noise" which is caused by long-period drifts in the data set. Unfortunately, the oscillations of the giant stars are expected to be found below 60 $\mu$Hz where the noise starts to increase. The drifts are difficult to avoid for data obtained during 39 nights over a period of about 2.5 months with two different telescopes. For example, there may be small offsets in the measured flux in the reference images of different filters. I have used a reference image for every $\sim$five days which will lead to small offsets. I have removed these offsets by using several comparison stars found in each of the reference images. Still, there remains a significant "$1/f$–noise" component in the amplitude spectra.

In Figure 3.18 I show the amplitude spectra of two bump stars (# 229/# 244 in the *top* plots), two red horizontal branch stars (# 113 and # 155 in the *middle* plots), and two blue horizontal branch stars (# 96 and # 230 in the *bottom* plots). Except for the red HB star # 155 the $1/f$–noise is quite dominant at low frequencies. Also, for the blue HB star # 96 the $1/f$–noise appears to become significant around $40\,\mu$Hz while in the amplitude spectra of the other stars the noise starts to increase at $\simeq 60\,\mu$Hz.

As a crude attempt to remove the "drift noise" I simply tried to subtract the median magnitude of each star on every night (in each filter). This is a very efficient "filter" for removing any signal below $35\,\mu$Hz. Unfortunately, this is also in the range of the expected oscillations of the bump stars. Indeed there remains an envelope of excess power around 30–60 $\mu$Hz for both the red HB stars and the bump stars but this might be an artifact of the drift noise – and *not* the expected oscillation signal.

Obviously, further detailed studies are required to minimize the "$1/f$–noise" before I can tell if the apparent excess power is real.

I note that stochastically excited oscillations are possible not only in the bump stars, but also in the red HB stars since they also have deep convection zones. However, the blue HB stars have had larger mass loss than the red HB stars which means that they are hotter, and their outer convection zone will thus be very shallow. Hence, stochastically excited oscillations are not expected in the blue HB stars.

### 3.8.2 Solar-like Oscillations and the Large Separation•

The amplitude spectra in Figures 3.17 and 3.18 do not allow for a direct identification of any significant modes. I have proposed that serious problems with $1/f$-noise are present, since the same trend is seen for stars on the blue part of the horizontal branch and which should be stable. However, *if* the oscillations are "solar-like" the giant stars are expected to show a distinct spacing of the modes which is called the "large separation" (see *e.g.* Kjeldsen & Bedding (1995)).

The large separation is approximately equal to the inverse of the sound travel-time through the star. Theoretical predictions based on asymptotic theory give that the frequencies can be approximated by

$$\nu_{n,l} = \Delta\nu_0 \cdot (n + l/2 + \epsilon), \tag{3.4}$$

where $n$ is the radial order, $l$ is the degree, and $\epsilon$ is a constant term (Tassoul 1980). To first order, the modes with the same $l$ value and increasing radial order will be evenly spaced.

The large separation is proportional to the square root of the mean density of the star, and is given by (Kjeldsen & Bedding 1995)

$$\Delta\nu_0 = 134.9\mu\text{Hz} * (M/M_\odot)^{1/2}\,(R/R_\odot)^{-3/2}. \tag{3.5}$$

Kjeldsen & Bedding (1995) have estimated the frequency at which maximum power is expected based on scaling from the Sun, *i.e.*

$$\nu_{\max} = 3.05\text{mHz} * (M/M_\odot)/[(R/R_\odot)^2 (T_{\text{eff}}/T_{\text{eff};\odot})^{1/2}]. \tag{3.6}$$

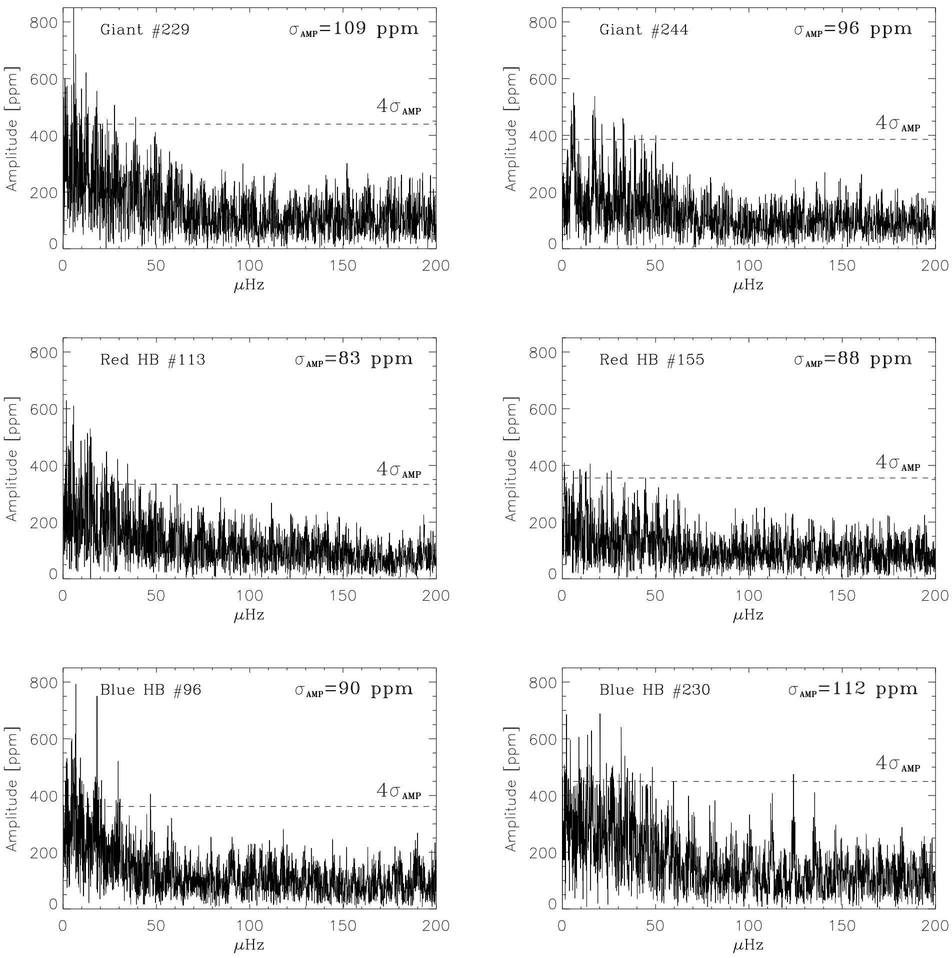


**Figure 3.18** Amplitude spectra of two bump stars in M 4 (# 229 / # 244; *top*), two stars on the red part of the horizontal branch (# 113 / # 155; *middle*), and two stars on the blue part of the horizontal branch (# 96 / # 230; *bottom*). I used weighted data for computing the amplitude spectra. Notice that the noise increases towards low frequencies for all six stars. The noise level is given in the top right corner and the dashed line marks the $4\sigma$ level.

For the stars around the bump region in M 4 I find $\Delta\nu_0 = 1 - 6\,\mu$Hz and $\nu_{\max} = 15 - 50\,\mu$Hz for absolute magnitudes $M_V$ in the range = 0.5 to 1.5 (corresponding to the bump region of M 4 when assuming a distance modulus of $(m - M)_V = 12.5$ (Richer et al. 2002). These estimates for $\Delta\nu_0$ and $\nu_{\max}$ are found from Equations 3.6 and 3.5 when using stellar mass, radius, and temperature from an isochrone (VandenBerg 2000) with an age of 12 Gyr and metallicity [Fe/H] = −1.14.

Below I describe how I have searched for groups of peaks in the observed amplitude spectra that have a characteristic separation. I have only used the frequencies in the amplitude spectrum below 80 $\mu$Hz, since frequencies much higher than this should not be possible due to the limit set by the acoustic cut-off frequency, $\nu_{\rm ac}$. The maximum frequency I have used here is based on the relation between the $\nu_{\rm ac}$ and $\nu_{\max}$ for the Sun. Brown et al. (1991) discuss this and find $\nu_{\rm ac} \simeq 1.8 \cdot \nu_{\max}$, and I assume that it is approximately valid for the giant stars.

### 3.8.3 Auto-correlation: Searching for Structure in Amplitude Spectra•

To search for structure in the amplitude spectra I have used auto-correlation in which the *power spectrum*[12] is shifted by small frequency steps, and the total sum of the product with the original power spectrum is calculated. For each frequency shift of the power spectrum the auto-correlation function is calculated as

$$C(\delta\nu) = \sum_{\nu=\nu_{\min}}^{\nu_{\max}} [P(\nu) * P(\nu+\delta\nu) * W(\nu) * T(\nu)], \tag{3.7}$$

where $\delta\nu$ is the shift, $P$ is the observed power spectrum, $W$ is a "window" function, and $T$ is a "threshold" function. The window function $W$ is applied to suppress signal at very low or high frequencies (*e.g.* above 2–3 times the acoustic cut-off frequency) and the threshold function $T$ will set values below a certain threshold to zero (I used two times the noise level measured at high frequencies).

Before analyzing the observed giant stars in M 4 I will give an illustrative example of the use of the auto-correlation in the next section.

### 3.8.4 Recovering the Large Separation for an Artificial Light Curve••

To illustrate how the auto-correlation technique works, I have constructed an artificial light curve for an "ideal" variable star. I used the same observing times as the M 4 data and inserted five modes with equal spacing in frequency, *i.e.* $f_i = 3.5 + 0.3 * (i - 3)$ c/day, where $i$ in an integer from 1 to 5. The amplitudes were chosen to be equal for each of the five modes (500 ppm), but the phases were random.

Figure 3.19 illustrates how I have "recovered" the large separation of 0.3 c/day present in the light curve. The *top* panel is the amplitude spectrum of the artificial light curve where the five frequencies and the "1/day" aliases are marked. Also, the weight function $W$ is shown with a dashed line, and the horizontal line marks the threshold used for the $T$ function (*cf.* Eq. 3.7). The auto-correlation function is shown in the second panel: the two most significant peaks correspond

[12]The amplitude spectrum squared gives the power spectrum.

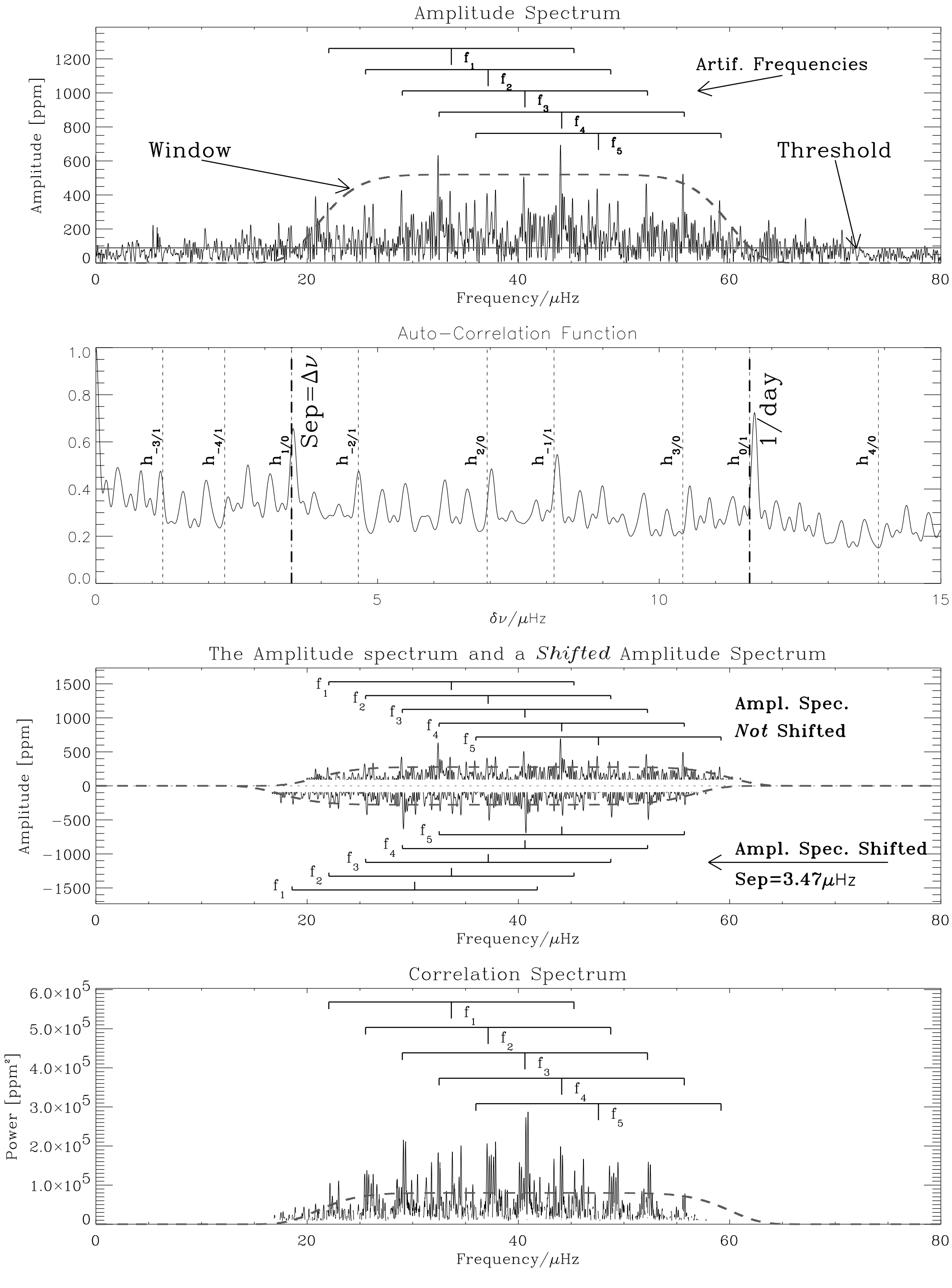


**Figure 3.19** The four panels illustrate how the large separation is found for from an artificial light curve with five evenly spaced modes with equal amplitude. The amplitude spectrum is given in the *top* panel and the second panel is the auto-correlation function in which the peaks corresponding to the large separation, the 1/day alias, and the possible combinations of these two frequencies are marked. In the third panel two copies of the amplitude spectrum are displayed, where the lower one has been shifted by the large separation: notice how several peaks overlap. In the *bottom* panel the sum of the product of the amplitude spectrum and the amplitude spectra shifted by the large separation in both positive and negative (as in the third panel) directions are given. The position of the five artificial oscillations are marked.

to the 1/day alias at $\nu_{1/\mathrm{day}} \simeq 11.606\,\mu\mathrm{Hz}$[13] and the large separation of $\Delta\nu_0 = 0.3\,\mathrm{c/day} = 3.47\,\mu\mathrm{Hz}$. The harmonics of these two frequencies are marked with dotted vertical lines marked by $h_{n,m}$, where $n$ and $m$ are the integers in the equation $\nu_{\mathrm{harm}} = n\,\Delta\nu_0 + m\,\nu_{1/\mathrm{day}}$. The third panel in Figure 3.19 shows two copies of the amplitude spectrum multiplied by the weight functions $W$ and $T$. The first amplitude spectrum is shown with positive values while the second has negative values and the frequecies are *shifted by the large separation*. In the fourth panel I show the correlation spectrum. It is given by the sum of the amplitude spectrum multiplied by the amplitude spectra shifted by the large separation in the positive and negative direction (as in the third panel). Thus, the fourth panel gives the power or correlation when applying the large separation found in the second panel. It is clear that several peaks overlap in the two spectra, which is indiciative of the presence of the large separation.

In this ideal case the identification of the large separation seems to be straight forward. I note that since I knew in advance the frequency range in which to search, I could place the $W$ function in order to maximise the auto-correlation function. Still, I find that the exact location and width of the $W$ function is not too important, as long as most of the power from the frequencies is included.

I have tried similar experiments with a slightly more realistic case. I have used an *observed* light curve and inserted the same artificial signal which was described above. I have used star # 96 which is found on the blue part of the horizontal branch (*cf.* Figure 3.1) and hence is not expected to oscillate. I was also able to identify the large separation for the same artificial modes described above. Thus, I have found that the detection limit for oscillations of the giant stars is around 4–500 ppm in frequency range 10-60 $\mu$Hz. However, this limit is very sensitive to the presence of $1/f$-noise.

### 3.8.5 Searching for the Large Separation in the Giant Stars in M 4•

I have used the auto-correlation technique to search for any "repetitive structure" in the amplitude spectra of the observed giant stars near the bump region. Below I will use the term "large separation" instead of "repetitive stucture", but I stress that my results are very preliminary, and further detailed studies are needed to tell if the "large separations" measured here are really the characteristic spacings expected to be seen in amplitude spectra of solar-like oscillations.

In Figure 3.20 I show the panels similar to Figure 3.19 but for bump star # 200 which is the most convincing case I have found. In the auto-correlation I find a significant peak at 2.00 $\mu$Hz (second panel in Figure 3.20). From the correlation spectrum in the *bottom* panel of Figure 3.20 it can be seen that the power yielding the peak in the auto-correlation function at $\Delta\nu_0 = 2\,\mu\mathrm{Hz}$ comes from the peaks in the amplitude spectrum around $20 \pm 5\,\mu\mathrm{Hz}$ and a contribution from peaks at frequencies below 10 $\mu$Hz, the latter of which is very likely "$1/f$"-noise.

[13] If each night of observation has the same duration and the nights are separated by exactly one siderial day, the "1/day" alias would be at 11.606 $\mu$Hz. But since the weather conditions determine when a given night begins and ends the 1/day peak will not be located exactly at 11.606 $\mu$Hz.

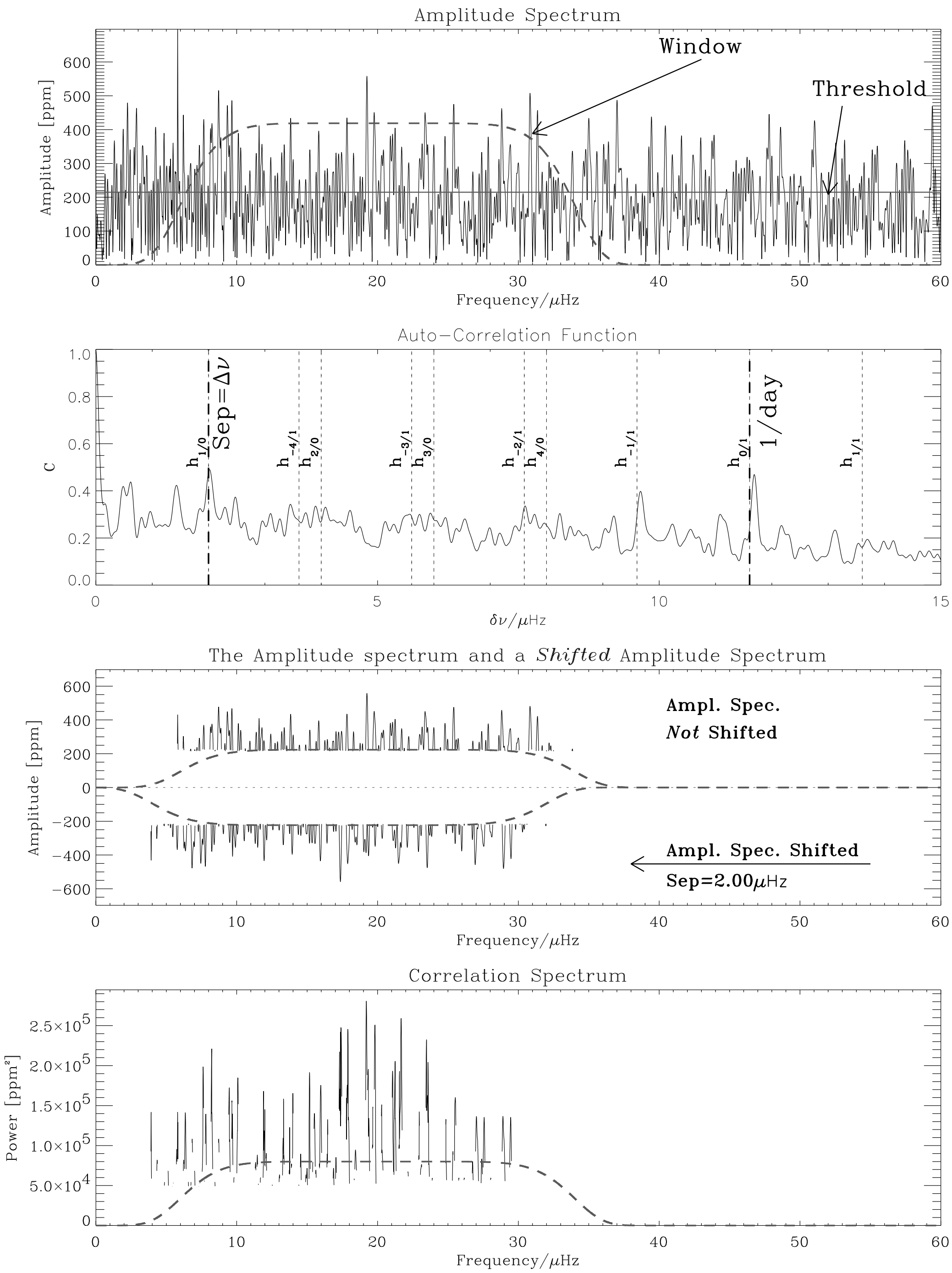


**Figure 3.20** The four panels illustrate how the large separation is determined from the amplitude spectrum of a giant star (#200) in M 4. In the second panel a significant peak at $\Delta\nu_0 = 2.00\,\mu$Hz is found. In the *bottom* panel the peaks that give rise to the detection of the separation have the highest power. See the caption of Figure 3.19 for details.

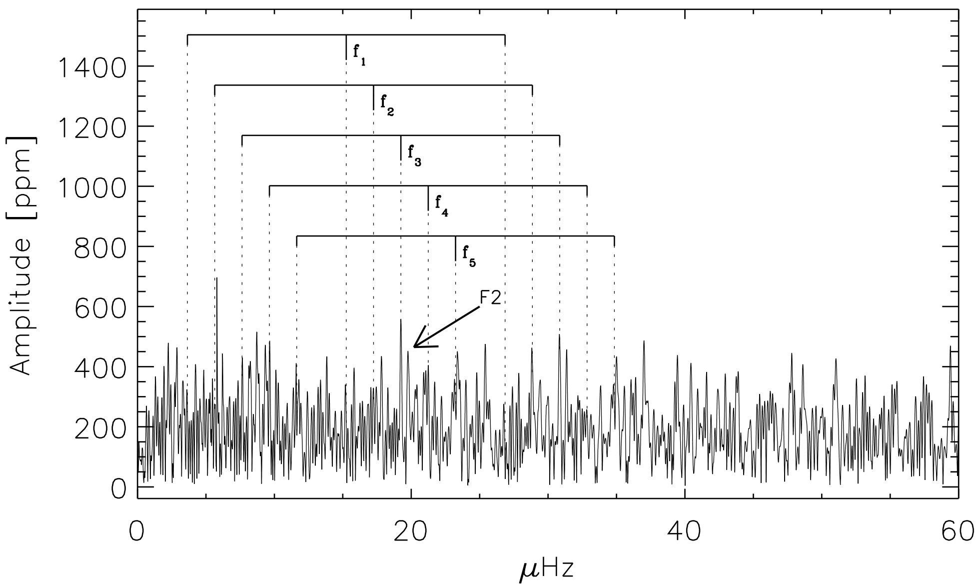


**Figure 3.21** The amplitude spectrum of the giant star #200 that was analysed in Figure 3.20. The highest peak is at 19.24 $\mu$Hz and this is marked by $f_3$ and the corresponding 1/day alias peaks. Four additional frequencies which are shifted by -2, -1, 1, and 2 times the large separation have been marked ($\Delta\nu_0 = 2.00\,\mu$Hz was found from the auto-correlation, *cf.* second panel in Figure 3.20). As discussed in the text, a second family of peaks centered on F2 $= 19.77\,\mu$Hz is present in the amplitude spectrum.

To emphasize the case of bump star #200 I show its amplitude spectrum in Figure 3.21. I have marked the most dominant peak with the label $f_3 = \nu_{\max} = 19.24\,\mu$Hz and the frequencies at $f_i = \nu_{\max} + (i-3) * \Delta\nu_0$, where $i = 1, 2 ... 5$ and the large separation is $\Delta\nu_0 = 2.00\,\mu$Hz. The 1/day aliases are also marked for each frequency $f_i$. It seems plausible that the large separation is present in the amplitude spectrum. I note that there is an additional "family" of peaks present in the amplitude spectrum centered on F2 $= 19.77\,\mu$Hz (also marked in Figure 3.21). This second group of peaks is easily recognized in the *bottom* panel of Figure 3.20 where the peaks around $20{\pm}5\,\mu$Hz are found in *pairs* separated by F2 $- f_3 \simeq 0.5\,\mu$Hz. I emphasize that these are very preliminary results, and I will not attempt to interpret these potentially interesting observations here.

I have made a similar analysis for the 40 least crowded stars on the giant branch. In *most cases* there is no evidence of any significant repetitive structure in the amplitude spectra in the frequency range where I expect to find the large separation, *i.e.* from the scaling relations (Kjeldsen & Bedding 1995) the range should be $\Delta\nu_0 = 1 - 6\,\mu$Hz.

In the *left* panel in Figure 3.22 I plot the large separation found for 13 stars that lie on the giant branch, *i.e.* for *these stars* I have found evidence for structure in the amplitude spectrum. Their positions in the colour-magnitude diagram are given in the *right* panel. The solid line in the *right* panel of Figure 3.22 is an

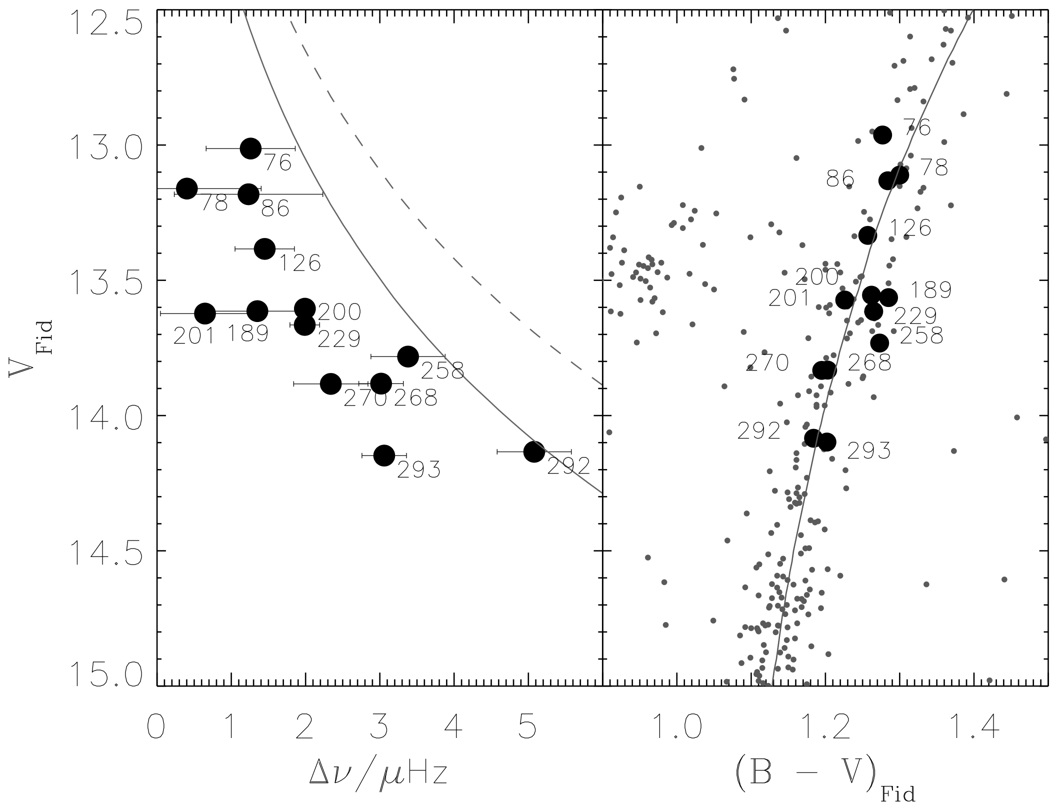


**Figure 3.22** The *left* panel shows the $V$ magnitudes *vs.* the measured large separation for several stars on the giant branch in M 4. The solid line is the theoretical large separation calculated from the scaling relation by Kjeldsen & Bedding (1995), a 12 Gyr isochrone ([Fe/H] = −1.14) from VandenBerg (2000), and a distance modulus of $(m - M)_V = 12.9$. The dashed lines is for a lower distance modulus of $(m - M)_V = 12.5$. The position of the giant stars in the CMD is given in the *right* panel (magnitudes as in Figure 3.1). The solid line is the 12 Gyr isochrone from VandenBerg (2000).

isochrone from VandenBerg (2000). I have used an isochrone with an age of 12 Gyr and a metallicity of [Fe/H] = −1.14. These global parameters are close to the values found in the literature for M 4 (*cf.* Table 3.2). The large scatter of the giant stars in the CMD is due to the significant differential reddening in the cluster, which is of the order $\Delta E(B - V) = 0.03$ or $\Delta A_V \simeq 0.1$ (Ivans et al. 1999).

For each point on the isochrone I calculate the large separation using the relation found in Eq. 3.5. The result is shown as the solid line in the *left* panel in Figure 3.22 for an assumed distance modulus of $(m - M)_V = 12.9$. This estimate is determined from the true distance modulus $(m - M)_0$ found by Ferraro et al. (1999) and using the relation $A_V = 3.2 \cdot E(B - V)$. The dashed line is for a distance modulus of $(m - M)_V = 12.5$ taken from Richer et al. (2002).

It seems that the measured large separations are somewhat lower than predicted by theory, but they follow the trend predicted from the scaling relation, namely that the large separation increases with the magnitude of the giant stars, *i.e.* the densities of the fainter and hence less evolved stars are higher. Again, I stress that the results presented here are preliminary, but the general agreement with the scaling relation is encouraging.

I note that I have also attempted to determine $\Delta\nu_0$ for a few stars on the blue part of the horizontal branch. These hot stars have shallow convection zones and are thus not expected to be variable like the giant stars. It is interesting that I find no evidence of a characteristic spacing in any of the amplitude spectra of the blue HB stars.

### The Need for Improvement of the Photometric Reduction••

In order to confirm the results presented here, the quality of the photometric reduction must be improved. The main task will be to reduce the $1/f$-noise present in the light curves. I will seek advice from scientists familiar with ISIS, since so far I have not been able to use the photometry package that is part of ISIS due to implementation problems (*cf.* section 3.3.2). For the results presented here, I have used DAOPHOT aperture photometry on the subtracted images, which is certainly not optimal. I also note that Frank Grundahl (University of Aarhus) is in the process of reducing the entire M 4 data set with DAOPHOT, and this may perhaps give better results than the photometry presented here.

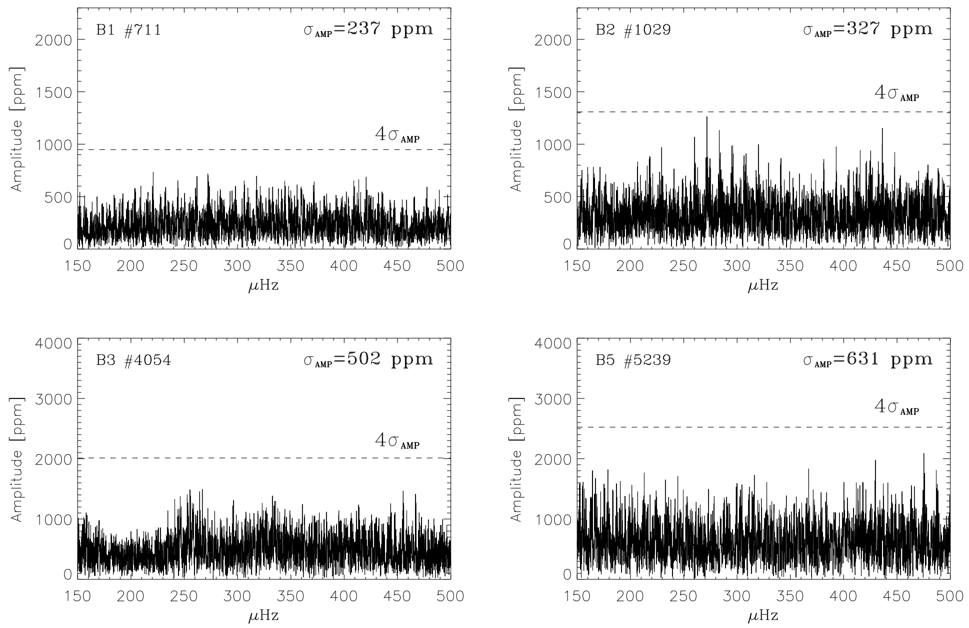


**Figure 3.23** Amplitude spectrum of the four sdB candidates: the *top* plots are B1 and B2 and the *bottom* plots are B3 and B5. No significant peaks can be seen.

## 3.9 sdB Candidates in M 4••

Mochejska et al. (2002a) have made a search for faint variable stars in M 4. From the position in the CMD and spectral classification they found three candidates for pulsating blue sub-dwarf stars (sdB-type variables, see *e.g.* O'Toole et al. (2002)). I have found a new candidate from the position in the CMD (Figure 3.1 on page 39), which I will tentatively label B5. Unfortunately, this star is close to or on a bad column on some of the nights. These data points have been removed in the Fourier analysis below.

The positions of the candidate sdB stars are shown in Figure 3.1. To summarize, B1 and B2 lie at a $V$ magnitude similar to the turn-off while B3 and B5 are 1 magnitude fainter than the turn-off. All four candidate sdB stars have similar colours ($B - V$ within $\pm 0.05$ mag).

For the four sdB candidates I have not detected any significant periodic signal below 500 $\mu$Hz. In Figure 3.23 I show the amplitude spectra of the four candidates. From this I estimate that the lower limit for variability in these stars is about 700–2 000 ppm for the four stars.

**Table 3.3** Summary of the measured noise levels for V46 and the candidate sdB stars. The second and third column give the noise level when using the raw data and when applying point weights.

| ID | $\sigma_{\mathrm{raw}}$ [ppm] | $\sigma_{\mathrm{wei}}$ [ppm] |
|---|---|---|
| V46 | 1134 | 1071 |
| B1 | 400 | 237 |
| B2 | 650 | 327 |
| B3 | 680 | 502 |
| B5 | 1120 | 631 |

A summary of the measured noise levels for the sdB candidate stars is given in Table 3.3. The second column gives $\sigma_{\mathrm{raw}}$ which is the noise level obtained early on in the reduction, *i.e.* before decorrelation (section 3.4) and the assignment of weights to each data point (section 3.5). In the third column I give the final noise level: the reduction in the noise level after decorrelation and weighting is quite impressive, *i.e.* up to a factor of two.

Mochejska et al. (2002a) also discuss the blue variable star V46 which has a single pulsation mode at $\simeq$ 22.946 c/day with an amplitude of $\simeq$ 20 mmag in $B$. From the spectrum and observed period of V46 Mochejska et al. (2002a) suggest that V46 is likely to be a binary system or possibly a field SX Phe star.

The amplitude spectrum of V46 is shown in Figure 3.24. Is it computed from weighted data points from 39 nights of observations and I find a well defined peak at 22.94787 c/day. The amplitude in $V$ is 16 mmag and the signal-to-noise ratio is $\sim$16. I note that when using equal weights for the data points, the amplitude is unchanged within the uncertainties, but the signal-to-noise ratio is $10-15\,\%$ lower. I find no additional low-amplitude signal after pre-whitening[14] of the frequency at $\nu \sim 23$ c/day.

[14] Pre-whitening is the subtraction of the determined frequency (or frequencies) when using a sine-wave to describe the variation.

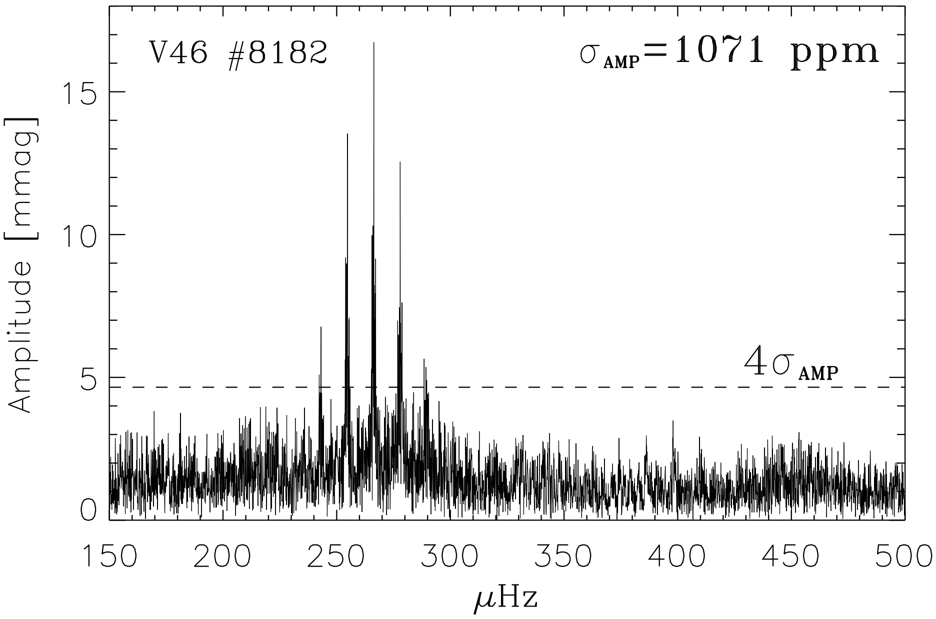


**Figure 3.24** Amplitude spectrum of V46 in M 4 using $\simeq$ 4 000 data points taken over a period of 2.5 months with 39 nights of data. The data has been decorrelated and the data points are weighted as described in sections 3.4 and 3.5. Note that the amplitude is measured in mmag. The dashed line marks the $4\,\sigma$ level and the noise level is given in the top right corner.

From the CMD in Figure 3.1 it is apparent that V46 lies much closer to the main sequence than the sdB candidates. There are several other stars in the CMD with colour and magnitude similar to V46. I examined the amplitude spectra of all of these stars, but I have found no significant variability at frequencies below 35 c/day.

## 3.10 The Known Variable Stars in M 4••

Clement et al. (2001) have searched the literature for variables in globular clusters and list 74 variables for M 4[15]. I have identified 53 of these in the field of M 4 covered by the Danish 1.54 m telescope. Here I present the phased light curves for a few of the already known variables.

The variables presented here have much larger amplitude than the amplitude expected for the bump stars. Thus they will be much less affected by the long-period drifts seen for the bump stars.

In Figure 3.25 I plot the phased light curve of an RR Lyrae star in M 4. The light curve was extracted with DAOPHOT in the three filters $B$, $V$, and $R$ for the DFOSC data.

[15] An updated list is available at `http://www.astro.utoronto.ca/~cclement/read.html`.

In Figure 3.26 I plot phased light curves from ISIS photometry of the eclipsing binaries V68 and V72 (first reported by Rucinski (2000)). I have only plotted the $V$ filter observations but for all 39 nights. The complete light curve of V68 is also shown in Figure 3.27 for the $B$ and $V$ observations. The time of observation is given in the upper right corner, *i.e.* the number is HJD $-$ 2 452 000. The solid line in that plot corresponds to a sine wave with half the period of V68. The reason for the deviation from the sine wave is that the star is a contact binary and the depths of the eclipses are not the same.

While the work presented here has been focused solely on the giant stars in M 4, the study of the RR Lyrae stars, contact binaries, and possible discovery of detached eclipsing binaries will be the subject of future study.

## 3.11 Conclusion

The ultimate goal of the M 4 campaign is to detect the oscillation of the giant stars in the bump region. The results presented here are the preliminary results of the data reduction using the image subtraction software ISIS. Apart from the data reduction with ISIS, I have also made algorithms for decorrelating the data and for weighting the data points. I have demonstrated the importance of assigning weights to the data points because the quality of the data change significantly from night to night. The reduction in the noise level when using weights is 20–40%.

I have used auto-correlation to search for structure in the amplitude spectra of the observed giant stars, and in particular to determine the large separation expected from solar-like oscillations – provided they exist in these stars (this will be assumed from this point). Indeed, I have found evidence for such structure for 13 stars around the bump region. The measured large separations are in rough agreement with theory, *i.e.* I find larger separations for the less evolved stars which have the highest densities. The results presented here are very preliminary, but the agreement with theory is indeed encouraging.

In order to test whether the structure found in the amplitude spectra is real, further studies of simulated light curves and light curves of observed non-variable stars must be carried out.

Further improvements of the photometry will hopefully result in lower noise levels. I have demonstrated that the ISIS reduction is far from optimal for the DFOSC images with the best seeing. The noise levels obtained with CTIO during good seeing is a factor of two lower for the brightest stars compared to the data from DFOSC.

A serious problem with $1/f$-noise is seen in the current light curves, and this must be suppressed – if possible. The expected oscillation frequencies of the giant stars lie in the range 15–50 $\mu$Hz, and this is the range where the $1/f$-noise becomes dominant. To minimize the $1/f$-noise I will have to overcome the problems I have encountered with ISIS, or alternatively use different software for the photometry: F. Grundahl (University of Aarhus) is currently reducing the data with DAOPHOT.

If these improvements can be made, I hope to be able to measure the large separation with a higher precision for a large number of giant stars. First of all, I could then constrain the distance modulus $(m-M)_V$, although it will still depend on the

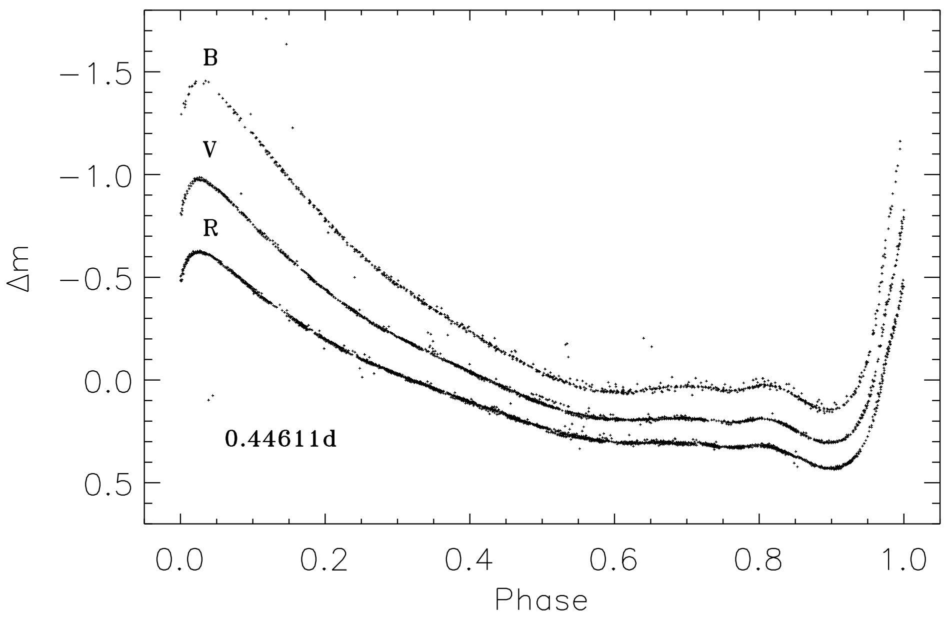


**Figure 3.25** Phased light curves using DAOPHOT reductions of 33 nights of observations with the Danish 1.54 m telescope in $B$, $V$, and $R$ for an RR Lyrae star. The period is given in the lower left corner.

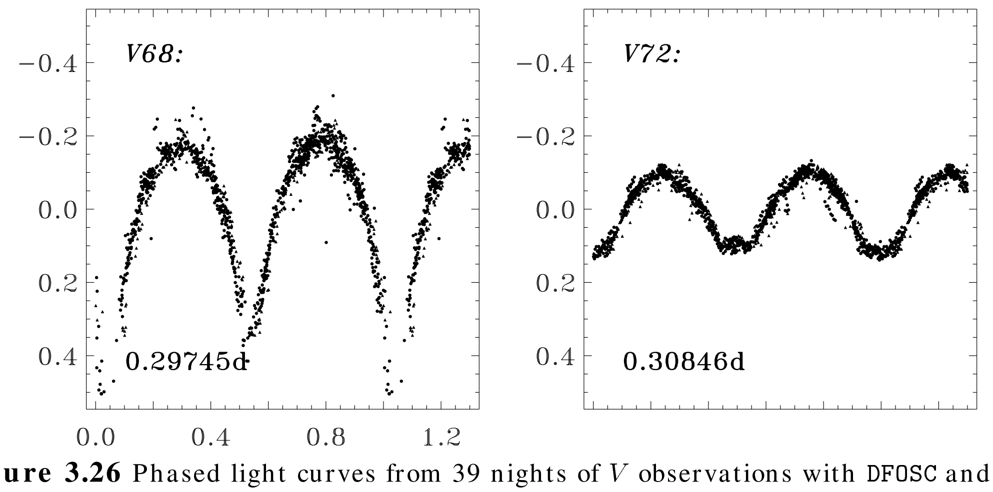


**Figure 3.26** Phased light curves from 39 nights of $V$ observations with DFOSC and CTIO for two eclipsing binary stars. The period is given in the lower left corner.

isochrone models. To improve this would require spectroscopy of the giant stars in order to measure $T_{\text{eff}}$ and individual interstellar reddenings (see *e.g.* Ivans et al. (1999)). Potentially, one could then also examine how the *relative* temperatures, luminosities, and radii change for the giant stars during their evolution across the bump region.

In the near future the reduction of $\sim 12$ nights of observations of M 4 from SSO in Australia will be carried out. Although the quality of this data is bad (mainly due to the bad seeing conditions) it may improve the noise level for the bump stars somewhat. More importantly, it will improve the window function. This will be important for the RR Lyrae stars in which closely spaced modes can perhaps be detected. The stellar mass can then be constrained for the double-mode RR Lyrae stars.

The data set will be used to search for detached eclipsing binaries. If we detect such candidates, follow-up spectroscopy will allow us to constrain the masses of the components of the binary system. If the mass of one of the binary components lies close to the turn-off the age of the cluster could be determined. This in turn will put firm constrains on the theoretical isochrones, which could then be tested in detail by comparison with the properties of the stars (potentially derived from the large separation) in the bump region.

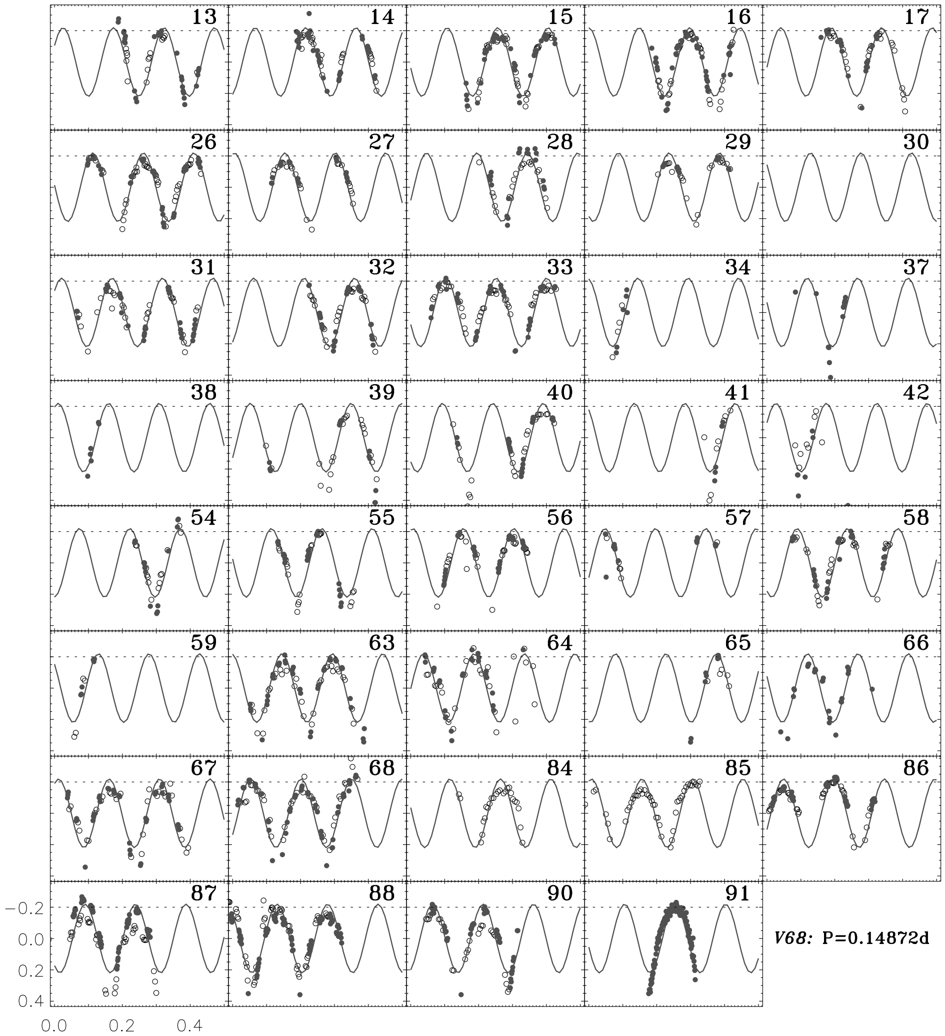


**Figure 3.27** The light curve of the eclipsing binary V68 from 39 nights as seen with DFOSC and CTIO (panels 63–68). I plot only the $B$ (∘ symbols) and $V$ (• symbols) observations. The solid curve is a sine wave with a period equal to half the period of the binary. The dotted horizontal lines mark the estimated maximum brightness for V68.

# Chapter IV

# A Search for Planets in NGC 6791

> "It therefore appears that approximately 10% of stars with [Fe/H] > 0.2 dex are accompanied by short period planets. In other words, the most metal-rich stars have a 10 times increased probability of harbouring a short-period planet" – Laughlin (2000)

Since the detection of the first extra-solar giant planet (Mayor & Queloz 1995) more than 100 have been found through extensive radial velocity searches of near-by stars (Butler et al. (2002), *cf.* section 1.4). In this chapter I will describe a project with the aim of detecting giant planets by the identification of photometric transits caused by a close-in giant planet transiting its parent star. The target stars belong to the old metal-rich open cluster NGC 6791.

## 4.1 The Detection of Transits of Giant Planets

The search for giant planets through radial velocity surveys of nearby stars have been very successful (Butler et al. 2002). From the velocity curves of stars one obtains several parameters of the orbiting giant planets, *i.e.* orbital period, eccentricity, and a *lower* mass estimate – the latter due to the ambiguity of the inclination of the orbit with respect to the line of sight (Marcy & Butler 1998). As has been demonstrated by Charbonneau et al. (2000), the detection of a photometric transit leads to a determination of the radius ratio of the star and planet in addition to the "true" mass of the planet. From the knowledge of the spectral type of the star and by assuming an appropriate mass–radius relation for the star, one can constrain the density of the planet. More detailed searches for moons, rings or evidence for the atmosphere of the transiting planet can in principle be carried out (Charbonneau et al. 2002).

Several projects aim at detecting planets by photometric transits (a list is given by Pepper et al. (2002)). I will briefly mention some of them below.

Howell et al. (1999) discuss the problems of observing transit events from the ground and stress that the radial-velocity searches are limited to planets with masses larger than Saturn with current state-of-the-art spectrographs. Hence, photometric searches are at present the only tool available that can detect transits of planets with the size of the Earth. Observations from the ground will ultimately be limited by problems with long-term stability of the atmosphere. For this reason astronomers need to observe from space if the aim is to detect Earth-sized planets. Examples of such planned missions are COROT (Baglin et al. 2001), EDDINGTON (Favata 2002), KEPLER (Borucki et al. 1997), GAIA (Sozzetti et al. 2001; Høg 2002), and the Danish RØMER/MONS satellite (Christensen-Dalsgaard 2002). Before going to space it would be extremely helpful to learn more about the transits of planets from ground in order to be able to plan the observations from space more efficiently.

An example of a successful planet search which used ground-based photometry was carried out by Udalski et al. (2002a) who used data from the impressive OGLE-III project – the Optical Gravitational Lensing Experiment – which uses small telescopes to monitor stars in dense fields (*e.g.* Wozniak et al. (2002)). Udalski et al. (2002a) selected a sample of 52 000 stars with photometry better than 1.5% observed for 32 nights over a period of 45 days. They used the image subtraction software ISIS by Alard & Lupton (1998) for the photometry which is optimal for extracting differential light curves in crowded fields. Udalski et al. (2002a) reported 47 transits of which 42 were multiple transits. An additional 13 objects were later reported by Udalski et al. (2002b) when using a refined search algorithm. In a subsequent paper Dreizler et al. (2002) presented spectra of 16 of the most promising planet transit candidates from the OGLE-III data. From the spectra Dreizler et al. (2002) could determine the spectral class of the stars and in turn constrain the mass and radius ratios of the orbiting object and the parent star. Dreizler et al. (2002) found that only two of the 16 transiting objects have radii and masses consistent with being giant planets. The other objects are probably brown dwarfs or M-type stars.

Among other projects with the aim of detecting planetary transits from the ground are the STEPPS project (Burke et al. 2002) which will monitor open clusters and the search with the WASP telescope (Street et al. 2003). See also Pepper et al. (2002) in which the best telescope design, observation strategy *etc.* for a ground-based all-sky search is discussed. Finally, the EXPLORE project deserves mention and I will discuss this in the following section.

## 4.2 Recognizing a Planetary Transit: the EXPLORE Project

According to Yee et al. (2002) the typical light curve of the transit of a close-in giant planet will have a duration of 1–4 hours, a depth less than 3–4%, a steep ingress and egress, a flat-bottomed light curve, there will be no secondary transit, and the transit will be grey, *i.e.* it will have the same depth measured in different filters.

Yee et al. (2002) mention four situations that could mimic a shallow planetary transit:

- (1) A grazing eclipse of one normal star by another.
- (2) A normal star eclipsing a much larger primary.
- (3) An eclipsing binary blended with a non-variable star.
- (4) A normal star eclipsed by a much smaller M dwarf or brown dwarf.

Yee et al. (2002) stress that to be able to tell if a detected transit is truly a planetary transit one needs good time sampling. With such data the steepness of the ingress / egress and flatness of the photometric transit can be determined. This will help rule out a grazing eclipse (point 1) which will have a "U"-shaped transit. Point 2 will typically have a longer transit-duration (than the typical close-in giant planet, *i.e.* $\sim$ few hours). Point 3 is difficult to distinguish from a planetary transit from photometry alone but this can be determined from the radial velocity curve which requires spectroscopy with a large telescope. This is also the only option for point 4. The problem is that planets and brown dwarfs with masses $< 100\,M_{\rm Jup}$ will have the same approximate radius (Hubbard et al. 2002).

A very ambitious project with the aim of detecting planetary transits among stars in dense fields is the EXPLORE project (Yee et al. 2002; Mallén-Ornelas et al. 2002). They use 4 m class telescopes to monitor selected fields for two weeks or more. A report on the first two EXPLORE fields was given by Yee et al. (2002) based on 11 (6 clear) and 16 (14 clear) nights with the CTIO 4 m and the CFHT 3.6 m telescopes in a single filter. Yee et al. (2002) found several examples of transit-like light curves which could be ruled out from the $U$-shape of the transits. Yee et al. (2002) also found a few planet transit candidates for which limited spectroscopy with HIRES / KECK and UVES / VLT has already been carried out. Only in one case does the radial velocity curve indicate an object of about 2.5 $M_{\rm Jup}$, but Yee et al. (2002) stress that additional photometric and spectroscopic data is needed to confirm this result.

---

## A Paper in Preparation: "a Search for Planet Transits in NGC 6791"

In the following sections, I will describe the results of the search for planet transits in the open cluster NGC 6791. Most of the material in the following sections will appear in *Astronomy & Astrophysics* (Bruntt et al. 2003b).

From this point I will use the first person singular ("I") to emphasize the work I have done, and the third person singular ("we") for the work that was done in collaboration with others. In particular, the ALLFRAME reductions described in section 4.4.1 were done by P. B. Stetson, the search for planet transits described in section 4.6 was done by B. Tingley, and the periods of the variable stars were determined by B. Tingley and S. Frandsen (section 4.7).

Bruntt, H, Tingley, B., Grundahl, F., Frandsen, S., Stetson, P. B., Thomsen, B.

2003, A&A, *in preparation*

---

## 4.3 A Search for Planetary Transits in the Metal Rich Cluster NGC 6791

Gilliland et al. (2000) conducted a search for planetary transits in the globular cluster 47 Tuc (*cf.* section 2.1) by using 8.3 days of observations with the Hubble Space Telescope. The fact that no transits were found is perhaps due to the lower probability of finding planets in a metal-poor system (*cf.* section 1.4 and Laughlin (2000)). Another possible explanation is that the extreme conditions in a globular cluster may have influence on the evolution of proto-planetary discs, or the long-term stability of planetary systems that may have formed.

Inspired by the null result of Gilliland et al. (2000) for 47 Tuc and the correlation with the metallicity of stars harbouring planets documented by Laughlin (2000), Frank Grundahl, Søren Frandsen, and myself (all from the University of Aarhus) proposed to observe the old and metal rich open cluster NGC 6791 with the Nordic Optical Telescope (`NOT`).

We were granted eight nights with the `NOT` telescope – seven of which produced excellent data. I was observing from July 9–17 2001 and in this chapter I will describe the results of the analysis of this data set (labelled *NOT01* from this point).

The fundamental parameters of NGC 6791 are given in Table 4.1.

### 4.3.1 Observations with the Nordic Optical Telescope in July 2001

I used the `ALFOSC` instrument which gives a field of view of $6\farcm5 \times 6\farcm5$. A 2k × 2k thinned Loral CCD with a pixel size of $0\farcs188$, read-out noise 6.5 $e^-$ (rms), and a gain of 2.5 $e^-$/ADU was used as detector. The time series observations were made using $V$ and $I$ filters to be able to distinguish between grey and coloured transits. To first order, planets will cause the same transit depth regardless of colour, while eclipses due to a binary component or variations due to the star itself (spots) will most likely have different amplitudes in different filters. The typical exposure times used were 180 s and 90 s for $V$ and $I$, chosen such that stars above the turn-off of the cluster at around $V = 16$ would be at the saturation limit. In order to limit the overhead in connection with changing filters I grouped the observations as five exposures in $I$ followed by three in $V$. The read-out time of the detector was 70 s.

A few observations were collected in the $B$ filter as well, to be used for the construction of the colour–magnitude diagram of the cluster.

In order to achieve the highest possible precision of the differential photometry I made small corrective offsets of the telescope during the night to keep the stars in the same position.

Flat fields were obtained with different rotations of the camera (to minimize scattered light effects) during evening and morning twilight on each night. A master flat field was constructed by using all flat field images, since no significant night-to-night variations were seen.

On each night I observed several standard fields from Stetson (2000)[1] in order to provide a good transformation to the standard $BVI$ system. The details of this will appear in Stetson et al. (2003).

[1] Available from `http://cadcwww.hia.nrc.ca/cadcbin/wdb/astrocat/stetson/query/`.

**Table 4.1** Fundamental properties of NGC 6791: right ascension, declination, age, distance modulus, metallicity, and reddening. The values are taken from Chaboyer et al. (1999) except the metallicity which is from Taylor (2001). Note that the quoted errors are probably too optimistic and do not include systematic errors (except the error on the metallicity).

| $\alpha_{2000.0}$ | $\delta_{2000.0}$ | Age [Gyr] | $(m-M)_V$ | [Fe/H] | $E(B-V)$ |
|---|---|---|---|---|---|
| $19^{\mathrm{h}}20^{\mathrm{m}}53^{\mathrm{s}}$ | $+37°46'30''$ | $8 \pm 0.5$ | 13.37(10) | +0.30(15) | 0.10(2) |

### 4.3.2 The Expected Number of Transits for the *NOT01* Campaign

Mallén-Ornelas et al. (2002) have calculated the probability of detecting the transit of a close-in giant planet once or twice from a single-site campaign for observing runs of different lengths. They assumed that the duration of the night was 10.8 hours. They find that the optimal duration of the campaign would be roughly $21 \pm 5$ days (this gives the maximum probability per night). For the *NOT01* campaign I observed for $\simeq 8$ hours on each of seven nights, hence the approximate probability of detecting a single transit is $P_{\mathrm{single}} = 50\%$ and $P_{\mathrm{twice}} = 7\%$ for detecting a transit twice for the same star (see Figure 3b in Mallén-Ornelas et al. (2002)). The probability that a local G or F-type field star harbours a close-in giant planet is around 0.7 % (Butler et al. 2002) while the geometric probability that the planet will cause a transit is 10 %. There are $N_{\sigma<1\%} = 4\,000$ stars in the sample with light curves with a precision better than 1%. Assuming that the binary fraction $P_{\mathrm{bin}}$ of the cluster is 15% the expected number of planets that will be detected is

$$N_{\mathrm{NOT01}} = N_{\sigma<1\%} * P_{\mathrm{GF}} * P_{\mathrm{geom}} * (1 - P_{\mathrm{bin}}) * P_{\mathrm{single}} = 4\,000 * 0.007 * 0.10 * 0.85 * 0.5 \simeq 1.2 \tag{4.1}$$

The metallicity of NGC 6791 is significantly higher than the field stars and I expect to find at least a few candidates with single transits. According to Laughlin (2000) the fraction of stars harbouring planets is $\simeq 10$ times higher for metal rich stars (*cf.* the quotation introducing this chapter).

### 4.3.3 Similar Attempts to Detect Planets in Open Clusters

In this context I mention the preliminary report by Burke et al. (2002), who made a similar search of the open cluster NGC 1245. This cluster has solar metallicity and around 1 500 members. The field was monitored for 19 nights (15 clear) with the 2.4 m MDM telescope and a total of 4 300 stars had light curves to better than 1% precision. Burke et al. (2002) reported a grazing eclipse with a depth of 4% but no planet-like transits. Another interesting campaign which is related to the present work is the KECK radial velocity search of the Hyades cluster (Cochran et al. 2002). Despite five years of monitoring, no planets have been detected.

### 4.3.4 Previous Time-Series Studies of NGC 6791

In this chapter we used data from three photometric campaigns on NGC 6791 which we will describe briefly here. The complete data set was reduced using ALLFRAME while the new *NOT01* data was also reduced using the ISIS image subtraction software (Alard & Lupton 1998). Rucinski et al. (1996) carried out a campaign on NGC 6791 for 14 nights in July 1995 to search for detached eclipsing binaries. Despite good weather conditions the noise level in this data set (labelled *SMR95* from this point on) is higher compared to the *NOT01* data due to the smaller telescope: the apertures are 1 m for *SMR95* and 2.5 m for *NOT01*. The *SMR95* data is still useful for constraining the periods of long-period variables and will be used to search for detached eclipsing binary stars. Rucinski et al. (1996) discovered 11 variable stars (four new ones) and among them were three detached binaries. I refer to Rucinski et al. (1996) for a list of earlier studies on NGC 6791.

A more recent study was made by Mochejska et al. (2002b) who have selected NGC 6791 as their first target to search for a planetary transits. They have used the FLWO 1.2 m telescope at Mt. Hopkins, Arizona, from July 6 to August 1th 2001 (this data set is labelled *MOCH01*), *i.e.* partly overlapping with the *NOT01* observations from La Palma. Unfortunately, the weather conditions were quite poor with a median seeing in $V$ of $2''.1$ (for *NOT01* the median seeing was $1''.0$). Mochejska et al. (2002b) state that the search for transit-like events still remains to be done, and that a new campaign on the cluster is being planned.

In Table 4.2 we give a summary of the observations of NGC 6791 that we have used. For the *MOCH01* data we have only used the light curves of the variable stars from Mochejska et al. (2002b), thus we have not reduced these data ourselves as we have for *NOT01* and *SMR95*. Note that the photometric precision of the *NOT01* campaign is superior to the other telescopes, and only these data (seven nights) were used to search for planetary transits.

In addition to the data listed in Table 4.2 several images taken outside the centre of NGC 6791 from *NOT01* and several images from other telescopes were reduced with ALLFRAME as described by Stetson et al. (2003).

**Table 4.2** Log of observations of NGC 6791 from three campaigns. The columns contain the adopted abbreviation of the campaign, the name of the telescope, the duration of the campaign, the number of useful nights ($n$), the median seeing in the $V$ filter, and the number of images obtained in the $V$, $R$, and $I$ filters. The last column gives information on which reduction technique we have used. Note that we have not reduced the *MOCH01* data set, but we have obtained the light curves of the variable stars published by Mochejska et al. (2002b).

| Campaign | Telescope | Dates UT | $n$ | ["] | Number of images $N_V$ | $N_R$ | $N_I$ | Reduction Method |
|---|---|---|---|---|---|---|---|---|
| *NOT01* | 2.5 m NOT | 9/7–17/7 01 | 7 | $1''.0$ | 264 | - | 444 | ALLFRAME/ISIS |
| *MOCH01* | 1.2m FLWO | 6/7–1/8 01 | 18 | $2''.1$ | 36 | 204 | - | *Not Reduced* |
| *SMR95* | 1.0m JKT | 11/7-24/7 95 | 14 | $1''.6$ | 601 | - | 153 | ALLFRAME |

## 4.4 Photometry of NGC 6791

We have used two different methods for obtaining the differential time series photometry: (1) the profile fitting (PSF) approach viz. DAOPHOT/ ALLSTAR/ ALLFRAME (Stetson 1987, 1994) and (2) the image-subtraction method using the ISIS software (Alard & Lupton 1998). We shall describe our approach for these two methods below.

### 4.4.1 ALLFRAME Reductions

The time series photometry from *SMR95*, the new *NOT01* data set, as well as a few frames from other campaigns were reduced using the DAOPHOT / ALLFRAME photometric software (Stetson 1987, 1994) and will be described in our companion paper (Stetson et al. 2003). The individual light curves of the variable stars (and the planetary candidates found from the ISIS light curves) were derived from this data as follows. Initially, a given star was assumed to have a "typical" colour. Then, for each individual measured instrumental magnitude, the colour-transformation terms obtained from the observations of the primary and secondary stars and the image-specific photometric zero points derived from the local standards in the NGC 6791 field, were used to predict a magnitude on the standard photometric system. Then a robust average was computed from all available $B$ magnitudes for the star, and likewise for $V$ and $I$, from which improved estimates of the colour indices of the star were derived. The improved colour was used in the colour transformations to re-derive new standard-system magnitudes for all the observational epochs, and new mean magnitudes and colours were computed. Because the colour terms in the transformations are quite small, with absolute values of well under 0.1 mag/mag, this process converges very quickly. This approach does have the drawback that at each epoch the instrumental magnitude is transformed to a standard-system magnitude based upon the star's *mean* colour, averaged over all epochs. In the case of a constant star, this is an optimal approach, but in the case of a variable star it could introduce small systematic errors in the magnitudes observed at the extremes of the star's colour cycle. It would be better to correct each instrumental magnitude according to the star's *instantaneous* colour, which is possible when light curves are being fitted at the same time as the photometric observations are being calibrated. This was done, for instance, when this same software was used for the *Hubble Space Telescope Key Project on the Extragalactic Distance Scale*, where template Cepheid light curves were being fitted to variable-star candidates (see Stetson (1996); Stetson et al. (1998)). In the present case, we had no preconceived notions as to the forms of individual variable stars' light curves, so we did not try to fit light curves during the photometric reductions in order to predict instantaneous colours; the extraction of light curves was done *ex post facto* after the calibration of the photometry. Note that this procedure may bias *instantaneous* standard-system magnitudes by amounts not larger than the colour-transformation terms times half the colour amplitude of a variable star, which will generally lead to a *maximum* systematic error less than 0.01 mag in the instantaneous magnitudes at the epochs of extreme colour. Systematic errors in the periods, *mean* magnitudes, and colours of the variable stars should be negligible.

### 4.4.2 Difference Imaging with ISIS

I have used the difference imaging software ISIS version 2.1 developed by Alard & Lupton (1998). For each of the filters $V$ and $I$, I selected the images with the best seeing, which were used to generate the reference images. For each image a kernel is computed which describes the variations of the PSF across the image relative to the reference image. The final step is to convolve the reference image by this kernel and subsequently subtract the convolved reference image from each individual image. In principle what will be left in the subtracted images will be the signal that is *intrinsically* different from the reference image, *e.g.* variable stars.

One of the advantages of using the difference image technique is that the signal from variable stars in crowded regions will be less affected by the neighbouring stars, *e.g.* when compared to profile fitting photometry. Another important point is that variations due to airmass and transparency variations are removed as a part of the image subtraction.

Unfortunately, I was not able to make the photometry package of ISIS work on the subtracted images (*cf.* section 3.3.2). Instead I used the DAOPHOT package to extract aperture photometry in the subtracted image around the position of all stars in the field (found by using ALLSTAR). Normally, DAOPHOT calculates the magnitude of a star as $m = -2.5 * \log(N) + 25.0$, where $N$ is the number of counts. But since the number of counts in an aperture can be negative for the difference images, we had to add a short piece of code in the original DAOPHOT program to account for this. In particular, we defined a new stellar magnitude as $m_{\rm ISIS} = -2.5\log((N + \sqrt{N_0^2 + N^2})/2.) + 25.0$. The zero-point magnitude is $m_0 = -2.5\log(N_0) + 25.0$ and we used $N_0 = 1$, *i.e.* $m_0 = 25.0$. One can show that the number of counts will be $N = N_0 \sinh[0.4\ln(10)(m_0 - m + 2.5\log(2))]$.

I used a range of increasing aperture sizes which were scaled with the seeing (*i.e.* the measured FWHM) of each image. I then defined magnitude intervals with a width of 1 magnitude and selected the aperture size to be used within each interval which gave the lowest noise level. For bright stars I used large apertures and smaller apertures for the faintest stars (the latter will be affected by relatively higher sky background noise). Based on growth curves constructed for the direct images (Stetson 1990) I then scaled the counts in each aperture to include all the light (for more details see section 3.3.2).

The relative magnitudes were then computed as $\Delta m = -2.5\log[(N_{\rm ref} - N_i)/N_{\rm ref}]$, where $N_{\rm ref}$ are the counts in the reference image and $N_i$ is the number of counts in the chosen aperture after applying the correction from the growth curve.

### 4.4.3 Repairing the Images

Any major defects in the images will cause residuals in the subtracted images. There are three major contributors to the defects: cosmic rays, bad columns, and saturated stars. While cosmic rays are rejected as part of the ISIS reduction the latter two effects may influence the "quality" of the image subtraction. In particular the image subtraction gives large residuals around the most saturated stars. I thus decided to repair the saturated pixels in the cores of bright stars and the flux from stars which fall on bad columns. As a result of this, the residuals in the subtracted images were still present, but only very close to the saturated star.

I wrote a short IDL code to replace pixels on the bad columns and the saturated pixels. For each image the code examines the pixels around the brightest stars to look for pixels above the saturation limit (60 000 ADU). I also identified stars for which the centroid is within 20 pixels of a bad column. I then computed an "artificial" image where the stars found above were inserted using the PSF model found with DAOPHOT for each image. For the magnitudes and positions of these artificial stars I used the results found when using ALLSTAR. I then replaced the saturated pixels and the signal on the bad columns in the observed image with the data from the artificial image (including estimated background level and photometric noise). Several bright giants were saturated in the images and they cause significant "bleeding" signal on the CCD, and there are a few bad columns on the CCD. I replaced both the bleeding pixels and the bad columns with the values in the artificial images.

I stress that when searching the light curves for planetary transits and variable stars, I clearly mark the points in the light curves where the star is close to a bad column or a neighbouring saturated star, since the validity of the measured signal in these cases is indeed questionable.

### 4.4.4 Photometric Noise in the ISIS Light Curves

In Figure 4.1 I plot the point-to-point noise level (*cf.* Eq. 2.1) of the light curves of the *NOT01* data set reduced with ISIS. The dashed lines mark the contribution to the noise from photon statistics and aperture noise calculated using the expressions in Kjeldsen & Frandsen (1992). The solid line gives the combined theoretical noise level. The brightest stars in the cluster reach a noise level of 1 mmag per point while the turn-off stars ($I_{\rm Inst} = 12$) typically have 3 mmag per point.

The fact that the measured noise level is much higher than the photon noise level for the faint stars shows that the combination of image-subtraction and aperture photometry on the subtracted images is indeed not optimal.

The relative transit depth caused by a close-in giant planet is equal to the square of the radius ratio of the planet and the parent star. For stars below the turn-off region ($I_{\rm Instr} \simeq 12$) the transit depth of a Jupiter-sized planet will be of the order 1–3% (*cf.* Figure 2 in Mochejska et al. (2002b)). Thus the photometric noise limit is well below the limit for detection of transits since I will have several measurements during a transit which is expected to be of the order 1–3 hours.

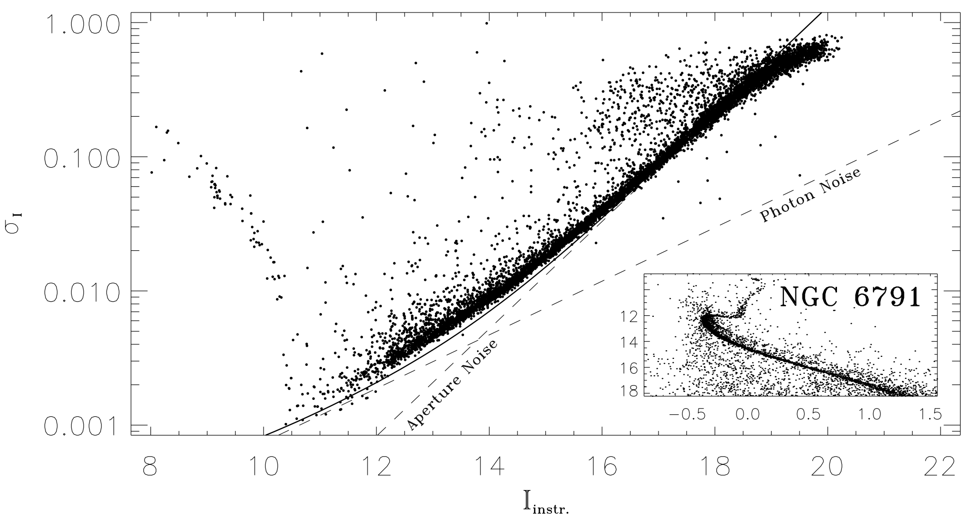


**Figure 4.1** Measured noise level in $I$ filter measured over seven nights from the *NOT01* data set. The reductions were made with ISIS (Alard & Lupton 1998). The dashed lines mark the photon noise and the aperture noise while the solid line is the quadratic combination of these two.

## 4.5 The Calibrated Colour-Magnitude Diagram of NGC 6791

In Figure 4.2 we present the colour-magnitude diagram of NGC 6791. It is the result of the ALLFRAME reduction of 958 $V$ and 737 $I$ frames which is described in our companion paper (Stetson et al. 2003). The magnitudes are calibrated to the standard $V$ and $I_C$ system. The formal error on the turn-off stars is around 0.5 mmag in both $V$ and $I$ for stars around the turn-off while the calibration errors are less than 2 mmag. The calibrated photometry is very useful as a standard field and will be available from the Canadian Astronomy Data Centre (Stetson 2000).

The cover of this dissertation is a combined colour image of part of the NGC 6791 field observed from NOT. It is fascinating to note the population of faint red stars on the lower main sequence, and the much brighter stars near the turn-off, and the beautiful giant stars.

## 4.6 The Search for Transit-like Events

We only used the first seven nights of the *NOT01* campaign to search for planet transits. The quality of the eighth night from *NOT01* is too bad and we found that the quality of the data from the *SMR95* campaign was not suitable for detecting transits.

The light curves were searched for transit-like events according to the method outlined for single transit searches in Tingley (2003). Fortunately, the signal-to-noise ratio in the *NOT01* data set varied very little from night to night, simplifying the process significantly.

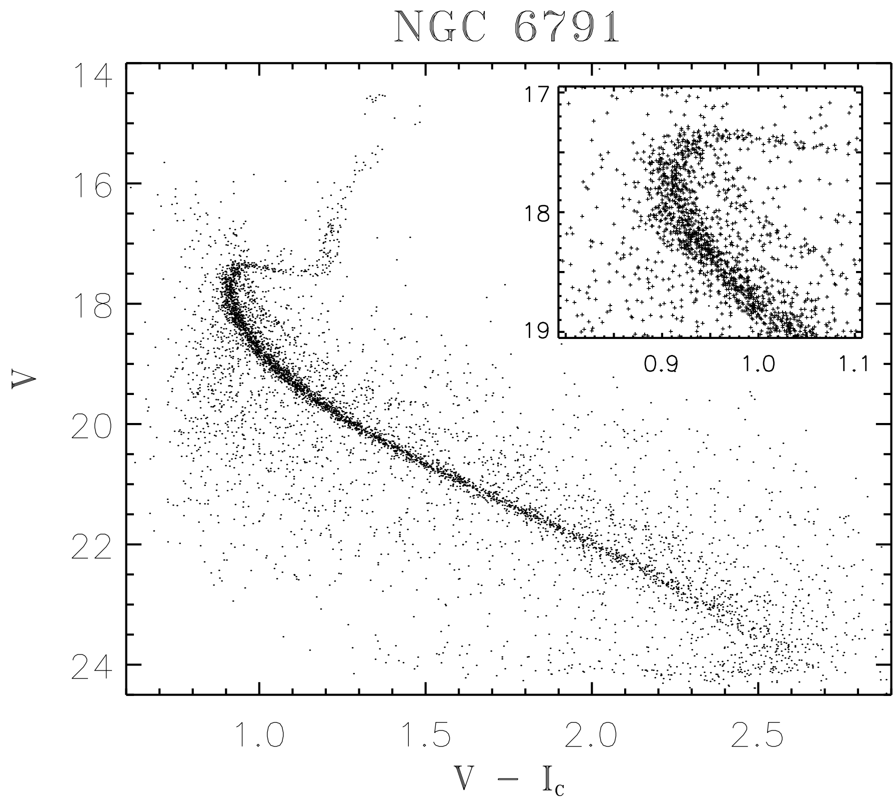


**Figure 4.2** The calibrated colour-magnitude diagram of NGC 6791. The inserted plot shows the turn-off region: notice the narrow main sequence and the binary sequence.

The software that performed the search used a simple square-well for identifying transit-like signatures. The software would slide the square-well through the light curves and sum the convolution of the square-well and the light curve. Thus we were able to identify transit-like events and their location in time. We used transit durations of 2, 3, and 4 hours and depths of 1,2 and 3 %.

We created a histogram showing the times of the detected transits to determine if there were any particular times in the data set as a whole that seemed to over-produce spurious events. One would expect that the triggering events would be more or less evenly distributed in time, whether they arise from transits or stellar variability. Any regions in time that seemed to over-produce large numbers of events would then be removed, and the analysis was repeated. The reasons for recurring bad data could be periods of bad seeing or erroneous tracking of the telescope.

We found that a significant number of false alarms were generated. From inspection of the images the false alarms could often be explained by the contamination of a star by a variable / saturated neighbour star, or the star being close to the edge of the CCD.

It is interesting to note that many of the transit-like events are found for different depths and durations for the "sliding square-well" used with our planet search software. This suggests that the algorithms are fairly insensitive to the duration and depth parameters (see Tingley (2003)).

Finally we note that in the course of the search for transits we also found low-amplitude variable stars which were *not* clearly identified from the Stetson $J$-index (*cf.* section 4.7).

### 4.6.1 Transit-like Light Curves

After rejection of obvious false alarms, we have found nine stars with transit-like events in their light curves. The position of these stars in the CMD is given in Figure 4.3. We have also plotted the stars with the best photometry, *i.e.* 3581 stars having the following quality-indices from ALLFRAME: $|sharp| < 0.25$, $|\chi - 1| < 0.25$, $\sigma_V < 0.04$, and $\sigma_I < 0.04$ (see Stetson et al. (2003) for details). We have summarized the properties of the nine stars with transits-like events in Table 4.3.

In Figure 4.4 we present part of the light curves for the nine stars with transit-like light curves in the *NOT01* data set. The black points are $V$ measurements while the grey points are $I$ measurements. The times indicated on the plots as $t_0$ are HJD − 2 452 000 for the tick-mark corresponding to 0.0.

We note that the telescope was offset slightly on the first night at the time $t_0 = 100.52$ to the position which was used for the rest of the *NOT01* campaign. This time coinsides with the transits seen in T1, T2, and T3. We have only observed single transits except for T6. However, the durations of the two transit events seen for T6 are very different. The observed transit-like event of T2 is very likely due to the star being on a bad column on the CCD. Finally, T9 is found to be a long-period low-amplitude variable (V69, *cf.* Figure 4.7), so quite possibly the dip seen at HJD = 106.7 could be the beginning of an eclipse in a binary pair. This seems plausible from the position of T9 in the CMD in Figure 4.3. The transit-like event seen for T4 is very odd, since the $I$ measurements indicate a much longer transit duration than the $V$ measurements.

In the remaining three cases we have found (T5, T7, and T8), the transit events have a duration of 1–3 hours. Furthermore, the depths are around 10 mmag in both the $V$ and $I$ filters. These facts are not in contradiction with the expected transit light curves of the short-period giant planets which are known from radial-velocity searches (Butler et al. 2002). As pointed out by Yee et al. (2002), the shape of a transit caused by a planet will be characterized by steep ingress/egress and a flat bottom during the transit. The precision of the present photometry is not good enough to see the detailed shape of these shallow transits. We need further data of higher precision to confirm the transits and also to detect multiple transits.

We finally note that the age of NGC 6791 is $8.0 \pm 0.5$ according to Chaboyer et al. (1999). Hence the expected rotational periods of the stars at the turn-off would be $\sim$few days at least. Hence, star spots do not seem like a plausible explanation.

To summarize, we cannot claim that what we have observed is indeed caused by a giant planet in any of the cases presented in Figure 4.4 and Table 4.3.

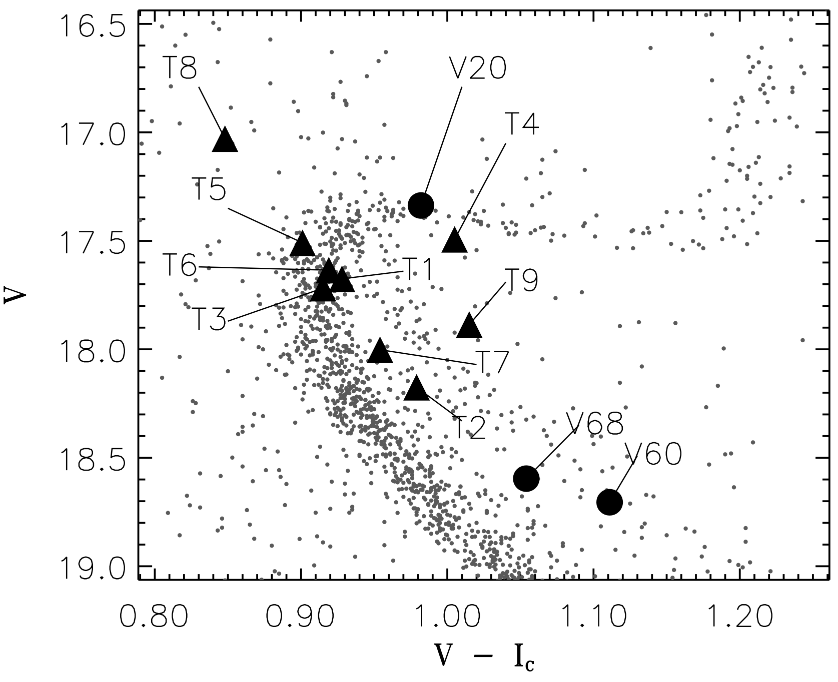


**Figure 4.3** Colour-magnitude diagram where the transit candidates (triangles) and the eclipsing binaries (circles) are marked. The stars with the best photometry are also plotted to emphasize the location of the main sequence, the turn-off, and the red giant branch.

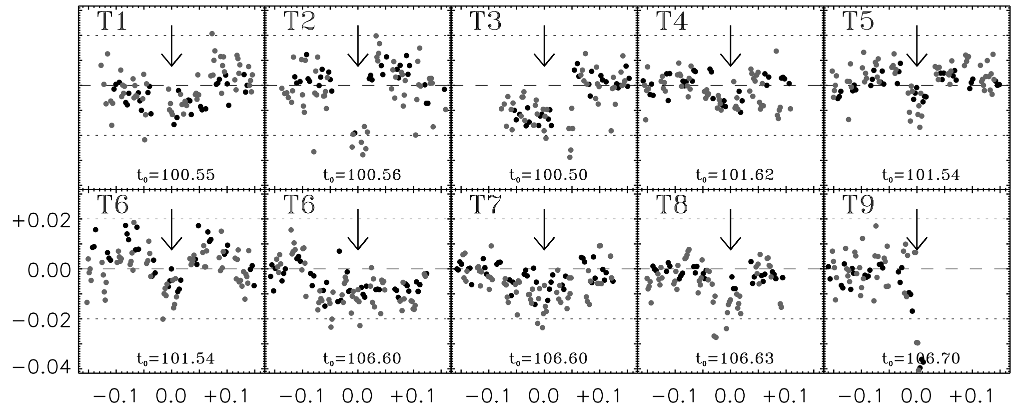


**Figure 4.4** Light curves of transit candidates. Black and grey symbols are $V$ and $I$ measurements, respectively. The time $t_0$ in each panel corresponds to the time HJD − 2 452 000 of the tick-mark at 0.0. Note that T6 has two transits-like events but of very different duration.

**Table 4.3** We give the name, ID number, $\alpha$, $\delta$, $V$, $V - I_C$, and $B - I_C$ for the stars with transit-like light curves. All information except the adapted name in the first column is from Stetson et al. (2003). The positions of the stars in the CMD is shown in Figure 4.3 and the light curves can be seen in Figure 4.4. As discussed in the text, the transits seen for T1–4, T6, and T9 are not likely to be due to eclipsing giant planets (they are marked by a $*$ symbol).

| Name | ID | $\alpha_{2000.0}$ | $\delta_{2000.0}$ | $V$ | $V - I_C$ | $B - I_C$ |
|---|---|---|---|---|---|---|
| T1* | 4891 | $19^h20^m43\overset{s}{.}37$ | $+37°47'31''.5$ | 17.675 | 0.928 | 1.818 |
| T2* | 6598 | $19^h20^m48\overset{s}{.}65$ | $+37°47'41''.1$ | 18.175 | 0.979 | 1.901 |
| T3* | 12616 | $19^h21^m07\overset{s}{.}28$ | $+37°47'39''.9$ | 17.718 | 0.915 | 1.809 |
| T4* | 9049 | $19^h20^m55\overset{s}{.}47$ | $+37°44'06''.1$ | 17.493 | 1.005 | 1.839 |
| T5 | 3671 | $19^h20^m39\overset{s}{.}07$ | $+37°47'26''.1$ | 17.509 | 0.901 | 1.784 |
| T6* | 3567 | $19^h20^m38\overset{s}{.}63$ | $+37°45'33''.3$ | 17.635 | 0.919 | 1.811 |
| T7 | 3723 | $19^h20^m39\overset{s}{.}25$ | $+37°45'39''.3$ | 18.002 | 0.954 | 1.827 |
| T8 | 9020 | $19^h20^m55\overset{s}{.}40$ | $+37°47'23''.4$ | 17.029 | 0.848 | 1.670 |
| T9* | 12390 | $19^h21^m06\overset{s}{.}48$ | $+37°47'27''.8$ | 17.886 | 1.015 | 1.947 |

## 4.7 The Variable Stars in NGC 6791

To search for variable stars I used the Stetson $J$-index (Stetson 1996). To summarize, the $J$-index is a normalized sum of the deviation of each point (or pair of points with small separation in time) in the light curve compared to *expected* noise level of a star of the same magnitude. To determine the *expected* noise level for a given star I used the mean of a large number of stars with similar magnitude.

In the following we present the phased light curves of some of the variable stars in NGC 6791. In addition to 19 known variables in our field we present 23 new variables. The locations in the CMD of the 23 new variables are shown in Figure 4.5. The new variables all have low amplitudes and long periods. This explains why they were not found by Rucinski et al. (1996) or Mochejska et al. (2002b) due to the lower signal-to-noise ratio in their data sets.

In Table 4.4 we give a list of the variable stars we have observed. The columns in Table 4.4 contain the variable name, the ID number, right ascension, declination, period, the approximate amplitude in the $V$ filter, and the variable type.

The information in columns 2–4 is from Stetson et al. (2003). We have determined the periods of each star by using PERIOD98 (Sperl 1998). For some of the new long-period variables the time series is not long enough or the amplitude is too small to give a safe estimate of the period. In these cases we have only given an approximate period (indicated by the "$\sim$" symbol).

In Figure 4.6 we show the phased light curves of some of the known variables and in Figure 4.7 we present some the new variables. The ordinate gives the change in magnitudes in the $V$ filter (scaled by the central wavelength of the filters) and the phase is on the abscissa. The *MOCH01* and *SMR95* data are not plotted in Figures 4.6 and Figure 4.7 if the amplitude of the variable is comparable to the noise level in these data sets.

An interesting eclipsing binary is V9 which was observed in all three data sets. It is classified as an RS Canum Venaticorum type star (RS CV, see *e.g.* Hall (1972)).

**Table 4.4** The variables in the *NOT01* field. The first column contains the variable name, where the new variables are printed with *italics* (*V67-V90*). Columns 2, 3, and 4 contain ID, right ascension, and declination from Stetson et al. (2003). Columns 5 and 6 are the periods and amplitudes (in the $V$ filter) we have determined. The last column gives the variable star type. The positions of the variables in the colour-magnitude diagram are given in Figures 4.3 and 4.5 while the phased light curves of some of the stars are shown in Figures 4.6, 4.7, and 4.8.

| Name | ID | $\alpha_{2000.0}$ | $\delta_{2000.0}$ | $P$ [days] | $A$ | Var. Type |
|---|---|---|---|---|---|---|
| V1 | 6271 | $19^h20^m47^s.61$ | $+37^\circ44'32''.0$ | 0.2676766 | 0.194 | EB, close |
| V4 | 8576 | $19^h20^m54^s.22$ | $+37^\circ48'23''.8$ | 0.325667 | 0.046 | EB, close |
| V5 | 5883 | $19^h20^m46^s.53$ | $+37^\circ48'47''.9$ | 0.312666 | 0.017 | EB, close |
| V6 | 11376 | $19^h21^m02^s.72$ | $+37^\circ48'49''.1$ | 0.279062 | 0.042 | EB, close |
| V9 | 6371 | $19^h20^m47^s.88$ | $+37^\circ46'37''.4$ | 3.19174 | 0.040[a] | EB, close |
| V16 | 12695 | $19^h21^m07^s.59$ | $+37^\circ48'09''.6$ | 4.53 | 0.026 | EB, close |
| V31 | 11307 | $19^h21^m02^s.47$ | $+37^\circ47'09''.3$ | 3.34154 | 0.015 | EB, close |
| V33 | 3886 | $19^h20^m39^s.81$ | $+37^\circ43'54''.4$ | 2.35944 | 0.040 | EB, close |
| V38 | 11652 | $19^h21^m03^s.69$ | $+37^\circ46'05''.9$ | 3.845 | 0.023 | EB, close |
| V20 | 8600 | $19^h20^m54^s.30$ | $+37^\circ45'34''.7$ | 14.4698 | 0.3[a] | EB, detached |
| V60 | 10746 | $19^h21^m00^s.70$ | $+37^\circ45'45''.1$ | 7.510/7.1[b] | 0.4/0.015[b] | EB, detached |
| *V68* | 8943 | $19^h20^m55^s.21$ | $+37^\circ46'39''.7$ | ~9.0038 | 0.15[a] | EB, detached |
| V14 | 7637 | $19^h20^m51^s.67$ | $+37^\circ45'24''.8$ | 5.4–5.8 | 0.028 | Periodic Var. |
| V17 | 3626 | $19^h20^m38^s.88$ | $+37^\circ49'04''.6$ | 6.42566 | 0.036 | Periodic Var. |
| V41 | 7397 | $19^h20^m50^s.97$ | $+37^\circ48'24''.8$ | 0.4807278 | 0.039 | Periodic Var. |
| V53 | 10798 | $19^h21^m00^s.84$ | $+37^\circ44'35''.4$ | 7.815 | 0.039 | Periodic Var. |
| *V69 = T9*[c] | 12390 | $19^h21^m06^s.48$ | $+37^\circ47'27''.8$ | 4.447 | 0.014 | Periodic Var., EB? |
| *V70* | 3268 | $19^h20^m49^s.65$ | $+37^\circ48'08''.7$ | 7.58 | 0.008 | Periodic Var. |
| *V71* | 3857 | $19^h20^m39^s.71$ | $+37^\circ47'36''.1$ | 7.58886 | 0.010 | Periodic Var. |
| *V72* | 5848 | $19^h20^m46^s.40$ | $+37^\circ44'14''.1$ | 7.014 | 0.037 | Periodic Var. |
| *V73* | 6305 | $19^h20^m47^s.71$ | $+37^\circ44'58''.2$ | 1.6333 | 0.03 | Periodic Var. |
| *V74* | 7011 | $19^h20^m49^s.86$ | $+37^\circ45'50''.9$ | 4.100 | 0.007 | Periodic Var., EB? |
| *V75* | 7099 | $19^h20^m50^s.13$ | $+37^\circ48'31''.7$ | 7.39 | 0.011 | Periodic Var. |
| *V76* | 8033 | $19^h20^m52^s.78$ | $+37^\circ44'58''.8$ | 6.971 | 0.006 | Periodic Var. |
| *V77* | 8088 | $19^h20^m52^s.91$ | $+37^\circ46'36''.9$ | 6.91 | 0.008 | Periodic Var. |
| *V78* | 9432 | $19^h20^m56^s.64$ | $+37^\circ46'36''.2$ | 5.7617 | 0.028 | Periodic Var. |
| *V79* | 10169 | $19^h20^m58^s.86$ | $+37^\circ44'47''.2$ | 5.71 | 0.008 | Periodic Var. |
| *V80* | 10699 | $19^h21^m00^s.54$ | $+37^\circ48'40''.7$ | 5.13 | 0.011 | Periodic Var. |
| *V81* | 11380 | $19^h21^m02^s.73$ | $+37^\circ46'00''.8$ | 7.24 | 0.008 | Periodic Var. |
| *V82* | 12049 | $19^h21^m05^s.23$ | $+37^\circ47'08''.5$ | 0.94928 | 0.007 | Periodic Var. |
| B7 | 12652 | $19^h21^m07^s.40$ | $+37^\circ47'56''.5$ | ~13.3 | 0.15 | Long period |
| V62 | 11475 | $19^h21^m03^s.06$ | $+37^\circ43'51''.8$ | ~17 | 0.027 | Long period |
| V65 | 7920 | $19^h20^m52^s.47$ | $+37^\circ47'30''.5$ | 8.613 | 0.008 | Long period |
| V67 | 11645 | $19^h21^m03^s.67$ | $+37^\circ48'03''.7$ | ~10 | 0.05 | Long period |
| *V83* | 4640 | $19^h20^m42^s.50$ | $+37^\circ44'36''.9$ | ~15.57 | 0.01 | Long period |
| *V84* | 4805 | $19^h20^m43^s.05$ | $+37^\circ47'32''.5$ | 9.477 | 0.012 | Long period |
| *V85* | 5485 | $19^h20^m45^s.26$ | $+37^\circ45'48''.8$ | 9.307 | 0.012 | Long Period |
| *V86* | 6777 | $19^h20^m49^s.17$ | $+37^\circ49'14''.8$ | 9.563 | 0.013 | Long period |
| *V87* | 8108 | $19^h20^m52^s.97$ | $+37^\circ46'52''.5$ | ~20.9 | 0.02 | Long Period |
| *V88* | 9353 | $19^h20^m56^s.42$ | $+37^\circ45'38''.4$ | ~8.99 | 0.01 | Long period |
| *V89* | 9568 | $19^h20^m57^s.06$ | $+37^\circ48'12''.2$ | ~10 | 0.003 | Long period |
| *V90* | 11111 | $19^h21^m01^s.81$ | $+37^\circ45'42''.0$ | 12.5215 | 0.01 | Long period |

(*a*) For the eclipsing binaries V9, V20, and *V68* the depth of the primary eclipse in the $V$ filter is given.
(*b*) V60 is variable with a low amplitude and a period of $P \sim 7.1$ days while the period estimated from the secondary and primary eclipses is $7.510 \pm 0.005$ days. The primary eclipse depth is 0.4 mag in $V$.
(*c*) *V69* was detected in our search for planetary transits and is also given the name *T9* (*cf.* Figure 4.4). Furthermore, *V69* is variable with a low amplitude.

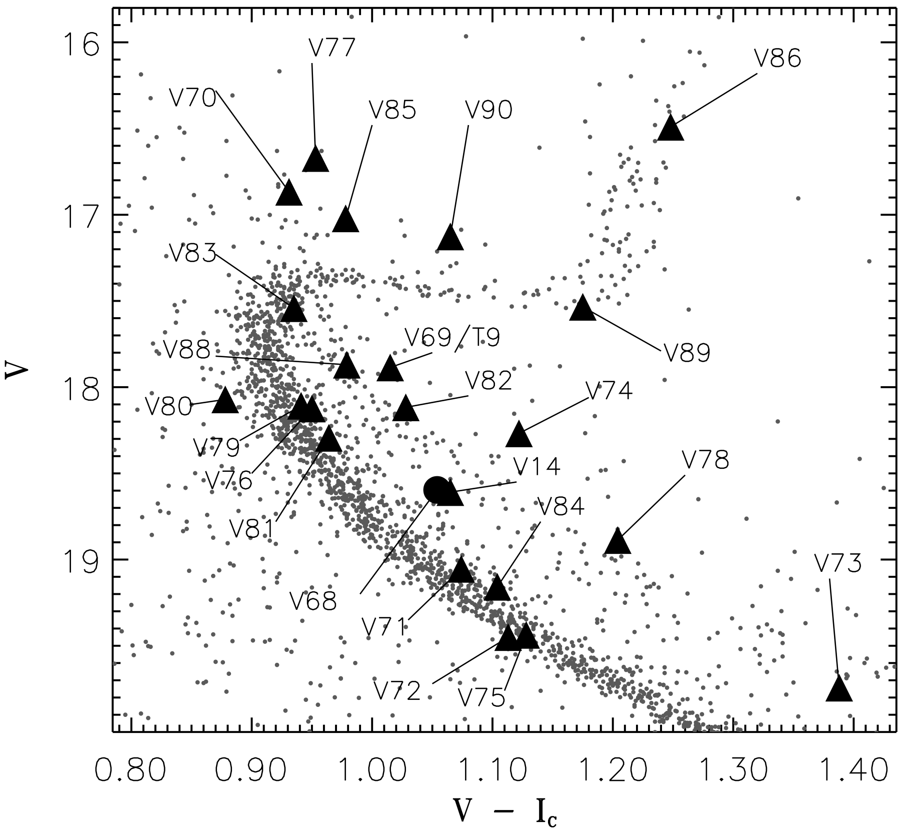


**Figure 4.5** Colour-magnitude diagrams where the 23 newly discovered variables are marked. Only the stars with the best photometry are plotted to emphasize the location of the main sequence, the turn-off, and the red giant branch.

The light curves in the $V$ (*left*) and $I$ filters are shown in Figure 4.8 where the "+" symbols are used for the *NOT01* data, the filled grey symbols are the *MOCH01* data, while the squares are the *SMR95* data. The light curve of V9 is characterized by a deep eclipse which is modulated by a "distortion wave" probably due to dark spots on the surface of one of the stars in the binary pair. It is interesting to note that while the phase of the eclipse is unchanged the modulation wave has shifted phase from 1995 (*SMR95*) to 2002 (*NOT01* and *MOCH01*). The shape of the modulation wave seems to be unchanged, as was also noted by Mochejska et al. (2002b)).

We finally note that the light curves presented here will be available from the Canadian Astronomy Data Centre (Stetson 2000).

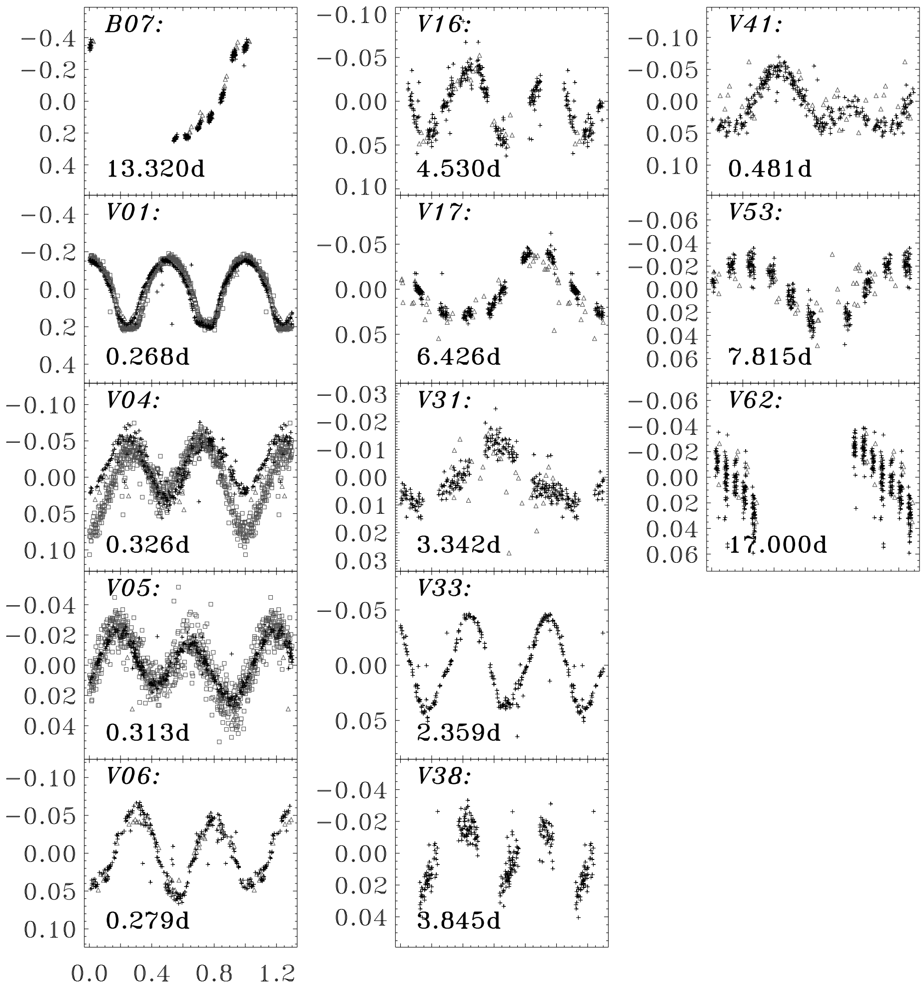


**Figure 4.6** Phased light curves in the $V$ filter for some of the known variables in NGC 6791. In most panels only the *NOT01* data (+ symbols) are plotted due to the much lower noise level compared to *MOCH01* (triangle symbols) and *SMR95* (box symbols). Notice the change in the light curve of V4.

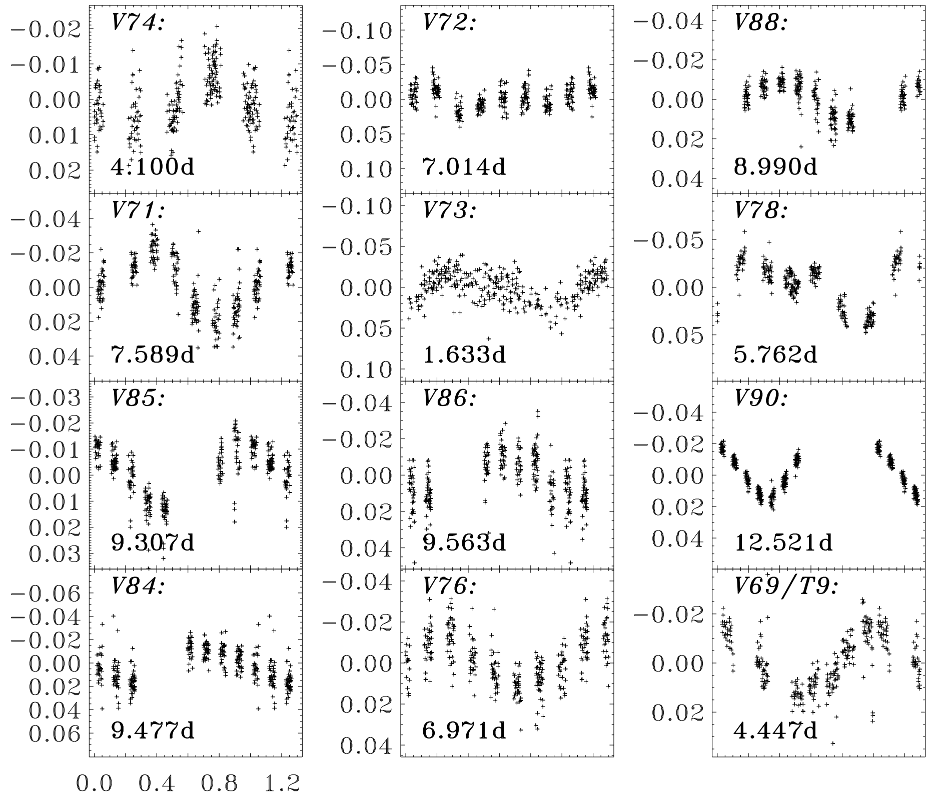


**Figure 4.7** Phased light curves of some of the new low-amplitude variables. Only the *NOT01* data are plotted. The ID number is given in the top left corner of each panel and correspond to Stetson et al. (2003). The period (in days) is given in the lower left corner. More details are given in Table 4.4.

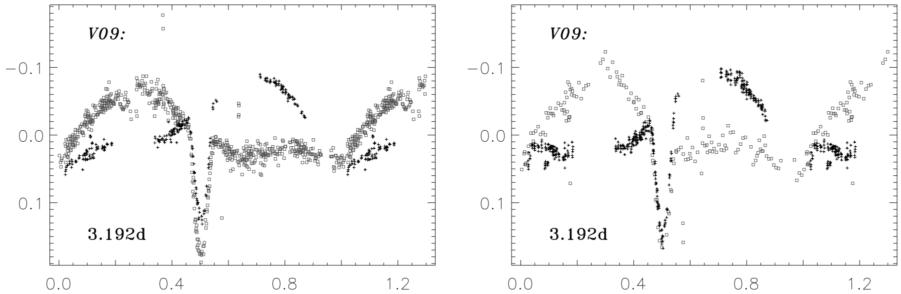


**Figure 4.8** Phased light of the RS CV-type variable V9 in NGC 6791 in the *V* (*left*) and *I* filter (*right*). The black + symbols are data from *NOT01* while the grey symbols are from either *SMR95* (box symbol) or *MOCH01* (filled grey symbols) The *MOCH01* data are not plotted in the *right* plot since Mochejska et al. (2002b) did not observe in *I*.

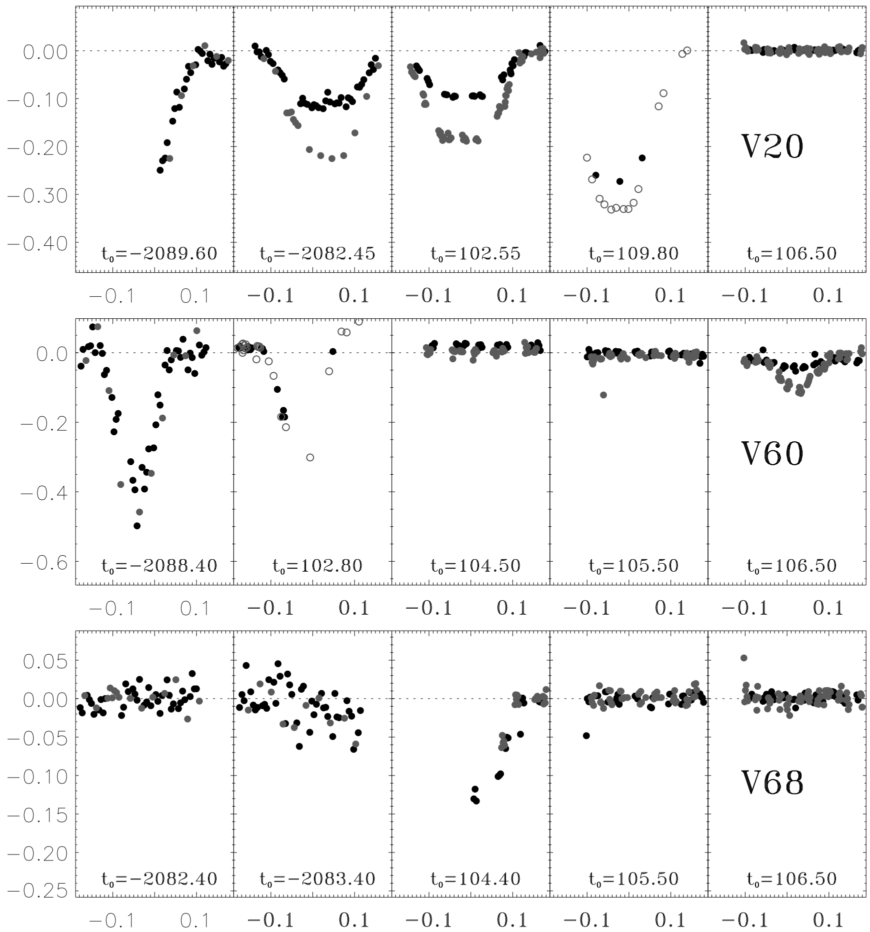


**Figure 4.9** Light curves of three eclipsing binary stars. The time corresponding to 0.0 on the abscissa is HJD − 2 452 000 and is given at the bottom of each panel as $t_0$. One or more nights *without* eclipses are shown for comparison. Black and grey symbols are $V$ and $I$ measurements, while the open circles are $R$ measurements from *MOCH01*.

## 4.8 Three Eclipsing Binary Stars in NGC 6791

In Figure 4.9 I show the light curves of three detached eclipsing binaries. In each panel $t_0$ is the time HJD − 2 452 000 for the tick-mark corresponding to 0.0. The black and grey points are $V$ and $I$ measurements, while open circles are $R$ measurements from *MOCH01*.

For each of the eclipsing binaries V20, V60, and V68 I show the light curves from five nights, *i.e.* the nights on which the eclipses occur and one or more nights without eclipses for comparison.

The eclipses of V20 and V60 were noted before by Rucinski et al. (1996) and Mochejska et al. (2002b), but now for the first time I have enough time coverage to be able to constrain the periods. From the difference in time between the eclipses I find periods of $P_{\rm bin} = 14.470 \pm 0.001$ and $7.510 \pm 0.005$ days for V20 and V60, respectively. I note that V60 is variable with an amplitude of 0.015 mag in $V$ at a period of $P_{\rm var} \simeq 7.1 \pm 0.2$ days.

### 4.8.1 The Detached Binary V20

The detached binary V20 is located right after the turn-off. We have been granted observing time to do a more detailed photometric coverage of the primary and secondary eclipses, and we plan to carry out spectroscopic measurements to obtain the radial velocity curve. With these observations it will be possible to constrain the masses, radii, and luminosities of the binary components of V20.

As will be demonstrated in the next section, the primary component of V20 is very close to the turn-off. From the knowledge of the mass of the primary component, we expect to be able to determine the age of NGC 6791 with good accuracy. This can be done, since from theoretical isochrones one can determine the relation between age and mass the turn-off stars, *i.e.* the age can be found from the derived mass of the primary component of the detacted binary V20.

This has recently been done for the globular cluster $\omega$ Cen by Kaluzny et al. (2002) for eclipsing stars around the turn-off. Their masses could be determined to just 1 % including systematic errors. In this case one of the systems is right after the turn-off and Kaluzny et al. (2002) were able to constrain the position of the theoretical isochrones and in turn estimate the age of $\omega$ Cen to within 0.6 Gyr – at least a factor of two better than any previous age determination for a globular cluster.

### 4.8.2 Estimating the Parameters of the Detached Binary V20

In Figure 4.10 the colour-magnitude diagram of NGC 6791 is shown. The location of the eclipsing binary V20 is shown with a star symbol above the turn-off region. In the following we will describe how we have determined the parameters of the two components that make up the binary V20.

We have fitted a fiducial to the turn-off region shown as the solid "primary" curve, and in the following we assume the primary component will be on this curve within $\pm 0.015$ mag, which is the observed width of the main sequence. For each point on the "primary" curve we calculate what the magnitude and colour of the secondary component should be, while requiring that the *combined* colour and luminosity of the primary and secondary component must yield the *observed* position of V20. The inferred position of the secondary component is shown as the dashed "secondary" curve.

For three positions on the "primary" curve we have marked the corresponding position on the "secondary" curve: at the turnoff (TO), on the main sequence (MS), and the point where the main sequence and the "secondary" curve intersect (Bin).

**Table 4.5** The derived parameters for the two components of the binary star V20. We found the colours from Figure 4.10, and in the text we explain how $T_{\rm eff}$ was determined. The estimated errors are given in parenthesis.

| Component | $V$ | $V-I_C$ | $(V-I_C)_0$ | $T_{\rm eff}$ | $BC_V$ |
|---|---|---|---|---|---|
| Primary | 17.38(1) | 0.95(1) | 0.82(6) | 5200(200) | -0.20(5) |
| Secondary | 20.94(1) | 1.61(1) | 1.48(6) | 4070(200) | -0.96(10) |

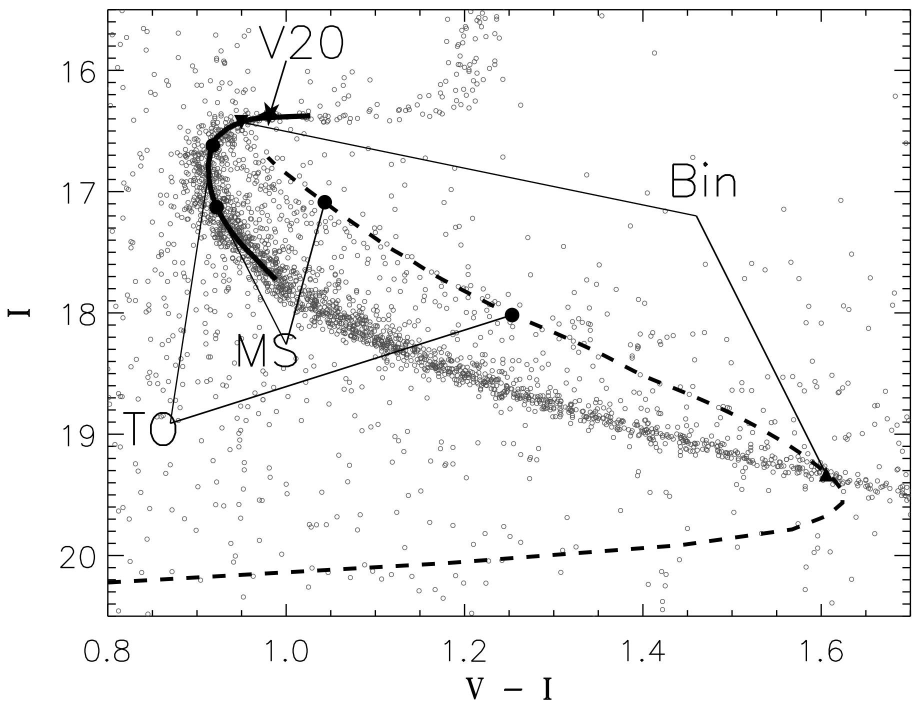


**Figure 4.10** The $I$ *vs.* $V-I$ colour-magnitude diagram of NGC 6791 on the standard system. The location of the eclipsing binary V20 above the turn-off is shown with a star symbol. To find the possible positions of the two components of the binary V20, we assume that the primary star is on the solid black curve and calculate the corresponding colour and magnitude for the secondary component which is given as the dashed line. For three points we have shown the location of the primary and secondary star, *i.e.* for the primary star being at the turn-off (TO), further down the main sequence (MS), and the point where the dashed curve intersects the main sequence (Bin).

The latter is the best fit of the location of the two components making up the binary V20. Their colours are determined to within less than $\pm 0.01$ mag and are given in Table 4.5. We will now use these colour estimates to infer the properties of the components of V20.

We have used the calibration of $T_{\text{eff}}$ *vs.* $(V-I)_J$ for main sequence stars with solar metallicity by Alonso et al. (1996). The calibration of Alonso et al. (1996) refer to *Johnson* $I_J$ magnitudes, and so we have used the calibration of Fernie (1983) to convert from the *Kron-Cousins* system we have used, *i.e.* $(V-I)_J = -0.005 + 1.273\,(V-I)_C$. For the interstellar reddening we use $E(B-V) = 0.105 \pm 0.025$ (Chaboyer et al. 1999) and using Taylor (1986) we find $E(V-I) = 0.13 \pm 0.03$. We note that the error given on $E(B-V)$ does not include systematic errors which could very likely be of the order $\sigma(E(B-V)) \simeq 0.05$.

From these numbers we can determine the de-reddened magnitudes and colours and thus estimate $T_{\text{eff}}$ of the two components of V20 to within 200 K including systematic errors in $E(B-V)$. The results are given in Table 4.5. We obtain the bolometric correction from Bessell et al. (1998) for atmospheric models with solar metallicity and no overshooting. We can then determine the relative luminosities of the stars using $M_{\mathrm{bol;p}} - M_{\mathrm{bol;s}} = (V_{\mathrm{p}} + BC_{\mathrm{p}}) - (V_{\mathrm{s}} + BC_{\mathrm{s}}) = -2.84 \pm 0.14$ which is equal to $-2.5\log(L_{\mathrm{p}}/L_{\mathrm{s}})$, and hence the luminosity ratio is $L_{\mathrm{p}}/L_{\mathrm{s}} = 13.7 \pm 1.8$. When using $L \propto R^2\, T_{\mathrm{eff}}{}^4$ we find a radius ratio of $R_{\mathrm{s}}/R_{\mathrm{p}} = 0.41 \pm 0.08$.

J. V. Clausen (*private communication*) has independently estimated the relative luminosities of the binary components by modelling the observed light curve of V20. He assumed that $T_{\mathrm{eff}} = 5\,200$ K for the primary as we have found above. From the modelling of the light curves using only the light curve in $V$ he found $T_{\mathrm{eff}} = 4\,400 \pm 250$ K for the secondary component. The large error in $T_{\mathrm{eff}}$ is mainly due to the depth of the secondary eclipse being different by $\simeq 0.02$ mag in the *SMR95* and *NOT01* data set. He also derived the radius ratio to be $R_{\mathrm{s}}/R_{\mathrm{p}} = 0.55 \pm 0.1$. Both $T_{\mathrm{eff}}$ and the radius ratio are in good agreement with what we have found.

Obviously, much more detailed photometric coverage of the primary and secondary eclipses of V20 are needed to further constrain the properties of the two components. As already mentioned, we need spectroscopic observations of the complete orbit to be able to constrain the masses of the components.

## 4.9 Conclusion and Future Prospects

We have described the seach for planet transits in the open cluster NGC 6791 from seven nights of observations with the Nordic Optical Telescope. The photometric precision is adequate for detecting eclipses by close-in Jupiter-sized planets. We have found nine stars with transit-like events in the light curves, but we argue that at least six of these are probably not caused by an eclipsing giant planet. The observed transit events may be due to instrumental effects (bad columns, offset of the telescope) and in one case there is evidence that the star (T9) belongs to a binary system. For the remaining three transit-like events the precision (3 mmag) is not good enough compared to the very shallow eclipse depth ($\sim 10$ mmag) to tell if the transits are really caused by giant planets, *e.g.* to see if the light curves are flat during the transit. To confirm the validity of these three planetary transit candidates the observation of multiple transits with higher precision are required.

In July 2002 Piotto, Stetson et al. have carried out a more ambitious multi-site campaign on NGC 6791 to search for planet transits. Stetson and I carried out ten nights (eight clear) of observations from the CFHT 3.6 m telescope in Hawaii from July 2–12 2002. In the same period of time observations from Mexico and Italy were carried out. The weather was not optimal during the multi-site campaign on NGC 6791 in 2002, but we have a higher signal-to-noise ratio compared to the *NOT01* data and also a higher duty-cycle over 10 nights. This will improve the statistics for detecting multiple eclipses. The reduction of data from the 2002 campaign data is now being undertaken.

In addition to our own data from *NOT01* we have used data from two previous photometric campaigns. The photometric precision of these other data sets is not high enough to confirm the shallow eclipses we have found. We have used the complete data set to redetermine the periods of the 19 known variables in the

*NOT01* field. Furthermore, we have discovered 23 new long-period stars with low amplitudes.

We have determined the periods of two detached eclipsing binaries V20 and V60. From the position of V20 in the colour-magnitude diagram we are able to constrain the temperatures of the binary components. This is in good agreement with results from the modelling of the primary and secondary eclipses. We find that the primary component is located just after the turn-off, while the secondary component is a much fainter main sequence star. We plan to make thorough photometric and spectroscopic observations of V20 to constrain the masses of the binary components. From the mass of the primary star we can determine the age of NGC 6791 from a comparison with the calculated turn-off mass for isochrones of different ages. This will give an age estimate independent of interstellar reddening.

# Chapter V

# Characteristics of Targets for Asteroseismology Space Missions

## 5.1 Constraining the Fundamental Stellar Parameters

Several space missions are planned to make multi-colour photometric studies of stars with the aim of taking asteroseismology to a new level of accuracy: the ultimate aim is to study samples of stars that are expected to oscillate, *e.g.* from $\delta$ Scuti stars to solar-like stars. Missions like `COROT` (Baglin et al. 2001), `RØMER/MONS` (Christensen-Dalsgaard 2002), and `EDDINGTON` (Roxburgh 2002) are planned to be launched in the period 2005–2008 and will bring the science of asteroseismology into a new era.

For this purpose knowledge of accurate fundamental parameters of the stars becomes extremely important. This information is needed to be able to interpret the frequency signals that are measured through comparison with theoretical pulsation models. Another crucial problem is the mode *identification* which I will not discuss here, but optimistically note that mode identification is not expected to be a serious problem for solar-like oscillations if the frequency resolution is good. I refer to the proceedings on *$\delta$ Scuti and Related Stars* (Breger & Montgomery 2000) in which many aspects of mode identification are discussed.

I have emphasized the importance of knowing the fundamental parameters in chapter 3.2 in connection to the modelling of giant stars in the globular cluster M4. In this case one has the advantage that one can compare the location of the star in the colour-magnitude diagram with theoretical isochrones and hence constrain $T_{\rm eff}$ and $\log g$, in addition to the age of the cluster. Furthermore, the metallicity can be expected to be roughly the same for stars in the same cluster and hence can be determined with good accuracy. This approach has been attempted for the $\delta$ Scuti stars in the open cluster Praesepe by Michel et al. (1999) and Hernandez et al. (1998) who found that the principle of obtaining the fundamental stellar parameters "for free" if a star is a member of a stellar cluster is not quite true[1]. A

[1]Michel et al. (1999) find evidence that $T_{\rm eff}$ for the stars in the Praesepe cluster is not well-defined by the position in the colour-magnitude diagram. They speculate that since the stars are observed at different angles relative to their rotation axis different degrees of gravitational darkening affect the observed luminosity and colour. For a rapidly rotating star $T_{\rm eff}$ will be hotter by $\sim$few 100 K at the poles than at the equator.

more powerful possibility for constraining the fundamental parameters is to study variable stars in binary systems since here the masses can be constrained if the orbit parameters can be measured (see *e.g.* Brown et al. (1994)). This has been used for $\alpha$ Cen in which solar-like oscillations have been detected by Bouchy & Carrier (2001).

When studying normal field stars one can use Strömgren photometry to determine the fundamental parameters $T_{\rm eff}$, $\log g$, and [Fe/H] with an accuracy of about 200–250 K, 0.2–0.3 dex, and 0.2–0.3 dex (Rogers 1995). This accuracy is not quite satisfactory for detailed modelling. The solution is to obtain medium or high resolution spectra of the stars. From detailed abundance analysis of individual spectral lines one can constrain the fundamental parameters with an accuracy of 100–150 K, 0.2 dex, and 0.1 dex in $T_{\rm eff}$, $\log g$, [Fe/H][2]. From HIPPARCOS parallaxes one can constrain $\log g$ independently and often more accurately than with the Strömgren $c_1$ index. The accuracy of $\log g$ from HIPPARCOS parallaxes also depends on a good estimate of the temperature and mass of the star, the latter of which can be inferred from theoretical evolutionary tracks. Another fundamental parameter can be determined using interferometry, namely the radii of nearby field stars (see *e.g.* Nordgren et al. (1998)).

In the case of the asteroseismology space missions COROT and RØMER/MONS the main cameras will measure the light curves of about 10 and 25 stars for 150 and 30 days, respectively. Since these are quite limited samples of stars, it is very important to select the target stars with care. It is important to stress that not only do we need to know the fundamental parameters of the targets. It is also important to look for chemical peculiarities, contamination of nearby stars, or binarity, in order to select the most suitable targets for learning about the structure of stars in general. Different people in *the COROT/ MONS/ MOST ground based support group* (Sterken 2001) are assessing these problems. See also Pijpers (2003) for a discussion of the fundamental parameters of the RØMER/MONS targets.

In this chapter I will describe my work on constraining the fundamental parameters of the proposed COROT targets from detailed abundance analysis.

## 5.2 The Need for Automated Analysis Software

Since *the first COROT/ MONS/ MOST ground-based support workshop* was held in Ghent (Sterken 2001) I have been involved in the study of the proposed COROT and RØMER/-MONS main targets. I have analysed the spectra of the COROT main targets and will also analyse the RØMER/MONS targets. The spectra of the COROT targets were obtained with the ELODIE instrument (Baranne et al. 1996) while the spectra of (some of) the RØMER/MONS targets have been obtained with the FEROS instrument

[2]A suitable example is the study of HD 209458 which is the parent star of a giant gas planet and which was the first star to show a transit light curve (Charbonneau et al. 2000). Mazeh et al. (2000) have used KECK high resolution spectra (R=70 000, S/N = 300) and they found the parameters $T_{\rm eff} = 6000 \pm 50$ K, $\log g = 4.25 \pm 0.2$, and [Fe/H]=$0.00 \pm 0.02$ ($v \sin i = 4.1 \pm 0.6$ km s$^{-1}$). Although the KECK spectra are of higher quality than the data I have used it still gives an idea of the accuracy that can be achieved.

(Stahl et al. 1999). Both these spectrographs have a resolution of about $R = 45\,000$ and the typical $S/N$ for the spectra is 150–250 (both values refer to a region around 6 000 Å).

Early on, I recognized that the abundance analysis of such a relatively large number of stars would need some degree of automization. The analysis of stars with low $v \sin i$ can be done fairly easily by measuring equivalent widths of isolated lines, hence ignoring the blending of lines. But a significant fraction of the proposed target stars for RØMER/MONS and COROT have $v \sin i$ in the range 40-200 km s$^{-1}$. Thus, in order to make the abundance analysis one must rely on the calculation of a synthetic spectrum to take moderate blends of (mostly weaker) lines into account. My experience is that this can be done manually for a small number of stars, and would take a day or two for each star once one is acquainted with the available software. But in order to estimate the sensitivity of the abundance results to the model parameters, and *to constrain* the model parameters as precisely as possible, one must repeat the analysis for a grid of models with different parameters, *i.e.* $T_{\rm eff}$, $\log g$, and microturbulence. Needless to say, this work is extremely time-consuming when manually fitting the spectral lines.

I have spent eight months at the *Institut für Astronomie, Universität Wien* in Austria with Werner W. Weiss as my external supervisor. It was here that I started the development of the IDL software package VWA which I have used for the abundance analysis of several stars.

The name VWA is an abbreviation for the three tasks the software was originally designed carry out: (1) $\underline{v}$ $\sin i$ determination (projected rotational velocity), (2) <u>w</u>avelength shift determination (*i.e.* radial velocity), and (3) <u>a</u>utomatic abundance analysis. At the present time only the main task has been developed, *i.e.* the automatic abundance analysis. In this chapter I will describe the analysis and results for the COROT main targets when using the VWA software.

At this point I will take the opportunity to briefly mention the publications where I have used VWA:

- One of the COROT targets is the newly discovered $\gamma$ Dor star HD 49434. The analysis of this star gave me the ideas for the VWA software and it was published in Bruntt et al. (2002) (reproduced on page 133). The star has high $v \sin i = 84 \pm 4$ km s$^{-1}$ and hence "manual" computation of the synthetic spectrum for several lines is a tedious task when being done for a grid of different atmospheric parameters. Due to the high $v \sin i$ I could not constrain $T_{\rm eff}$ and $\log g$ for this star with better accuracy than what is found from the calibration of Strömgren indices.

- The $\delta$ Scuti stars in the open cluster NGC 6134 (Rasmussen et al. 2002). For my master's thesis I obtained Strömgren photometry to determine the fundamental parameters of the $\delta$ Scuti stars in NGC 6134, some of which are multi-mode pulsators and potential targets for asteroseismic studies (Frandsen et al. 1996). This was published in the paper Bruntt et al. (1999). For the master's thesis project by Rasmussen (2001) spectra were obtained with the DFOSC on the Danish 1.54 m telescope, La Silla with $R = 4\,300$ to determine the $v \sin i$ of the $\delta$ Scuti stars. I analysed these data with VWA despite the low resolution, S/N $\simeq 75 - 150$, and the fact that some of the $\delta$ Scuti stars have moderately high $v \sin i$. Still, I was able to confirm the high metallicity found from the Strömgren photometry (Bruntt et al. 1999). This work has been published by Rasmussen et al. (2002). The results are also summarized in the IAU 210 proceedings and my contribution is reproduced on page 147.

- The giant star $\xi$ Hya: solar-like oscillations have been observed in this star (Frandsen et al. 2002). I used a combination of the best spectra used for the spectroscopic study of the oscillations (CORALIE spectra, $R = 50\,000$) to make the abundance analysis. The results can be found in the Uppsala IAU 210 proceedings (Bruntt & Frandsen (2003); reproduced on page 147) and in Teixeira et al. (2003).

- The two "standard" A-type stars HD 32115 and HD 37594. In collaboration with Ilfan Bikmaev[3] and Tanya Ryabchikova[4] I analysed these stars which both have low $v \sin i$. We made a careful comparison of the VWA technique and the "classical" method of using equivalent width measurements of non-blended lines. We found that our two approaches produced the same results to within the uncertainty of the abundance determination (0.05 dex) of each individual element. I note that these two A-type stars are important as reference comparison stars in the abundance studies of peculiar A-type stars. These results were published by Bikmaev et al. (2002).

## 5.3 Semi–automatic Abundance Analysis Software: VWA

In the following I will give a detailed description of how VWA[5] works:

- A brief discussion of the atmospheric models I have used.
- I will explain how the least blended atomic lines are selected by VWA.
- I will show how VWA iteratively adjusts the input abundance for the computation of the synthetic spectrum in a wavelength region around each selected line.

In section 5.4 I will give examples of how VWA can be used, and in particular discuss how the correlation of derived abundances with atomic line parameters can be used to constrain the fundamental atmospheric parameters.

I note that the following sections are edited and expanded versions of the descriptions given in Bruntt et al. (2002) and Bruntt et al. (2003a). Here I provide a more detailed description, including illustrations of how the software works – which was not possible to include in the original papers.

[3] Department of Astronomy, Kazan State University, Russia

[4] Institute of Astronomy, Russian Academy of Sciences, Moscow, Russia

[5] The abbreviation VWA is explained in section 5.2 on page 103.

### How Abundance Analysis Works

To determine the overall photospheric abundances in a star, one must have a model that describes the physical conditions in a thin upper envelope of the star, *i.e.* how temperature, gravity, electron density, *etc.* change when going from the deeper to the outer layers of the stellar atmosphere (for an introductory text consult Gray (1992)). I have used a modified version of the ATLAS9 1D LTE[6] models (Kurucz 1993) as described by Kupka (1996). In this version of ATLAS9 the turbulent convection theory in the formulation of Canuto & Mazzitelli (1991, 1992) is implemented. The applied convection theory is particularly important for the stars of spectral class G and later ($T_{\rm eff} < 6000$ K). To synthesize a stellar spectrum one also needs a list of spectral lines with accurate atomic data for each line, namely oscillator strengths and damping constants. These atomic parameters are extracted from VALD (Kupka et al. 1999) which is one of the most complete data bases of atomic data available. An example of the data extracted from VALD is given in Table 5.1 and the synthetic spectrum is given in Figure 5.1 for the COROT target star HD 55057 ($T_{\rm eff} = 7270$ K, $\log g = 3.6$; see further discussion below).

Abundance analysis consists of changing the input abundance of a given element until the computed spectrum in a wavelength region around the selected line matches the observed stellar spectrum. To check the correctness of the atmosphere parameters one must calculate correlations between the abundances from

**Table 5.1** Information extracted from VALD for lines forming the spectrum in Figure 5.1 for the COROT target star HD 55057.

| Element | W.L.(Å) | $E_{\rm low}$ | $\xi_t$ | $\log gf$ | Radiat. Damp. | Stark | van der Waals | Landé Factor | Central Depth |
|---|---|---|---|---|---|---|---|---|---|
| Ni I | 6223.9810 | 4.1050 | 2.0 | −0.910 | 8.322 | −5.233 | −7.224 | 0.840 | 0.094 |
| V II | 6226.3040 | 2.5560 | 2.0 | −2.554 | 8.398 | −6.615 | −7.953 | 1.160 | 0.010 |
| Cr II | 6226.6380 | 4.7560 | 2.0 | −2.981 | 8.410 | −6.649 | −7.926 | 1.500 | 0.015 |
| Fe I | 6226.7363 | 3.8830 | 2.0 | −2.220 | 7.734 | −5.353 | −7.208 | 1.350 | 0.075 |
| Fe I | 6229.2283 | 2.8450 | 2.0 | −2.805 | 8.161 | −6.095 | −7.592 | 0.990 | 0.119 |
| Fe II | 6229.3490 | 2.8280 | 2.0 | −4.824 | 8.462 | −6.687 | −7.946 | 0.660 | 0.117 |
| Ni I | 6230.0900 | 4.1050 | 2.0 | −1.260 | 8.321 | −5.788 | −7.226 | 0.960 | 0.047 |
| Fe I | 6230.7230 | 2.5590 | 2.0 | −1.281 | 8.009 | −6.320 | −7.597 | 1.240 | 0.609 |
| V I | 6230.7980 | 0.2670 | 2.0 | −1.340 | 6.468 | −6.262 | −7.742 | 1.360 | 0.015 |
| Ti II | 6231.2990 | 1.8920 | 2.0 | −3.881 | 8.441 | −6.545 | −7.908 | 1.220 | 0.013 |
| Fe I | 6232.6412 | 3.6540 | 2.0 | −1.223 | 7.906 | −5.467 | −7.622 | 1.990 | 0.450 |
| Fe II | 6233.5340 | 5.4840 | 2.0 | −2.939 | 8.476 | −6.601 | −7.914 | 1.130 | 0.085 |
| Ti II | 6234.4820 | 1.8930 | 2.0 | −3.150 | 8.441 | −6.542 | −7.908 | 2.110 | 0.057 |
| Si I | 6237.3190 | 5.6140 | 2.0 | −0.530 | 0.000 | +0.000 | +0.000 | 99.000 | 0.470 |
| Fe II | 6237.6550 | 5.5710 | 2.0 | −3.640 | 8.603 | −6.667 | −7.944 | 1.110 | 0.015 |
| Si I | 6238.2860 | 5.0820 | 2.0 | −2.340 | 0.000 | +0.000 | +0.000 | 99.000 | 0.066 |
| Fe II | 6238.3920 | 3.8890 | 2.0 | −2.630 | 8.529 | −6.590 | −7.945 | 1.460 | 0.556 |
| Fe II | 6239.3660 | 2.8070 | 2.0 | −4.538 | 8.464 | −6.686 | −7.946 | 0.820 | 0.207 |
| Cr II | 6239.7740 | 4.7610 | 2.0 | −2.991 | 8.410 | −6.649 | −7.926 | 0.000 | 0.016 |
| Fe II | 6239.9530 | 3.8890 | 2.0 | −3.680 | 8.529 | −6.590 | −7.945 | 2.150 | 0.210 |
| Fe I | 6240.3120 | 4.1430 | 2.0 | −1.661 | 7.866 | −5.961 | −7.833 | 1.460 | 0.154 |
| Fe I | 6240.6462 | 2.2230 | 2.0 | −3.233 | 7.196 | −6.258 | −7.661 | 0.990 | 0.134 |

[6] Local Thermal Equilibrium, see *e.g.* Chapter 9 in Gray (1992).

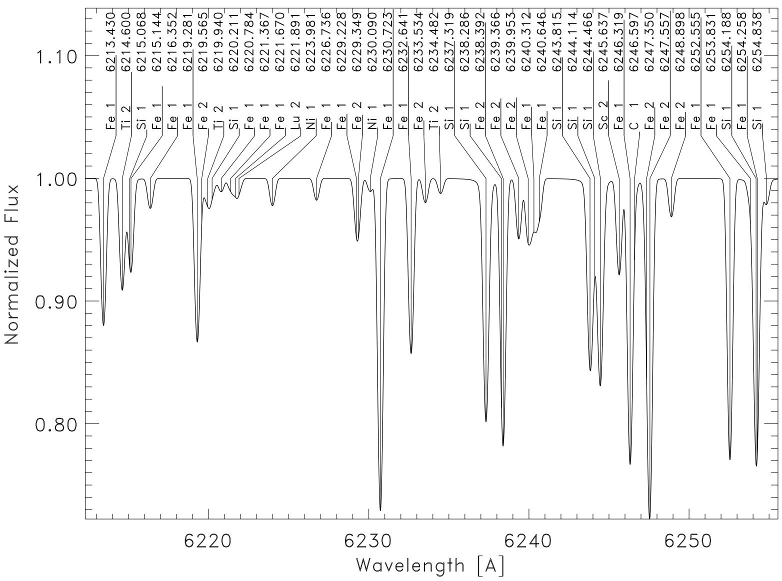


**Figure 5.1** Synthetic spectrum from the program SYNTH (Valenti & Piskunov 1996) for the COROT target star HD 55057. Each atomic line contributing to the spectrum are marked and the central wavelength and the element forming the line is given. The length of the vertical line under the element name scales with the depth of the line, *e.g.* the deepest Fe line is at $\lambda$6230.7 Å. The complete atomic line information is given in Table 5.1.

the individual lines and the specific line characteristics, *e.g.* excitation energy of the lower level: a temperature indicator – or the observed line's equivalent width: an indicator of the microturbulent velocity. An absence of these two correlations means that the effective temperature of the star and microturbulent velocity are chosen correctly (provided the LTE approximation is valid). Another criterion is ionization balance, *i.e.* that lines from different ionization stages yield the same abundance. This is used to establish the correct surface gravity, but one has to remember that ionization balance depends on the effective temperature, too. By computing abundances for a grid of models one can find the best model and determine how accurately $T_{\rm eff}$, $\log g$, microturbulence, and the abundances of each element have been determined (*cf.* section 5.4.3).

### Fundamental Atmospheric Parameters

To calculate the atmospheric model one needs to know the basic parameters of the star, *i.e.* $T_{\rm eff}, \log g$, and [Fe/H]. These parameters may be estimated from the Strömgren indices of the star by using the program TEMPLOGG (Rogers 1995) which will choose the most appropriate among several published photometric calibrations. To determine the basic atmospheric parameters of the star TEMPLOGG interpolates the de-reddened photometric indices in the atmospheric ATLAS6 model grid by Kurucz (1979) with the improvements suggested by Napiwotzki et al. (1993). I note that TEMPLOGG does not use the bare results from the ATLAS6 grids but rather an experimental calibration, *i.e.* the colour grids are transformed so as to match well-calibrated fundamental stars before the calibration is made.

### Selecting Atomic Lines for Abundance Analysis

For the abundance determination I make use of a complete list of atomic line data for the entire observed spectral range. The line list is extracted from the VALD database (Kupka et al. 1999; Ryabchikova et al. 1999) where all lines deeper than 1% of the continuum are included (this depends on the model atmosphere). From the line list the least blended lines will be selected by VWA. There are typically 10–15 thousand lines to choose from in the range 4 500–6 800 Å, and typically 400–600 lines will be used for the abundance analysis (for slowly rotating stars).

The selection consists of two steps which are described in the following:

- The initial selection is based on the analysis of the degree of blending based on the information in the atomic line list from the VALD database.
- These lines are then analysed in the *observed* spectrum and any "suspicious" lines are *rejected*.

### Selecting Lines: The Atomic Line List

The first step is to select the lines most appropriate for abundance analysis. For slowly rotating stars the idea is to select lines which suffer from no or very little blending due to contributions from the neighbouring lines. For stars with moderate or high $v \sin i$ the automatic selection becomes a matter of choosing the lines *least* affected by blending.

The content of Table 5.1 is an example of the information extracted from the VALD database for the COROT target star HD 55057 ($T_{\rm eff}$ = 7270 K, $\log g$ = 3.6): element name, ion state, wavelength, lower excitation potential, adopted microturbulence, $\log gf$, as well as line broadening parameters and the central line depth relative to the continuum level. Damping parameters with values of "0.000" or "99.000" indicate that the corresponding data is not available.

The calculated spectrum for HD 55057 is shown in Figure 5.1 for a region including the lines in Table 5.1. The deep Fe and Si lines are easily recognized. The effect of the rotation of the star is to broaden the line profiles due to the Doppler effect. For example, the COROT target star HD 55057 has $v \sin i$ = 120 km s$^{-1}$ and hence line blending is a serious problem.

The principle of selecting lines automatically can be seen in Figure 5.2 for two lines: Ba II and Ti II. The ordinate measures the line depths (increasing upwards) while the abscissa is the wavelength relative to the central wavelength for the line being examined. The cross at 0.0 Å marks the central line, while the other points mark the central line depth and relative wavelength position of all neighbouring lines. In the *top* panels I plot the raw central line depths from VALD while in the *bottom* plot the line depths have been convolved by a Gaussian with a FWHM of 4 Å (the over-plotted dot–dashed curve). The convolution is made in order to suppress lines which lie far from the central line and consequently affect the central line much less.

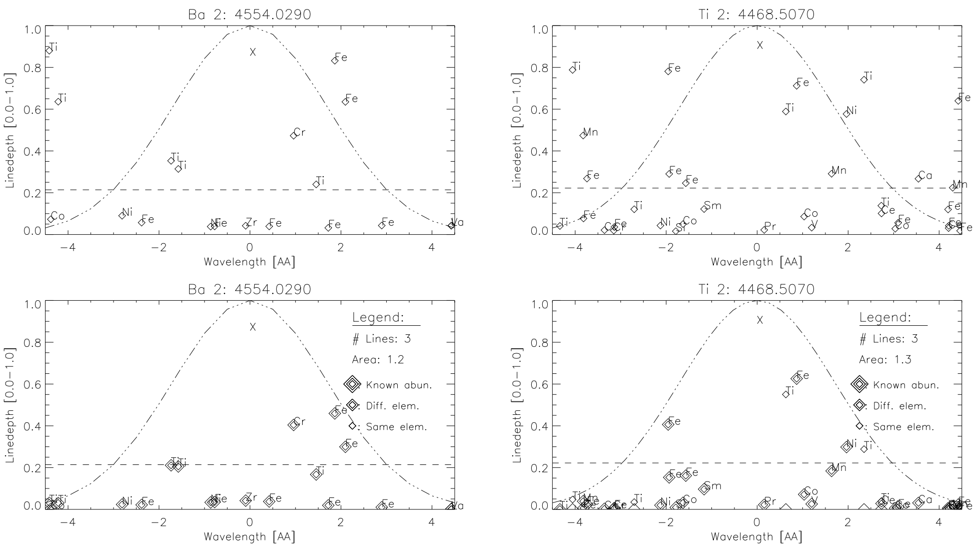


**Figure 5.2** The plots illustrate how the "blending parameters" are determined from the central line depths given in the atomic line list from VALD. The *top* plots show the line depths of lines around a Ba and a Ti line located at 0.0 Å in relative wavelength given on the abscissa. In the *bottom* plots the line depths have been convolved by a Gaussian (dot-dashed line), thus *suppressing* the lines which are likely to affect the central line the least. The dashed horizontal lines are placed at 25% of the depth of the central line. The VWA program counts the number of lines above the dashed line, *i.e.* the "deep" neighbouring lines. The total number of deep lines and the total sum of their central line depths (these "blending parameters" are written on the *bottom* plots) are used to determine if the central line is contaminated or not: the limits for these and also the FWHM of the Gaussian must be supplied by the user.

The VWA software then computes three "blending parameters":

- (1) The *depth ratio* of the central line to the deepest neighbouring line (but *not* convolved by the Gaussian).
- (2) The *number of "deep" neighbouring lines*, *i.e.* lines with a depth of at least 25% of the central line.
- (3) The *sum of the central line depths* of the "deep" lines.

These parameters are used to describe the degree of blending of the central line. For a line to be selected the *depth ratio* must be greater than 1 but the limit can be specified by the user. Thus, only the deepest line in a given wavelength interval (the width is supplied by the user) is chosen. The second and third blending parameters are measures of the blending of the central line by the neighbouring lines, where lines that are close to the central line are given higher weight.

For the two examples in Figure 5.2 the "deep" lines are the points above the dashed horizontal lines in the *bottom* plots. The numbers corresponding to points (2) and (3) are written on the *bottom* plots as "# Lines" and "Area".

The lines that will be selected from the VALD line lists depend on the choosen FWHM of the Gaussian used for the convolution and the three limits for the "blending parameters": (1), (2), and (3). Generally, the FWHM of the Gaussian must increase with $v \sin i$ of the star, *e.g.* a Gaussian with a FWHM of two times the FWHM of lines around 6 000 Å is a good starting guess. It is difficult to recommended values for the blending parameters since they also depend on $v \sin i$, but values in the range 1.5–4.0, 0–4, and 0.1–0.7 for points (1–3) are useful for stars with $v \sin i < 40\,\mathrm{km\,s^{-1}}$.

### Rejecting Lines: the Observed Spectrum

When the lines have been selected from the list of atomic lines, VWA will analyse the *observed* spectrum in the region around each selected line. The aim is to automatically reject lines that are not suitable for abundance analysis. This is done by fitting a Voigt profile to the observed spectrum. While stars with high $v \sin i$ certainly do not have Voigt profiles this way of detecting truly bad data seems to work.

The following "selection parameters" must be specified by the user, and will determine if a given atomic line will be used. This will depend on the parameters of the fitted Voigt profile.

- The minimum depth of the fitted profile.
- The maximum and minimum FWHM of the fitted profile.
- The maximum value of $\chi^2$ for the fitted profile.
- The maximum flux asymmetry between the wings of the *observed* line.

Optionally, the user is provided with a plot of the observed spectrum in a region around each of the selected and rejected lines. The user may then interactively choose (with a click on the mouse) if a rejected (accepted) line should be included (or rejected) in the abundance analysis. In practice the VWA_INTERACT program creates two files with the wavelengths of lines that will be rejected / accepted in the final selection of lines to be used for abundance analysis, *i.e.* these line lists *over-rule* the automatic selection. The line lists may also be edited manually if, for example, the user already knows which lines he wants to use for the abundance analysis, *e.g.* only Fe I and Fe II lines (added in accepted line list) – or if the user knows that the atomic parameters of certain lines are known to be uncertain, *e.g.* lines with bad experimental $\log gf$ values or lines near the edge of an Echelle order (put them in the rejected line list).

### Two Methods for Abundance Determination

The abundance determination is made for each of the selected lines. It can be done by either of two methods: (1) By the measurement of equivalent widths of lines in the observed spectrum which are then given as input to the WIDTH9 code by Kurucz (1993). (2) By the adjustment of the abundance of the element responsible for the central line of the blend until the computed and observed spectrum around each line match, *i.e.* they have the same equivalent width. For the computation of

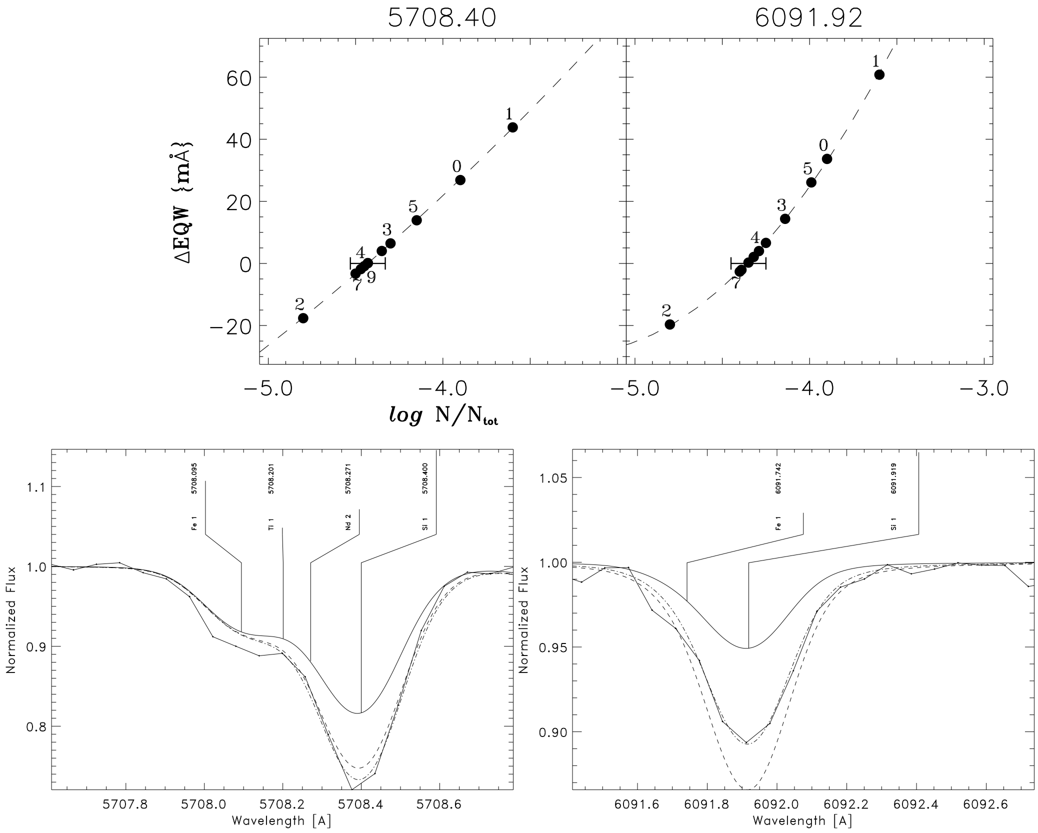


**Figure 5.3** Examples of two Si I lines fitted with VWA. In the *top* plot I show the difference in equivalent width (EQW) versus the input abundance. In the *bottom* panel I show the observed spectrum along with three different synthetic spectra corresponding to different input abundances (the observed spectrum is recognized as being more "noisy" than the smooth curves of the synthetic spectra).

the synthetic spectrum I used the program SYNTH kindly provided by N. Piskunov (version 2.5, Valenti & Piskunov (1996)).

The first method can only be used for stars where blending is not a problem, *i.e.* slowly rotating stars ($v \sin i < 15$ km s$^{-1}$). The second method is much slower but it is the only option for moderate or fast rotators ($v \sin i > 30$ km s$^{-1}$).

In Figure 5.3 I show an example of how two Si lines are fitted by VWA. The *top* plots show the difference in equivalent width between the synthetic and observed spectrum. The *bottom* plots show the observed spectrum and some of the computed synthetic spectra for different input abundances of Si. For the line at $\lambda 5708.4$ Å (*left* plot) there is a mild blend with an Fe line which is also included in the synthetic spectrum (it can be seen that the Fe abundance should be increased slightly).

In Figure 5.4 I show examples of four different lines fitted with VWA for two different COROT target stars: the four *top* panels are for HD 43318 ($T_{\rm eff}$ = 6400 K, $\log g = 4.20$, $v \sin i = 8$ km s$^{-1}$) and the *bottom* four panels are for HD 184663 ($T_{\rm eff}$ = 6600 K, $\log g = 4.25$, $v \sin i = 53$ km s$^{-1}$). Figure 5.4 emphasizes the advantages of VWA. (1) One can easily identify problems with the continuum level, *i.e.* the

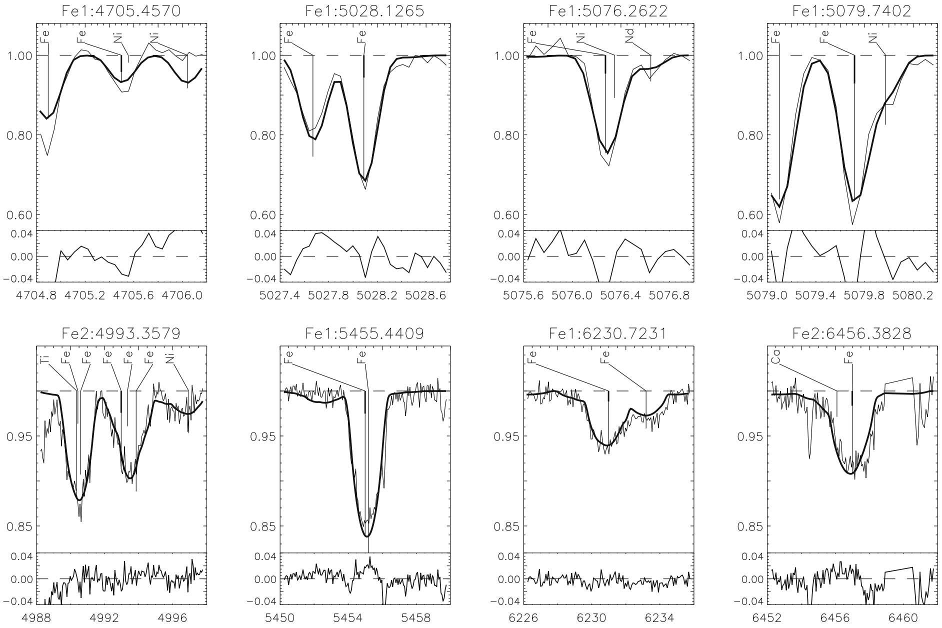


**Figure 5.4** Four different lines fitted with VWA for the COROT targets HD 43318 (*top*) and HD 184663 (*bottom*). The thin line is the observed spectrum while the thick line is the synthetic spectrum. The deepest atomic lines forming the spectrum are labelled and the lengths of the tick marks scale linearly with the line depth. The spectra of the two stars have very different line widths due to the difference in $v \sin i = 8$ and 63 km s$^{-1}$.

continuum level is too low at $\lambda$4705.5Å and $\lambda$5076.3 Å for HD 43318, and there are data points missing at the right wing of the line at $\lambda$6456.4 Å in HD 184663. (2) One can use blended lines to determine abundances, *i.e.* $\lambda$5079.7Å in HD 43318 and all four lines in HD 184663.

## 5.4 Examples of Using VWA

In the following sections I will discuss various results obtained by using VWA with the emphasis of the various problems that can be solved.

### 5.4.1 Comparison of VWA with other Methods

In Bruntt et al. (2003a) I have compared the abundance results found with VWA with a more conventional abundance analysis method (from this point called "classical"). In the "classical" method unblended lines are usually chosen manually and their equivalent widths are measured and adjusted by some other routines (for example, using a Gaussian approximation). After that the very fast WIDTH9 code is applied (Kurucz 1993). This must be compared to VWA which computes the synthetic spectrum which is more demanding in terms of computer power. In Figure 5.5 I show the difference in the derived abundances in the sense "VWA *minus* classical" for four F and G–type subdwarfs which are COROT targets (further details can be found in Bruntt et al. (2003a)). For most elements the agreement

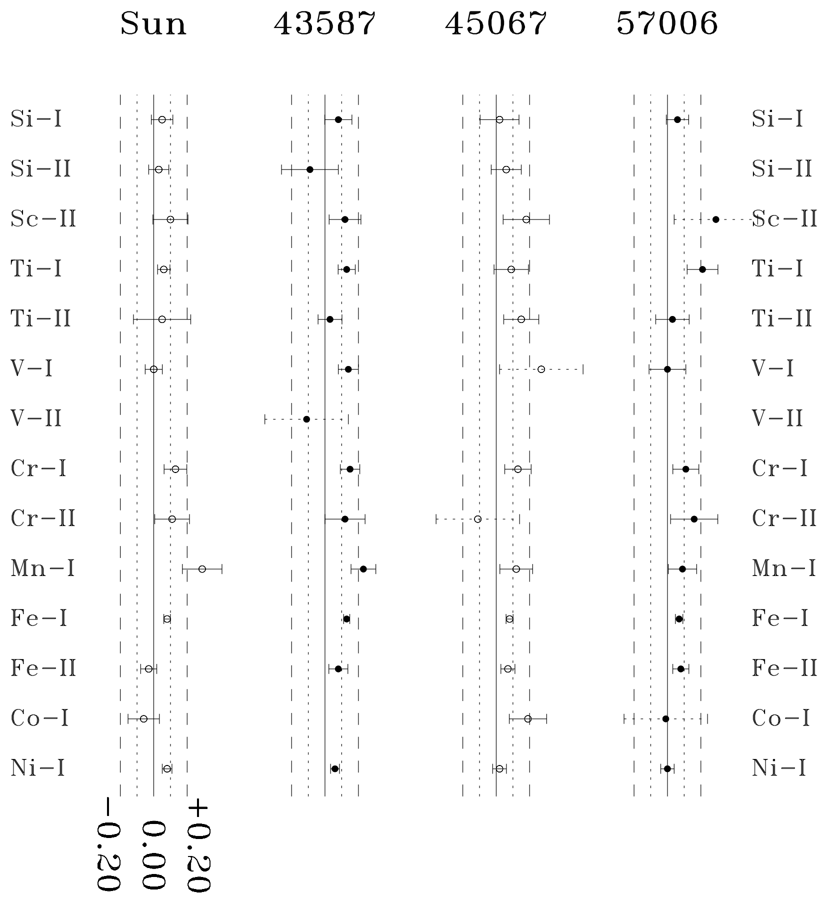


**Figure 5.5** A comparison of the abundances found by VWA and the "classical" equivalent width method. I show the results for several elements for the Sun and three COROT target stars (Bruntt et al. 2003a). The spectral types are F and G and their HD number is given in the *top*. The points indicate the difference in abundance found by the two methods – in the sense "VWA" *minus* "classical".

is within the error estimates. The exception is for Mn, where hyperfine structure is not taken into account with VWA since this data is not available in the VALD database. It should be noted that in addition to the measured internal errors (plotted in Figure 5.5), systematic errors of the order 0.05 dex may be present, *e.g.* due to problems with the atmospheric models or the assumtion of LTE.

In the paper by Bikmaev et al. (2002) we also compared VWA and the classical method for two A–type stars and found an excellent agreement.

### 5.4.2 Identifying Erroneous Line Data

Several problems can result in erroneous abundances derived from the observed spectra. For example, if the continuum level is wrong, if the sensitivity of the spectrograph is not adequately calibrated (*e.g.* scattered light), if a line is blended with unidentified lines, or if the atomic line data is erroneous. Furthermore, non–LTE effects (Local Thermal Equilibrium is assumed in ATLAS9) and the difference of the real turbulent velocity field from the parameterized description of turbulence by the microturbulent velocity may result in systematic errors of the abundances.

It is far beyond the scope of this chapter to access all these fundamental problems. However, I will note an "empirical" way of identifying lines which may be seriously affected by systematic effects. The elements for which the abundance is determined from several lines, significant outliers can easily be identified. If the abundance determined from a given spectral line is found to be an outlier in different stars, one can identify it as probably having erroneous atomic line data.

For example, the oscillator strengths ($\log gf$) from VALD for Si I lines can be wrong by several tenths of dex which results in systematic errors for most stars. I have been involved in the study of the two standard A–type stars (Bikmaev et al. 2002) in which we identified several Si lines with erroneous $\log gf$ values. We then located the same lines in the solar spectrum in which case the Si abundance is well known. In many cases we could then adjust the $\log gf$ value of the erroneous lines to make the lines fit the Solar spectrum.

Thus, one is effectively using the observed stellar spectrum as an atomic physics laboratory.

### 5.4.3 Constraining Model Parameters

I have carried out the abundance analysis of nine proposed main targets for the COROT asteroseismology space mission (Bruntt et al. 2003a). The aim is to characterize the target stars, *i.e.* to constrain the atmospheric parameters. This has been done by a detailed abundance analysis in which the correlations of individual line abundances with different line parameters are minimized. As pointed out in section 5.1 the COROT mission will only observe a small sample of stars and from a certain point of view the mission should concentrate on relatively "simple" stars, *i.e.* slowly rotating stars with a "normal" abundance distribution.

To determine the fundametal parameters of the "base" model I used the Strömgren indices from the catalogue of Hauck & Mermilliod (1998). I used the program TEMPLOGG (Rogers 1995) which selects the appropriate calibration to obtain $T_{\rm eff}$, $\log g$, and $[{\rm M/H}]_{\rm phot}$. In order to measure the sensitivity of the derived abundances on the model parameters I have done the abundance analysis for a grid of models for each star, *i.e.* I have determined abundances for models with somewhat lower and higher $T_{\rm eff}$ and $\log g$.

For each model I adjust the microturbulence to minimize the dependence of the individual abundances of Fe I lines on the measured equivalent widths. I have also calculated results for the base model but with somewhat higher microturbulence than the best fit in order to measure the sensitivity to this parameter.

The model parameters of four COROT stars are plotted in Figure 5.6.

Changes in the model temperature will affect the depth of Fe I lines while changes in $\log g$ will mostly affect the Fe II lines. Furthermore, changes in $T_{\rm eff}$ and $\log g$ produces changes in the slope when plotting the derived Fe I abundance *vs.* the lower excitation potential $E_{\rm low}$ of each line. This can be used to constrain

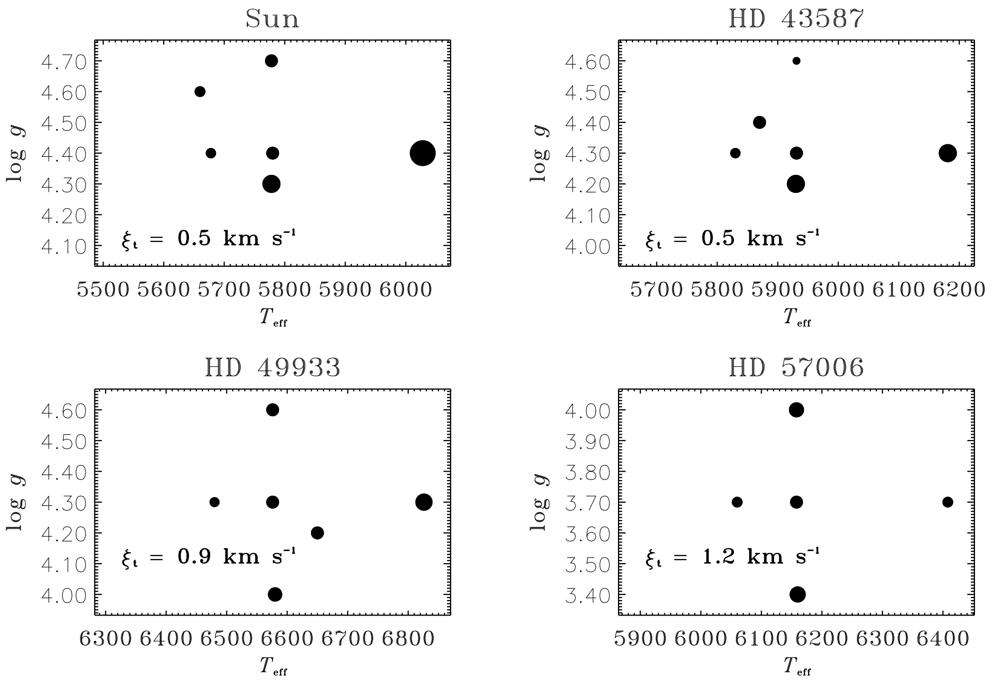


**Figure 5.6** The plots show a grid of atmosphere model parameters for four stars: $\log g$, $T_{\rm eff}$, and microturbulence ($\xi_t$). The symbol size is scaled with the microturbulence of the base model (in the centre of each plot) the value of which is given in the bottom left corner.

$T_{\rm eff}$ and $\log g$ for the slow rotators with $v \sin i < 50 - 60$ km s$^{-1}$. For fast rotators there are few non-blended lines and it is more difficult to constrain the fundamental parameters.

In Figure 5.7 I show the abundances of Fe found from about 160 Fe I lines (black • symbols) and 12 Fe II lines (grey • symbols) for the star HD 43587. In the *left* plot the abundances are plotted *vs.* equivalent width for two models. For the *top* plot I have used the $T_{\rm eff}$ found from the photometic indices, and in the *bottom* plot $T_{\rm eff}$ is increased by 250 K. In the *right* plots in Figure 5.7 I plot the abundances of the same lines *vs.* the lower excitation potential. The dashed lines mark the mean abundance found from the Fe I lines. It can be seen that the Fe I / Fe II balance is not perfect for either model, but worse for the model with high $T_{\rm eff}$. There is also a negative slope in the Fe I *vs.* $E_{\rm low}$ for the hot model (lower *right* plot): the solid line is a linear fit. From these results I estimate that $T_{\rm eff}$ is correct to within 100–150 K (see further discussion below).

The significance of the correlation with $E_{\rm low}$ is measured by the slope of a linear fit to the Fe I abundance versus $E_{\rm low}$. If the slope of the fit is $s$ and the corresponding standard deviation is $\sigma(s)$ then the "significance" of the slope is measured by the "correlation parameter" $S_{\rm low} = s/\sigma(s)$. This factor will be numerically small if there is no correlation or, alternatively, if the data is too uncertain to measure any correlation. In a similar manner I calculate the significance of the correlation of Fe I lines and equivalent width, which I denote $S_{\rm eqw}$.

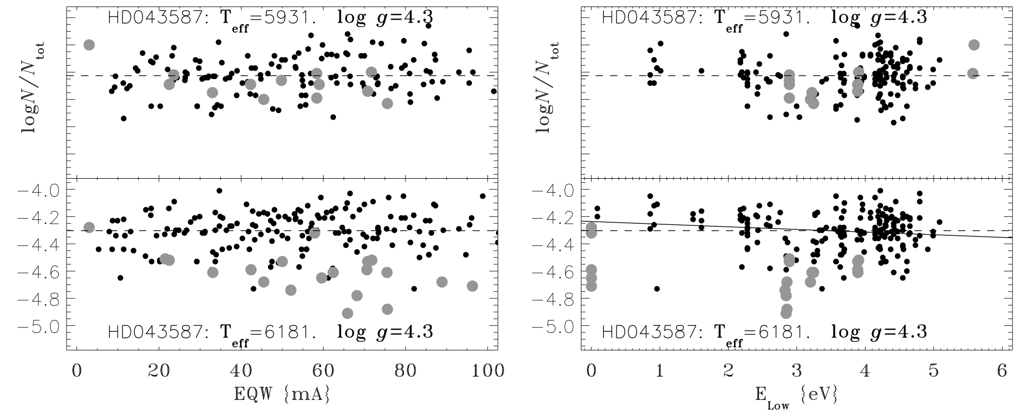


**Figure 5.7** The *left* plot shows the Fe abundance *vs.* equivalent width for two model atmospheres with different temperature for the star HD 43587. The black symbols are for Fe I lines while the grey points are Fe II lines. The *right* plot are the same lines for the two models, but here the abundance is plotted *vs.* the lower excitation potential.

I have measured the difference in the Fe abundance found from Fe I and Fe II lines: $\Delta A_{\mathrm{Fe}}$ is the difference $\Delta A_{\mathrm{Fe}} = \log N_{\mathrm{FeI}}/N_{\mathrm{tot}} - \log N_{\mathrm{FeII}}/N_{\mathrm{tot}}$ and the corresponding standard deviation is written $\sigma(\Delta A_{\mathrm{Fe}})$. Similarly, I define the correlation parameter for the "ion balance" $S_{\mathrm{Fe}} = \Delta A_{\mathrm{Fe}}/\sigma(\Delta A_{\mathrm{Fe}})$, where $\sigma(\Delta A_{\mathrm{Fe}})$ is the combined standard deviation of the mean for the Fe I and Fe II abundances (an additional systematic error of 0.05 dex is added quadratically). Analogously, correlation parameters are calculated for Cr and Ti which are also sensitive to changes in $T_{\mathrm{eff}}$ and $\log g$.

To constrain the parameters I measure how the correlation parameters $S_{\mathrm{low}}$, $S_{\mathrm{Fe}}$, $S_{\mathrm{Cr}}$, and $S_{\mathrm{Ti}}$ change when varying $T_{\mathrm{eff}}$ and $\log g$ of the model atmosphere.

The correlation parameters are plotted in Figure 5.8 for HD 43587 (*cf.* Figure 5.7). The results are shown for six different atmospheric models corresponding to the "grid" in the *top right* panel in Figure 5.6. The legend in Figure 5.8 explains the meaning of the symbols, *i.e.* • symbols are for $S_{\mathrm{eqw}}$, the star symbol is for $S_{\mathrm{low}}$, the triangle is for $S_{\mathrm{Cr}}$ *etc.* It can be seen that $S_{\mathrm{Fe}}$ (box symbol) is quite sensitive to changes in both $T_{\mathrm{eff}}$ and $\log g$ while changes in $S_{\mathrm{low}}$ can also be seen when changing the temperature.

Note that the negative correlation of Fe I lines with equivalent width ($S_{\mathrm{eqw}} = \bullet$ symbols) can normally be removed by using lower microturbulence. This is not the case for HD 43587 for the models with low $T_{\mathrm{eff}}$ and high $\log g$. Decreasing the microturbulence below 0.4 km s$^{-1}$ does not remove the (negative) correlation.

To estimate the fundamental parameters of a star one must determine which model parameters are needed to (a) minimize the correlation with the lower excitation potential and to (b) minimize the difference in abundance found from lines of the neutral and ionized species of Cr, Fe, and Ti (the "ion balance").

From Figure 5.8 I estimate $T_{\mathrm{eff}} = 6000 \pm 100$ K and $\log g = 4.4 \pm 0.2$ for HD 43587.

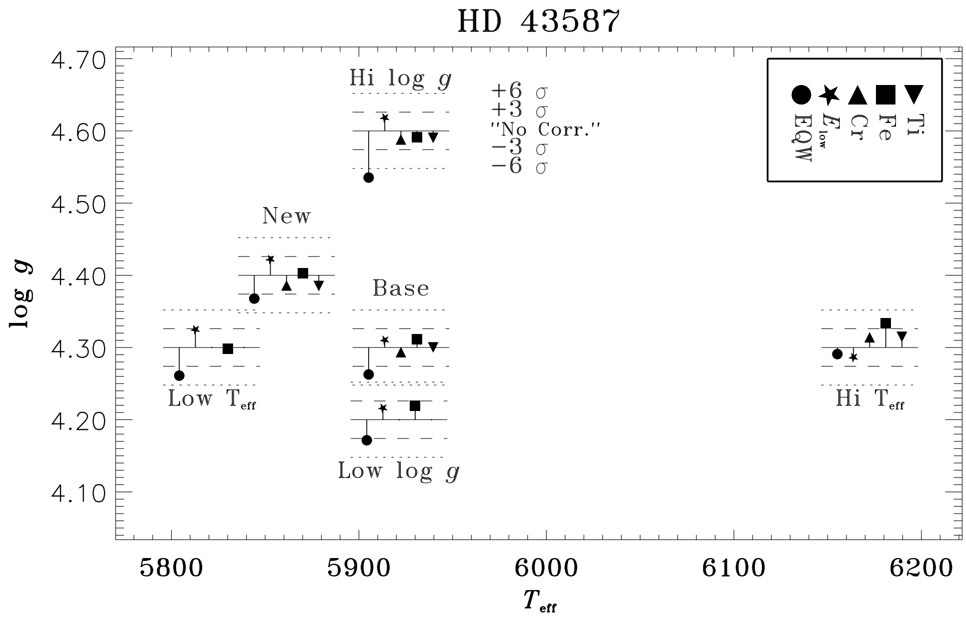


**Figure 5.8** Each of the six panels labelled "Low $T_{\text{eff}}$", "Base", "Hi $T_{\text{eff}}$" *etc.* corresponds to different atmospheric models for HD 43587. The $T_{\text{eff}}$ and $\log g$ is given by the position the panel. Within each panel five parameters (see legend) are plotted which measure how "good" the model is. The circle and star symbols measure the significance of the slope in a linear fit of the Fe I abundance *vs.* equivalent width (circles) and lower excitation potential (stars). The three remaining symbols are the significance of the ion-balance for Cr, Fe and Ti. For example, the box symbol is the significance of the difference in the abundance found from Fe I lines and Fe II lines.

In Table 5.2 I compare the results of various studies to determine the fundamental parameters of three COROT targets. The results I have found with VWA agree very well with all the previous studies. While $\log g$ cannot be constrained better than with the parallax from HIPPARCOS it gives an independent estimate. It is important to note that both $T_{\text{eff}}$ and the metallicity can be determined with higher precission than from Strömgren photometry.

## 5.5 Conclusions and Future Use of VWA

In this Chapter I have given a detailed description of how the semi-automatic software VWA works. I have given a few examples of how the software can be used with emphasis on how the fundamental atmospheric parameters of stars can be constrained. I have used this for the proposed targets for the COROT asteroseismology mission and the case of HD 43587 was discussed in detail. The detailed results of the abundance analysis will be published as Bruntt et al. (2003a) and the paper in preparation can be found on page 155. Furthermore, a paper describing VWA and the abundance analysis of the $\gamma$ Dor star HD 49434 can be found on page 133.

- I am now in the process of using VWA for the stars proposed as targets for the RØMER/MONS asteroseismology mission. As in the case of the COROT targets it is vital to obtain as much information about the target stars as possible before the missions are launched. Possibly some of the proposed targets must be excluded if their parameters are unsuitable for asteroseismology (see Pijpers (2003)).

- I have also begun the analysis of a sample of $\gamma$ Dor star stars. C. Aerts (Instituut voor Sterrenkunde in Leuven, Belgium) have studied the pulsation of these stars, and it is important to know the fundamental parameters with good accuracy before any detailed theoretical modelling can be carried out.

**Table 5.2** Results of this and previous studies to determine the fundamental parameters of three COROT targets and the Sun. The references are given at the bottom.

| HD | $T_{\rm eff}$ | $\log g$ | [Fe/H] | Ref. |
|---|---|---|---|---|
| 43587 | 6000(100) | 4.4(0.2) | +0.01(0.1) | *This Study* |
| - | 5931(200) | 4.31(0.2) | −0.11(0.2) | 1 |
| - | 5720(100) | 4.3(0.4) | −0.2(0.10) | 2a |
| - | 6000(250) | 4.5(0.5) | −0.1(0.20) | 2b |
| - | | | −0.03 | 3 |
| - | 5795 | | −0.03 | 4 |
| - | 5775 | | −0.08(0.04) | 5 |
| - | 5931(100) | | −0.03(0.05) | 6 |
| 49933 | 6650(120) | 4.18(0.16) | −0.40(0.01) | *This Study* |
| - | 6576(200) | 4.30(0.2) | −0.45(0.2) | 1 |
| - | 6600(150) | 4.3(0.25) | −0.6(0.15) | 2a |
| - | 6500(250) | 4.0(0.5) | −0.5(0.2) | 2b |
| - | 6472 | 4.17 | −0.35 | 7 |
| - | 6595 | 4.16 | −0.43 | 8 |
| - | 6545 | 4.00 | −0.35 | 9 |
| - | 6300 | 4.5 | −0.88 | 10 |
| 57006 | 6100(60) | 3.87(17) | −0.01(0.1) | *This Study* |
| - | 6158(200) | 3.72(0.2) | −0.13(0.2) | 1 |
| Sun | 5980(100) | 4.50(0.2) | ? | *This Study* |
| - | 5778 | 4.44 | 0.00 | - |

Ref. 1: TEMPLOGG: Rogers (1995)
Ref. 2a: Lastennet et al. (2001) (synthetic colours)
Ref. 2b: Lastennet et al. (2001) (spectroscopy)
Ref. 3: Zakhozhaj & Shaparenko (1996)
Ref. 4: Vogt et al. (2002)
Ref. 5: Favata et al. (1997)
Ref. 6: D. Fisher (*private communication*)
Ref. 7: Balachandran (1990)
Ref. 8: Edvardsson et al. (1993)
Ref. 9: Perrin (1976)
Ref. 10: Hartmann & Gehren (1988)

# Acknowledgements

Part of the data of the open cluster NGC 6791 was obtained using ALFOSC which is owned by the Instituto de Astrofisica de Andalucia (IAA) and operated at the Nordic Optical Telescope under agreement between IAA and the NBIfAFG of the Astronomical Observatory of Copenhagen.

The data of the M 4 campaign were obtained with the DFOSC instrument on the Danish 1.54 m telescope at the ESO La Silla Observatory, Chile, the Cerro Tololo Inter-American Observatory 1.5 m telescope, and the 40 inch telescope at Siding Springs Observatory.

This research has made use of the SIMBAD database, operated at CDS, Strasbourg, France.

I have used standard star fields from the Canadian Astronomy Data Center, which is operated by the Dominion Astrophysical Observatory for the National Resarch Council of Canada's Herzberg Institute of Astrophysics.

The first version of VWA was developed during my stay in Vienna with Werner Weiss as my external supervisor. Today I am still using the computer power in Vienna and I have direct access to the VALD data base which is supported by projects S7303 and P14984 funded by the *Fonds zur Förderung der wissenschaftlichen - Forschung*.

I am grateful for the finacial support from "ESA følgeforskning".

# List of publications

## In Preparation

- **Bruntt** H., Bikmaev I. F., Catala C., et al., *Abundance analysis of targets for the* `COROT / MONS` *asteroseimology missions: II. Abundance analysis of the COROT main targets*, 2003a, A&A, in preparation: **the paper is reproduced on page 155**

- **Bruntt** H., Grundahl, F., Tingley, B., Frandsen S., et al. *A Search for Planets in the Old Open Cluster NGC 6791*, 2003b, A&A, in preparation

- Kjeldsen H., Bedding T. R., Baldry I. K, **Bruntt** H., Butler R. P., Fischer D. A., Frandsen S., Gates E. L., Grundahl F., Lang K., Marcy G. W., Misch A., Vogt S. S., *Confirmation of Solar-like Oscillations in Eta Bootis*, ApJ, 2003, submitted

## Accepted Publications

- Stetson, P. B., **Bruntt** H., Grundahl, F., *Homogeneous Photometry III. A Star Catalog of the Open Cluster NGC 6791*, 2003, PASP, accepted

- **Bruntt**, H., Frandsen, S., *A Semi-automatic Method for Abundance Analysis: Two Case Studies: The Giant Star $\xi$ Hydrae and the $\delta$ Scuti stars in NGC 6134*, 2003, Proc. of Modelling of Stellar Atmospheres, IAU symp. 210, ed. N. E. Piskunov, W. W. Weiss, D. F. Gray: **the paper is reproduced on page 147**

- Teixeira, T. C., Christensen-Dalsgaard, J., Carrier, F., Aerts, C., Frandsen, S., Stello, D., Maas, T. Burnet, M., **Bruntt**, H., de Medeiros, J. R., Bouchy, F., Kjeldsen, H., Pijpers, F. *Giant vibrations in dip*, 2003, in "Asteroseismology across the HR diagram", M. J. Thompson, M. S. Cunha, M. J. P. F. G. Monteiro eds., Kluwer Academic Publishers

- **Bruntt**, H., Catala, C., Garrido, R. et al., *Abundance analysis of targets for the* `COROT / MONS` *asteroseimology missions: I. Semi-automatic abundance analysis of the $\gamma$ Dor star HD 49434*, 2002, A&A, 389, 345: **the paper is reproduced on page 133**

- Rasmussen, M. B., **Bruntt**, H., Frandsen, S., *Rotation of stars in NGC 6134: A comparison of $\delta$ Scuti stars and non-variable stars*, 2002, A&A, 390, 109

- Bikmaev, I. F., Ryabchikova, T., **Bruntt**, H., Musaev, F. A., Mashonkina, L., Belyakova, E. V., Shimansky, V., Barklem, P. S., *Abundance analysis of two late A-type stars HD 32115 and HD 37594*, 2002, A&A, 389, 537

- Frandsen, S., Carrier F., Aerts, C., Stello, D., Maas, T., Burnet, M., **Bruntt**, H., Teixeira, T. C., de Medeiros, J., Bouchy, F., Kjeldsen, H., Pijpers, F., Christensen-Dalsgaard, J., *Detection of Solar-like Oscillations in the G7 giant star $\xi$ Hya*, 2002, A&A, 394, L5

- Kjeldsen, H., Bedding, T. R., Baldry, I. K., Frandsen, S., **Bruntt**, H., Grundahl, F., Lang, K., Butler, R. P., Fischer, D. A., Marcy, G. W., Misch, A., Vogt, S. S. *Confirmation of Solar-Like Oscillations in $\eta$ Bootis*, 2002, ASP Conf. Series, 259, p. 470, IAU Colloq. 185, ed. C. Aerts, T. R. Bedding, J. Christensen-Dalsgaard
- Kupka, F., **Bruntt**, H., *Using* TEMPLOGG *to determine stellar parameters of MONS target stars*, 2001, Proc. of First COROT/MONS/MOST Ground-based Support Workshop, p. 39, ed. Sterken C., University of Brussels
- **Bruntt** H., Frandsen, S., Gilliland, R. L., Christensen-Dalsgaard, J., Petersen, J. O., Guhathakurta, P., Edmonds, P. D., Bono, G., *SX Phœnicis stars in the core of 47 Tucanae*, 2001, A&A, 371, 614
- Gilliland, R. L. Brown, T. M., Guhathakurta, P., Sarajedini, A., Milone, E. F., Albrow, M. D., Baliber, N. R., **Bruntt**, H., Burrows, A., Charbonneau, D., Choi, P., Cochran, W. D., Edmonds, P. D., Frandsen, S., Howell, J. H., Lin, D. N. C., Marcy, G. W., Mayor, M., Naef, D., Sigurdsson, S., Stagg, C. R., Vandenberg, D. A., Vogt, S. S., Williams, M. D., *A Lack of Planets in 47 Tucanae from a Hubble Space Telescope Search*, 1999, ApJ 545, L47-51
- **Bruntt**, H., Frandsen, S., Kjeldsen, H., Andersen, M. I., *Strömgren photometry of the open clusters NGC 6134 and NGC 3680*, 1999, A&AS, 140, 135
- Viskum, M., Kjeldsen, H., Bedding, T. R., Dall, T. H., Baldry, I. K., **Bruntt**, H., Frandsen, S., *Oscillation mode identifications and models for the $\delta$ Scuti star FG Virginis*, 1998, A&A, 335, 549
- Viskum, M., Dall, T. H., **Bruntt**, H., Frandsen, S., Kjeldsen, H., Baldry, I. K., Bedding, T. R., *New Techniques for Oscillation Mode Identification in the $\delta$ Scuti Star FG Virginis*, 1997, in A Half Century of Stellar Pulsation Interpretation: A Tribute to Arthur N. Cox, edited by Paul A. Bradley and J. A. Guzik, ASP Conference Series #135, p. 465.

# Bibliography


Alard, C. & Lupton, R. H. 1998, ApJ, 503, 325

Alcaino, G., Liller, W., Alvarado, F., Kravtsov, V., Ipatov, A., Samus, N., & Smirnov, O. 1997, AJ, 114, 189

Alonso, A., Arribas, S., & Martinez-Roger, C. 1996, A&A, 313, 873

Andersen, M. I., Freyhammer, L., & Storm, J. 1995, in Calibrating and Understanding HST and ESO Instruments, ESO Conf. and Workshop Proc., ed. P. Bienvenuti, Vol. 53, 87

Baglin, A., Auvergne, M., Catala, C., Michel, E., & COROT Team. 2001, Proceedings of the SOHO 10/GONG 2000 Workshop: Helio- and asteroseismology at the dawn of the millennium, 2-6 October 2000, Santa Cruz de Tenerife, Tenerife, Spain. Edited by A. Wilson, Scientific coordination by P. L. Pallé. ESA SP-464, Noordwijk: ESA Publications Division, ISBN 92-9092-697-X, 2001, p. 395 - 398, 464, 395

Balachandran, S. 1990, ApJ, 354, 310

Balona, L. A. & Evers, E. A. 1999, MNRAS, 302, 349

Baranne, A., Queloz, D., Mayor, M., Adrianzyk, G., Knispel, G., Kohler, D., Lacroix, D., Meunier, J.-P., Rimbaud, G., & Vin, A. 1996, A&AS, 119, 373

Bedding, T. R., Butler, R. P., Kjeldsen, H., Baldry, I. K., O'Toole, S. J., Tinney, C. G., Marcy, G. W., Kienzle, F., & Carrier, F. 2001, ApJ, 549, L105

Bedding, T. R. & Kjeldsen, H. 1998, in ASP Conf. Ser. 154: Cool Stars, Stellar Systems, and the Sun, Vol. 10, 301

Bedding, T. R. & Zijlstra, A. A. 1998, ApJ, 506, L47

Bessell, M. S., Castelli, F., & Plez, B. 1998, A&A, 333, 231

Bikmaev, I. F., Ryabchikova, T. A., Bruntt, H., Musaev, F. A., Mashonkina, L. I., Belyakova, E. V., Shimansky, V. V., Barklem, P. S., & Galazutdinov, G. 2002, A&A, 389, 537

Bono, G., Caputo, F., Castellani, V., & Marconi, M. 1996, ApJ, 471, L33

Borucki, W. J., Koch, D. G., Dunham, E. W., & Jenkins, J. M. 1997, in ASP Conf. Ser. 119: Planets Beyond the Solar System and the Next Generation of Space Missions, 153

Bouchy, F. & Carrier, F. 2001, A&A, 374, L5

Breger, M., Garrido, R., Handler, G., Wood, M. A., Shobbrook, R. R., Bischof, K. M., Rodler, F., Gray, R. O., Stankov, A., Martinez, P., O'Donoghue, D., Szabó, R., Zima, W., Kaye, A. B., Barban, C., & Heiter, U. 2002, MNRAS, 329, 531

Breger, M. & Montgomery, M., eds. 2000, Delta Scuti and Related Stars, Reference Handbook and Proceedings of the 6th Vienna Workshop in Astrophysics, held in Vienna, Austria, 4-7 August, 1999. ASP Conference Series, Vol. 210. (San Francisco: ASP) ISBN: 1-58381-041-2

Breger, M., Pamyatnykh, A. A., Pikall, H., & Garrido, R. 1999, A&A, 341, 151

Brown, T. M. 1998, in ASP Conf. Ser. 154: Cool Stars, Stellar Systems, and the Sun, Vol. 10, 289

Brown, T. M., Christensen-Dalsgaard, J., Weibel-Mihalas, B., & Gilliland, R. L. 1994, ApJ, 427, 1013

Brown, T. M. & Gilliland, R. L. 1990, ApJ, 350, 839

Brown, T. M., Gilliland, R. L., Noyes, R. W., & Ramsey, L. W. 1991, ApJ, 368, 599

Bruntt, H., Bikmaev, I. F., Catala, C., & Weiss, W. W. 2003a, A&A, *in preparation*

Bruntt, H., Catala, C., Garrido, R., Rodríguez, E., Stütz, C., Knoglinger, P., Mittermayer, P., Bouret, J. C., Hua, T., Lignières, F., Charpinet, S., Van't Veer-Menneret, C., & Ballereau, D. 2002, A&A, 389, 345

Bruntt, H. & Frandsen, S. 2003, in Proc. of Modeling of Stellar Atmospheres, Vol. 210, *in press*

Bruntt, H., Frandsen, S., Gilliland, R. L., Christensen-Dalsgaard, J., Petersen, J. O., Guhathakurta, P., Edmonds, P. D., & Bono, G. 2001, A&A, 371, 614

Bruntt, H., Frandsen, S., Kjeldsen, H., & Andersen, M. I. 1999, A&AS, 140, 135

Bruntt, H., Tingley, B., Grundahl, F., Frandsen, S., Stetson, P. B., & Thomsen, B. 2003b, A&A, *in preparation*

Burke, C. J., DePoy, D. L., Gaudi, B. S., Marshall, J. L., & Pogge, R. W. 2002, astroph/0208305

Butler, R. P., Marcy, G. W., Fischer, D. A., Vogt, S., Tinney, C. G., Jones, H. R. A., Penny, A. J., & Apps, K. 2002, in Planetary Systems in the Universe: Observation, Formation and Evolution, ed. A. P. et al., Vol. IAU Symp. 202, ASP Conf. Ser., *in press*

Buzasi, D., Catenzarite, J., Laher, R., Contow, T., & Shupe, D. e. a. 2000, ApJL, 532, 133

Canuto, V. M. & Mazzitelli, I. 1991, ApJ, 370, 295

—. 1992, ApJ, 389, 724

Carrier, F., Bouchy, F., Kienzle, F., Bedding, T. R., Kjeldsen, H., Butler, R. P., Baldry, I. K., O'Toole, S. J., Tinney, C. G., & Marcy, G. W. 2001, A&A, 378, 142

Carrier, F., et al., & . 2003, in Asteroseismology Across the HR Diagram, ed. M. J. Thompson, M. S. Cunha, & M. J. P. F. G. Monteiro (Kluwer Academic Publishers)

Chaboyer, B., Green, E. M., & Liebert, J. 1999, AJ, 117, 1360

Charbonneau, D., Brown, T. M., Latham, D. W., & Mayor, M. 2000, ApJ, 529, L45

Charbonneau, D., Brown, T. M., Noyes, R. W., & Gilliland, R. L. 2002, ApJ, 568, 377

Christensen-Dalsgaard, J. 2002, Proceedings of the First Eddington Workshop on Stellar Structure and Habitable Planet Finding, 11 - 15 June 2001, Córdoba, Spain. Editor: B. Battrick, Scientific editors: F. Favata, I. W. Roxburgh & D. Galadi. ESA SP-485, Noordwijk: ESA Publications Division, ISBN 92-9092-781-X, 2002, p. 25 - 34, 485, 25

Clement, C. M., Muzzin, A., Dufton, Q., Ponnampalam, T., Wang, J., Burford, J., Richardson, A., Rosebery, T., Rowe, J., & Hogg, H. S. 2001, AJ, 122, 2587

Cochran, W. D., Hatzes, A. P., & Paulson, D. B. 2002, AJ, 124, 565

Dixon, R. I. & Longmore, A. J. 1993, MNRAS, 265, 395

Dreizler, S., Rauch, T., Hauschildt, P., Schuh, S. L., Kley, W., & Werner, K. 2002, A&A, 391, L17

Dziembowski, W. A., Gough, D. O., Houdek, G., & Sienkiewicz, R. 2001, MNRAS, 328, 601

Edmonds, P. D. & Gilliland, R. L. 1996, ApJ, 464, L157

Edvardsson, B., Andersen, J., Gustafsson, B., Lambert, D. L., Nissen, P. E., & Tomkin, J. 1993, A&A, 275, 101

Eyer, L., Grenon, M., Falin, J.-L., Froeschle, M., & Mignard, F. 1994, Sol. Phys., 152, 91

Favata, F. 2002, Proceedings of the First Eddington Workshop on Stellar Structure and Habitable Planet Finding, 11 - 15 June 2001, Córdoba, Spain. Editor: B. Battrick, Scientific editors: F. Favata, I. W. Roxburgh & D. Galadi. ESA SP-485, Noordwijk: ESA Publications Division, ISBN 92-9092-781-X, 2002, p. 3 - 10, 485, 3

Favata, F., Micela, G., & Sciortino, S. 1997, A&A, 323, 809

Fernie, J. D. 1983, PASP, 95, 782

Ferraro, F. R., Messineo, M., Fusi Pecci, F., de Palo, M. A., Straniero, O., Chieffi, A., & Limongi, M. 1999, AJ, 118, 1738

Frandsen, S., Balona, L. A., Viskum, M., Koen, C., & Kjeldsen, H. 1996, A&A, 308, 132

Frandsen, S., Carrier, F., Aerts, C., Stello, D., Maas, T., Burnet, M., Bruntt, H., Teixeira, T. C., de Medeiros, J. R., Bouchy, F., Kjeldsen, H., Pijpers, F., & Christensen-Dalsgaard, J. 2002, A&A, 394, L5

Garrido, R., Claret, A., Moya, A., Kupka, F., Heiter, U., Barban, C., Goupil, M.-J., & van't Veer-Menneret, C. 2002, Proceedings of the First Eddington Workshop on Stellar Structure and Habitable Planet Finding, 11 - 15 June 2001, Córdoba, Spain. Editor: B. Battrick, Scientific editors: F. Favata, I. W. Roxburgh & D. Galadi. ESA SP-485, Noordwijk: ESA Publications Division, ISBN 92-9092-781-X, 2002, p. 103 - 107, 485, 103

Gilliland, R. L., Brown, T. M., Guhathakurta, P., Sarajedini, A., Milone, E. F., Albrow, M. D., Baliber, N. R., Bruntt, H., Burrows, A., Charbonneau, D., Choi, P., Cochran, W. D., Edmonds, P. D., Frandsen, S., Howell, J. H., Lin, D. N. C., Marcy, G. W., Mayor, M., Naef, D., Sigurdsson, S., Stagg, C. R., Vandenberg, D. A., Vogt, S. S., & Williams, M. D. 2000, ApJ, 545, L47

Gilliland, R. L., Brown, T. M., Kjeldsen, H., McCarthy, J. K., Peri, M. L., Belmonte, J. A., Vidal, I., Cram, L. E., Palmer, J., Frandsen, S., Parthasarathy, M., Petro, L., Schneider, H., Stetson, P. B., & Weiss, W. W. 1993, AJ, 106, 2441

Gonzalez, G., Laws, C., Tyagi, S., & Reddy, B. E. 2001, AJ, 121, 432

Gough, D. 2001, Science, 291, 2325

Gray, D. F. 1992, The observation and analysis of stellar photospheres (Cambridge Astrophysics Series, Cambridge: Cambridge University Press, 1992, 2nd ed., ISBN 0521403200.)

Haisch, B. M. 1999, in The many faces of the sun: a summary of the results from NASA's Solar Maximum Mission., ed. K. T. Strong, J. L. R. Saba, B. M. Haisch, & J. T. Schmelz, 481

Hall, D. S. 1972, PASP, 84, 323

Handler, G., Arentoft, T., Shobbrook, R. R., Wood, M. A., Crause, L. A., Crake, P., Podmore, F., Habanyama, A., Oswalt, T., Birch, P. V., Lowe, G., Sterken, C., Meintjes, P., Brink, J., Claver, C. F., Medupe, R., Guzik, J. A., Beach, T. E., Martinez, P., Leibowitz, E. M., Ibbetson, P. A., Smith, T., Ashoka, B. N., Raj, N. E., Kurtz, D. W., Balona, L. A., O'Donoghue, D., Costa, J. E. S., & Breger, M. 2000, MNRAS, 318, 511

Hartmann, K. & Gehren, T. 1988, A&A, 199, 269

Hatzes, A. P. & Cochran, W. D. 1993, ApJ, 413, 339

—. 1994, ApJ, 422, 366

Hatzes, A. P. & Cochran, W. D. 1998, in ASP Conf. Ser. 154: Cool Stars, Stellar Systems, and the Sun, Vol. 10, 311

Hauck, B. & Mermilliod, M. 1998, A&AS, 129, 431

Henry, G., Marcy, G., Butler, R. P., & Vogt, S. S. 1999, IAU Circ., 7307

Henry, G. W., Fekel, F. C., & Henry, S. M. 2000, ApJS, 130, 201

Hernandez, M. M., Perez Hernandez, F., Michel, E., Belmonte, J. A., Goupil, M. J., & Lebreton, Y. 1998, A&A, 338, 511

Høg, E. 2002, ApSS, 280, 139

Houdek, G., Balmforth, N. J., Christensen-Dalsgaard, J., & Gough, D. O. 1999, A&A, 351, 582

Howell, S. B., Everett, M. E., Esquerdo, G., Davis, D. R., Weidenschilling, S., & van Lew, T. 1999, in ASP Conf. Ser. 189: Precision CCD Photometry, 170

Hubbard, W., Burrows, A., & Lunine, J. 2002, ARAA, *in press*

Ivans, I. I., Sneden, C., Kraft, R. P., Suntzeff, N. B., Smith, V. V., Langer, G. E., & Fulbright, J. P. 1999, AJ, 118, 1273

Jorissen, A., Mowlavi, N., Sterken, C., & Manfroid, J. 1997, A&A, 324, 578

Kaluzny, J., Thompson, I., Krzeminski, W., Olech, A., Pych, W., & Mochejska, B. 2002, astroph/0111089

Kippenhahn, R. & Weigert, A. 1994, Stellar Structure and Evolution (Stellar Structure and Evolution, XVI, 468 pp. 192 figs.. Springer-Verlag Berlin Heidelberg New York. Also Astronomy and Astrophysics Library)

Kjeldsen, H. & Bedding, T. R. 1995, A&A, 293, 87

Kjeldsen, H., Bedding, T. R., Baldry, I. K., Frandsen, S., Bruntt, H., Grundahl, F., Lang, K., Butler, R. P., Fischer, D. A., Marcy, G. W., Misch, A., & Vogt, S. S. 2002, in ASP Conf. Ser. 259: IAU Colloq. 185: Radial and Nonradial Pulsationsn as Probes of Stellar Physics, 470

Kjeldsen, H., Bedding, T. R., Viskum, M., & Frandsen, S. 1995, AJ, 109, 1313

Kjeldsen, H. & Frandsen, S. 1992, PASP, 104, 413

Kupka, F. 1996, in ASP Conf. Ser. 108: M.A.S.S., Model Atmospheres and Spectrum Synthesis, ed. S. J. Adelman, F. Kupka, & W. W. Weiss

Kupka, F., Piskunov, N., Ryabchikova, T. A., Stempels, H. C., & Weiss, W. W. 1999, A&AS, 138, 119

Kurucz, R. 1993, SYNTHE Spectrum Synthesis Programs and Line Data. Kurucz CD-ROM No. 18. Cambridge, Mass.: Smithsonian Astrophysical Observatory, 1993., 18

Kurucz, R. L. 1979, ApJS, 40, 1

Lastennet, E., Lignières, F., Buser, R., Lejeune, T., Lüftinger, T., Cuisinier, F., & van't Veer-Menneret, C. 2001, A&A, 365, 535

Laughlin, G. 2000, ApJ, 545, 1064

Mallén-Ornelas, G., Seager, S., Minniti, D., Gladders, M. D., Mallén-Fullerton, G. M., & Brown, T. M. 2002, ApJ, *submitted*; astroph/0203218

Marcy, G. W. & Butler, R. P. 1998, ARA&A, 36, 57

Martić, M., Schmitt, J., Lebrun, J.-C., Barban, C., Connes, P., Bouchy, F., Michel, E., Baglin, A., Appourchaux, T., & Bertaux, J.-L. 1999, A&A, 351, 993

Matthews, J. M., Kuschnig, R., Walker, G. A. H., Pazder, J., Johnson, R., Skaret, K., Shkolnik, E., Lanting, T., Morgan, J. P., & Sidhu, S. 2000, in ASP Conf. Ser. 203: IAU Colloq. 176: The Impact of Large-Scale Surveys on Pulsating Star Research, 74–75

Mayor, M. & Queloz, D. 1995, Nature, 378, 355

Mazeh, T., Naef, D., Torres, G., Latham, D. W., Mayor, M., Beuzit, J., Brown, T. M., Buchhave, L., Burnet, M., Carney, B. W., Charbonneau, D., Drukier, G. A., Laird, J. B., Pepe, F., Perrier, C., Queloz, D., Santos, N. C., Sivan, J., Udry, S., & Zucker, S. 2000, ApJ, 532, L55

Merline, W. J. 1999, in ASP Conf. Ser. 185: IAU Colloq. 170: Precise Stellar Radial Velocities, 187

Metcalfe, T. S., Winget, D. E., & Charbonneau, P. 2001, ApJ, 557, 1021

Michel, E., Hernández, M. M., Houdek, G., Goupil, M. J., Lebreton, Y., Hernández, F. P., Baglin, A., Belmonte, J. A., & Soufi, F. 1999, A&A, 342, 153

Mochejska, B. J., Kaluzny, J., Thompson, I., & Pych, W. 2002a, AJ, 124, 1486

Mochejska, B. J., Stanek, K. Z., Sasselov, D. D., & Szentgyorgyi, A. H. 2002b, AJ, 123, 3460

Napiwotzki, R., Schoenberner, D., & Wenske, V. 1993, A&A, 268, 653

Nordgren, T. E., Dyck, M., Sudol, J., Germain, M., Hummel, C. A., & Benson, J. A. 1998, Bulletin of the American Astronomical Society, 30, 917

O'Toole, S. J., Bedding, T. R., Kjeldsen, H., Dall, T. H., & Stello, D. 2002, MNRAS, 334, 471

Pepper, J., Gould, A., & DePoy, D. L. 2002, astroph/0208042

Perrin, M. N. 1976, Ph.D. Thesis

Petit, M. 1987, Variable stars (Chichester, England and New York, John Wiley and Sons, 1987, 268 p. Translation.)

Pijpers, F. 2003, A&A, *accepted*

Rasmussen, M. B. 2001, Master's thesis, Department of Physics and Astronomy, Aarhus University

Rasmussen, M. B., Bruntt, H., Frandsen, S., Paunzen, E., & Maitzen, H. M. 2002, A&A, 390, 109

Richer, H. B., Brewer, J., Fahlman, G. G., Gibson, B. K., Hansen, B. M., Ibata, R., Kalirai, J. S., Limongi, M., Rich, R. M., Saviane, I., Shara, M. M., & Stetson, P. B. 2002, ApJ, 574, L151

Rodríguez, E., López-González, M. J., & López de Coca, P. 2000, A&AS, 144, 469

Rogers, N. Y. 1995, Comm. in Asteroseismology, 78, 1

Roxburgh, I. W. 2002, Proceedings of the First Eddington Workshop on Stellar Structure and Habitable Planet Finding, 11 - 15 June 2001, Córdoba, Spain. Editor: B. Battrick, Scientific editors: F. Favata, I. W. Roxburgh & D. Galadi. ESA SP-485, Noordwijk: ESA Publications Division, ISBN 92-9092-781-X, 2002, p. 11 - 15, 485, 11

Rucinski, S. M. 2000, AJ, 120, 319

Rucinski, S. M., Kaluzny, J., & Hilditch, R. W. 1996, MNRAS, 282, 705

Ryabchikova, T. A., Piskunov, N. E., Stempels, H. C., Kupka, F., & Weiss, W. W. 1999, Phys. Scripta, 83, 162

Salaris, M., Cassisi, S., & Weiss, A. 2002, PASP, 114, 375

Sozzetti, A., Casertano, S., Lattanzi, M. G., & Spagna, A. 2001, A&A, 373, L21

Sperl, M. 1998, Comm. in Asteroseismology, 111, 1

Stahl, O., Kaufer, A., & Tubbesing, S. 1999, in ASP Conf. Ser. 188: Optical and Infrared Spectroscopy of Circumstellar Matter, 331

Stello, D. 2002, Master's thesis, Department of Physics and Astronomy, Aarhus University

Sterken, C., ed. 2001, First COROT/MONS/MOST Ground-based Support Workshop (University of Brussels)

Stetson, P. B. 1987, PASP

Stetson, P. B. 1990, PASP, 102, 932

—. 1994, PASP, 106, 250

—. 1996, PASP, 108, 851

—. 2000, PASP, 112, 925

Stetson, P. B., Bruntt, H., & Grundahl, F. 2003, PASP, *accepted*

Stetson, P. B., Saha, A., Ferrarese, L., Rawson, D. M., Ford, H. C., Freedman, W. L., Gibson, B. K., Graham, J. A., Harding, P., Han, M., Hill, R. J., Hoessel, J. G., Huchra, J. P., Hughes, S. M. G., Illingworth, G. D., Kelson, D. D., Kennicutt, R. C., Madore, B. F., Mould, J. R., Phelps, R. L., Sakai, S., Silbermann, N. A., & Turner, A. 1998, ApJ, 508, 491

Street, R., Pollacco, D., Fitzsimmons, A., Keenan, F., Horne, K., Kane, S., Collier, A. C., Lister, T. A., Haswell, C., Norton, A., Jones, B., Skillen, I., Hodgkin, S., Wheatley, P., West, R., & D., B. 2003, in Scientific Frontiers in Research on Extrasolar Planets, ASP Conf. Ser. / astroph/0208233

Tassoul, M. 1980, ApJS, 43, 469

Taylor, B. J. 1986, ApJS, 60, 577

—. 2001, A&A, 377, 473

Teixeira, T. C., Christensen-Dalsgaard, J., Carrier, F., Aerts, C., Frandsen, S., Stello, D., Maas, T., Burnet, M., Bruntt, H., de Medeiros, J., Bouchy, F., Kjeldsen, H., & Pijpers, F. 2003, in Asteroseismology across the HR diagram, ed. M. J. Thompson, M. S. Cunha, & M. J. P. F. G. Monteiro, Vol. accepted (Kluwer Academic Publishers)

Templeton, M., Basu, S., & Demarque, P. 2002, ApJ, 576, 963

Tingley, B. 2003, A&A, *submitted*

Toutain, T. & Froehlich, C. 1992, A&A, 257, 287

Udalski, A., Paczynski, B., Zebrun, K., Szymaski, M., Kubiak, M., Soszynski, I., Szewczyk, O., Wyrzykowski, L., & Pietrzynski, G. 2002a, Acta Astronomica, 52, 1

Udalski, A., Zebrun, K., Szymanski, M., Kubiak, M., Soszynski, I., Szewczyk, O., Wyrzykowski, L., & Pietrzynski, G. 2002b, Acta Astronomica, 52, 115

Valenti, J. A. & Piskunov, N. 1996, A&AS, 118, 595

VandenBerg, D. A. 2000, ApJS, 129, 315

Vogt, S. S., Butler, R. P., Marcy, G. W., Fischer, D. A., Pourbaix, D., Apps, K., & Laughlin, G. 2002, ApJ, 568, 352

Vorontsov, S. V. 2002, Proceedings of the SOHO 11 Symposium on From Solar Min to Max: Half a Solar Cycle with SOHO, 11-15 March 2002, Davos, Switzerland. A symposium dedicated to Roger M. Bonnet. Edited by A. Wilson, ESA SP-508, Noordwijk: ESA Publications Division, ISBN 92-9092-818-2, 2002, p. 107 - 110, 508, 107

Wolszczan, A. 1994, ApSS, 212, 67

Wozniak, P. R., Udalski, A., Szymanski, M., Kubiak, M., Pietrzynski, G., Soszynski, I., & Zebrun, K. 2002, Acta Astronomica, 52, 129

Yee, H. K. C., Mallén-Ornelas, G., Seager, S., Gladders, M. D., Brown, T., Minniti, D., Ellison, S., & Mallén-Fullerton, G. M. 2002, astroph/0208355

Zakhozhaj, V. A. & Shaparenko, E. F. 1996, Kinematika i Fizika Nebesnykh Tel, 12, 20

Zima, W. 1997, Delta Scuti Star Newsletter, 11, 37

# PAPERS

I

# Semi-automatic Abundance Analysis of the $\gamma$ Dor Star HD 49434

Bruntt, H., Catala, C., Garrido, R., Rodríguez, E., Stütz, C., Knoglinger, P., Mittermayer, P., Bouret, J. C., Hua, T., Lignières, F., Charpinet, S., Van't Veer-Menneret, C., Ballereau, D.

*Abundance Analysis of Targets for the COROT/MONS Asteroseismology Missions. I. Semi-automatic Abundance Analysis of the $\gamma$ Dor star HD 49434*

2002, A&A, **389**, 345-354

Astronomy & Astrophysics manuscript no.
(will be inserted by hand later)

# Abundance analysis of targets for the COROT / MONS asteroseimology missions

## I. Semi-automatic abundance analysis of the $\gamma$ Dor star HD 49434*

H. Bruntt[1], C. Catala[2,5], R. Garrido[3], E. Rodríguez[3], C. Stütz[4], P. Knoglinger[4], P. Mittermayer[4], J. C. Bouret[5], T. Hua[5], F. Lignières[2], S. Charpinet[2], C. Van't Veer-Menneret[6], and D. Ballereau[6]

1 Institute for Physics and Astronomy, University of Aarhus, Bygn. 520, DK-8000 Aarhus C, Denmark
2 Laboratoire d'Astrophysique de l'OMP, CNRS UMR 5572, Observatoire Midi-Pyrénées, 14, avenue Edouard Belin, F-31400 Toulouse, France
3 Instituto de Astrofísica de Andaluciá, Espanã
4 Institut für Astronomie, Universität Wien, Türkenschanzstrasse 17, A-1180 Wien, Austria
5 Laboratoire d'Astrophysique de Marseille, France
6 Observatoire de Paris, France

Received ..... / Accepted .....

**Abstract.** One of the goals of the ground-based support program for the COROT and MONS/Rømer satellite missions is to select and characterise suitable target stars for the part of the missions dedicated to asteroseismology. While the global atmospheric parameters may be determined with good accuracy from the Strömgren indices, careful abundance analysis must be made for the proposed main targets. This is a time consuming process considering the long list of primary and secondary targets. We have therefore developed new software called VWA for this task. The VWA automatically selects the least blended lines from the atomic line database VALD, and consequently adjusts the abundance in order to find the best match between the calculated and observed spectra. The variability of HD 49434 was discovered as part of COROT ground-based support observations. Here we present a detailed abundance analysis of HD 49434 using VWA. For most elements we find abundances somewhat below the Solar values, in particular we find [Fe/H] $= -0.13 \pm 0.14$. We also present the results from the study of the variability that is seen in spectroscopic and photometric time series observations. From the characteristics of the variation seen in photometry and in the line profiles we propose that HD 49434 is a variable star of the $\gamma$ Doradus type.

**Key words.** methods: data analysis – techniques: spectroscopic stars: abundances – stars: fundamental parameters – stars: individual: HD 49434 – stars: variables: $\gamma$ Dor

## 1. Introduction

We first observed HD 49434 (F2V-type) with the ELODIE spectrograph in December 1998 as part of a program with the aim of characterising and selecting potential targets for the asteroseismology space mission COROT (Catala 2001). The strategy is to obtain a number of high resolution, high signal-to-noise spectra of each potential target. For any stars that present line asymmetries or variable line profiles we then carry out more complete monitoring.

Before these observations the star was not considered to be variable, but we discovered systematic low-amplitude variations of the line profiles. Since then we have carried out more extensive spectroscopic and photometric observations.

The purpose of the present paper is to derive the global atmospheric parameters of HD 49434 and to perform an analysis of its photometric and spectroscopic variations.

The French COROT as well as the Danish MONS/Rømer satellite are both asteroseismology missions which will study mostly solar-like stars. Before the launch of these missions (around 2004–5) we need an accurate estimation of the atmospheric parameters and abundances of the proposed target stars. First of all stars with certain parameters may not be suitable for a detailed asteroseismological study, eg. chemically peculiar stars or

*Send offprint requests to*: H. Bruntt, e-mail: bruntt@ifa.au.dk

* Based on observations obtained at Observatoire d'Haute Provence, France and at the Observatory of Sierra Nevada, Granada, Spain

stars with high rotation rate. Also, in order to carry out the detailed asteroseismological modelling of the stars we need to be able to constrain as many of the global parameters of the stars as possible. Around 10 and 25 primary targets will be chosen for COROT and MONS/Rømer, respectively. It is a very time-consuming process to carry out the abundance analysis of all potential targets manually and we have therefore developed a fast semi-automatic abundance analysis procedure called VWA, which will be described here. The result for HD 49434 is presented, and we will also make comparisons with stars for which abundance analyses have already been carried out manually.

In Section 2 we describe the spectroscopic observations and in Section 3 we describe the VWA software and the result of the abundance analysis. In Section 4 we describe the analysis of the photometric time series, while in Section 5 we analyse the line profile variations in the spectroscopic time series.

## 2. Spectroscopic observations

HD 49434 is an F2V-type star of magnitude $V = 5.74$ (cf. Table 2). We monitored the star spectroscopically from Observatoire de Haute-Provence, using the ELODIE spectrograph, attached to the 1.93 m telescope. The spectrograph is a cross-dispersed spectrograph, providing a complete spectral coverage of the 3 800–6 800 Å region, with a resolving power of about $R = 45\,000$ (Baranne et al. 1996).

The first spectroscopic observations of HD 49434 were carried out in December 1998 as part of the search for potential COROT targets. The spectra revealed the presence of variable asymmetries of low amplitude in the line profiles, indicative of non-radial pulsations. Hence, the star was monitored more thoroughly in subsequent observing runs.

On January 26, 2000, HD 49434 was monitored continuously for 90 minutes, with one 5 min spectrum every 7 minutes. The weather and seeing conditions were very good, and the average S/N ratio at 6 000 Å is 250 per velocity bin of 10 $\mathrm{km\,s^{-1}}$.

The star was re-observed on December 10, 2000, almost continuously for 320 minutes, during which as many as 51 five-minute spectra were recorded. The observing conditions of this second monitoring were not as good as the previous one, so that the resulting average S/N ratio at 6 000 Å is only about 170 per pixel per velocity bin of 10 $\mathrm{km\,s^{-1}}$.

The data used for the abundance analysis of HD 49434 are the spectra obtained during the best weather conditions: 12 spectra from January 26, 2000. On the other hand, all of the observed spectra were used for the study of the variability of line profiles. Since the data analysis of the spectra was made by two groups independently, we will describe the data reduction in separate sections, i.e. abundance analysis in Section 3.1 below and the variability of line profiles in Section 5.1.

## 3. Abundance analysis

In this section we will describe the abundance analysis of HD 49434. For this purpose we have developed new software for the semi-automatic analysis of spectra. The abbreviation for the software is VWA which explains what the program can determine from the spectrum, i.e. projected rotational velocity ($v \sin i$) of the star, wavelength shift (due to radial velocity), and abundance analysis.

### *3.1. Data reduction*

The bias subtraction, flat fielding, scattered light subtraction, and extraction of the spectral orders were done with IRAF. The wavelength calibration was made using a combined Th-Ar comparison spectrum. We made low-order cubic spline fits to make the best continuum estimate. We made sure that the overlap between orders was better than 0.5%. We note that we have not used the region near the hydrogen lines for abundance analysis. The hydrogen lines cover several spectral orders and thus a determination of the continuum level is difficult. One possibility to overcome this problem is to use the average of the continuum level for orders adjacent to the hydrogen lines. This has been done by Lastennet et al. (2001) and they have estimated the effective temperature from the H$\alpha$ line to be $T_{\rm eff} = 7250 \pm 250$ K.

The signal to noise of the combined spectrum (12 spectra) at the maximum of a spectral order around 6 000 Å is S/N = 400 per velocity bin of 10 $\mathrm{km\,s^{-1}}$.

### *3.2. Automatic abundance analysis with* VWA

The VWA package can perform three different tasks: Automatic selection of lines for the determination of $v \sin i$, determination of any systematic shift of lines (due to radial velocity), and abundance analysis – the last being the most extensive part of the program.

The first two tasks are not fully implemented in VWA, but $v \sin i$ and $v_{\rm rad}$ can be determined quite easily by comparison of the observed spectrum and several synthetic lines: We convolve the synthetic spectrum with the instrumental profile and different rotation profiles and determine the best fit (we use the program ROTATE by Piskunov 1992). We find $v \sin i = 84 \pm 4$ $\mathrm{km\,s^{-1}}$ which is in agreement with Lastennet et al. (2001) who found $v \sin i = 79$ $\mathrm{km\,s^{-1}}$ from the same data set. From the wavelength shifts of non-blended lines we determine the helio-centric radial velocity to be $v_{\rm rad} = -12.3 \pm 1.0$ $\mathrm{km\,s^{-1}}$. Gernier et al. (1999) found $v_{\rm rad} = -14.0 \pm 0.8$ $\mathrm{km\,s^{-1}}$ from Hipparcos data. We remove the wavelength shift caused by the radial velocity, thus the wavelength scale is the same as the laboratory system.

#### 3.2.1. Input: model atmosphere and atomic data

To use VWA one must calculate an appropriate model for the atmosphere of the star. We have used a modified ver-

**Fig. 1.** Observed (thin line) and synthetic (thick line) spectrum around twelve lines which were used for the abundance determination. The lower portion of the each plotted line shows the relative difference between the observed and synthetic spectrum. The name of the element and the central wavelength (in Ångstrøm) of each fitted line is given at the top of each plot

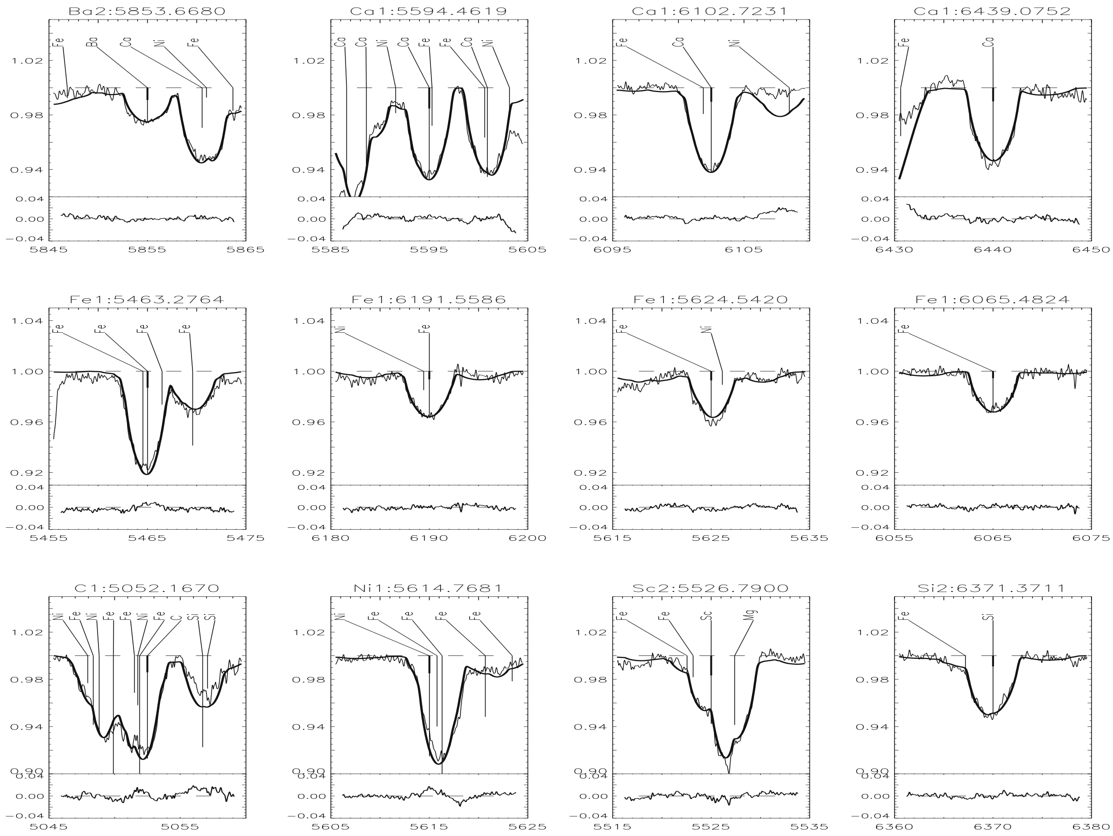


sion of the ATLAS9 code (Kurucz 1993) as described by Kupka (1996) – see also Smalley & Kupka (1997). In this version of ATLAS9 the turbulent convection theory in the formulation of Canuto & Mazzitelli (1991, 1992) is implemented.

To calculate the model one needs to know the basic parameters of the star, i.e. $T_{\rm eff}, \log g$, and [Fe/H]. These parameters may be estimated from the Strömgren indices of the star by using the program TEMPLOGG (Rogers 1995) which automatically chooses the most appropriate among several published photometric calibrations. To determine the basic atmospheric parameters of the star TEMPLOGG then interpolates the de-reddened photometric indices in the atmospheric ATLAS6 model grid by Kurucz (1979) with the improvements suggested by Napiwotzki et al. (1993). We note that TEMPLOGG does not use the bare results from the ATLAS6 grids but rather an experimental calibration, i.e. the colour grids are transformed so as to match well-calibrated fundamental stars before the calibration is made. To summarize, we have used a modified version of the recent ATLAS9 code for the computation of the atmospheric models where we use the atmosphere parameters found with TEMPLOGG which use colours from the older ATLAS6 grids which have been calibrated to match observed stars.

For the abundance determination we make use of a complete list of atomic line data for the entire observed spectral range. The line list is extracted from the VALD database (Kupka et al. 1999, Ryabchikova et al. 1999) where all lines deeper than 1% of the continuum are included. From the line list (about 13 000 lines for HD 49434) the least blended lines will be selected by VWA.

The selection consists of two steps: 1) Selection based on the analysis of the degree of blending based on the information in the line list from the VALD database. 2) These lines are then analysed in the observed spectrum and any "suspicious" lines are rejected. These steps are described in the following two sections.

### 3.2.2. Selecting lines: atomic line list

For each atomic line extracted from the VALD database we examine the line depths of the neighbouring lines. For a given line we examine lines within a certain range specified by the user; for HD 49434 we have used 3.0×FWHM of an unblended line (= 3.0 × 2.2 Å= 6.6 Å). The line depths of the neighbouring lines are convolved by a Gaussian with a FWHM of 1.5×FWHM of an unblended line, i.e. the line depths of lines far away from the central line are suppressed. The selection of lines from the VALD line list is based on the degree of blending which is described by three parameters. The user may set his own limits for these parameters, and thus determine which lines are selected. The parameters are: 1) The depth ratio of the central line to the deepest (non-convolved) line. This value must be greater than 1 but can specified by the user (we used 1.35). 2) The number of neighbours with a (convolved) line depth of 25% of the central line must be lower than some limit (we used 5). 3) The sum of the (convolved) line depths must be lower than some number (we used 0.7).

#### 3.2.3. Rejecting lines: the observed spectrum

When the lines have been selected from the list of atomic lines VWA analyses the *observed* spectrum in the region around each selected line. The aim is to automatically reject lines that are not suitable for abundance analysis. This is done by fitting a Voigt profile to the observed spectrum. A number of "selection parameters" specified by the user determines if a line will be used: the minimum depth of the fitted profile, the maximum and minimum width of the profile, the maximum value of $\chi^2$ for the profile fit, and the maximum flux asymmetry between the left and right part of the observed line.

Optionally the user is presented with a plot of the observed spectrum in a region around each of the selected and rejected lines. The user may then interactively choose if a rejected (accepted) line should be included (rejected) in the abundance analysis. In practice this part of the VWA program creates two lists of the lines that will be rejected / accepted in the final selection of lines to be used for abundance analysis, i.e. these line lists over-rule the automatic selection. The line lists may also be edited manually if, for example, the user already knows which lines he wants to use for the abundance analysis (in accepted line list) – or if the user knows that the atomic parameters of certain lines are known to be uncertain (in rejected line list).

#### 3.2.4. Two methods for abundance determination

The abundance determination is made for each of the selected lines. It can be done by either of two methods: 1) By the measurement of equivalent widths of lines in the observed spectrum which are then given as input to the WIDTH9 code by Kurucz (1993). 2) By the adjustment of the abundance of the element of the central line of the blend until the computed and observed spectrum around each line match, i.e. they have the same equivalent width. For the computation of the synthetic spectrum we used the program SYNTH (version 2.5) by N. Piskunov (see Valenti & Piskunov 1996).

The first method can only be used for stars where blending is not a problem, i.e. slowly rotating stars ($v \sin i < 15$ km s$^{-1}$). The second method is much slower but it is the only option for fast rotators like HD 49434.

#### 3.2.5. Deriving the abundances

For this study we have used the fitting of the abundance in the synthetic spectrum in a region 4 Å on both sides of the central line (the typical FWHM of a single line is about 2.2 Å at 6 000 Å). After all lines have been fitted the user is presented with a plot of the region around each line in which both the synthetic and observed spectrum is shown. Also, all lines with a line depth deeper than 25% of the central line are clearly marked. Several fitted lines are shown in Figure 1. In this "visual inspection" part of VWA the user can click on different sections of the plot which determines if the user thinks the line is fitted correctly, if there seems to be a problem with the continuum level, if the line is severely blended, if the line should simply be ignored, or if the automatic fit has failed. In the last case these lines can be fitted interactively by a separate program (VWA-INTERACT).

The abundance of each element is then calculated using only the lines accepted by the user. Additional constraints on which lines to use may be imposed here, i.e. to use only the least blended lines. For this the "sensitivity" parameter of the line can be used to select the best lines or to give higher weight to certain lines. We define the sensitivity parameter as the change in equivalent width when increasing the abundance, i.e. for a non-blended line this would be the slope of the "curve of growth" near the abundance of the fitted line. The parameter is measured for each line during the automatic determination of the abundance and we find that it depends both on the properties of the line and the degree of blending.

To be specific, the sensitivity, $S_i$, for each line $i$, is defined as $S_i = \Delta(\mathrm{EQW})/\Delta(\log N/N_{\mathrm{tot}})$. Typical values lie in the range 0.3–1.2 mÅ/ dex. For the present data we assume that the measured equivalent widths of all lines are measured with an accuracy of 5%, hence the error estimate of the abundance for a given line lies in the range 0.17–0.04 dex. To get a realistic error estimate for each line one must include systematic errors due to eg. erroneous $\log gf$ values (i.e. oscillator strengths), wrong determination of the continuum level, the possibility of erroneous abundances (or $\log gf$ values) of the lines that blend with the line, and uncertain stellar parameters used for the computation of the atmosphere model.

When calculating the abundance of each element based on several lines we assign weights to each line which depend on the sensitivity of the line. When computing the weights we have added an additional error of 0.07 dex which is the contribution from systematic errors as was discussed above. For the final abundance result of each element we calculate the weighted mean, where the weights are given by $W_i^{-1} = (0.05/S_i)^2 + (0.07)^2$. The standard

**Table 1.** Abundances of elements in HD 49434. The weighted mean abundance is given as the logarithm of number of atoms of a given element to the total number of atoms. The weighted standard deviation of the mean is given in parenthesis, $n$ is the number of lines that were used, while the last two columns are the abundances measured for the Sun (Grevesse & Sauval 1998) and the difference between the Sun and HD 49434

| Element | Ion | $\log N/N_{\rm tot}$ | $n$ | $(\log N/N_{\rm tot})_\odot$ | $\Delta$ |
|---|---|---|---|---|---|
| C | I | −3.46(0.13) | 1 | −3.52 | +0.06 |
| Mg | I | −4.55(0.07) | 3 | −4.46 | −0.09 |
| Si | I | −4.64(0.08) | 2 | −4.49 | −0.15 |
| Si | II | −4.57(0.06) | 3 | −4.49 | −0.08 |
| Ca | I | −5.51(0.06) | 7 | −5.68 | +0.17 |
| Sc | II | −8.89(0.11) | 2 | −8.87 | −0.02 |
| Ti | II | −7.16(0.07) | 2 | −7.02 | −0.14 |
| Cr | II | −6.45(0.05) | 4 | −6.37 | −0.08 |
| Fe | I | −4.67(0.02) | 16 | −4.54 | −0.13 |
| Fe | II | −4.43(0.07) | 2 | −4.54 | +0.11 |
| Ba | II | −9.75(0.09) | 3 | −9.91 | +0.16 |

error on the derived abundance is also calculated using these weights.

#### 3.2.6. Reliability of VWA

We have tested the program on two stars for which careful analyses have already been made: The Sun (Grevesse & Sauval 1998) and FG Vir (A-type star, $v \sin i = 21.3 \pm 1.0$ km s$^{-1}$; see Mittermayer 2001). For these stars we find good agreement with the previously derived abundances, i.e. within 0.1 dex for all elements.

We note that two future papers which make use of VWA are in preparation, i.e. Rasmussen et al. (2002) and Bikmaev et al. (2002). In the later paper we study two A-type stars and both have low $v \sin i$ (9 and 21 km s$^{-1}$). Thus we may compare the result of VWA with a "classical" abundance determination, i.e. by measuring equivalent widths of non-blended lines. The two methods agree within 0.03 dex for all elements. We conclude that VWA is indeed a reliable tool for fast semi-automatic abundance analysis.

### *3.3. Abundances for HD 49434*

We have estimated the fundamental atmospheric parameters of HD 49434 from the Strömgren photometry given in Table 2. We have used the TEMPLOGG code (Rogers 1995, see also Kupka & Bruntt 2001) and we find the atmospheric parameters of HD 49434 to be $T_{\rm eff} = 7\,300 \pm 200$ K, $\log g = 4.14 \pm 0.20$, and [Fe/H]$= -0.01 \pm 0.20$. The quoted errors are approximate and are dominated by the uncertainty from the photometric calibrations.

We determined the microturbulence parameter to be $\xi_t = 2.1 \pm 0.5$ km s$^{-1}$ (cf. discussion in Section 3.3.1). We used macroturbulence $v_{\rm macro} = 5.0$ km s$^{-1}$ and $v \sin i = 84 \pm 4$ km s$^{-1}$. The choice of $v_{\rm macro}$ is not important here, since the width of the lines is dominated by the rotational broadening.

Several lines fitted by VWA are shown in Figure 1. We have also shown the relative difference between the synthetic and observed spectrum. Neighbouring lines with a line depth of at least 25% of the fitted line are also shown. The length of the tick marks show the relative line depth of each neighbouring line compared to the fitted line.

From Figure 1 it can be seen that several lines that were used for the abundance analysis are blended. Due to the high $v \sin i$ of HD 49434 we simply had to use the least blended lines. Our strategy was to determine the Fe abundance accurately from non-blended lines. Consequently, we held the abundance of Fe fixed, and allowed VWA to select lines of other elements that were mildly blended by Fe lines, eg. the Ca lines at 5594.5 and 6102.7 Å. More extreme examples are the C, Ni, and Sc lines at 5052.2, 5614.8, and 5526.8 Å where the lines are heavily blended and the abundance determination is unreliable, i.e. the $S_i$ are 0.49, 0.24, and 0.22. If we again assume that the equivalent width is known to 5% the corresponding error is 0.1 dex for the C lines and 0.2 dex for the Ni and Sc lines. In addition, it is difficult to establish the location of the continuum level because the lines are so broad. Realistic error estimates lie in the range 0.2–0.4 dex for these three lines. Note that we did not find enough lines to give a reliable estimate for the abundance Ni and for C we found only one line that was usable.

The result of the abundance analysis is given in Table 1 and for comparison we also give the solar abundances from Grevesse & Sauval (1998). The abundances and errors are calculated using weights that are estimated from the errors on the individual lines (cf. Section 3.2.5). The error estimates that we give in Table 1 do not include the systematic error due to the uncertainty of the atmospheric model parameters which will be discussed in Section 3.3.1.

Generally we find that the abundances of most elements lie around the Solar value within the error bars. Only for Fe and Ca do we find enough lines (16 and 7) to make a truly reliable estimate of the abundances.

The Fe abundance is $\log N_{\rm Fe}/N_{\rm tot} = -4.67 \pm 0.02$ from 16 Fe I lines (we quote the internal weighted error; the internal RMS scatter is 0.18 dex). If we assume that the photospheric hydrogen and helium abundance is the same

**Fig. 2.** Differential magnitudes of HD 49434 minus comparison star HD 48922 in the Strömgren $b$ band (asterisks). The dots are the magnitude differences between the two comparison stars HD 49933 and HD 48922 (shifted to allow comparison). Individual days are marked in every panel as the corresponding HJD

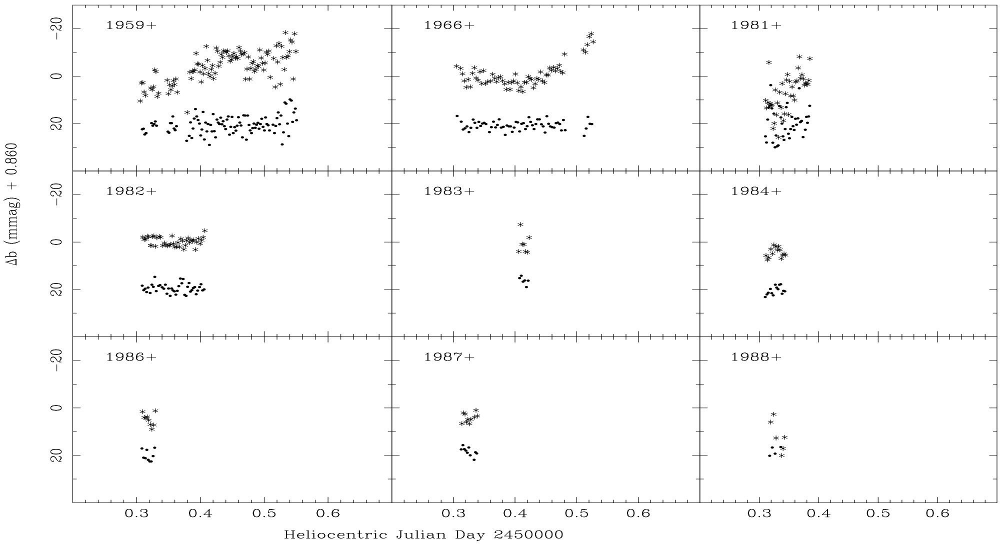


**Table 2.** Strömgren photometric indices taken from Hauck & Mermilliod (1998) for the four stars used for the HD 49434 observations from Sierra Nevada

| Star | $V$ | $b-y$ | $m_1$ | $c_1$ | $H_\beta$ |
|---|---|---|---|---|---|
| HD 48922 | 6.77 | -0.015 | 0.142 | 0.940 | - |
| HD 49933 | 5.78 | 0.270 | 0.127 | 0.460 | 2.662 |
| HD 50747 | 5.45 | 0.095 | 0.172 | 1.131 | 2.833 |
| HD 49434 | 5.74 | 0.178 | 0.178 | 0.717 | 2.755 |

in HD 49434 and the Sun this abundance corresponds to [Fe/H] $= -0.13 \pm 0.14$ (including systematic errors). This agrees roughly with the result from the Strömgren $m_1$ index which yields [Fe/H] $= -0.01 \pm 0.20$.

An interesting result is the ratio [Ca/Fe] $= +0.30 \pm 0.21$ which is a quite high value for a star with Solar-like abundances.

We note that we have adjusted the $\log gf$ for the Ca II line at 5857.451 Å line by comparing with the solar spectrum, i.e. from $\log gf = 0.257$ to 0.550. The $\log gf$ values for the Si lines are determined solely from theoretical calculations. Therefore we have computed the synthetic spectrum for the Si-lines we have used – using the solar abundance – and comparing this with the observed solar spectrum. We find that the $\log gf$ values seem to be right for the lines we have used.

Lastennet et al. (2001) have determined fundamental atmospheric parameters of HD 49434 by comparison of the observed and synthetic photometric colours. The star is among the nine potential COROT targets stars they have studied. From the combination $(B-V)$, $(U-B)$, $(b-y)$ they find $\log g = 4.0 \pm 0.4$, $T_{\rm eff} = 7\,240 \pm 100$ K and [Fe/H]$= -0.1 \pm 0.2$ (from Table 2 and Figure 7 and 8 in Lastennet et al. 2001). Thus, the metallicity they find is in agreement with our result from spectroscopy and all the fundamental parameters are in agreement with the estimates based on Strömgren photometry.

We finally note that HD 49434 is included in the $\Delta a$ photometry catalogue of bright B and A stars by Vogt et al. (1998) but they find no evidence for the star being chemically peculiar.

### 3.3.1. Accuracy of the derived abundances

The errors quoted in Table 1 for the abundances are the weighted internal errors (cf. Section 3.3.1). Here we will discuss the error contribution from the uncertainty of the atmospheric model parameters. The atmospheric model we used for the final abundance result have the parameters $T_{\rm eff} = 7\,300$ K and $\log g = 4.1$. To investigate the effect of the choice of atmospheric model we calculated Fe abundances for models with $T_{\rm eff} = 7\,100, 7\,300, 7\,500$ K and $\log g = 4.1$ and one model with $T_{\rm eff} = 7\,300$ and $\log g = 4.3$. We find that the effect of increasing $\log g$ by 0.2 dex decrease the Fe abundance by about $0.04 \pm 0.05$ dex (sd. of mean) which is not significant. On the other hand, if we increase the temperature of the atmospheric model by 200 K we find an increase of Fe by $0.10 \pm 0.05$ dex, i.e. a significant effect.

Another input parameter for the calculation of the synthetic spectrum is the microturbulence. The value used in the calculation of the Kurucz atmosphere model does not affect the derived abundances significantly, but when calculating the synthetic spectrum the effect is indeed signif-

**Fig. 3.** Power spectra corresponding to the variable star HD 49434 minus the comparison star HD 48922, in the upper panel, and that corresponding to the comparison stars HD 49933 minus HD 48922 in the bottom panel. The scales are milli-magnitudes and cycles/day

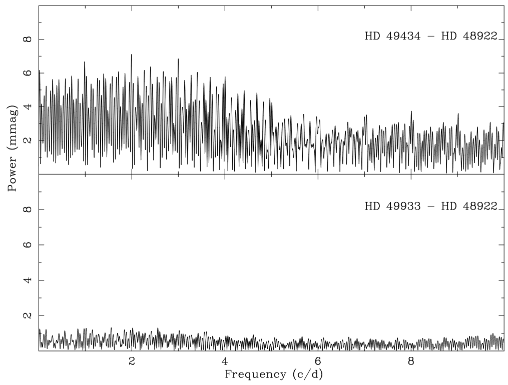


**Fig. 4.** Location of HD 49434 (star symbol) in the HR diagram together with the known $\delta$ Scuti (circles, Rodríguez & Breger 2001) and bona fide $\gamma$ Dor (triangles, Handler & Kaye 2001) pulsators. The edges of the $\gamma$ Dor region around $(b-y)_0 = 0.2$ are from Handler (1999). The absolute magnitude of HD 49434 is $M_V = 2.73 \pm 0.07$ and is derived from its Hipparcos parallax (ESA 1997)

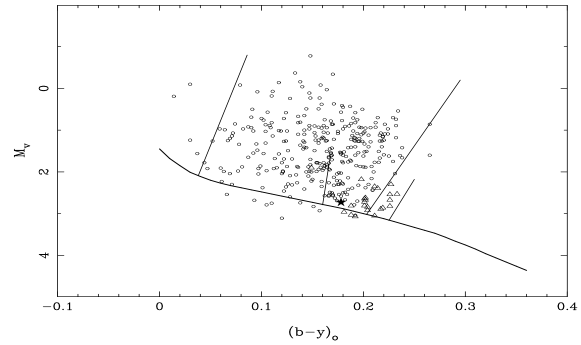


icant. When changing the microturbulence the change in equivalent width depends on the strength of the line. By using this fact, one can adjust the microturbulence until the abundance of individual lines do not correlate with equivalent width. We could not do this very accurately due to the high rotational velocity of HD 49434. Thus, we estimate the microturbulence to be $\xi_t = 2.1 \pm 0.5$ km s$^{-1}$.

We find that when increasing $\xi_t$ by 0.5 km s$^{-1}$ the abundance of Fe decreases by $0.10 \pm 0.04$ dex, i.e. a significant contribution to the uncertainty of the abundance.

We conclude that the contribution to the error of abundances due to uncertain model atmosphere parameters, i.e. $T_{\rm eff}$ and microturbulence, is of the order 0.14 dex. For a realistic estimate of the abundance of elements in HD 49434 this contribution must be added to the internal errors (sd. of mean) given in Table 1. For example for the metallicity of HD 49434 we get [Fe/H] $= -0.13 \pm 0.14$, i.e. the uncertainty of the model parameters is the main error source.

## 4. Strömgren photometry time series

We have observed HD 49434 with a Strömgren photometer on the 0.9m telescope at Sierra Nevada near Granada, Spain. We used a 45" diaphragm to observe HD 49434 and the comparison stars HD 48922=C1, HD 49933=C2, and HD 50747=C3. The star HD 49933 is a V = 5.78 double system with a faint companion of magnitude V = 11. This last star was included within the diaphragm because of its proximity but had no influence on the final differential photometry. The Strömgren parameters for the observed stars are given in Table 2.

Continuous photometric time series of comparison stars HD 48922, HD 49933 and HD 49434 were made in order to remove the sky transparency fluctuations to be able to see the variations of the target star. Magnitude differences between HD 49933 and HD 48922 are constant within 3.7 mmag (rms) and clear intrinsic variations can be seen for HD 49434. The light curve is shown in Figure 2.

The time series consist of data from nine nights spread unevenly over one month starting on July 2001. Unfortunately the weather conditions were not good during our first night of observation and HD 49434 was observed again a week later. Observations were possible only three weeks later where the star was included in a program where other targets were also measured. Thus the dedicated observing time was limited to only a few measurements but the data could be used to confirm the long-term variations that were seen in the first days.

In total the time series consists of 295 data points in the four Strömgren bands (*uvby*). In Figure 2 we show the time series of HD 49434 - HD 48922 (target - comparison star 1) and HD 49933 - HD 48922 (comparison star 2 - comparison star 1). The magnitude differences are plotted for the Strömgren *b* band.

From Figure 2 it is clear that the intrinsic photometric variations are associated with HD 49434. At first sight the star does not seem to have periodic variations. A power spectrum was calculated in order to search for possible frequency components which is shown in Figure 3. It can be seen that with the present data, no clear discrete frequency components are present. Instead the low frequency region has a significant contribution for HD 49434 which is not seen for the comparison stars.

This behaviour is typical among the recently discovered $\gamma$ Dor stars (Zerbi et al. 1999) which are g-mode pulsators. We believe that HD 49434 is a variable star of this type: the star is classified as a main sequence F2-type star from Strömgren photometry and its position in the Hertzsprung-Russell diagram in Figure 4 confirm our hypothesis. Because we have not detected any clear periodicity it is not possible to test the phase differences

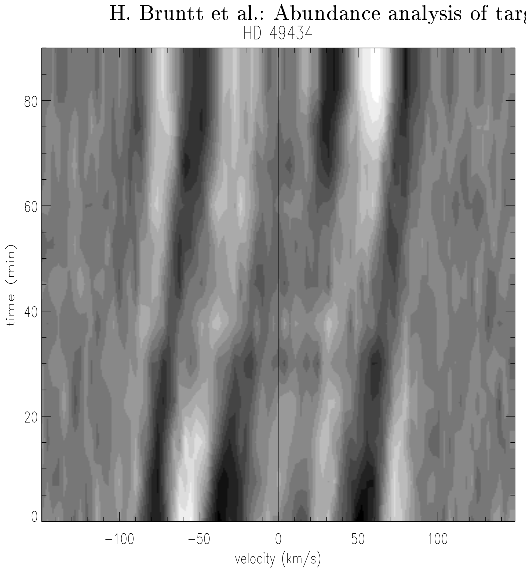

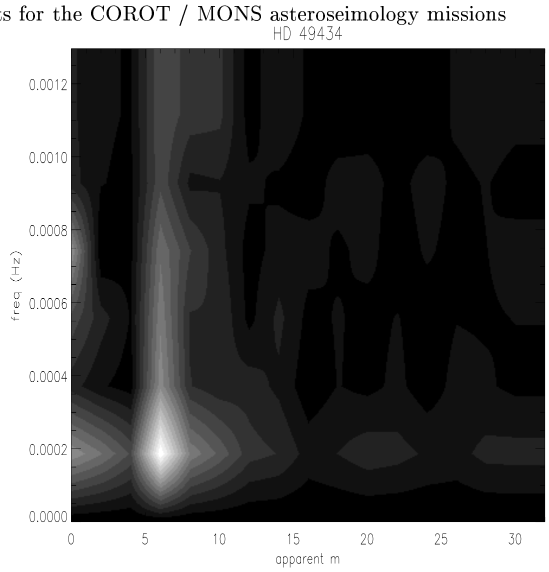


**Fig. 5.** The residual of the mean profile for the January 2000 series. *Left:* in velocity – time space; the maximum amplitude is of the order of $3 \times 10^{-3}$; *Right:* Spectral power density of the same data, in apparent order – frequency space, after the 2D Fourier transform

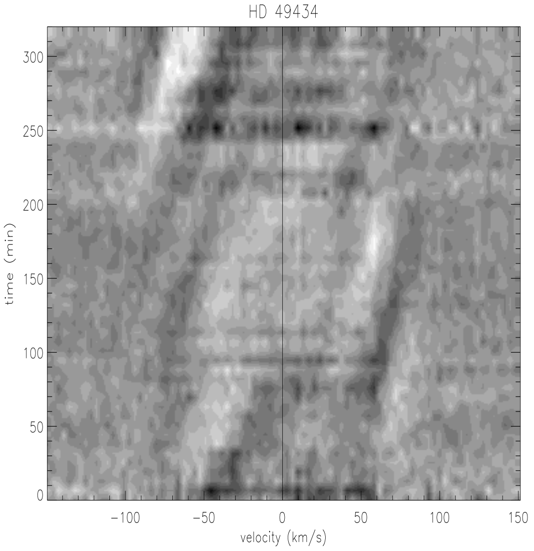

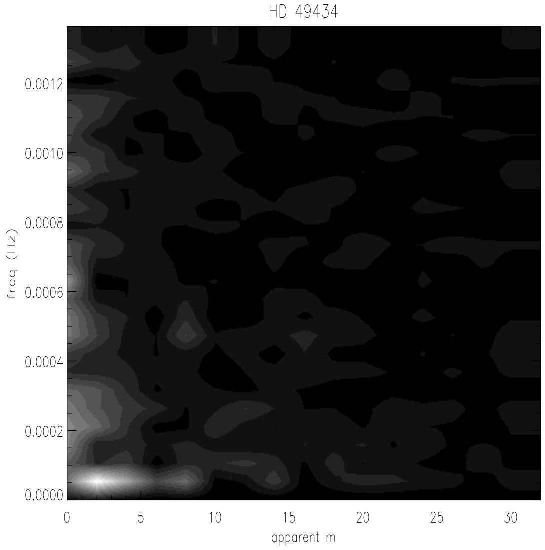


**Fig. 6.** The same as Figure 5 but for the December 2000 series; the maximum amplitude of the residuals is of the order of $4 \times 10^{-3}$

among the different photometric colours which is a clear signature of the non-radial pulsating nature of the $\gamma$ Dor stars – see Garrido (2000) for details.

## 5. Spectroscopic monitoring of HD 49434

In the following we will discuss the analysis of the time series of spectra of HD 49434 to look for any systematic variation of line profiles.

### 5.1. Data reduction

All data were reduced on-site, using the automatic INTER-TACOS procedure (Baranne et al. 1996), resulting in wavelength-calibrated, flat-field corrected spectra. Each spectrum is segmented into 67 segments corresponding to the 67 orders of the spectrograph present on the detector. We then performed a large scale normalisation of the overall spectrum, so that the resulting spectra are normalised to unity all across the covered wavelength domain, even though some local problems still remain with this normalisation on the edges of the orders.

The ELODIE spectrograph provides a wide enough spectral coverage to give access to a large number of photospheric lines. In order to take advantage of this, and to fully exploit the information contained in these numerous photospheric lines, we used the Least-Square Deconvolution (LSD) technique (Donati et al. 1997) to analyse the variations of a "mean" photospheric line. In this method, a line pattern function is constructed, containing all the lines supposedly present in the spectrum as Dirac functions, with heights set to the central line depths as calculated by Kurucz's (1979) "SYNTHE" program. The observed spectrum is then deconvolved with this line pattern function, yielding a "mean" photospheric line profile. With this technique, line blends are automatically taken into account when all the lines present in the spectrum are considered. Note that the depth of the resulting "mean" line has no physical meaning, but that time variations of this depth, as well as line profiles can be accurately analysed with this technique. We used a Kurucz model for $T_{\rm eff} = 7\,000$ K and log $g = 4$, sufficiently close to the values derived in this paper, for constructing the line pattern function.

A total of 1700 lines were finally used in this analysis. In the following of this work, we shall call "mean" photospheric line, the line constructed with the LSD technique, while the adjective "average" will be reserved for time averages of line profiles.

All mean profiles in each series were normalised to the same equivalent width. This procedure eliminates the effects of the large scale variations of the mean line profile, due for instance to normalisation problems that may vary from spectrum to spectrum. The time average of the mean profiles was then constructed for each series, and subtracted from the mean line profiles of the series.

We then performed a two-dimensional Fourier transform analysis, following the method described in Kennelly et al. (1996). This method is well suited for the analysis of the spectroscopic signature of non-radial pulsations. Each line profile was interpolated on a grid representing stellar longitudes, transforming velocities across the line profile into longitudes on the stellar equator using the relation $v - v_r = v \sin i \, \sin \phi$, where $v$ is the velocity in the profile, $v_r$ is the radial velocity of the star, measured to be $v_{\rm rad} = -12.3 \pm 1.0$ km s$^{-1}$, $\phi$ is the corresponding stellar longitude, and $v \sin i$ is the projected rotation velocity of the star, estimated to be $84 \pm 4$ km s$^{-1}$.

For the time series from January 2000, the spectra were recorded at constant time intervals during the whole monitoring, while a few short gaps exist in the December 2000 series. For this latter series, prior to the 2D Fourier transform, we had to build up a grid of constant time intervals, filling the gaps during which no spectrum was obtained with null data.

After these steps, the data were submitted to a 2D Fourier transform, resulting in a representation of the data in the (frequency – apparent $m$) space. The apparent $m$ is related to the structure of the modes present at the stellar surface, without being identical to the usual azimuthal order $m$, since the apparent $m$ depends for instance on the inclination angle $i$ of the rotation axis of the star with respect to the line of sight. The apparent $m$ is nevertheless indicative of the surface structure of the modes detected.

### 5.2. Detected variability of spectral lines

Figure 5 (and Figure 6) presents the results of this analysis for the series from January 2000 (and December 2000). At both epochs we detect the presence of line profile perturbations, crossing the profile from blue to red. Such perturbations are most probably the signature of non-radial pulsation modes at the stellar surface. The Figures 5 and 6 suggest the presence of one or several high-degree modes. These modes are particularly obvious in the January 2000 series, owing to the high signal-to-noise ratio of the spectra, while they are less conspicuous, although present without doubt, in the lower quality December 2000 data. The amplitudes of the residuals are of the order of $2$–$3 \times 10^{-3}$ at both epochs. They can be easily detected thanks to the very high signal-to-noise ratio (S/N) of the LSD mean line profiles combining hundreds of spectral lines, which reach S/N=3 000 in the December 2000 series and S/N=6 000 in the January 2000 series.

These modes seem to be long-period modes. This is particularly clear in Figure 6 (right), where the frequency of the detected modes are at the resolution limit of our dataset, i.e. 0.1 mHz, indicating a period longer than 160 minutes, that is to say longer than half the time span of the monitoring. These results therefore confirm those of the photometric observations, and suggest that HD 49434 is probably a variable of the $\gamma$ Doradus type.

The modes we detect in the January 2000 series are high-degree modes, with an apparent order of 6. In the December 2000 series, our lower quality data still indicates non-radial modes, but with more power on the apparent order 2, some signal still appearing at apparent order 8.

## 6. Conclusions and future prospects

We have presented the detailed abundance analysis of HD 49434. The analysis could not be made by simple equivalent width measurements since most lines are blended, because the star has high projected rotational velocity. We have described the VWA software which selects the least blended lines and derive abundances semi-automatically.

We find that the metallicity of HD 49434 is somewhat below the Solar value, i.e. [Fe/H]$= -0.13 \pm 0.14$. The quoted error includes the estimated error due to the uncertainty of the atmosphere parameters, especially $T_{\rm eff}$ and microturbulence.

The metallicity we find agrees with the results from Strömgren photometry and the work by Lastennet et al. (2001) who have compared observed and synthetic photometric colours. When taking into account the uncertainty of the basic atmosphere parameters the accuracy of VWA is only slightly more accurate than the photometric methods. The advantage of analysing the spectra with VWA is that we obtain estimates for several elements.

We have already used VWA for the analysis of several other stars which will be published soon (Bikmaev et al. 2002, Rasmussen et al. 2002). In the paper by Bikmaev et al. we have analysed two A-type stars, which have low $v \sin i$. Thus we have made a detailed comparison of the result obtained with VWA and with the "classical" method based on equivalent width measurements of non-blended lines – the agreement is excellent for nearly all lines (abundances $< 0.03$ dex).

With the confirmation that VWA can be used for reliable semi-automatic abundance analysis we will proceed to use the software for analysis of the proposed main targets for the asteroseismology satellite missions COROT and MONS/Rømer: the spectra have already been obtained.

For our future use of VWA we expect that for stars with low $v \sin i$ ($<$ 40–50 $\mathrm{km\,s^{-1}}$) it will be possible to constrain the atmospheric parameters (eg. microturbulence and $T_{\mathrm{eff}}$) by adjusting these so the abundances found from lines of the same element do not correlate with the line parameters (eg. equivalent width and excitation potential). For stars with higher $v \sin i$ ($>$ 100 $\mathrm{km\,s^{-1}}$) the selection of atomic lines for abundance analysis becomes exceedingly difficult. For such stars the metallicity and the basic parameters must be determined mainly from photometric colours, but it is still important to obtain spectra to be able to put constraints on $T_{\mathrm{eff}}$ (from the hydrogen lines) and $v \sin i$. For example, stars with too high $v \sin i$ may not be suitable for seismology since this will make the analysis much more complex.

In the present paper we have also presented the photometric light curve of HD 49434 based on observations during part of nine nights over a period of one month. We find that the star is indeed variable with excess power around 1-5 cycles per day, but no periodic signal could be found from the limited data set. We have also analysed the spectroscopic line profiles which show evidence for long-period variability at low amplitude. This behaviour is characteristic for the $\gamma$ Dor variables, and we propose that HD 49434 is indeed a variable of this type. A longer time series is needed to be able to detect any periodic pulsation signal.

The star has been chosen as a main target for COROT which means that the star will be observed for around 150 days. We will then be able to probe the interior of this star in detail by using seismic techniques. To do this one needs to constrain the fundamental parameters of the star which indeed has been aim of the work presented here.

*Acknowledgements.* The software VWA was developed during Bruntt's stay at the Astronomy Institute of the University of Vienna from November 2000 to June 2001 and was in part supported by projects S7303 and P14984 funded by the *Fonds zur Förderung der wissenschaftlichen Forschung*. We wish to thank Tanya Ryabchikova and Werner W. Weiss for advice on the development of the VWA program. We are grateful to Werner W. Weiss for letting us use the VALD database. We also wish to thank Nikolai Piskunov for letting us use his software for the calculation of synthetic spectra (SYNTH). Thanks to R. L. Kurucz for making his model atmosphere code and data available.

## References

Baranne A., Queloz D., Mayor M., Adriansyk G., Knispel G., Kohler D., Lacroix D., Meunier J. P., Rimbaud G., Vin A., 1996, A&AS 119, 373

Bikmaev I. F., Ryabchikova T., Bruntt H., Musaev F. A., Mashonkina L., Belyakova E. V., Shimansky V., Barklem P. S., 2002, A&A, accepted

Catala C., 2001, in First COROT/MONS/MOST Ground-based Support Workshop ed. Sterken C., University of Brussels, p. 9

Canuto V. M., Mazzitelli I., 1991, ApJ 370, 295

Canuto V. M., Mazzitelli I., 1992, ApJ 389, 724

Donati J. F., Semel M., Carter B. D., Rees D. E., Cameron A. C., 1997, MNRAS 291, 658

ESA, 1997, The Hipparcos and Tycho Catalogues, ESA SP-1200

Garrido R., 2000, in Delta Scuti and Related Stars, eds. M. Breger, M. H. Montgomery, ASP Conf. Series, 210, 67

Grenier S., Burnage R., Farraggiana R. et al., 1999, A&AS, 135, 503

Grevesse N., Sauval A. J., 1998, Space Science Reviews 85, 161

Handler G. 1999, MNRAS 309, L19

Handler G., Kaye A. B., 2001, "A catalogue of Gamma Doradus stars", `http://sirius.saao.ac.za/~gerald/gdorlist.html`

Hauck B., Mermilliod M., 1998, A&AS, 129, 431

Kennelly E. J., Walker G. A. H., Catala C., Foing B. H., Huang L., Jiang S., Hao J., Zhai D., Zhao F., Neff J. E., Houdebine E. R., Ghosh K. K., Charbonneau P., 1996, A&A 313, 571

Kupka F., 1996, ASP Conf. Ser., 108, p. 73, eds. Adelman S.J, Kupka F., Weiss W. W.

Kupka F., Piskunov N., Ryabchikova T. A., Stempels H. C., Weiss W. W., 1999, A&AS 138, 119

Kupka F., Bruntt H., 2001, First COROT/MONS/MOST Ground-based Support Workshop, p. 39, ed. Sterken C., University of Brussels

Kurucz, R. L., 1979, ApJS, 40, 1

Kurucz R. L., 1993, CD-ROM 18, ATLAS9 Stellar Atmosphere Programs and 2 km/s Grid

Lastennet E., Lignières F., Buser R., Lejeune T., Lüftinger T., Cuisinier F., van't Veer-Menneret C., 2001, A&A, 365, 535

Mittermayer P., 2001, Die Atmosphäre des $\delta$ Scuti Sterns FG Virginis, Master Thesis, University of Vienna

Napiwotzki R., Schoenberner D., Wenske V, 1993, A&A, 268, 653

Piskunov N. E., 1992, Stellar Magnetizm, eds. Yu. V. Glagolevsky, I. I. Romanjuk, St. Petersburg, Nauka, p. 92

Rasmussen M. B., Bruntt H., Frandsen S., Paunzen E., Maitzen H. M., 2002, A&A, accepted
Rodríguez E., Breger M., 2001, A&A 366, 178
Rogers N. Y., 1995, Comm. in Asteroseismology 78
Ryabchikova T. A., Piskunov N. E., Stempels H. C., Kupka F., Weiss W. W. 1999, Phys. Scripta 83, 162
Smalley B., 1993, A&A 274, 391
Smalley B., Kupka F., 1997, A&A 328, 349
Valenti J. A., Piskunov N., 1996, A&AS 118, 595
Vogt N., Kerschbaum F., Maitzen H. M., Faundez-Abans M. 1998, A&AS, 130, 455
Zerbi F. M., Rodríguez E., Garrido R. et al. 1999, MNRAS, 303, 275

# II

# Abundance Analysis of the Giant $\xi$ Hydrae & the $\delta$ Scuti Stars in NGC 6134

Bruntt, H. & Frandsen, S.

*A Semi-automatic Method for Abundance Analysis: Two Case Studies: The Giant Star $\xi$ Hya and the $\delta$ Scuti stars in NGC 6134*

2003, Proc. of Modelling of Stellar Atmospheres, IAU symp. 210, eds. N. E. Piskunov, W. W. Weiss, D. F. Gray, *in press*

*Modelling of Stellar Atmospheres*
*IAU Symposium, Vol. xxx, xxxx*
*N. E. Piskunov, W. W. Weiss, D. F. Gray, eds.*

# A Semi-automatic Method for Abundance Analysis Two Case Studies: The Giant Star $\xi$ Hydrae and the $\delta$ Scuti Stars in NGC 6134

H. Bruntt[1] and S. Frandsen[1]

*Institute for Physics and Astronomy, University of Aarhus, Denmark*

**Abstract.**
We have developed the software tool VWA to carry out abundance analysis semi-automatically. Here we present the abundance analysis with VWA for two case studies: The newly discovered G7-giant field star $\xi$ Hydrae and for several $\delta$ Scuti Stars in the open cluster NGC 6134.

## 1. Overview of the VWA Abundance Analysis Software

We have developed an IDL based software called VWA for semi-automatic abundance analysis (Bruntt et al. 2002). VWA runs though the line lists extracted from the VALD database (Kupka et al. 1999) and selects lines that suffer from the the least amount of blending: the allowed "degree" of blending is chosen by the user. For a specified wavelength region around each selected line the synthetic spectrum is calculated for different abundances of the element forming the line – until the equivalent width of the observed and synthetic spectrum match. When this is done, each fitted line can be inspected visually with VWA – and the abundance fit may either be accepted, rejected or improved manually.

Examples of lines fitted with VWA are shown in Figure 1 for two quite different stars: The $\gamma$ Dor star HD 49434 (F2-V) with $v \sin i = 84$ km s$^{-1}$ and the giant star $\xi$ Hya (G7-III) which has $v \sin i = 1.5$ km s$^{-1}$.

Because HD 49434 has a high $v \sin i$ the lines are very broad and blending is a severe problem. We determined the Fe abundance from the least blended lines and we then allowed blending of other elements with Fe: thus we could determine the abundances of other elements. An example of this is the Ca line at $\lambda 5594.46$ Å in the top plot of Fig. 1. While blending is not a huge problem in the slowly rotating giant star $\xi$ Hya, we used the same approach to find more lines. An example of using the blend of a Fe line and a Cr line at $\lambda 5478.37$ Å is shown in the bottom plot of Fig. 1.

## 2. Summary of Results with VWA

So far we have used VWA to do abundance analysis for several stars: The $\gamma$ Dor star HD 49434 (Bruntt et al. 2002), the standard A-type stars HD 32115 and HD 37594 (Bikmaev et al. 2002), four $\delta$ Scuti stars (presented here and published in Rasmussen et al. 2002), nine COROT stars (Bruntt et al. 2003), and the giant star $\xi$ Hydrae (presented here)

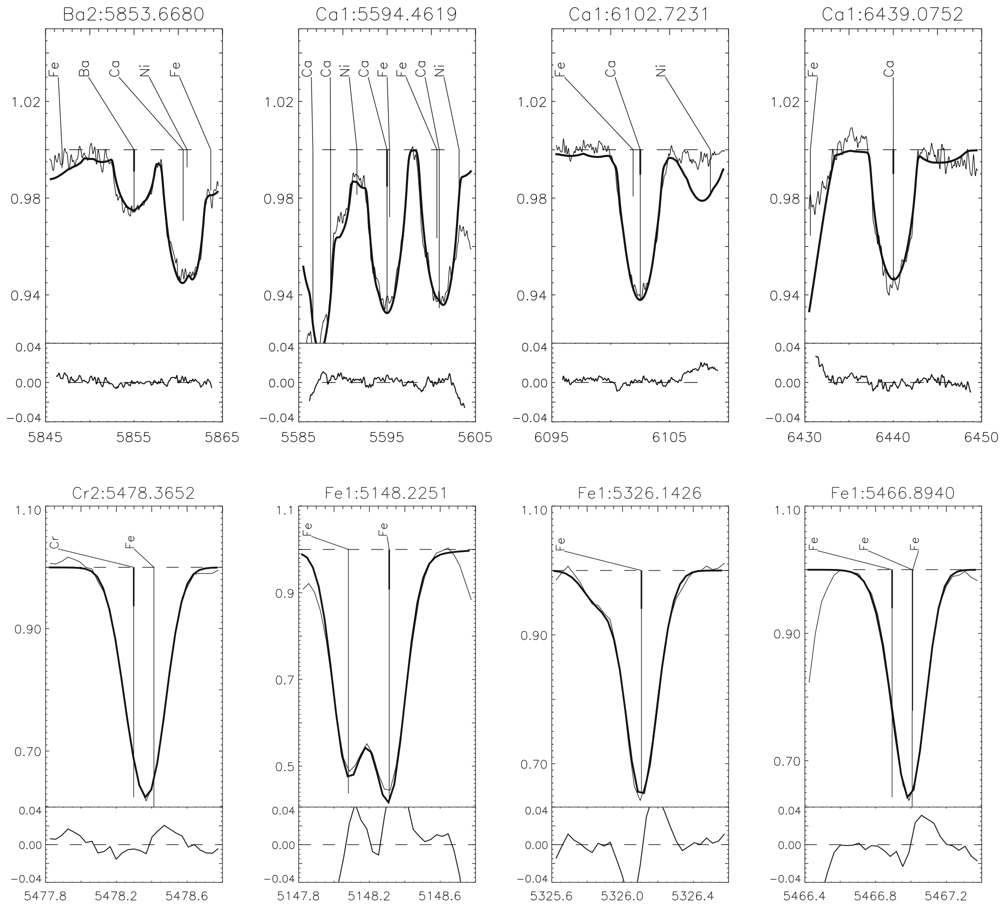


Figure 1. Examples of lines fitted with VWA for the $\gamma$ Dor star HD 49434 (Bruntt et al. 2002) (*above*) and the giant star $\xi$ Hya (*below*). The line styles are: *observed* (thin line) and *synthetic* (thick line). The lower portion of the each plotted line shows the relative difference between the observed and synthetic spectrum. The name of the element and the central wavelength (in Ångstrøm) of each fitted line is given at the top of each plot

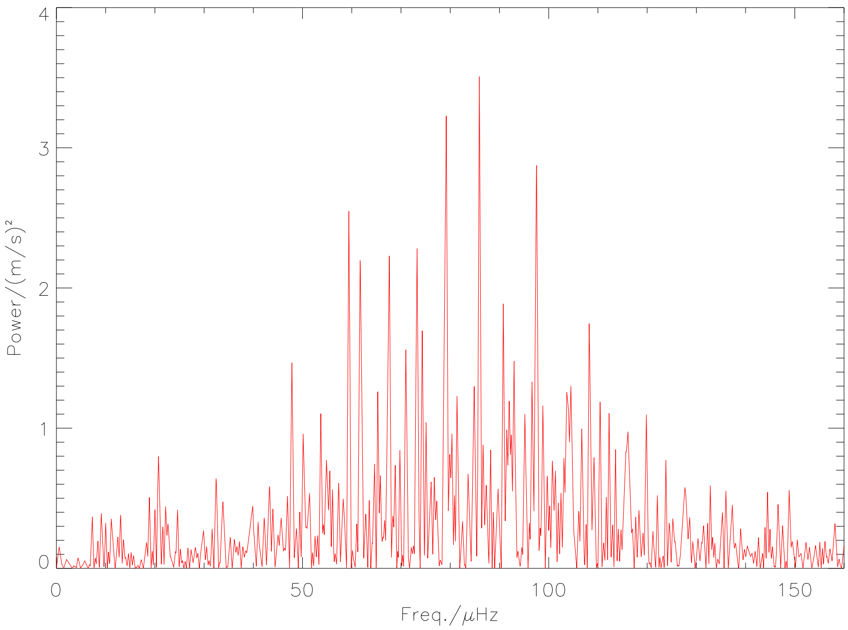


Figure 2. Power spectrum for $\xi$ Hya. Modes are clearly present in the range 50–130 $\mu$Hz, corresponding to periods of 2.0-5.5 hours

## 3. The G7-III Giant $\xi$ Hydrae

The stellar parameters for this star have become of particular interest due to the recent detection of solar-like oscillations. The announcement of this was made with the ESO Press Release 10/02 and more details can be found in Frandsen et al. 2002. The power spectrum in Fig. 2 shows the presence of several closely spaced modes.

Before we can extract the seismic information from the power spectrum we must know the fundanmental parameters of $\xi$ Hya to the best possible precision. Using the infrared flux method (Blackwell 1998) found $T_{\rm eff} = 5058$ K. In literature the metallicity of $\xi$ Hya has been determined from relatively few lines. Hence we have re-determined the over-all metal content.

## 4. Abundance Analysis of $\xi$ Hydrae

A small set of the best spectra observed with the CORALIE spectrograph have been combined and analysed using the VWA technique. In Fig. 3 (*top*) we show the result for six iron-group elements for three different models.

Our best estimate is for Model A where we see no correlation of the abundance of individual lines with equivalent width or the lower excitation potential. This indicates that the model atmosphere is correct: cf. *bottom* part of Fig. 3. From this figure we can also estimate the sensitivity of the metallicity when increasing $T_{\rm eff}$ or microturbulence. We estimate the model-dependent error to be $\Delta$[M/H]$\simeq 0.04$ dex.

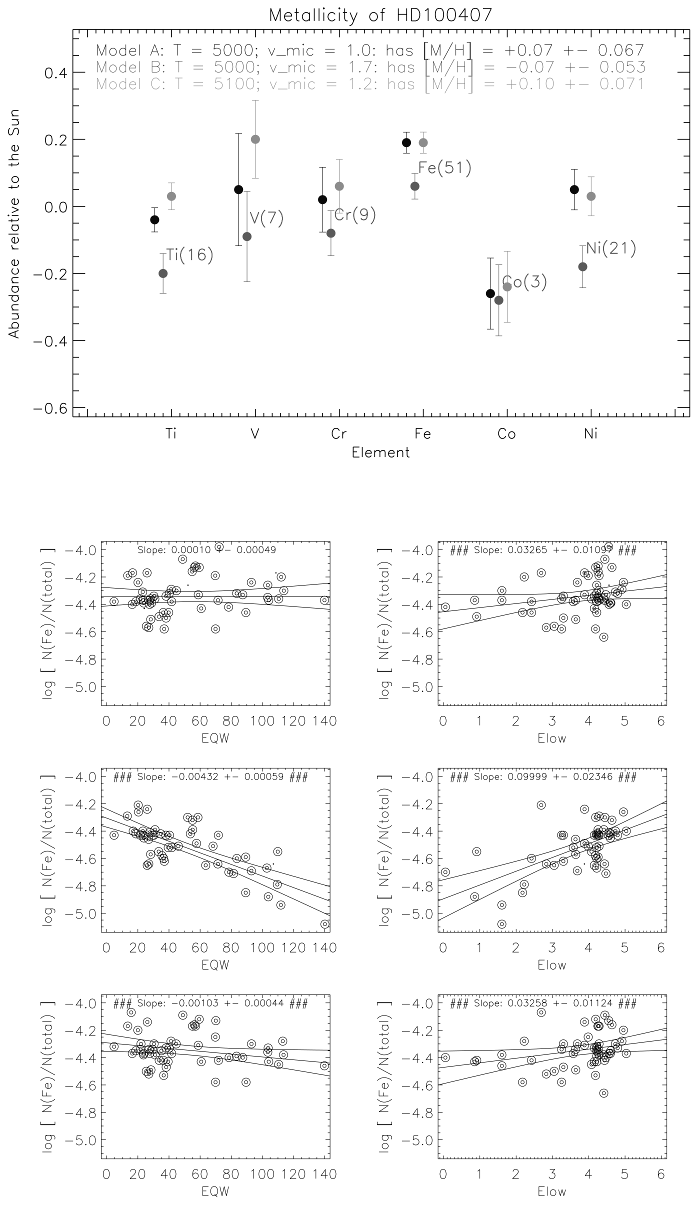


Figure 3. (*Top*) To determine the over-all abundance of heavy elements in $\xi$ Hya (HD 100407) we used abundances for six iron group elements. The results for three different models are shown. Model A is our final result, Model B has increased microturbulence, and model C has a somewhat higher temperature of the model atmosphere. (*Bottom*) We show the abundance of individual lines against the equivalent width (EQW) and the lower excitation potential ($E_{low}$). The three horizontal plots from top to bottom correspond to the three models A, B, and C.

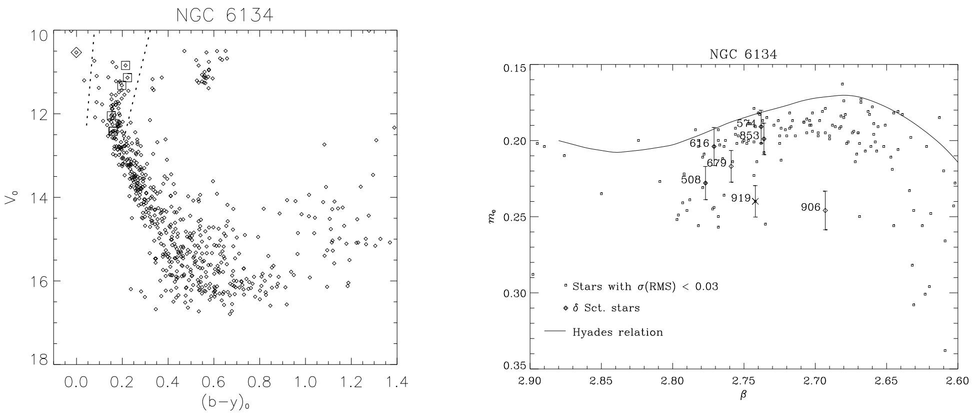


Figure 4. (*Left:*) Colour-magnitude diagram of NGC 6134 (Bruntt et al. 1999) The $\delta$ Scuti stars are marked with box symbols. The instability strip is shown with dashed lines. (*Right:*) The Strömgren $m_0$ index for the stars in NGC 6134. The standard relation for the Hyades cluster is shown as a solid line. Evidently, the stars in NGC 6134 have high metallicity. For many of the A-type stars ($\beta \simeq 2.77 \pm 0.03$) the $m_0$ index is very high. This may indicate that they are Am-type stars.

We find the over-all metallicity of $\xi$ Hya to be [M/H]$= 0.06 \pm 0.07$ which is in agreement with literature: McWilliam (1990) found [Fe/H]$= -0.04 \pm 0.12$.

## 5. Case 2: $\delta$ Scuti Stars in and the Metallicity of NGC 6134

We have made an attempt to answer the question: Why do variable and non-variable stars appear side by side in the instability strip in the HR diagram? We have searched for possible differences in metallicity and $v \sin i$ in pairs of stars in the open cluster NGC 6134.

We have obtained medium resolution Echelle spectra observed with the DFOSC at the Danish 1.54m at La Silla.

Strangely enough, there are no significant differences between variables and constant stars. There are a few marginal Am stars among the variables. Full Am character has never been seen in a $\delta$ Scuti star and the two groups of stars are thought to be exclusive (Kurtz 2000).

In Fig. 4 (*left*) we show the colour-magnitude diagram of NGC 6134. The instability strip is shown, and the six known $\delta$ Scuti stars have been marked by boxes. To the *right* we show the Strömgren $m_0$ index versus the $H_\beta$ index (temperature decreases to the right, [Fe/H] decreases upwards). We have used the spectra to carry out an abundance analysis of the $\delta$ Scuti stars in NGC 6134 to confirm the high metal content of the cluster found from the Strömgren $m_1$ index. From four $\delta$ Scuti stars we find [Fe/H] $= +0.38 \pm 0.05$ which is in agreement with the result obtained from Strömgren photometry, ie. $[\mathrm{Fe/H}]_{\mathrm{phot}} = +0.28 \pm 0.10$ (Bruntt et al. 1999).

In Fig. 5 we show the distribution of projected rotational velocities ($v \sin i$) for NGC 6134 and four other nearby open clusters. The coloured part of the

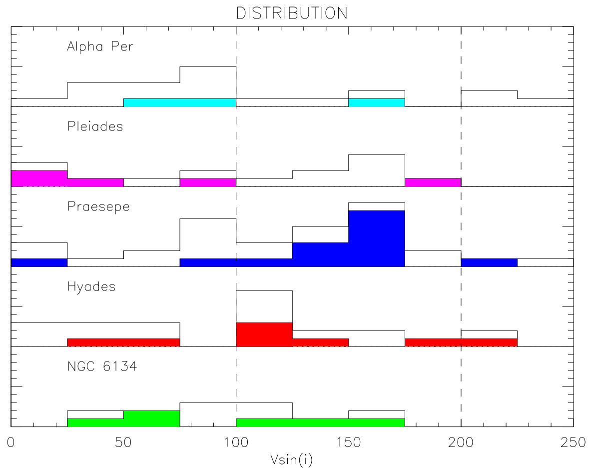


Figure 5. Histograms of the distribution of rotational velocities in five open clusters. The coloured areas indicate the fraction of $\delta$ Scuti stars in a given column, eg. in NGC 6134 there are two $\delta$ Scuti stars with $v \sin i$ between 50 and 75 km s$^{-1}$.

histograms indicate the $\delta$ Scuti stars. Although the number statistics are bad, it seems that there is no real difference in $v \sin i$ for $\delta$ Scuti stars and stable stars. Our result that the $v \sin i$ of the $\delta$ Scuti stars are evenly distributed from 30 to 180 km s$^{-1}$ is in good agreement with Solano & Fernley (1997).

## References

Bikmaev, I. F., Ryabchikova, T. A., Bruntt, H. et al., 2002, A&A, 389, 537

Blackwell, D. E., Lynas-Gray, A. E., 1998, A&AS, 129, 505

Bruntt, H., Frandsen, S., Kjeldsen, H., Andersen, M. I., 1999, A&AS, 140, 135

Bruntt, H., Catala, C., Garrido, R. et al., 2002, A&A, 389, 345

Bruntt, H., Bikmaev, I. F., Catala, C. et al., 2003, A&A, *in preparation*

Frandsen, S., Carrier, F., Aerts, C., Stello, D., Maas, T., Burnet, M., Bruntt, H., Teixeira, T. C., de Medeiros, J., Bouchy, F., Kjeldsen, H., Pijpers, F., Christensen-Dalsgaard, J., 2002, A&A, 394, L5

Kupka, F., Piskunov, N., Ryabchikova, T. A., Stempels, H. C., Weiss, W. W., 1999, A&AS, 138, 119

Kurtz, D., 2000, ASP Conf. Ser. 210, 287

McWilliam, A., 1990, ApJS, 74, 1075,

Rasmussen, M. B., Bruntt, H., Frandsen, S., Paunzen, E., Maitzen, H. M., 2002, A&A, 390, 109

Solano, E., Fernley, J., 1997, A&AS, 122, 131

# III

# Abundance analysis of the COROT main targets

Bruntt, H., Bikmaev, I. F., Catala, Weiss, W. W., Solano, E., Stütz, C. Bouret, J. C., Hua, T., Lignières, F., Charpinet, S., Van't Veer-Menneret, C., Ballereau, D.

*Abundance Analysis of Targets for the COROT/ MONS Asteroseismology Missions. II. Abundance analysis of the COROT main targets*

2003, A&A, *in preparation*

*Astronomy & Astrophysics* manuscript no.
(will be inserted by hand later)

# Abundance analysis of targets for the COROT / MONS asteroseismology missions

## II. Abundance analysis of the COROT main targets*

H. Bruntt[1], I. F. Bikmaev[2], C. Catala[3], E. Solano[4], W. W. Weiss[5], C. Stütz[5], D. Ballereau[6], J.C. Bouret[7], S. Charpinet[8], T. Hua[7], D. Katz[6], F. Lignières[8], T. Lüftinger[5], and C. Van't Veer-Menneret[6]

[1] Department of Physics and Astronomy, Aarhus University, Bygn. 520, DK-8000 Aarhus C, Denmark
[2] Department of Astronomy, Kazan State University, Kremlevskaya 18, 420008 Kazan, Russia
[3] Observatoire de Paris, LESIA, France
[4] Laboratorio de Astrofisica Espacial y Fisica Fundamental, P. O. Box 50727, 28080 Madrid, Spain
[5] Institut für Astronomie, Universität Wien, Türkenschanzstrasse 17, A-1180 Wien, Austria
[6] Observatoire de Paris, GEPI, France
[7] Laboratoire d'Astrophysique de Marseille, France
[8] Laboratoire d'Astrophysique de l'OMP, CNRS UMR 5572, Observatoire Midi-Pyrénées, 14, avenue Edouard Belin, F-31400 Toulouse, France

Received ..... / Accepted .....

**Abstract.** One of the goals of the ground-based support program for the COROT and MONS/Rømer satellite missions is to characterize suitable target stars for the part of the missions dedicated to asteroseismology. We present the detailed abundance analysis of nine COROT main targets and the Sun using the semi-automatic software VWA. For two additional COROT targets we could not perform the analysis due to the high rotational velocity of these stars. For four stars with low rotational velocity we have also performed abundance analysis by a classical equivalent width method in order to test the reliability of the much faster VWA software. We find that for most elements the derived abundances by the two methods produce the same results to within 0.05 dex. We have explored the correlation of Fe abundance with the lower excitation potential and the Fe I / Fe II ion balance when changing the model parameters and in turn constrained the global atmospheric parameters $T_{\rm eff}$, $\log g$, and [Fe/H] to within 100 K, 0.2 dex, 0.1 dex for five stars which are slow rotators ($v \sin i < 15$ km s$^{-1}$). We find good agreement with the parameters found from Strömgren indices, previous spectroscopic studies, and also $\log g$ determined from the HIPPARCOS parallaxes.

**Key words.** stars: abundances – stars: fundamental parameters –

## 1. Introduction

COROT (COnvection, ROtation, and planetary Transits) is a small space mission, dedicated to asteroseismology and the search for exo-planets (Baglin 2001). Among the targets of the asteroseismology part of the mission, a few bright stars will be monitored continuously over a period of 150 days. These bright targets will be chosen from a list of a dozen F & G-type stars, located in the continuous viewing zone of the instrument. The final choice of targets needs to be made early in the project, as it will impact on some technical aspects of the mission. A precise and reliable knowledge of the candidate targets is required, in order to optimize this final choice.

Among the information which needs to be gathered on the candidate targets, fundamental parameters like effective temperature, surface gravity and metallicity will play a major role in the selection of targets for COROT. Projected rotation velocities, as well as detailed abundances of the main chemical elements will also be taken into account in the selection process.

This information on the targets will subsequently be used for the selected stars, in conjunction with asteroseismological data obtained by COROT, to provide additional constraints for the modeling of the interior and the atmospheres of these stars.

In Section 2 we summarize the spectroscopic observations and data reduction, in Section 3 we discuss the de-

*Send offprint requests to*: H. Bruntt, e-mail: bruntt@phys.au.dk

* Based on observations obtained with the 193 cm telescope at Observatoire d'Haute Provence, France

**Table 1.** Log of the observations for the spectra of proposed COROT targets we have analysed. The signal-to-noise in the last column is calculated around 6 500 Å in bins of 3 km s$^{-1}$.

| HD— | Date | UT start | $t_{\rm exp}$ [s] | S/N |
|---|---|---|---|---|
| 43318 | 19-Jan-98 | 22:38 | 900 | 120 |
| 43587 | 14-Jan-98 | 22:32 | 1800 | 250 |
| 45067 | 15-Jan-98 | 22:20 | 1200 | 260 |
| 49434 | 17-Jan-98 | 22:33 | 600 | 160 |
| 49933 | 21-Jan-98 | 22:17 | 1200 | 210 |
| 55057 | 15-Jan-98 | 23:10 | 900 | 270 |
| 57006 | 10-Dec-00 | 00:41 | 1800 | 250 |
| 171834 | 05-Sep-98 | 19:00 | 1800 | 300 |
| 184663 | 18-Jun-00 | 01:30 | 1000 | 170 |
| 46304 | 17-Jan-98 | 22:05 | 600 | 170 |
| 174866 | 04-Jul-01 | 00:39 | 1500 | 190 |

**Table 2.** Strömgren photometric indices of the COROT main targets taken from Hauck & Mermilliod (1998). HD 46304 and HD 174866 are shown separately: abundance analysis has not been made for these two stars due to their high $v \sin i$.

| HD | $V$ | $b-y$ | $m_1$ | $c_1$ | $H_\beta$ |
|---|---|---|---|---|---|
| 43318 | 5.65 | 0.322 | 0.154 | 0.446 | 2.644 |
| 43587 | 5.70 | 0.384 | 0.187 | 0.349 | 2.601 |
| 45067 | 5.87 | 0.361 | 0.168 | 0.396 | 2.611 |
| 49434 | 5.74 | 0.178 | 0.178 | 0.717 | 2.755 |
| 49933 | 5.76 | 0.270 | 0.127 | 0.460 | 2.662 |
| 55057 | 5.45 | 0.185 | 0.184 | 0.876 | 2.757 |
| 57006 | 5.91 | 0.340 | 0.168 | 0.472 | 2.625 |
| 171384 | 5.45 | 0.254 | 0.145 | 0.560 | 2.682 |
| 184663 | 6.37 | 0.275 | 0.149 | 0.476 | 2.665 |
| 46304 | 5.60 | 0.158 | 0.175 | 0.816 | 2.767 |
| 174866 | 6.33 | 0.122 | 0.178 | 0.960 | 2.822 |

termination of the fundamental parameters from photometry and HIPPARCOS parallaxes and we summarize previous spectroscopic studies of the target stars. In Section 4 we describe the two different methods we have used for abundance analysis, and in Section 5 we give the result of these. In Section 6 we discuss how we constrain the fundamental atmospheric parameters using abundance results for a grid of models. Lastly, we give our conclusions in Section 7.

## 2. Spectroscopic observations

We have obtained multiple spectra of each one of the 11 candidate main targets of COROT, using the ELODIE spectrograph attached to the 1.93 m telescope at Observatoire de Haute-Provence (OHP). ELODIE is a fiber-fed cross-dispersed Echelle spectrograph, providing a complete spectral coverage of the 3800–6800 Å region, at a resolution of $R = 45\,000$ (Baranne et al. 1996). Table 1 gives the log of the observations for the spectra used in this analysis.

### 2.1. Data reduction

We used the on-line INTER-TACOS reduction package available at OHP (Baranne et al. 1996). This software performs bias and background light subtraction, spectral order localization, and finally extracts spectral orders using the optimal extraction procedure (Horne 1986). The high spatial frequency instrumental response is corrected by dividing the stellar spectra by the spectrum of a flat-field lamp. Wavelength calibration is provided by spectra of a Th/Ar lamp, using a two-dimensional Chebychev polynomial fitting of the Th/Ar lines.

Special care was taken to correct for the grating blaze function, as differences in the spectrograph illumination between stellar and flat-field light beams usually result in an imperfect correction. Instead of using a flat-field spectrum, we have therefore used a high signal-to-noise spectrum of an O-type star, 10 Lac, to determine the blaze function. The orders of the 10 Lac spectrum were examined one by one, and the line-free regions of each order were identified. The blaze function at each spectrograph order was then represented by low-order cubic splines fitted to these line-free regions, and the stellar spectra were subsequently divided by this newly determined blaze function. This procedure results in an adequate blaze correction, producing in particular a good match of adjacent orders in the overlapping region. Note also that ELODIE is a very stable instrument, so that only one spectrum of 10 Lac was used to define the blaze function, although the observations reported here span several years.

Since the overall blaze function was removed by a star of much earlier spectral class than the observed F and G-type stars the continuum level was not entirely flat. Hence we made low-order cubic spline fits to make the final continuum estimate. For the overlapping part of the orders we made sure that the overlap was better than 0.5%.

We are aware of the problem of fitting low-order splines to correct the continuum. In this process we manually mark the points in the spectrum which we assume are at the continuum level. When using the VWA software (Bruntt et al. 2002, cf. Section 4.2) we can inspect the fitted lines and in this way detect problems with the continuum level. In these cases we reject the abundances found for these lines. Alternatively, one could select continuum points from a synthetic spectrum. In this case one assumes the abundances given to the model are correct which in turn will affect the final abundance estimates. Although this is a second-order effect we have not used this method for selecting continuum points. Problems with the continuum level will also be discussed in Section 5.1.

## 3. Fundamental atmospheric parameters

In this Section we will discuss previous results for the fundamental atmospheric parameters of the proposed COROT targets. First we will present the results from the calibration of Strömgren photometry and when using the HIPPARCOS parallaxes to determine $\log g$.

**Fig. 1.** Evolution tracks from Girardi et al. (2000) for solar metallicity. The position of the proposed COROT targets and the Sun are shown.

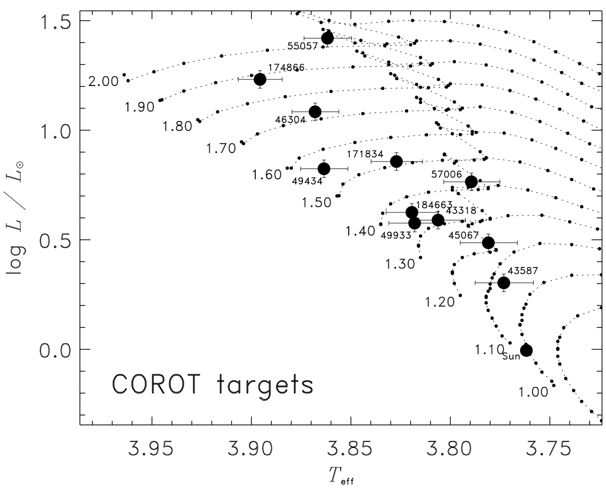


**Table 3.** Overview of the parameters of the proposed COROT main targets. The first column is the HD number followed by the parameters from the TEMPLOGG software. Column 5 and 6 are the masses found from evolution tracks (cf. Fig. 1) and the $\log g_\pi$ values found from the HIPPARCOS parallaxes. The numbers in parenthesis is the estimated standard error. The determination of $v \sin i$ is described in Section 4.2.

| HD | $T_{\rm eff}$ | $\log g$ | $[{\rm M/H}]_{\rm phot}$ | $M/M_\odot$ | $\log g_\pi$ | $v \sin i$ |
|---|---|---|---|---|---|---|
| 0 | 5778 | 4.44 | +0.00 | 1 | 4.44 | 6 |
| 43318 | 6400 | 4.19 | −0.15 | 1.23(17) | 3.96(14) | 8 |
| 43587 | 5931 | 4.31 | −0.11 | 1.02(20) | 4.19(15) | 2.5 |
| 45067 | 6038 | 4.03 | −0.22 | 1.08(17) | 3.95(15) | 6 |
| 49434 | 7304 | 4.14 | −0.01 | 1.55(14) | 4.25(11) | 84 |
| 49933 | 6576 | 4.30 | −0.45 | 1.17(18) | 4.20(14) | 14 |
| 55057 | 7274 | 3.61 | +0.10 | 2.12(22) | 4.22(12) | 120 |
| 57006 | 6158 | 3.72 | −0.13 | 1.28(17) | 3.58(16) | 9 |
| 171834 | 6716 | 4.03 | −0.22 | 1.40(17) | 4.13(13) | 63 |
| 184663 | 6597 | 4.25 | −0.17 | 1.29(14) | 3.63(15) | 53 |
| 46304 | 7379 | 3.93 | −0.09 | 1.68(14) | 4.18(11) | 200 |
| 174866 | 7865 | 3.86 | −0.18 | 1.77(14) | 3.86(15) | 165 |

**Fig. 2.** Comparison of the $\log g_\pi$ values found from the HIPPARCOS parallaxes and $\log g_{\rm phot}$ from TEMPLOGG using Strömgren indices. The straight line is added to aid the eye. Typical error bars are shown on top of HD 184663.

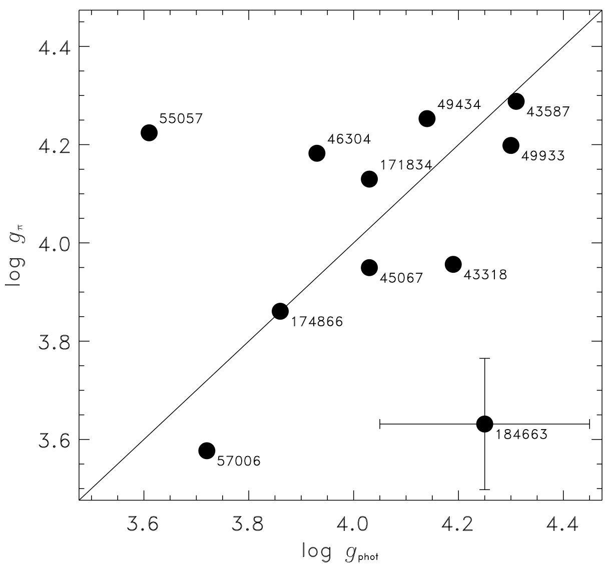


### 3.1. Strömgren photometry

The Strömgren indices of the target stars are taken from the catalogue of Hauck & Mermilliod (1998) and are listed in Table 2. We have used the software TEMPLOGG (Rogers 1995, see also Kupka & Bruntt 2001) to find the appropriate calibration to obtain the basic parameters, i.e. $T_{\rm eff}, \log g$, and $[{\rm M/H}]_{\rm phot}$ which are used to calculate the first iteration of model atmospheres. These parameters are given in Table 3. The accuracy of the parameters $T_{\rm eff}$, $\log g$, and $[{\rm M/H}]_{\rm phot}$ are around 200–250 K, 0.3 dex, and 0.2 dex according to Rogers (1995).

### 3.2. Using HIPPARCOS parallaxes to determine $\log g$

We have used HIPPARCOS parallaxes to find the surface gravities of the stars. We use the equation $\log g_\pi = 4[T_{\rm eff}] + [M] + 2\log\pi + 0.4(V + BC_V + 0.26) + 4.44$, where $[X] = \log(X/X_\odot)$. We use $T_{\rm eff}$ from TEMPLOGG and we determine the bolometric correction $BC_V$ from Bessell et al. (1998): we used their results for solar metallicity and no overshoot. We have estimated the masses of the stars by using the evolution tracks by Girardi et al. (2000). The evolution tracks for solar metallicity is shown in Figure 1 in which the locations of the COROT targets are also shown along with error bars. We have made interpolations in models for metallicity $Z = 0.019$ (solar) and $Z = 0.008$. For example, HD 49933 has the lowest metallicity in the sample: the derived mass is $M/M_\odot = 1.17$, significantly lower than estimated from its position relative to the solar-metallicity isochrones in Figure 1.

The determination of $\log g$ when using the calibration of Strömgren indices and the HIPPARCOS parallax are shown in Figure 2. Mean error bars which are representative for all the stars are shown on top of HD 184663. The results agree very well except for HD 55057 and HD 184663. HD 55057 has $v \sin i = 120\ {\rm km\,s^{-1}}$ which could alter the Strömgren $c_1$ index and hence give erroneously large $\log g$ (Nissen 1988 discussed several reasons for observed anomalous $c_0$ in open clusters). When rejecting the two outliers the difference of the remaining nine stars is $(\log g_{\rm phot} - \log g_\pi) = 0.013 \pm 0.13$.

### 3.3. Previous spectroscopic studies

Lastennet et al. (2001) (herafter LLB) have analyzed some of the potential COROT targets and they used the same spectra we have used in this study: we have six stars in common with LLB (compared in Table 4). LLB have used the H $\alpha$ hydrogen lines to determine $T_{\rm eff}$. The fact that the H $\alpha$ line covers three Echelle orders makes the determination of the continuum a difficult task, hence the error on $T_{\rm eff}$ is around 250 K. LLB have compared Johnson and Strömgren photometric indices of observations and calculated model atmospheres in order to determine $T_{\rm eff}$, $\log g$, and [Fe/H]. The $T_{\rm eff}$ estimates made by LLB agree well with the results from TEMPLOGG although the two different techniques (H $\alpha$ lines and photometry) show systematic differences at the 100 K level. LLB have used Fe I and Fe II lines in a limited spectral region to estimate [Fe/H] and $\log g$ to within 0.2 dex and 0.5 dex and these results also agree with TEMPLOGG. The exception is for their star HD 46304 but this is probably due to its high $v \sin i = 200$ km s$^{-1}$.

Vogt et al. (2002) have found a low-mass companion around HD 43587 in a campaign to search for exo-planets. From their Keck spectra they find $T_{\rm eff} = 5795$ K, [Fe/H] = $-0.03$, and $v \sin i = 2.7$ km s$^{-1}$ (Vogt et al. 2002 have not quoted errors on $T_{\rm eff}$ and metallicity). D. Fisher (private communication) has reanalysed the Keck spectrum and finds $T_{\rm eff} = 5931 \pm 100$ and [Fe/H] $= 0.00 \pm 0.05$.

The extensive catalogue by Cayrel de Strobel et al. (2001) contains fundamental atmospheric parameters found in the literature based on analyses of medium-high resolution spectra. We have found results from several studies for most of the stars examined here. Unfortunately, no individual error estimates are given by the original authors.

In Table 4 we summarize the results for the previous studies mentioned above and our new results (cf. Section 6). The references in column five of Table 4 are given in Table 5. Note that for LLB we give two results: (9a) which corresponds to their result when comparing observed and synthetic colour-indices in $B-V$, $U-B$, and $b-y$; (9b) $T_{\rm eff}$ is determined from the H $\alpha$ line while $\log g$ and [Fe/H] are determined from a set of Fe I and Fe II lines in a region around 6 130 Å.

## 4. Abundance analysis

In this Section we first discuss the atmospheric models we have applied before describing the two methods we have used to determine abundances.

### 4.1. Atmospheric models

We have used a modified version of the ATLAS9 code (Kurucz 1993) for the calculation of the atmospheric models (Kupka 1996, Smalley & Kupka 1997) in which turbulent convection theory in the formulation of Canuto & Mazzitelli (1991, 1992) is implemented.

For the extraction of models in a grid with different $T_{\rm eff}$ and $\log g$ we have used interpolation in the grid of models (also modified ATLAS9 models) distributed by Heiter et al. (2003). We use these interpolated models to make abundance analysis in order to constrain the fundamental parameters in Section 6.

The final abundance results presented in Section 5 are based on individually calculated models.

### 4.2. Automatic abundance analysis with VWA

We have used the semi-automatic software package VWA (Bruntt et al. 2002) to carry out the abundance analysis of nine COROT targets. For each star the software selects the least blended lines from atomic line list data extracted from the VALD data base (Kupka et al. 1999). For each selected line the synthetic spectrum is calculated and the input abundance is changed iteratively until the equivalent width of observed and synthetic line match. We used SYNTH which was kindly provided by N. Piskunov (version 2.5, see Valenti & Piskunov 1996) to calculate the synthetic spectrum.

In order to be able to compare the observed and synthetic spectra the latter is convolved by the instrumental profile (approximated by a Gaussian) and a rotational broadening profile. The projected rotational velocities were determined by fitting the synthetic spectrum of a few of the least blended lines to the observed spectrum by convolving with different rotation profiles. The accuracy of $v \sin i$ by this method is about 10-15%. LLB used a more refined method (see Donati et al. 1997) but our results agree within the estimated errors – except for HD 43587. Vogt et al. (2002) find $v \sin i = 2.7$ km s$^{-1}$ (D. Fisher finds $v \sin i = 2.2$ km s$^{-1}$ from the same spectrum, private communication) for HD 43587 which agrees with LLB and consequently we have used a low value of $v \sin i = 2.5$ km s$^{-1}$. The reason for the apparent discrepancy is the limit of the spectral resolution of the ELODIE spectrograph i.e. $v = c/R = 6.7$ km s$^{-1}$. Note that since VWA relies on the measurement of equivalent widths small errors in $v \sin i$ will have a negligible effect on the derived abundances.

### 4.3. "Classical" abundance analysis

"Classical" abundance analysis has been applied to three slowly rotating COROT targets – HD 43587, HD 45067, and HD 57006 – and to the solar spectrum (observed reflection from the Moon).

Equivalent widths of all identified unblended and some partialy blended spectral lines were measured by using DECH software based on PC (Galazutdinov, 1992). Abundance calculations were performed in the LTE approximation by using WIDTH9 (Kurucz 1993; with modifications by V.Tsymbal and L.Mashonkina for PC, private communication). Atomic parameters of the spectral lines were extracted from the VALD data base with correc-

**Table 4.** Results of previous studies to determine the fundamental parameters of the COROT targets. The references are given in Table 5.

| HD | $T_{\rm eff}$ | $\log g$ | [Fe/H] | Ref. |
|---|---|---|---|---|
| 43318 | 6400(120) | 4.1(0.2) | +0.08(07) | 1a |
| - | 6347 | 4.07 | −0.17 | 4 |
| - | 6257 | 4.09 | −0.19 | 7 |
| - | 6320(100) | 4.5(0.2) | +0.0(0.15) | 9a |
| - | 6250(250) | 4.0(0.5) | −0.3(0.2) | 9b |
| - | 6400(200) | 4.19(0.2) | −0.15(0.2) | 11 |
| 43587 | 6000(100) | 4.4(0.2) | +0.01(0.07) | 1a |
| - | 5780(100) | 4.25(0.15) | | 1b |
| - | 5775 | | −0.08(0.04) | 5 |
| - | 5720(100) | 4.3(0.4) | −0.2(0.10) | 9a |
| - | 6000(250) | 4.5(0.5) | −0.1(0.2) | 9b |
| - | | | −0.03 | 13 |
| - | 5795 | | −0.03 | 12 |
| - | 5931(200) | 4.31(0.2) | −0.11(0.2) | 11 |
| - | 5931(100) | | −0.00(0.05) | 6 |
| 45067 | 6040(100) | 4.1(0.2) | −0.02(0.07) | 1a |
| - | 6050(100) | 4.00(0.15) | | 1b |
| - | 6056 | 4.17 | −0.16 | 2 |
| - | 5940(100) | 3.8(0.35) | −0.1(0.08) | 9a |
| - | 6000(250) | 4.0(0.5) | −0.1(0.2) | 9b |
| - | 6038(200) | 4.03(0.2) | −0.22(0.2) | 11 |
| 49434 | | | −0.11(0.15) | 1a |
| - | 7240(150) | 4.0(0.25) | −0.1(0.25) | 9a |
| - | 7250(250) | | | 9b |
| - | | | −0.14 | 3 |
| - | 7304(200) | 4.14(0.2) | −0.01(0.2) | 11 |
| 49933 | 6650(100) | 4.2(0.2) | −0.40(0.09) | 1a |
| - | 6545 | 4.00 | −0.35 | 10 |
| - | 6300 | 4.5 | −0.88 | 8 |
| - | 6472 | 4.17 | −0.35 | 2 |
| - | 6595 | 4.16 | −0.43 | 4 |
| - | 6600(150) | 4.3(0.25) | −0.6(0.15) | 9a |
| - | 6500(250) | 4.0(0.5) | −0.5(0.2) | 9b |
| - | 6576(200) | 4.30(0.2) | −0.45(0.2) | 11 |
| 55057 | | | +0.02(0.08) | 1a |
| - | 7274(200) | 3.61(0.2) | +0.10(0.2) | 11 |
| 57006 | 6160(100) | 3.87(0.2) | −0.01(0.07) | 1a |
| - | 6100(100) | 3.50(0.15) | −0.01(0.01) | 1b |
| - | 6158(200) | 3.72(0.2) | −0.13(0.2) | 11 |
| 171834 | 7000(250) | 4.0(0.5) | −0.28(0.15) | 1a |
| - | 6670 | 4.05 | −0.42 | 2 |
| - | 6700(150) | 3.9(0.25) | −0.5(0.15) | 9a |
| - | 6750(250) | | | 9b |
| - | 6716(200) | 4.03(0.2) | −0.22(0.2) | 11 |
| 184663 | 6600(250) | 4.2(0.5) | −0.14(0.15) | 1a |
| - | 6535 | 4.22 | +0.03 | 2 |
| - | 6597(200) | 4.25(0.2) | −0.17(0.2) | 11 |

tions of oscillator strengths in a few cases as described in the paper of Bikmaev et al. (2002). Lines with equivalent widths < 100 mÅ were used when possible to decrease influences of microturbulence and inaccurate damping constants. Model atmospheres were calculated as it described in Section 4.1 with the adopted parameters of $T_{\rm eff}$, $\log g$, and solar composition. Effective temperatures were determined by using Johnson and Strömgren color-indices ex-

**Table 5.** The references for Table 4.

Ref. 1a: Found in this study using VWA
Ref. 1b: Parameters used for "classical" analysis
Ref. 2: Balachandran (1990)
Ref. 3: Bruntt et al. (2002)
Ref. 4: Edvardsson et al. (1993)
Ref. 5: Favata et al. (1997)
Ref. 6: Fisher, D. (private communication)
Ref. 7: Gratton et al. (1996)
Ref. 8: Hartmann & Gehren (1988)
Ref. 9a: Lastennet et al. (2001) (colours)
Ref. 9b: Lastennet et al. (2001) (spectroscopy)
Ref. 10: Perrin (1976)
Ref. 11: Rogers (1995): TEMPLOGG
Ref. 12: Vogt et al. (2002)
Ref. 13: Zakhozhaj & Shaparenko (1996)

**Fig. 3.** Comparison of the abundance analysis results for the two different approaches. We show the differences in the overall abundances for several elements for four different stars with low $v \sin i$. The full error bars are the standard deviation of the mean. If less than five lines were used in the estimate of the deviation we have used a dashed "error-bar" corresponding to 0.15 dex.

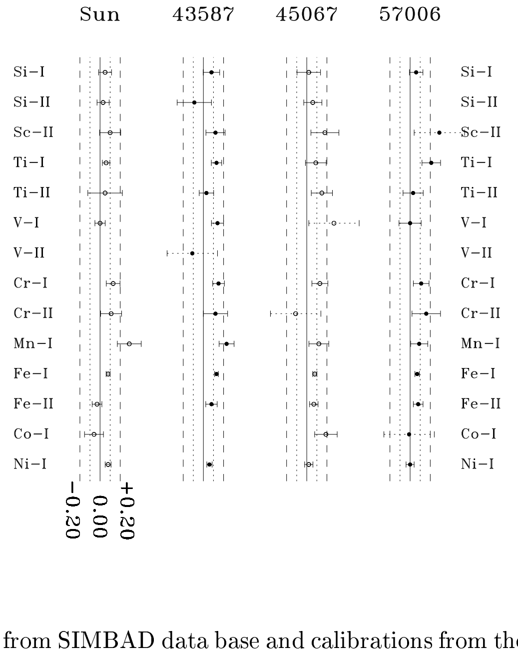


tracted from SIMBAD data base and calibrations from the $\log g$ parameter was determined by using HIPPARCOS parallaxes as indicated in Section 3.2. Within of the estimated errors these independently determined values of $T_{\rm eff}$ and $\log g$ are very close to those indicated in the Table 3. For completion the values we have used are given in Table 4 marked with Ref. 1b.

For each star microturbulent velocity was choosen as to minimize the correlation between the abundances and equivalent widths found for Fe, Cr, Ti, Ni, and Co lines.

Results of abundance determination is given in Table 7 and in Figure 4.

**Table 6.** Comparison of the abundances of the main elements by two different methods. The differences are given in the sense VWA minus "classical". The number $n$ indicates the number of lines used with VWA while in the "classical" analysis more lines were selected (cf. Table 7). The numbers in parenthesis are the combined RMS standard deviations while the number 9.99 is used if only one line is present. This data is plotted in Figure 3 but here the error bars are the standard deviation of the mean.

| Element | Sun | | HD 43318 | | HD 43587 | | HD 45067 | |
|---|---|---|---|---|---|---|---|---|
| Si I | 0.05(0.17) | 8 | 0.08(0.23) | 9 | 0.02(0.26) | 6 | 0.06(0.15) | 6 |
| Si II | 0.03(0.06) | 2 | −0.09(0.17) | 2 | 0.06(0.09) | 2 | | |
| Sc II | 0.10(0.21) | 5 | 0.12(0.19) | 5 | 0.18(0.24) | 4 | 0.29(0.36) | 3 |
| Ti I | 0.06(0.17) | 22 | 0.13(0.24) | 23 | 0.09(0.40) | 16 | 0.21(0.26) | 9 |
| Ti II | 0.05(0.42) | 7 | 0.03(0.16) | 6 | 0.15(0.21) | 5 | 0.03(0.20) | 5 |
| V I | −0.00(0.17) | 12 | 0.14(0.17) | 9 | 0.27(0.53) | 3 | 0.00(0.11) | 2 |
| V II | | | −0.11(9.99) | 1 | | | | |
| Cr I | 0.13(0.28) | 18 | 0.15(0.21) | 14 | 0.13(0.25) | 11 | 0.11(0.22) | 9 |
| Cr II | 0.11(0.18) | 4 | 0.12(0.24) | 5 | −0.11(0.44) | 2 | 0.16(0.20) | 3 |
| Mn I | 0.29(0.29) | 7 | 0.23(0.21) | 9 | 0.12(0.17) | 4 | 0.09(0.17) | 5 |
| Fe I | 0.08(0.23) | 137 | 0.13(0.22) | 143 | 0.08(0.25) | 141 | 0.07(0.24) | 116 |
| Fe II | −0.03(0.16) | 12 | 0.08(0.18) | 11 | 0.07(0.14) | 12 | 0.08(0.18) | 15 |
| Co I | −0.06(0.21) | 6 | | | 0.19(0.25) | 6 | −0.01(9.99) | 1 |
| Ni I | 0.08(0.19) | 44 | 0.06(0.18) | 47 | 0.02(0.21) | 27 | −0.00(0.20) | 26 |

## 5. Abundances of the COROT targets

The result of the abundance analysis of the COROT targets is given in Table 7. The abundances are given relative to the solar abundances found by Grevesse et al. (1998). In parenthesis we give the RMS standard deviation based on the line-to-line scatter. When only one line was used we write 9.99 in parenthesis.

The abundances of the COROT main targets and the Sun given in Table 7 are also shown graphically in Figure 4. The plotted error bars are the combined standard deviations of the mean of each element measured in the star and for the Sun, i.e. the results by Grevesse et al. (1998). The typical standard errors from Grevesse et al. (1998) is 0.05 dex. Note that the spectrum we have analysed for the Sun is taken from reflected moon light.

From the abundance patterns in Figure 4 we find no evidence of classical chemically peculiar stars.

We have made the abundance analysis of HD 49434, which was also analysed by Bruntt et al. (2002). In the present study we have included more Fe I lines. While our result agrees with Bruntt et al. (2002) for Fe I we note that the abundances for the other elements are based on only a few lines and thus large systematic errors will dominate. This will also be the case for HD 55057, HD 171834, and HD 184663 which are also moderate rotators. Still, we have included the results for all elements for completion.

We have adjusted the microturbulence $\xi_t$ of each star until we see no correlation between the abundances and equivalent widths found for the Fe I lines. For the slowly rotating stars ($v \sin i < 25$ km s$^{-1}$) the error on $\xi_t$ is about 0.2 km s$^{-1}$, for the stars rotating moderately fast ($50 < v \sin i < 85$ km s$^{-1}$) the error is 0.5 km s$^{-1}$, and 0.7 km s$^{-1}$ for HD 55057 which has $v \sin i = 120$ km s$^{-1}$. The constribution to the error on the abundances from the uncertainty of the microturbulence is about 0.03 dex for Fe for the low rotators while for stars with the highest $v \sin i$ (HD 49434 and HD 55057) the errors in the abundances are of the order 0.07–0.10 dex. This systematic error has not been included in the rms errors given in parenthesis in Table 7.

### 5.1. Comparison of the abundance analysis methods

The two methods described above have different advantages and disadvantages. Most importantly VWA relies on the computation of the synthetic spectrum and thus this method can be used for stars with moderately high $v \sin i$ and a mild degree of blending of lines is tolerated. Also, VWA is a semi-automatic program and the user may easily inspect if the fitted lines actually match the observed spectrum. When comparing the observed and synthetic spectrum obvious problems with the continuum level can be found: errors of just 2 % of the continuum level will give large differences in the derived abundance — perhaps as much as 0.1–0.2 dex and such lines are rejected after visual inspection.

In Figure 3 and in Table 6 we show the comparison of the final abundance analysis results using the two methods described above. We show the differences in the sense "VWA" *minus* "classical" for four different stars with low $v \sin i$ for which both methods are applicable. The differences refer to the mean abundances, i.e. the lines are not necessarily the same in the two analyses. We only show the differences for elements for which either the neutral or the ionized element has at least five lines in both studies.

The plotted error bars in Figure 3 are calculated as the quadratic sum of the the standard deviation of the mean for each method. In the cases where we have fewer than five lines we have no good estimate of the error but from the elements with more lines we find that an overall error of 0.15 dex seems plausible. For these elements we have plotted a dashed "error-bar" corresponding to 0.15 dex for the difference in abundance estimates.

**Table 7.** Results of abundance analysis of COROT targets. The abundances are given relative to the standard solar abundances (Grevesse et al. 1998 subtracted). The results are given for the "classical" method for the Sun, HD 43587, HD 45067, and HD 57006, while for the remaining stars the results are from VWA. The results are also plotted in Figure 4.

| Element | Sun | | HD 43318 | | HD 43587 | | HD 45067 | | HD 55057 | |
|---|---|---|---|---|---|---|---|---|---|---|
| Li I | 0.19(9.99) | 1 | | | | | | | | |
| C I | -0.13(0.15) | 5 | 0.00(0.07) | 3 | 0.05(0.13) | 6 | -0.19(0.19) | 7 | -0.18(0.15) | 4 |
| O I | -0.13(0.15) | 2 | | | -0.20(0.12) | 3 | -0.40(0.17) | 3 | -0.29(0.07) | 3 |
| Na I | 0.02(0.07) | 6 | -0.14(0.15) | 2 | -0.08(0.11) | 6 | -0.03(0.12) | 3 | -0.17(0.08) | 5 |
| Mg I | -0.15(0.11) | 6 | 0.02(9.99) | 1 | -0.09(0.18) | 4 | -0.20(0.18) | 5 | -0.15(0.13) | 5 |
| Al I | 0.06(0.11) | 3 | | | -0.20(0.10) | 3 | -0.09(0.09) | 3 | -0.05(0.14) | 3 |
| Si I | 0.12(0.15) | 20 | 0.06(0.08) | 7 | -0.01(0.19) | 25 | 0.09(0.19) | 16 | 0.08(0.15) | 16 |
| S I | 0.01(0.13) | 5 | | | -0.12(0.19) | 4 | -0.14(0.07) | 4 | -0.19(0.15) | 3 |
| Ca I | 0.07(0.20) | 9 | 0.07(0.09) | 5 | -0.10(0.12) | 8 | 0.03(0.15) | 8 | -0.02(0.14) | 5 |
| Sc I | -0.14(0.17) | 4 | | | 0.02(0.27) | 3 | -0.14(9.99) | 1 | | |
| Sc II | 0.05(0.18) | 15 | 0.20(0.15) | 6 | 0.01(0.15) | 12 | 0.03(0.14) | 12 | -0.07(0.18) | 11 |
| Ti I | -0.03(0.15) | 81 | -0.07(0.21) | 21 | -0.14(0.12) | 55 | -0.12(0.13) | 42 | -0.19(0.12) | 29 |
| Ti II | 0.02(0.11) | 27 | 0.07(0.22) | 18 | -0.05(0.13) | 23 | -0.01(0.19) | 24 | -0.12(0.10) | 16 |
| V I | -0.01(0.13) | 27 | 0.14(0.63) | 3 | -0.17(0.10) | 18 | -0.18(0.11) | 14 | -0.18(0.12) | 6 |
| V II | 0.09(0.14) | 8 | 0.37(0.22) | 2 | -0.02(0.10) | 5 | -0.15(0.08) | 5 | -0.01(0.24) | 6 |
| Cr I | 0.03(0.17) | 68 | -0.06(0.23) | 21 | -0.08(0.09) | 42 | -0.03(0.16) | 44 | -0.11(0.16) | 21 |
| Cr II | 0.07(0.09) | 15 | -0.01(0.21) | 11 | 0.05(0.11) | 9 | 0.06(0.14) | 14 | 0.05(0.13) | 9 |
| Mn I | 0.16(0.20) | 27 | -0.01(0.21) | 6 | -0.05(0.16) | 20 | -0.08(0.15) | 22 | -0.10(0.13) | 12 |
| Fe I | 0.09(0.17) | 332 | 0.01(0.15) | 188 | -0.01(0.17) | 210 | 0.02(0.17) | 244 | 0.00(0.15) | 167 |
| Fe II | 0.02(0.13) | 40 | -0.07(0.13) | 25 | -0.06(0.15) | 38 | -0.08(0.12) | 35 | -0.09(0.13) | 26 |
| Co I | 0.01(0.19) | 46 | 0.27(0.84) | 2 | -0.09(0.17) | 34 | -0.11(0.19) | 26 | -0.14(0.13) | 12 |
| Ni I | 0.05(0.13) | 90 | -0.15(0.21) | 50 | -0.04(0.11) | 83 | -0.05(0.14) | 75 | -0.09(0.13) | 41 |
| Cu I | -0.09(0.07) | 2 | -0.10(0.06) | 2 | 0.11(0.31) | 3 | -0.01(0.23) | 3 | -0.23(0.15) | 2 |
| Zn I | 0.10(0.15) | 3 | | | -0.02(0.08) | 3 | -0.06(0.09) | 3 | -0.13(0.17) | 3 |
| Sr I | | | | | 0.42(9.99) | 1 | 0.56(9.99) | 1 | 0.57(9.99) | 1 |
| Sr II | -0.23(0.39) | 2 | | | -0.28(0.26) | 3 | -0.22(0.19) | 3 | -0.11(0.15) | 3 |
| Y II | 0.13(0.19) | 14 | 0.04(0.08) | 2 | -0.01(0.18) | 11 | -0.03(0.11) | 12 | -0.09(0.16) | 8 |
| Zr I | -0.25(0.17) | 4 | | | -0.32(0.11) | 3 | -0.28(9.99) | 1 | -0.06(0.11) | 2 |
| Zr II | 0.14(0.16) | 4 | | | -0.19(0.10) | 3 | -0.04(0.34) | 4 | -0.13(0.22) | 4 |
| Ba II | 0.21(0.08) | 2 | | | 0.22(0.06) | 3 | 0.29(0.11) | 5 | 0.33(0.10) | 4 |
| La II | 0.03(0.06) | 5 | | | 0.18(0.20) | 3 | 0.07(0.11) | 4 | 0.05(0.07) | 5 |
| Ce II | 0.01(0.14) | 9 | | | -0.00(0.20) | 15 | -0.12(0.11) | 12 | -0.26(0.17) | 12 |
| Pr II | -0.04(9.99) | 1 | | | -0.09(0.21) | 3 | -0.06(9.99) | 1 | -0.08(9.99) | 1 |
| Nd II | 0.10(0.30) | 19 | | | 0.05(0.28) | 19 | -0.04(0.17) | 16 | -0.23(0.15) | 10 |
| Sm II | -0.09(0.10) | 4 | | | -0.06(0.27) | 7 | 0.14(0.10) | 6 | -0.03(0.15) | 6 |
| Eu II | -0.12(0.06) | 2 | | | 0.01(0.29) | 2 | -0.03(0.10) | 2 | 0.26(0.54) | 2 |
| Element | HD 49434 | | HD 49933 | | HD 57006 | | HD 171834 | | HD 184663 | |
| C I | | | -0.18(0.06) | 2 | | | -0.46(9.99) | 1 | 0.41(9.99) | 1 |
| Na I | | | -0.34(9.99) | 1 | | | | | | |
| Mg I | | | -0.22(9.99) | 1 | | | | | | |
| Si I | | | -0.28(0.07) | 3 | | | | | | |
| S I | | | -0.31(9.99) | 1 | | | -0.09(0.26) | 2 | | |
| Ca I | | | -0.35(0.08) | 3 | | | | | 0.32(9.99) | 1 |
| Sc II | 0.03(9.99) | 1 | -0.32(0.20) | 8 | | | | | -0.12(0.25) | 2 |
| Ti I | | | -0.45(0.17) | 6 | | | | | | |
| Ti II | -0.11(9.99) | 1 | -0.29(0.23) | 12 | | | -0.14(9.99) | 1 | -0.25(9.99) | 1 |
| V II | 0.00(9.99) | 1 | | | | | | | | |
| Cr I | | | -0.36(0.17) | 13 | | | 0.31(9.99) | 1 | -0.32(0.51) | 4 |
| Cr II | -0.15(0.06) | 2 | -0.36(0.12) | 8 | | | | | -0.31(9.99) | 1 |
| Mn I | | | -0.13(9.99) | 1 | | | 0.03(9.99) | 1 | | |
| Fe I | -0.17(0.19) | 11 | -0.33(0.14) | 142 | -0.07(0.88) | 3 | -0.01(0.22) | 28 | 0.04(0.20) | 28 |
| Fe II | | | -0.34(0.16) | 19 | | | -0.17(0.20) | 3 | -0.09(0.38) | 2 |
| Ni I | | | -0.48(0.12) | 27 | | | -0.01(0.43) | 6 | -0.05(0.31) | 7 |
| Y II | | | -0.01(9.99) | 1 | | | | | 0.15(9.99) | 1 |
| Ba II | 0.02(9.99) | 1 | 0.49(0.20) | 3 | | | 0.26(9.99) | 1 | 0.09(9.99) | 1 |

For most elements the two methods are in agreement. The exceptions are systematic differences for Si and Mn. For Si this is due to erroneous $\log gf$ values found in VALD for many of the lines, and for Mn the hyperfine structure levels are not always found in VALD. In the "classical" analysis we have taken care to check the $\log gf$ values by comparison with the same lines observed in the Sun. For the automatic analysis with VWA we have rejected the Si and Mn lines selected by the software if they are *not used* in the "classical" analysis for any of the four slowly rotating stars. Thus, when using the same lines with VWA as used in the "classical" analysis we find good agreement for both Si and Mn for the four stars compared in Figure 3. The same Si and Mn lines are used for the stars only analysed with VWA.

Based on the generally good agreement between the two methods we have used the results of the "classical" method for the Sun, HD 43587, HD 45067, and HD 57006 in the final results and the VWA results for the other stars, cf. Table 7 and Figure 4.

## 6. Constraining model parameters

In order to measure the sensitivity of the derived abundances on the model parameters we have made the abundance analysis for a grid of models for each star. For this purpose we used the VWA software. For the initial model we have used the parameters from TEMPLOGG, cf. Table 3. We have then carried out abundance analysis of Ti, Cr, and Fe for models with lower and higher values of $T_{\rm eff}$ and $\log g$, i.e. at least five models for each star. For each model we adjust the microturbulence to minimize the correlation between abundance of Fe I lines and the measured equivalent width. We note that when using model atmospheres with low $T_{\rm eff}$ or high $\log g$ it was *not always* possible to remove the correlation with equivalent width by using a very low microturbulence ($\xi_t < 0.3 - 0.4$). We take this into account when estimating $T_{\rm eff}$ and $\log g$ of a given star.

We also calculated results for the initial model but with somewhat higher microturbulence than the best fit in order to measure the sensitivity of this parameter.

Changes in the model temperature will affect the depth of Fe I lines while changes in $\log g$ will mostly affect the Fe II lines. Furthermore changes in $T_{\rm eff}$ can be seen from the correlation of Fe I abundances and the lower excitation potential, $E_{\rm low}$ (cf. the Boltzmann equation). This can be used to constrain $T_{\rm eff}$ and $\log g$ for the slow rotators with $v \sin i < 50 - 60$ km s$^{-1}$. For the faster rotators there are few non-blended lines and it is more difficult to constrain the fundamental parameters.

Using the abundance results for models with different $T_{\rm eff}$ but the same $\log g$ we estimate the temperature of the star from the models where there is no correlation of Fe I and $E_{\rm low}$. For models with different $\log g$ but the same $T_{\rm eff}$ we can constrain $\log g$ by forcing "ion-balance" for Ti, Cr, and Fe, i.e. we estimate $\log g$ by minimizing the difference in the abundances found from neutral and ionized lines. For the slowly rotating stars ($v \sin i < 15$ km s$^{-1}$) we can constrain $T_{\rm eff}$ and $\log g$ to within 100 K and 0.2 dex, respectively.

While $\log g$ cannot be constrained better than with the parallax from HIPPARCOS it gives us an independent estimate. On the other hand $T_{\rm eff}$ can be determined more accurately than from Strömgren photometry, i.e. the estimated error is lower by a factor of two. From the many iron lines the metallicity can be determined to within 0.1 dex for the slow rotators ($v \sin i < 15$ km s$^{-1}$) and 0.2 dex for the faster rotators. In the former case this is a factor of two better than the metallicity determined from Strömgren photometry.

Our final $T_{\rm eff}$ and $\log g$ estimates are given in Table 4 along with the [Fe/H] found from the abundance analysis, cf. Section 5.

## 7. Conclusions and future prospects

- We have performed a detailed abundance analysis of the proposed COROT main targets. For the two stars HD 46304 and HD 174866 abundance analysis was not possible due to very high $v \sin i$.
- We have constrained $T_{\rm eff}$, $\log g$, and metallicity to within 100 K, 0.2 dex, and 0.1 dex for the five slow rotators in our sample. For the moderate rotators we cannot constrain the fundamental parameters very well. Our results agree within the errors with all previous studies cited literature.
- We have found no evidence for chemically peculiar stars.
- We have compared two different methods for the analysis which show very good agreement except for Si and Mn in which case special care has to be taken due to erroneous or missing atomic line data. We have shown that the VWA software can potentially be used for larger samples of stars. We note that a future paper in this series will present similar results for the proposed MONS/Rømer targets.

*Acknowledgements.* We are grateful to Nikolai Piskunov for providing us with his software for the calculation of synthetic spectra (SYNTH). This research has made use of the SIMBAD database, operated at CDS, Strasbourg, France. I.B. is grateful to RFBR (grant 02-02-17174) for financial support.

## References

Baglin, A., Auvergne, M., Catala, C., Michel, E., COROT Team, Proceedings of the SOHO 10/GONG 2000 Workshop Ed. A. Wilson, P. L. Pallé, 2001, ESA SP-464, 395

Balachandran, S., 1990, ApJ, 354, 310

Baranne A., Queloz D., Mayor M., Adriansyk G., Knispel G., Kohler D., Lacroix D., Meunier J. P., Rimbaud G., Vin A., 1996, A&AS 119, 373

Bessell M. S., Castelli F., Plez B., 1998, A&A, 333, 231

Bikmaev, I.F., Ryabchikova, T.A., Bruntt, H., Musaev, F.A., Mashonkina, L.A., Belyakova, E.V., Shimansky,

**Fig. 4.** Results of the abundance analysis of the proposed COROT main targets. For each star we plot the derived abundance relative to the Sun (Grevesse et al. 1998) and standard error for elements with at least three lines (cf. Table 7). The scale on the abscissa is given for the Sun. Note that the offset is different for HD 49933 which is the most metal deficient star. To make the plot easier to read, the error bar is plotted with a dashed line style if the standard deviation exceeds 0.25 dex in which case the error bar is set to this value.

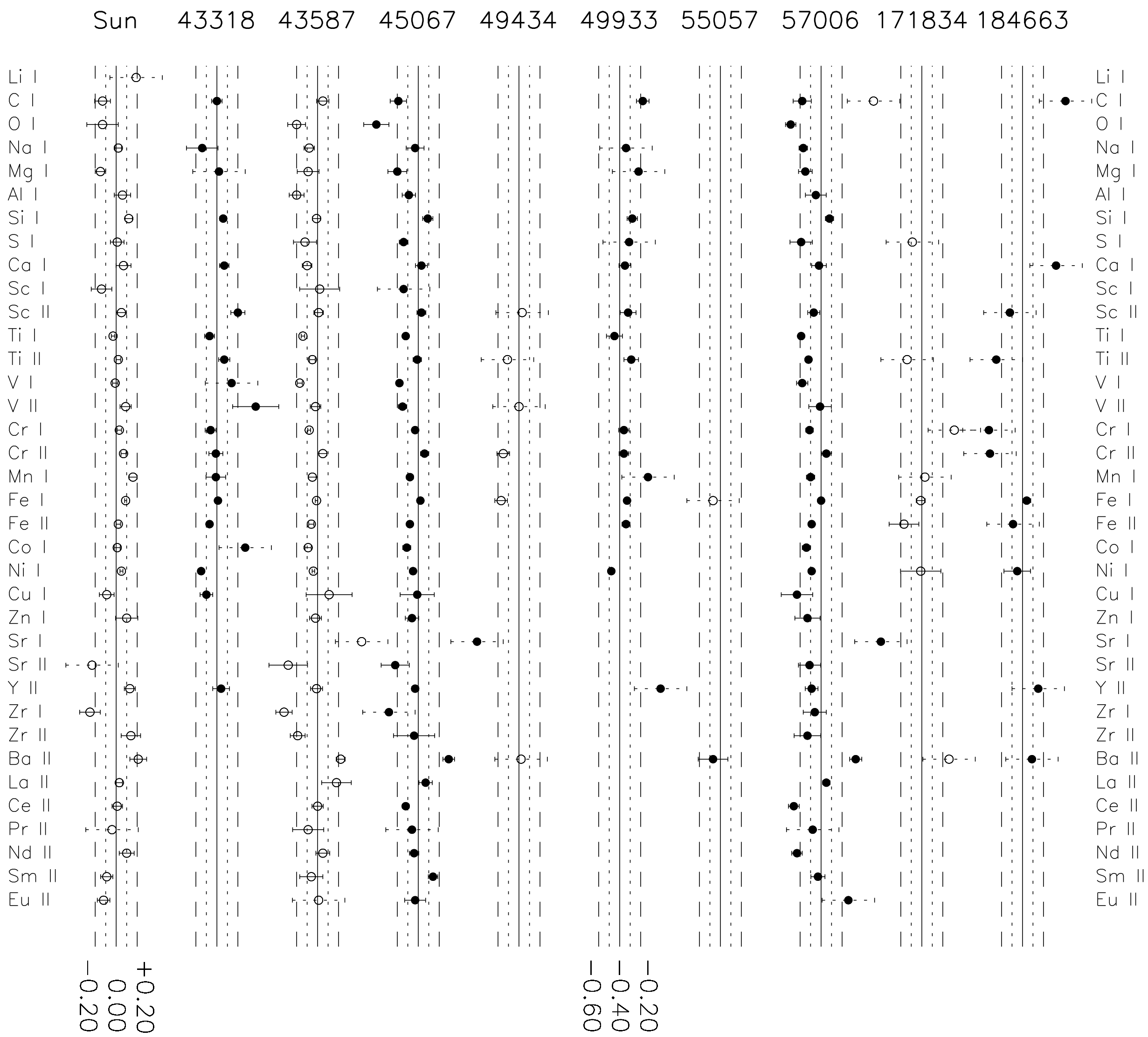


V.V., Barklem, P.S., Galazutdinov G., 2002, A&A, 389, 537
Bruntt H., Catala C., Garrido R. et al., 2002, A&A, 389, 345
Canuto V. M., Mazzitelli I., 1991, ApJ 370, 295
Canuto V. M., Mazzitelli I., 1992, ApJ 389, 724
Cayrel de Strobel, G., Soubiran, C., Ralite, N., 2001, A&A, 373, 159
Donati J. F., Semel M., Carter B. D., Rees D. E., Cameron A. C., 1997, MNRAS 291, 658
Edvardsson, B., Andersen, J., Gustafsson, B., Lambert, D. L., Nissen, P. E., Tomkin, J., 1993, A&A, 275, 101
ESA, 1997, The Hipparcos and Tycho Catalogues, ESA SP-1200
Favata, F., Micela, G., Sciortino, S., 1997, A&A, 323, 809,
Galazutdinov, G., 1992, SAO RAS Preprint N. 92.

Girardi L., Bressan A., Bertelli G. and Chiosi C., 2000, A&AS 141, 371

Gratton, R. G., Carretta, E., Castelli, F., 1996, A&A, 314, 191

Grevesse N., Sauval A. J., 1998, Space Science Reviews 85, 161

Hartmann, K., Gehren, T., 1988, A&A, 199, 269

Hauck B., Mermilliod M., 1998, A&AS, 129, 431

Heiter, U. et al., 2003, *in preparation*

Kupka F., 1996, ASP Conf. Ser., 108, p. 73, eds. Adelman S.J, Kupka F., Weiss W. W.

Kupka F., Piskunov N., Ryabchikova T. A., Stempels H. C., Weiss W. W., 1999, A&AS 138, 119

Kupka F., Bruntt H., 2001, First COROT/MONS/MOST Ground-based Support Workshop, p. 39, ed. Sterken C., University of Brussels

Kurucz R. L., 1993, CD-ROM 18, ATLAS9 Stellar Atmosphere Programs and 2 km/s Grid

Lastennet E., Lignières F., Buser R., Lejeune T., Lüftinger T., Cuisinier F., van't Veer-Menneret C., 2001, A&A, 365, 535

Nissen, P. E., 1988, A&A, 199, 146

Perrin, M. N., 1976, Ph.D. Thesis

Rogers N. Y., 1995, Comm. in Asteroseismology 78

Smalley B., Kupka F., 1997, A&A 328, 349

Valenti J. A., Piskunov N., 1996, A&AS 118, 595

Vogt, S. S., Butler, R. P., Marcy, G. W., Fischer, D. A., Pourbaix, D., Apps, K., Laughlin, G., 2002, ApJ, 568, 352

Zakhozhaj, V. A., Shaparenko, E. F., 1996, Kinematika i Fizika Nebesnykh Tel, 12, 20-29

# Index